

# Active cooling in additively man- ufactured liquid rocket engines

Comparing regenerative, film  
and transpiration cooling  
S. T. Koehler



# Active cooling in additively manufactured liquid rocket engines

Comparing regenerative, film and  
transpiration cooling

by

S. T. Koehler

to obtain the degree of Master of Science  
at the Delft University of Technology,  
to be defended publicly on Tuesday August 25, 2020 at 13:00.

Student number:	4235436	
Thesis committee:	Prof. Dr. E.K.A. Gill	TU Delft; chair
	Ir. B.T.C. Zandbergen	TU Delft; supervisor
	Ir. J.A. Melkert	TU Delft

An electronic version of this thesis is available at <http://repository.tudelft.nl/>.

Cover page: an additively manufactured rocket engine, credit: NASA





# Preface

This thesis has been performed as the final part of the Master of Science degree at Aerospace Engineering at the Delft University of Technology. The work presented was performed at Rocket Factory Augsburg (RFA), a company developing a small satellite launcher. In my view, the results obtained can serve as an excellent road map for further investigations in transpiration cooling in liquid rocket engines. The found sensitivities and accuracies of the models used in this thesis, combined with literature, can serve as a basis for the (engineering) decisions required to develop a transpiration cooled flight engine.

I would like to thank David for the suggestion of the topic and his calm and always on point guidance. Furthermore, I have to thank everybody at RFA for the opportunity to perform my thesis there. The feedback, advice, critical questions and the friendliness of everybody at the company has helped me a lot. Special thanks to Michael for the help with the test setup.

My gratitude goes out to Ir. Barry Zandbergen for his supervision and critical and elaborate feedback to ensure the best academic value of this thesis. Additional thanks to Tobias Langener who provided extra validation data.

*Stijn Koehler  
Delft, July 2020*



# Contents

Preface	iii
Summary	ix
List of figures	xi
List of tables	xv
Abbreviations	xxi
1 Introduction	1
1.1 Background and relevance	1
1.2 Existing transpiration cooled engines	3
1.3 Reference engine and coolant properties	4
1.4 Wall materials and additive manufacturing capabilities	6
1.5 Research goals and research questions	7
1.6 Research plan	9
1.7 Thesis outline	10
2 Regenerative cooling model	13
2.1 Model description	13
2.1.1 Combustion gas properties	14
2.1.2 Heat transfer hot gas side	14
2.1.3 Heat transfer coolant side	16
2.1.4 Model summary	18
2.2 Verification and validation	19
2.2.1 Comparison with CIRA engine	20
2.2.2 Calibration of the hot gas heat transfer coefficient	22
2.3 Conclusions	23
3 Transpiration cooling model	25
3.1 Reference frame	25
3.2 Governing equations	26
3.2.1 Continuity equation	26
3.2.2 Momentum equation	27
3.2.3 Energy equation	28
3.2.4 Equation of state	32
3.2.5 Reduction in heat transfer due to presence of blowing	32
3.2.6 Model summary	34
3.3 Boundary conditions	36
3.3.1 Boundary conditions definition	36
3.3.2 Boundary condition study	38
3.3.3 Conclusions	39
3.4 Verification and validation	40
3.4.1 Verification	40
3.4.2 Validation	43
3.5 Parametric analysis	46
3.5.1 Effect of pore size	47
3.5.2 Effect of porosity	48
3.5.3 Effect of porosity distribution	49
3.5.4 Effect of pore size distribution	50
3.5.5 Effect of wall thermal conductivity	51

3.5.6	Other coolants . . . . .	52
3.5.7	Conclusions . . . . .	55
3.6	Sensitivity analysis . . . . .	57
3.6.1	Choice of volumetric heat transfer model . . . . .	57
3.6.2	Sensitivity to pressure drop over the wall. . . . .	58
3.6.3	Sensitivity to chamber pressure change . . . . .	58
3.6.4	Sensitivity to increase in heat flux . . . . .	60
3.6.5	Conclusions . . . . .	61
3.7	Optimized coolant distribution . . . . .	61
3.8	Conclusions and recommendations . . . . .	63
4	Film cooling model . . . . .	65
4.1	General aspects film cooling modelling . . . . .	65
4.2	Governing equations . . . . .	66
4.2.1	Adaptation liquid film behaviour . . . . .	67
4.2.2	Gaseous behaviour from NASA Annex B . . . . .	69
4.2.3	Model summary . . . . .	71
4.3	Verification, validation and calibration . . . . .	72
4.3.1	Comparison to experimental data . . . . .	72
4.3.2	Comparison to film cooling model of Rocket Propulsion Analysis . . . . .	75
4.4	Film cooling results . . . . .	78
4.5	Conclusions. . . . .	79
5	Comparison cooling techniques . . . . .	81
5.1	Wall temperature comparison . . . . .	81
5.2	Specific impulse losses . . . . .	85
5.3	Engine dry mass . . . . .	88
5.4	Delta-v budget . . . . .	90
5.5	Conclusions. . . . .	92
6	Pressure drop experiments . . . . .	93
6.1	Test goals . . . . .	93
6.2	Test setup . . . . .	94
6.2.1	Sensor . . . . .	94
6.2.2	Data acquisition system . . . . .	95
6.3	Test procedures . . . . .	95
6.4	Validation of test setup . . . . .	96
6.5	Test samples . . . . .	96
6.5.1	Sheet gyroid sample . . . . .	97
6.5.2	Visco jet sample . . . . .	98
6.6	Test results . . . . .	99
6.6.1	Validation results . . . . .	99
6.6.2	Sheet gyroid . . . . .	100
6.6.3	Visco jet . . . . .	101
6.6.4	Uncertainty analysis . . . . .	102
6.7	Analysis of test results. . . . .	104
6.7.1	Comparison permeability coefficients . . . . .	104
6.7.2	Effect on pressure drop . . . . .	105
6.8	Conclusions and recommendations . . . . .	106
7	Conclusions and recommendations . . . . .	109
7.1	Answering research questions. . . . .	109
7.2	Conclusions and recommendations of results . . . . .	112
7.3	Conclusions and recommendations of methodology . . . . .	113

---

Bibliography	115
A Additional regenerative cooling model verification	121
B CoolProp validation for ethanol and methane properties	123
B.1 Ethanol . . . . .	123
B.2 Methane . . . . .	124
C Implementation of the transpiration cooling model	129
C.1 Code implementation energy equations . . . . .	129
C.1.1 Energy equation local thermal equilibrium . . . . .	129
C.1.2 Energy equation local thermal non-equilibrium . . . . .	130
C.2 Grid . . . . .	131
D Abstract Space Propulsion Conference 2020	133





# Summary

The heat fluxes in (liquid) rocket engines can go up to high values and they need active cooling to prevent the chamber wall to fail. Transpiration cooling is identified as a way to achieve lower wall temperatures than commonly used regenerative cooling and regenerative cooling with additional film cooling (referred to as film cooling from now on). This can lead to higher performance of the engine. However, transpiration cooled engines are not in use today and this is mainly attributed to problems with the required porous wall materials. Additive manufacturing is a promising solution for these material problems. Better cooling is especially useful for Inconel additively manufactured rocket engines as such engines experience higher wall temperatures due to the low thermal conductivity of the material.

This thesis has two purposes. Firstly, an analysis was performed to see if transpiration cooling actually performs better than regenerative and film cooling in total engine performance. Secondly, it was investigated if additive manufacturing can be used to create the porous walls required for transpiration cooling.

To compare the cooling techniques, a simplified model for each cooling technique was developed. These models were verified and validated using data from literature. As no adequate film cooling model was found, a new (transcritical) film cooling model was created by combining three existing film cooling models. The wall temperatures obtained from the three cooling methods were compared by applying them to a 68 kN reference liquid rocket engine with either Inconel or copper as wall material. Subsequently, the losses in specific impulse and dry mass were determined. Then, a delta-v calculation for each cooling method was made to objectively compare them.

The conclusions on the comparison of the cooling techniques are that the regenerative cooled engine reaches wall temperatures above the material limits. Therefore, it is not a feasible to use this cooling method for the reference engine. Film and transpiration cooling can both achieve temperatures below the limit, depending on how much coolant is injected. Transpiration cooling requires less coolant than film cooling to achieve the same temperature. This will result in lower losses in specific impulse compared to film cooling. However, to achieve these low coolant mass flows, thick chamber walls are required to achieve the specified pressure drop over the wall. A minimum pressure drop is required to prevent the hot gases from flowing back into the wall. When comparing transpiration cooling to film cooling on the total delta-v achieved, it is found that the Inconel chamber performs better when pore sizes of 0.05 mm are used. Film cooling starts to perform better when larger pore sizes are used as the wall thickness for the transpiration cooled engine needs to increase to achieve the required pressure drop. This increases the dry mass of the engine. The film cooled copper chambers always achieve higher delta-v than the transpiration cooled ones for pore sizes down to 0.05 mm. Smaller pore sizes are not realistic with current manufacturing techniques.

Additionally, it was found that, when using conventional geometries, the pore sizes that are producible with additive manufacturing are an order of magnitude too large to create the required pressure drop in a transpiration cooled wall. Therefore, experiments were performed on the pressure drop over additively manufactured porous walls with different geometries. The first goal was to see how an additively manufactured geometry compares to the 'bed of packed spheres' geometry used in the transpiration cooling model of this thesis. A well-established empirical relation provides the pressure drop for this shape. A secondary goal was to find a geometry that achieves an as large as possible pressure drop as this could reduce the wall thickness.

With these pressure drop experiments, it was found that a new porous wall geometry made using additive manufacturing techniques has a lower pressure drop than the bed of packed spheres. It is in the same order of magnitude, but only 0.76 of the value for a bed of packed spheres. The geometry designed to achieve an as large as possible pressure drop increased the pressure drop 24.9 times. At the conditions relevant for a transpiration cooled wall and pore sizes producible with current techniques, this can bring the wall thickness down from above 50 m to 3.5 cm. However, this geometry does not achieve a uniform coolant injection required for transpiration cooling, so further research is required.



# List of figures

1.1	Schematic of slot film cooling, adapted from [1]	2
1.2	A representation of the transpiration cooling mechanism, adapted from [2].	3
1.3	An overview of DLR's transpiration cooled engine [3].	4
1.4	The contour of the reference engine.	5
1.5	The peak in isobaric specific heat for different temperatures for ethanol at 65 bar, obtained using CoolProp [4].	6
2.1	Parameters used in the calculations of the convective heat transfer and that describe the cooling channel geometry.	17
2.2	A flowchart of the program for regenerative cooling.	18
2.3	The heat flux of the CIRA engine [5] calculated with the model and the reference values; surface roughness $1.0\ \mu\text{m}$ instead of $6.3\ \mu\text{m}$ to make sure coolant pressure values remain above zero.	21
2.4	The convective heat transfer coefficient of the CIRA engine [5] calculated with the model and the reference values; surface roughness $1.0\ \mu\text{m}$ instead of $6.3\ \mu\text{m}$ to make sure coolant pressure values remain above zero.	21
2.5	The wall temperature of the CIRA engine calculated with the model using $T_{\text{aw}}$ and $h_g$ values from [5] compared to the reference values of [5], radiation heat transfer is disabled.	22
2.6	The total temperature of the coolant in the CIRA engine calculated with the model using $T_{\text{aw}}$ and $h_g$ values from [5] and the reference values of [5], at a coolant temperature of 190.6 K [6], the methane becomes supercritical.	22
2.7	The total pressure in the coolant channel of the CIRA engine calculated with the model using $T_{\text{aw}}$ and $h_g$ values from [5] compared to the reference values of [5].	23
2.8	The overprediction in % of the heat flux for the 37 mm engine with the Bartz equation for the second cylindrical segment in the engine [7].	24
3.1	The reference frame for the transpiration cooling model.	26
3.2	A representation of a bed of packed spheres [8].	28
3.3	An example of a porous structure created using additive manufacturing [9].	28
3.4	A representation of the local thermal equilibrium (LTE) temperature in a wall.	28
3.5	A representation of the local thermal non-equilibrium temperature (LTNE) in a wall.	28
3.6	Comparison of the Nusselt numbers relations from Table 3.1 for $Pr$ of 0.7 and porosity of 0.39.	31
3.7	The volumetric heat transfer coefficient determined with the Kuwahara Nusselt number relation for different porosities; $Pr=0.7$ , $D_p=0.1\ \text{mm}$ , $k=1\ \text{W/mK}$ ; the dashed lines are outside the porosity range of the relation.	32
3.8	The volumetric heat transfer coefficient determined with the Kuwahara Nusselt number relation for different pore sizes; $Pr=0.7$ , $\epsilon=0.2$ , $k=1$ .	32
3.9	An example calculation for the reduction in convective heat transfer coefficient versus blowing ratio; for ethanol as coolant; located in the cylindrical section of the reference engine.	34
3.10	A flowchart of the program that calculates the wall temperature for a transpiration cooled wall for a single station and for the local thermal non-equilibrium (LTNE) assumption. The local thermal equilibrium (LTE) case is similar with the exception that no solid wall temperature is calculated.	35
3.11	Temperature distribution for a convective boundary condition on the cold side for a wall length of 0.05 m.	39
3.12	Temperature distribution for a convective boundary condition on the cold side for a wall length of 0.02 m.	39
3.13	Temperature distribution for a constant temperature boundary condition on the cold side for a wall length of 0.02 m.	40

3.14	The effect of smaller pore diameters on the solid temperature (solid lines) and the coolant temperature (dashed lines); porosity 15%; $k=11.4$ W/mK; $\Delta P=1$ bar; ethanol as coolant. . . . .	41
3.15	A comparison between the temperature data of Figure 3.14 with pore size of 0.08 mm to the LTE case with the same parameters. . . . .	41
3.16	Comparison between the numerical and analytical solution for the LTE case with constant properties as given in Table 3.5. . . . .	42
3.17	The numerical results compared to the analytical solution in case when the heat transfer in the wall is set to zero. . . . .	43
3.18	The numerical results compared to the analytical solution in case when the volumetric heat transfer is specified and the coolant temperature is kept constant. . . . .	44
3.19	Grid convergence. . . . .	44
3.20	The pressure drop per unit length for the bed of packed spheres with $\epsilon$ of 0.37 and $D_p$ of 2.5mm, the velocity is the Darcy velocity at the inlet. The reference data is obtained from [1]. . . . .	45
3.21	The measured wall temperatures from Langener [1] (markers) and the wall temperature from the model (lines) for three different blowing ratios for the PH1606-1 sample. . . . .	46
3.22	The maximum wall temperature occurring for different mass fluxes and pore sizes; porosity 0.2; thermal conductivity 11.4 W/mK. . . . .	48
3.23	The maximum wall temperature gradient occurring for different mass fluxes and pore sizes; porosity 0.2; thermal conductivity 11.4 W/mK. . . . .	48
3.24	The maximum wall temperature as a function of wall thickness; porosity 0.2; thermal conductivity 11.4 W/mK. . . . .	49
3.25	The maximum wall temperature occurring for different mass fluxes and porosities; pore size 0.1 mm; thermal conductivity 11.4 W/mK. . . . .	49
3.26	The maximum wall temperature gradient occurring for different mass fluxes and porosities; pore size 0.1 mm; thermal conductivity 11.4 W/mK. . . . .	50
3.27	The maximum wall temperature occurring for different mass fluxes and porosity distributions; pore size 0.1 mm; thermal conductivity 11.4 W/mK. . . . .	50
3.28	The maximum wall temperature gradient occurring for different mass fluxes and porosity distributions; pore size 0.1 mm; thermal conductivity 11.4 W/mK. . . . .	51
3.29	The maximum wall temperature occurring for different mass fluxes and pore size distributions; porosity 0.2; thermal conductivity 11.4 W/mK. . . . .	51
3.30	The maximum wall temperature gradient occurring for different mass fluxes and pore size distributions; porosity 0.2; thermal conductivity 11.4 W/mK. . . . .	52
3.31	The effect of the solid material thermal conductivity on the maximum temperature and maximum temperature gradient for two different pore sizes. . . . .	53
3.32	The effect of the solid material thermal conductivity on the mass flux for two different pore sizes. . . . .	53
3.33	The maximum wall temperature for Inconel walls ( $k=11.4$ W/mK) and copper walls ( $k=220$ W/mK) as function of mass flux; porosity is 0.2 and pore size 0.05 mm. . . . .	54
3.34	The maximum wall temperature gradient for Inconel walls ( $k=11.4$ W/mK) and copper walls ( $k=220$ W/mK) as function of mass flux; porosity is 0.2 and pore size 0.05 mm. . . . .	54
3.35	The temperature distribution in a transpiration cooled wall for two Inconel and copper. . . . .	55
3.36	The maximum wall temperature for different coolants versus the mass flux; $k=11.4$ W/m; porosity 0.2; pore size 0.05mm. . . . .	56
3.37	The maximum wall temperature gradient for different coolants versus the mass flux; $k=11.4$ W/m; porosity 0.2; pore size 0.05mm. . . . .	56
3.38	The maximum wall temperature gradient for different coolants versus the mass flux; $k=11.4$ W/m; porosity 0.2; pore size 0.05 mm. . . . .	57
3.39	The change in mass flux for different specified pressure drops over the wall, $k=11.4$ W/mK, porosity 0.2, pore size 0.1 mm and wall thickness 20 mm. . . . .	59
3.40	A diagram of the engine, the tap-off line from the main fuel supply to the injector and the valve that regulates the flow. . . . .	60
3.41	The effect of a chamber pressure change on the mass flux and maximum wall temperature; thermal conductivity 11.4 W/m; porosity 0.2; pore size 0.05 mm. . . . .	60
3.42	The effect of a heat flux change on the mass flux and maximum wall temperature; thermal conductivity 11.4 W/m; porosity 0.2; pore size 0.05 mm. . . . .	61



3.43	The mass flux distribution required to maintain a wall temperature of 923 K for the Inconel transpiration cooled engine. . . . .	62
4.1	Modelling of the transcritical film [10]. . . . .	68
4.2	The ratio of heat transfer coefficient $h_g$ with reduction due to blowing effects to the one without for the Höglauer engine with $\mu$ is 15%, the blue area is oscillatory behaviour of the ratio. . . . .	69
4.3	The entrainment fraction multiplier $\psi_m$ as a function of expansion ratio in the divergent section, taken from [11]. . . . .	70
4.4	A flowchart of the steps taken in the film cooling model. . . . .	72
4.5	The engine used in the Höglauer tests [12], the film coolant is injected after the second (small) segment. . . . .	72
4.6	The measured and calculated wall heat flux without (left) and with film cooling (right) from [10], $\mu = 15\%$ and $P_c = 60$ bar; note that two tests were performed. . . . .	73
4.7	The heat flux of the model compared to the heat flux of the reference for $\mu=15\%$ , OF 2.9 and $P_c=60$ bar. . . . .	74
4.8	The calibrated heat flux of the model compared to the heat flux of the reference for $\mu=15\%$ , OF 2.9 and $P_c=60$ bar with a calibrated value for $\Psi_L$ of 0.06. . . . .	74
4.9	The heat flux of the model compared to the heat flux of the reference for $\mu=10\%$ , OF 2.9 and $P_c=60$ bar with a specified value for $\Psi_L$ of 0.06. . . . .	75
4.10	The total heat flux of the uncalibrated model compared to the RPA film cooling model for $\mu=17\%$ , the coolant transitions to gas/supercritical state at the start of the arrows. . . . .	77
4.11	The total heat flux of the uncalibrated model compared to the RPA film cooling model for $\mu=34\%$ , the coolant transitions to gas/supercritical state at the start of the arrows. . . . .	77
4.12	The total heat flux of the calibrated model compared to the RPA film cooling model for $\mu=17\%$ with a calibration factor for heat transfer coefficient of 6 and specified $\Psi_L$ of 0.003, the coolant transitions to gas/supercritical state at the start of the arrows. . . . .	78
4.13	The total heat flux of the calibrated model compared to the RPA film cooling model for $\mu=34\%$ with a calibration factor for heat transfer coefficient of 6 and specified $\Psi_L$ of 0.003, the coolant transitions to gas/supercritical state at the start of the arrows. . . . .	78
4.14	The wall temperature on the hot side of the inner wall for the Inconel chamber for regenerative cooling and film cooling. . . . .	80
4.15	The wall temperature on the hot side of the inner wall for the copper chamber for regenerative cooling and film cooling. . . . .	80
5.1	The configuration for the transpiration cooled section and the coolant flow (a) and for the film cooled engine (b). . . . .	82
5.2	The maximum wall temperature versus the percentage injected coolant of the total mass flow for transpiration, film and regenerative cooling for Inconel; pore size 0.05 mm and porosity of 0.2. . . . .	83
5.3	The maximum wall temperature gradient versus the percentage injected coolant of the total mass flow for transpiration, film and regenerative cooling for Inconel; transpiration cooling pore size 0.05 mm and porosity of 0.2. . . . .	83
5.4	The maximum wall temperature versus the percentage injected coolant of the total mass flow for transpiration, film and regenerative cooling for copper; pore size 0.05 mm and porosity of 0.2. . . . .	84
5.5	The maximum wall temperature gradient versus the percentage injected coolant of the total mass flow for transpiration, film and regenerative cooling for copper; transpiration cooling pore size 0.05 mm and porosity of 0.2. . . . .	84
5.6	The vacuum specific impulse for RP-1 and ethanol combustion with liquid oxygen for a chamber pressure of 65 bar, obtained using NASA's CEA [13]; this shows the combustion without reductions due to the introduction of coolant in the chamber. . . . .	86
5.7	The vacuum specific impulse given for different wall region OF ratios; for the different cooling methods and for the different OF ratios for the Inconel engine. . . . .	86
5.8	The vacuum specific impulse given for different wall region OF ratios; for the different cooling methods and for the different OF ratios for the copper engine. . . . .	87
5.9	A representation of the regeneratively cooled wall. . . . .	89
5.10	A representation of the transpiration cooled wall . . . . .	89

5.11	The allowed extra engine mass for the Inconel and copper transpiration cooled chamber compared to the different film cooled engines for different film layer OF ratios; the markers indicate the OF ratio where below it the transpiration cooled engines perform better. If no marker is given, the film cooled engine always performs better. . . . .	91
6.1	The feed system for the test setup. . . . .	94
6.2	The test section . . . . .	95
6.3	The used sample for validation of the test setup threaded into its mounting plate. . . . .	97
6.4	A different view of the validation sample where the difference in inner and outer diameter is visible, note that no Teflon is applied yet. . . . .	97
6.5	The shape of one unit cell of the sheet gyroid. . . . .	98
6.6	The additively manufactured sheet gyroid sample. . . . .	98
6.7	The working principle of the Lee visco jet [14]. . . . .	99
6.8	A 3D representation on one 'channel' of the visco jet sample. . . . .	99
6.9	A drawing of one cell of the visco jet sample, dimensions in mm. . . . .	99
6.10	The additively manufactured visco jet sample. . . . .	100
6.11	An example of the unfiltered data for pressure drop and mass flow for the validation sample. . .	101
6.12	The pressure drop over length versus the superficial velocity of the experiment and the theoretical lower and upper ranges. . . . .	101
6.13	The pressure drop over length versus the superficial velocity of the gyroid sample and the obtained trend line; error bars indicate $1\sigma$ in both directions. . . . .	103
6.14	The pressure drop over length versus the superficial velocity of the visco jet sample and the obtained trend line; error bars indicate $1\sigma$ in both directions. . . . .	103
6.15	The normalized pressure drop for the additively manufactured geometries, normalized to a bed of packed spheres, for liquid ethanol . . . . .	106
6.16	A CT scan of a by SLM additively manufactured (too) porous wall. . . . .	107
A.1	The heat transfer coefficient of the model compared to one obtained from RPA for the verification case. . . . .	121
A.2	The difference between the convective heat transfer coefficient of the model and RPA. . . . .	121
A.3	The difference between the convective heat transfer coefficient of the model and RPA. . . . .	122
A.4	The difference between the convective heat transfer coefficient of the model and RPA. . . . .	122
B.1	Comparison if the density of ethanol of CoolProp (markers) to the one of REFPROP (lines) at different pressures and temperatures. . . . .	124
B.2	Comparison of the isobaric specific heat of ethanol of CoolProp (markers) to the one of REFPROP (lines) at different pressures and temperatures. . . . .	125
B.3	Comparison of the viscosity of ethanol of CoolProp (markers) to the one of REFPROP (lines) at different pressures and temperatures. . . . .	125
B.4	Comparison of the thermal conductivity of ethanol of CoolProp (markers) to the one of REFPROP (lines) at different pressures and temperatures. . . . .	126
B.5	Comparison of the density of methane of CoolProp (markers) to the one of NIST [6] (lines) at different pressures and temperatures. . . . .	126
B.6	Comparison of the isobaric specific heat of methane of CoolProp (markers) to the one of NIST [6] (lines) at different pressures and temperatures. . . . .	127
B.7	Comparison of the viscosity of methane of CoolProp (markers) to the one of NIST [6] (lines) at different pressures and temperatures. . . . .	127
B.8	Comparison of the thermal conductivity of methane of CoolProp (markers) to the one of NIST [6] (lines) at different pressures and temperatures. . . . .	128
C.1	An example of the Chebyshev nodes used as grid. . . . .	131

# List of tables

1.1	The specifications of the reference engine. . . . .	5
1.2	Comparing some properties of RP-1 and ethanol; ethanol properties following from CoolProp [4]. . . . .	6
1.3	The material properties for the selected additive manufacturing metals. . . . .	6
2.1	The inputs for the regeneratively cooling model. . . . .	19
2.2	The specifications of the CIRA engine. . . . .	20
3.1	The various Nusselt number relations found for heat transfer in porous media; the corresponding ranges of validity for the relations can be found in Table 3.2. . . . .	30
3.2	The range in different parameters for the Nusselt relations listed in Table 3.1. . . . .	30
3.3	The additional inputs of the code modelling a transpiration cooled wall, in addition to the ones listed in Table 2.1 (minus the cooling channel parameters). . . . .	35
3.4	The constant properties for the analysis. . . . .	38
3.5	Inputs for the verification case of the simplified solid energy equation . . . . .	42
3.6	Inputs for the verification case where the heat transfer in the wall is set to zero. . . . .	42
3.7	Inputs for the verification case where the heat transfer in the wall is set to zero. . . . .	43
3.8	The properties of the PH1606-1 CMC sample [1]. . . . .	45
3.9	The input data for the CMC sample PH1606-1 for different blowing ratios [1]. . . . .	46
3.10	The molecular mass, density and isobaric specific heat of the different coolants analyzed; determined using CoolProp [4]; density and isobaric specific heat determined at 65 bar and 298 K. . . . .	55
3.11	The increases in solid wall temperature for Whitaker and Kuwahara x2 volumetric heat transfer model and their differences for various pore sizes; wall thickness 40 mm, $k=11.4$ W/mK. . . . .	58
3.12	The calibration factors used for different axial locations in the engine, obtained from [7]. . . . .	62
4.1	The engine properties of the Höglauer tests. . . . .	73
4.2	The engine properties for the RPA comparison. . . . .	76
4.3	The percentage of film coolant compared to the total mass flow required to keep the maximum wall temperature in the whole engine below the set limits for Inconel and copper. . . . .	79
5.1	The coolant required as percentage of the total mass flow in the engine to keep the wall temperatures to the maximum allowable temperature. . . . .	85
5.2	The vacuum specific impulses for the the case when RP-1 is used as coolant for the lowest wall OF ratio as given in Figure 5.7 and Figure 5.8. . . . .	87
5.3	The yield stresses and densities for the materials used in the mass calculations, all properties are for additive manufacturing variants. . . . .	88
5.4	The masses of the cylindrical part of the regenerative and film cooled engine for different materials. . . . .	89
5.5	The masses of the cylindrical part of the transpiration cooled engine to achieve the maximum allowable wall temperature. . . . .	89
5.6	The mass increases compared to a dry mass for the regeneratively and film cooled engine, the regenerative and film cooled mass are determined by the relation from Zandbergen [15] and the mass from Table 5.5 is added to find the transpiration cooled engine mass. . . . .	90
5.7	The masses and other parameters used for the delta-v calculation. . . . .	91
5.8	The OF ratio in the wall zone for which the transpiration cooled engines outperform the film cooled engines with respect to total delta-v achieved. . . . .	92
6.1	The properties of the used calibration sample. . . . .	96

6.2	The properties of the additively manufactured sheet gyroid sample. . . . .	98
6.3	The properties of the additively manufactured visco jet sample. . . . .	100
6.4	The processed data from the experiments with the validation sample and the standard deviation $\sigma$ , for the minimum area of 534.6 mm <sup>2</sup> . . . . .	102
6.5	The processed data from the experiments with the sheet gyroid sample and the standard deviation $\sigma$ . . . . .	102
6.6	The processed data from the experiments with the visco jet sample and the standard deviation $\sigma$ . . . . .	104
6.7	The determined permeability coefficients for the tested shapes compared to the empirical ones for a bed of packed spheres, all for the same volumetric porosity and a minimum pore size of 1.5 mm. . . . .	104
6.8	The used properties for liquid ethanol, obtained using CoolProp [4]. . . . .	105
B.1	Summary of the uncertainties for ethanol in REFPROP and the differences with CoolProp. . . . .	123
B.2	Summary of the uncertainties for methane in NIST [6] and the differences with CoolProp. . . . .	124

# Nomenclature

## Latin symbols

$A$	Area	$\text{m}^2$
$c^*$	Characteristic velocity	$\text{m/s}$
$c_p$	Isobaric specific heat	$\text{J/kgK}$
$D$	Diameter	$\text{m}$
$D$	Hydraulic diameter	$\text{m}$
$F$	Blowing ratio	–
$f$	Friction factor	–
$f$	Velocity-ratio correlation factor (NASA annex B film cooling model)	–
$h$	Convective heat transfer coefficient	$\text{W/m}^2\text{K}$
$h$	Height	$\text{m}$
$H$	Enthalpy	$\text{J}$
$I_{sp}$	Specific impulse	$\text{s}$
$k$	Thermal conductivity	$\text{W/mK}$
$k^*$	Correction factor	–
$K_D$	Darcy permeability coefficient	$\text{m}^2$
$K_F$	Forchheimer permeability coefficient	$\text{m}$
$K_v$	Flow factor	$\text{m}^2\text{h}^{-1}\text{bar}^{-0.5}$
$L$	Length	$\text{m}$
$\dot{m}$	Mass flow	$\text{kg/s}$
$M$	Mach number	–
$M$	Molecular mass	$\text{g/mol}$
$m$	Mass	$\text{kg}$
$Nu$	Nusselt number	–
$OF$	Oxidiser to fuel ratio (mass)	–
$P$	Pressure	$\text{Pa}$
$Pr$	Prandtl number	–
$\dot{Q}$	Heat transfer rate	$\text{W}$
$Q$	Flow rate	$\text{m}^3/\text{h}$
$q$	Heat flux	$\text{W/m}^2$



$R$	Roughness	m
$r$	Radius	m
$r$	Recovery factor	—
$Re$	Reynolds number	—
$SG$	Specific gravity	—
$s_i$	Height of the mixing layer at the phase transition point (NASA annex B film cooling model)	m
$St$	Stanton number	—
$T$	Temperature	K
$t$	Thickness	m
$V$	Volume	m <sup>3</sup>
$v$	Darcy velocity or superficial velocity	m/s
$v$	Velocity	m/s
$W$	Total mass flow in the chamber (NASA annex B film cooling model)	kg/s
$w$	Width	m
$W_C$	Film coolant mass flow (NASA annex B film cooling model)	kg/s
$W_E$	Entrainment mass flow (NASA annex B film cooling model)	kg/s
$(W_E)_L$	Entrainment ratio at the start of the gaseous phase (NASA annex B film cooling model)	—
$\bar{x}$	Effective contour distance	m
<b>Greek symbols</b>		
$\alpha$	Under-relaxation factor	—
$\epsilon$	Porosity	—
$\eta$	Adiabatic film cooling effectiveness	—
$\eta$	Downstream effectiveness (NASA annex B film cooling model)	—
$\eta$	Efficiency	—
$\gamma$	Ratio of specific heats	—
$\Lambda$	Ratio of film temperature to the critical temperature	—
$\mu$	Dynamic viscosity	Pa · s
$\mu$	Film coolant mass fraction	—
$\Pi$	Ratio of heat used to evaporate the film coolant to the total heat flowing into the film	—
$\Psi$	Correction factor for effect of roughness of cooling channel	—
$\psi_L$	Reference entrainment ratio (NASA annex B film cooling model)	—
$\psi_m(x)$	Entrainment fraction multiplier (NASA annex B film cooling model)	—
$\rho$	Density	kg/m <sup>3</sup>
$\sigma$	Standard deviation	—

$\sigma$	Stress	Pa
$\theta$	Shape factor of the mixing layer (NASA annex B film cooling model)	–
$\xi$	Ratio of friction factor of rough to smooth channel	–

**Subscripts**

–	Mean value
0	Initial
0	Reservoir/inlet condition
0	Stagnation condition
^	Value determined from an empirical relation
aw	Adiabatic wall
$c$	Chamber
$c$	Coolant side
$c$	Coolant
conv	Convection or convective
crit	Critical
eff	Effective
$f$	Fin
$f$	Final
$g$	Hot gas
$M$	Molecular mass
$m$	Medium
$p$	Particle
$p$	Pore
$s$	Solid
$T$	Temperature
$t$	Throat
tot	Total
vap	Vaporization
$w.h$	Hot side combustion chamber wall



# Abbreviations

<b>AM</b>	Additive manufacturing
<b>C/C</b>	Carbon carbon
<b>CEA</b>	Chemical Equilibrium with Applications
<b>CFD</b>	Computational Fluid Dynamics
<b>CIRA</b>	Italian Aerospace Research Center
<b>CMC</b>	Ceramic matrix composites
<b>DED</b>	Directed energy deposition
<b>DLR</b>	German Aerospace Center
<b>FDM</b>	Fused deposition modeling
<b>LOX</b>	Liquid oxygen
<b>LTE</b>	Local thermal equilibrium
<b>LTNE</b>	Local thermal non-equilibrium
<b>NASA</b>	National aeronautics and space administration
<b>RP-1</b>	Rocket Propellant-1 or Refined Petroleum-1
<b>RPA</b>	Rocket Propulsion Analysis
<b>SLM</b>	Selective laser melting
<b>SMILE</b>	Small Innovative Launcher for Europe
<b>TPMS</b>	Triply periodic minimal surface
<b>TUM</b>	Technical University Munich





# Introduction

This thesis was performed at Rocket Factory Augsburg in cooperation with the Delft University of Technology and focuses on comparing transpiration cooling in rocket engines to regenerative and film cooling. The background and relevance of this research is discussed in section 1.1. In this section, the physical principles of film and transpiration cooling are explained. A brief overview of the historical developments regarding transpiration cooled engines and some tested transpiration cooled engines are given in section 1.2. The comparison between the three cooling techniques is applied to an RP-1 and a liquid oxygen fuelled reference engine which is introduced in section 1.3. The reference engine is designed to be manufactured by additive manufacturing with Inconel. Additionally, it will be investigated what the effect of using copper is. The material properties of additively manufactured Inconel and copper are described in section 1.4. In this section, also the smallest possible pore size currently producible with conventional metal printing techniques is discussed. Then, the research goals and research questions are given in section 1.5. In section 1.6, the method to answer these questions is discussed. Lastly, an outline of the thesis is given in section 1.7.

## 1.1. Background and relevance

The heat flux in modern rocket engines can go up to very high values and generally has its maximum in the throat of the engine [16]. For example, in the Space Shuttle main engine the heat flux was  $163 \text{ MW/m}^2$  in the throat [17]. In the cylindrical part of the engine, the heat flux tends to be lower - for the rocket engine analysed in this thesis it is estimated to only be 40% of the value in the throat (determined in Appendix A). Furthermore, the heat flux drops quickly in the divergent part of the nozzle. Still, these heat fluxes require that bipropellant liquid rocket engines are actively cooled to prevent failure of the combustion chamber wall material. The most common cooling method in liquid rocket engines is regenerative cooling [16]. In this case, one of the propellants, usually the fuel, is injected into a jacket around the chamber at the end of the nozzle. The coolant then flows up to the injector and cools down the wall. The heat is absorbed by the coolant.

The heat flux in the engine depends on the chamber pressure to the power of 0.8 [16], and thus, if the chamber pressure increases, the heat flux (almost) linearly increases as well. When the heat flux becomes higher or when less thermally conductive wall materials are used, additional cooling is required. Many of the high performance engines currently operational use film cooling to lower the heat flux to the wall [18]. Another option would be to create a fuel rich layer next to the wall by changing the mixture ratio in this zone, but this is less effective [17]. While quantifying the differences between mixture ratio bias and film cooling is difficult, it can be reasoned that the combustion temperature in this zone for mixture ratio bias is always higher (as combustion is still intended) than when only fuel is injected. Thus, film cooling will result in lower heat fluxes due to the lower temperature. Therefore, mixture ratio bias is not considered in this thesis. In a liquid film cooled engine, coolant (usually the fuel) is injected into the chamber via slots or holes. This can happen at the injector, but also at other locations in the engine. This creates a coolant layer between the wall and the hot combustion gases that protects the wall from heat. After the injection of the film layer, this layer will decrease in thickness as it evaporates and mixes with the main flow. A schematic of slot film cooling can be seen in Figure 1.1.

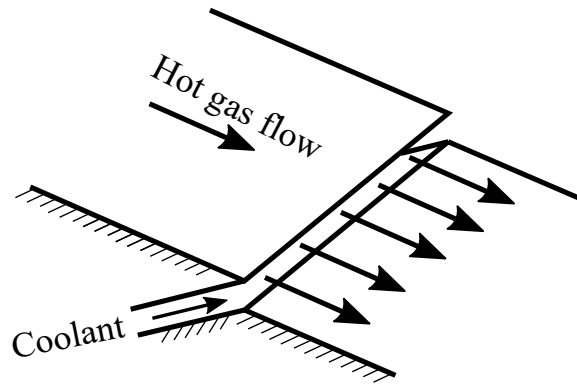


Figure 1.1: Schematic of slot film cooling, adapted from [1]

Another cooling method is transpiration cooling and aside from some research projects [3, 19], no flight engine currently uses transpiration cooling. In a transpiration cooled engine, a coolant film is also injected into the chamber. However, instead of injecting it at discrete locations, a porous wall is used to inject coolant along the complete wall length. A schematic of this process can be seen in Figure 1.2. The coolant flows from a reservoir through the porous material and is then injected into the main hot gas flow. The boundary layer that is present increases in thickness [1]. Transpiration cooling cools the wall by two different methods. Within the wall, the heat is absorbed by the coolant flowing through it. Once the coolant is injected into the chamber, it forms a film layer that reduces the heat transfer to the wall, similar to what happens with film cooling [2].

Among all different rocket engine cooling techniques, transpiration cooling is claimed to outperform regenerative and film cooling [20, 21]. Better cooling is beneficial as this can lead to increased engine performance in two ways. Firstly, when better cooling is present, the chamber can handle higher heat fluxes and thus the pressure can be increased. A higher chamber pressure results in a higher specific impulse [17]. Secondly, transpiration cooling requires less injected coolant than film cooling [21]. This injected coolant burns at a non-optimal OF ratio and thus lowers the performance. So, when less coolant is required, the specific impulse will increase [22, 23].

While interest in transpiration cooling began around the 1950's [21, 24], problems with development of adequate materials have prevented the practical application of transpiration cooling in rocket engines [20]. The flexibility of additive manufacturing (AM) could be the solution for the problems with the material developments. Additive manufacturing can allow for tailoring of the wall such that the coolant can be precisely distributed. Furthermore, additive manufacturing makes it possible to produce complex geometries as one part and thus the transpiration cooled wall can be connected to the outer wall without the need of any joints. Additive manufacturing is currently used to produce combustion chambers for several rocket engines. Furthermore, using AM to create transpiration cooled walls has attained interest in recent years [25, 26]. Especially rocket engines made from additively manufactured Inconel could benefit from better cooling as the low thermal conductivity of Inconel causes higher maximum temperatures and higher thermal gradients.

Rocket Factory Augsburg has designed an Inconel additively manufactured rocket engine for a small satellite launcher currently under development<sup>1</sup>. This engine uses a combination of regenerative and film cooling. The company wondered if transpiration cooling could solve the problems that arise when a low thermal conductivity material is used. These problems are that the engine is more difficult to cool and this in the end

<sup>1</sup><https://www.rfa.space/launcher/>

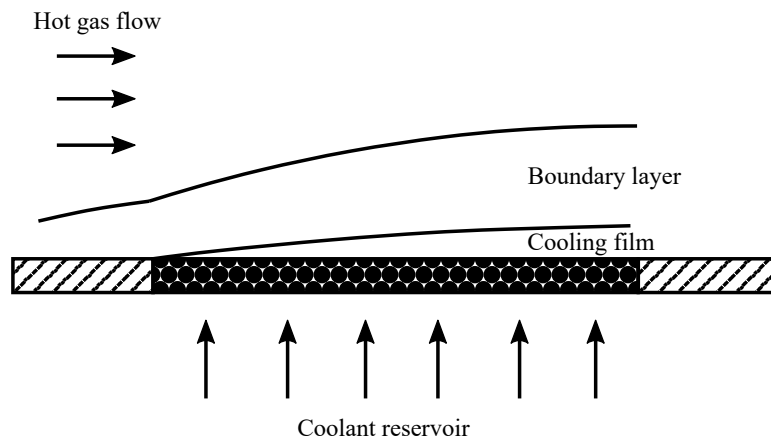


Figure 1.2: A representation of the transpiration cooling mechanism, adapted from [2].

lowers the specific impulse as the chamber pressure is limited or the engine operates at a less optimal OF ratio [17]. Therefore, the work in this thesis is applied to this reference engine which will be described in further detail in section 1.3. Note that when the term 'film cooled engine' is used, that this applies to a combination of a regenerative and film cooling.

Film and transpiration cooling are similar in nature. One could say that when starting with a film cooled engine, and then increasing the number of injection points, it will converge to transpiration cooled engine. So, ideally, a model will be used that can model film cooling and when more and more holes are added, it predicts the transpiration cooled wall. Then both cases have the same underlying assumptions. Sadly, no such model was found and two different models are required to model the transpiration and film cooled engine. These models will be extensively discussed in chapter 3 and chapter 4.

## 1.2. Existing transpiration cooled engines

As mentioned, interest in transpiration cooling for rocket engines started in the 1950's, but the lack of appropriate material development hindered the practical application. While no flight engine that uses transpiration cooling has been found literature, some small scale transpiration cooled engines have been built and tested. The best documentation on transpiration cooled engines is from the German Aerospace Centre (DLR) and is discussed below. In recent developments, transpiration cooling was chosen as one of the key propulsion elements in the European Union's SMILE project that researched the development of a small satellite launcher [27, 28].

The best documentation on transpiration cooled engines is from DLR's long-term development project [29]. This engine used CMC (Ceramic Matrix Composites) liners and uses hydrogen and oxygen as fuel and oxidizer respectively. The hydrogen is used as the transpiration coolant. An overview of the engine can be seen in Figure 1.3. The coolant is injected into the liner on the outside and then flows radially inwards. The distribution of coolant is achieved by axial grooves in the liner [30]. The liner's permeability can be changed in the axial direction by changing the porosity to adjust the coolant flow [30, 31]. Unfortunately, no detailed test data on the heat fluxes in the engine is available and this can thus not be used as validation data in this thesis.

Other transpiration cooled engines that are less well documented exist. One of these engines is the Ultramet engine [32]. The porous wall in this engine was made from metal or ceramic foam. A third engine was tested in the TEHORA development program. The porous materials used were copper and nickel based alloys [33] and a nickel-based alloy was used for hot firing [19]. The wall material consisted of metal particles and had a porosity of 18% and the diameter of the particles was 63 to 180  $\mu\text{m}$  [19]. The propellants were gaseous hydrogen and liquid oxygen. In total 32 hot fire tests were performed with most of them having a duration of 30 seconds.

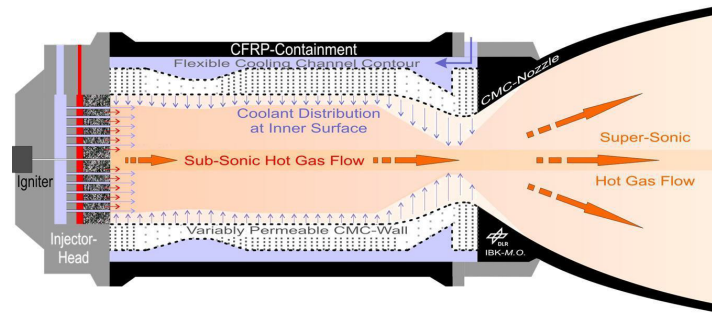


Figure 1.3: An overview of DLR's transpiration cooled engine [3].

The above described engines used hydrogen as the transpiration coolant. The reference engine to which the analysis is applied will use RP-1, although the coolant will be substituted by ethanol as RP-1 properties are difficult to obtain. This will be discussed in section 1.3. RP-1 has long hydrocarbons and is known to create soot when combusting fuel rich. This might block the porous wall. A Jet A-1 (a different type of kerosene) and LOX transpiration cooled engine was developed for the Small Innovative Launcher for Europe (SMILE) program by the Institute of Structures and Design of DLR. Hot fires test campaigns were performed, but no literature on the results is available [28].

### 1.3. Reference engine and coolant properties

The comparison between regenerative, film and transpiration cooling is applied to a reference engine. The engine design is a regenerative cooled rocket with additional film coolant injected at the injector. It is designed for production using additive manufacturing with Inconel 718. The propellants are RP-1 and liquid oxygen. The properties of the engine can be seen in Table 1.1 and the engine contour in Figure 1.4. All the RP-1 is used as regenerative coolant and the amount of injected RP-1 that acts as film coolant is to be determined in this thesis. The cooling channel geometry was designed taking in mind Inconel as wall material. In this report, some calculations are done using a copper alloy as wall material. In practice, one would then redesign the cooling channels, but this is not done. Note that the burn time of 190 s ensures that steady state operation is achieved in the engine. This means that the analysis can be limited to steady state and transient behaviour is not considered.

The reference engine is only a preliminary design and no engine tests have been performed with it. So, no data is available to compare the theoretical results from this thesis.

As said, the reference engine uses RP-1 as coolant and ideally the properties of RP-1 or kerosene would be used to model the behaviour of the coolant. However, no complete data set of the various required properties at the required pressures and temperatures was found. Therefore, RP-1 is substituted by ethanol as coolant. The combustion gas properties are still calculated using RP-1. An overview of relevant properties of RP-1 and ethanol can be seen in Table 1.2.

The density of ethanol and RP-1 are very close and the RP-1 is 1.5% denser at 298 K and 65 bar. The isobaric specific heat of RP-1 is 16.3% lower at 65 bar and 298 K. However, this comparison happens at the chamber pressure and the initial temperature. At higher temperatures, larger differences occur in the isobaric specific heat. As the RP-1 properties are difficult to obtain this comparison happens at 59.8 bar and 800 K. At this condition RP-1 has a 91.3% higher isobaric specific heat. For the transpiration cooling performance, a higher isobaric specific heat will yield better cooling results, as will be discussed in chapter 3. So, in this aspect, ethanol will give a higher wall temperature. On the other hand, RP-1 has a higher molecular mass and the transpiration cooling performance lowers with higher molecular mass which will be discussed in chapter 3. Lastly, RP-1 is 37.7% more viscous and this will increase the pressure drop over a porous wall compared to ethanol. To compare the exact differences, one would need to model a transpiration cooled wall with RP-1 and compare it to an ethanol one, but this requires the properties which are difficult to obtain for the full

Table 1.1: The specifications of the reference engine.

Parameter	Value	Unit
Fuel	RP-1	
Oxidizer	Liquid oxygen	
Regenerative coolant	All fuel	
Film coolant	Fuel (amount to be determined)	
Fuel mas flow	6.41	kg/s
Oxidizer mass flow	15.39	kg/s
Total mass flow	21.8	kg/s
Overall OF ratio	2.4	-
Chamber pressure	65	bar
Chamber diameter	152.8	mm
Throat diameter	88.3	mm
Thrust	~68	kN
Wall material	Inconel 718	
Fuel coolant channel inlet temperature	298	K
Fuel coolant channel inlet pressure	100	bar
Burn time	190	s

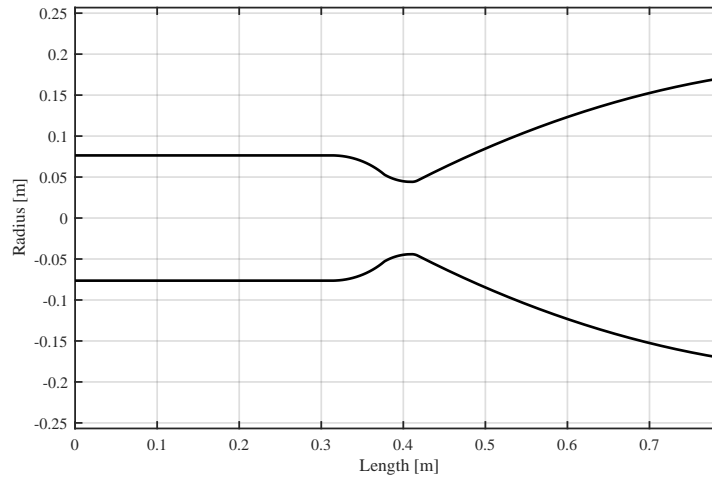


Figure 1.4: The contour of the reference engine.

range of temperature and pressure. So, this was deemed too difficult and outside the scope of this thesis.

Another difference between the fuels is the critical point. RP-1 has a critical pressure of 23.44 bar compared to ethanol's one that is 62.7 bar. On the other hand, the critical temperature of RP-1 is higher with 684 K compared to the 516 K of ethanol. The chamber pressure of the reference engine of 65 bar means that the RP-1 will always be above the critical pressure. The same applies to the ethanol coolant substitute. So, in this behaviour ethanol behaves the same as RP-1. The coolant will behave transcritical, meaning that it goes from a compressible liquid to a supercritical fluid when it surpasses the critical temperature. For modelling, this has one benefit and one disadvantage. The benefit is that the coolant will instantly change phase and it is not needed to model two-phase flow within the porous wall. This saves extra numerical effort, as for example seen in [39, 40]. A disadvantage is that the coolant is close to the critical point and thus large variations in coolant properties occur. Especially the peak in isobaric specific heat - see Figure 1.5 - causes problems with convergence of the numerical solution.

Value	Unit	RP-1	Source	Ethanol	Comment
Density	kg/m <sup>3</sup>	802.7	Interpolated from [34]	790.9	at 65 bar and 298 K
Isobaric specific heat	J/kgK	2029.1	Interpolated from [35]	2425.0	at 65 bar and 298 K
Isobaric specific heat	J/kgK	5530	[36]	2891.4	at 59.8 bar and 800 K
Viscosity	mPa·s	1.487	[37]	1.08	at 100 bar and 301 K
Critical pressure	bar	23.44	[38]	62.7	
Critical temperature	K	684.26	[38]	516.3	

Table 1.2: Comparing some properties of RP-1 and ethanol; ethanol properties following from CoolProp [4].

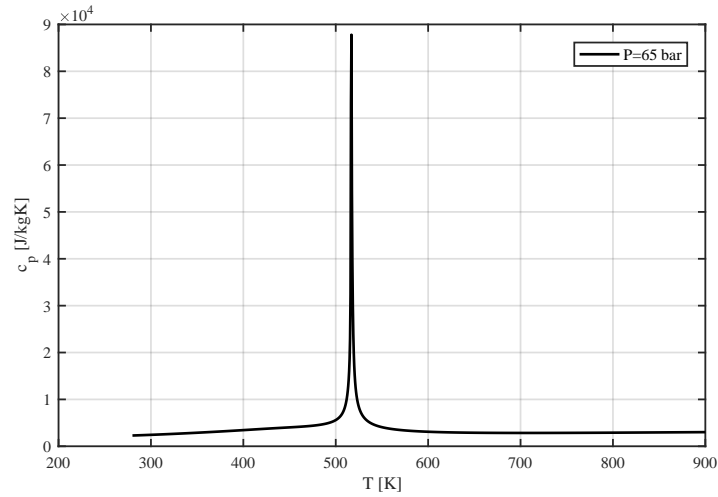


Figure 1.5: The peak in isobaric specific heat for different temperatures for ethanol at 65 bar, obtained using CoolProp [4].

## 1.4. Wall materials and additive manufacturing capabilities

The reference engine is designed to be produced using additive manufacturing with Inconel. Furthermore, part of the focus of this thesis is to see if additive manufacturing can be used to make the porous walls required for transpiration cooling. Therefore, it is important to know what the material properties are of these additive manufactured materials and what the printing capabilities are. The 3D printer used is a commonly used Selective Laser Melting (SLM) printer.

While the baseline for the reference engine is Inconel as wall material, it is also interesting to see how the cooling capabilities change when a higher conductive material is used. The material properties for the selected Inconel and copper alloy that can both be used on metal 3D printers can be seen in Table 1.3. The maximum allowable temperatures are the temperatures at which the yield stress starts to decline rapidly. The thermal conductivities are taken as constant. The Inconel thermal conductivity increases at higher temperatures, but the value at room temperature is taken. This is a conservative approach.

Material	Maximum temperature [K]	Thermal conductivity [W/mK]	Density [kg/m <sup>3</sup> ]	Source
Inconel	923	11.4	8200	[41]
Copper	723	220	8840	RFA

Table 1.3: The material properties for the selected additive manufacturing metals.

The smallest possible hole sizes producible with SLM printers follows from literature and is in the range between 0.3 mm and 0.5 mm. Often the actual printed size differs from the specified size. Porous metal structures are a research topic for bone implants, and an example of small sizes achieved in this field is 401  $\mu\text{m}$ ,

while the target was 500  $\mu\text{m}$  [42]. When printing straight holes in plates, the achieved hole diameter can be 250  $\mu\text{m}$  while the goal was 300  $\mu\text{m}$  [25]. A supplier of AM products states that a minimum gap size of 300  $\mu\text{m}$  is required to make sure the gaps are penetrable and also that a minimum wall thickness of 0.4 mm is required [43].

Comparing these values to pore sizes in transpiration cooled walls and rocket engines in literature, it can be seen that the additively manufactured pores will be larger. Sintered porous metals have pore sizes between 34 and 226  $\mu\text{m}$  [44, 45]. The earlier mentioned TEHORA engine used particles of 63 to 180  $\mu\text{m}$  [19]. So, it seems that AM porous materials are on the upper end of the possibilities available with sintered metals. It will be interesting to see how these larger sizes will affect the performance of a transpiration cooled engine.

An important aspect of every porous medium is the porosity. In this work the porosity is defined as the ratio of open to total volume, see Equation 1.1. Other ways to determine porosity are measuring the mass or looking at the cross sectional area [46]. As long as no trapped voids are present and the material is isotropic, all these methods should yield the same results. The porosity in the wall is not only present to provide cooling in the wall, but also to evenly distribute the coolant so that it is injected uniformly. One can imagine that a wall with, for example, a porosity of only 0.01 will not provide proper cooling even though a porosity can be defined. No exact limit on the low-end of the porosity is known from literature. Therefore, as a lower limit a porosity of 0.2 is used in this thesis. The lowest values found in literature for transpiration cooling applications are 0.156 [1] and 0.18% [19].

$$\epsilon = \frac{V_{\text{open}}}{V_{\text{total}}} \quad (1.1)$$

## 1.5. Research goals and research questions

As discussed in section 1.1, it is claimed that transpiration cooling provides better cooling than regenerative and regenerative + film cooling. However, no comparison between the methods that focuses on wall temperature and overall engine performance can be found in literature. Therefore, the primary research goal of this thesis is:

***Determine how regenerative, regenerative + film cooling and transpiration cooling compare with respect to total engine performance for a 68 kN bipropellant liquid rocket engine.***

The term 'total engine performance' takes into account (potential) increases in specific impulse that require a dry mass penalty. In the end, the comparison between the cooling methods will thus be on the feasibility (i.e. can it work at all?) and the total impulse achieved by the engine with different cooling methods.

As mentioned, additive manufacturing could be an option for the material limitations that have hindered the use of transpiration cooling until now. Therefore, the secondary goal is:

***Determine if additive manufacturing of a rocket combustion chamber wall can be used to produce a transpiration cooled 68 kN bipropellant liquid rocket engine that can compete with its regenerative + film cooled variant.***

These two research goals lead to the following research questions:

1. Goal: *determine how regenerative, regenerative + film cooling and transpiration cooling compare with respect to total engine performance for a 68 kN bipropellant liquid rocket engine.*
  - (a) *What are the differences in maximum wall temperature between the three cooling techniques in steady state?*

At high temperatures, the combustion chamber wall will fail due to lower mechanical strength at elevated temperatures. Therefore, it is important to know if transpiration cooling can result in lower wall temperatures. If they are indeed lower, this would allow for higher chamber pressure to

increase the performance. Steady state is assumed to occur as the burn time of the engine is 190 s.

- (b) *What are the differences in thermal gradients in the wall between the three cooling techniques in steady state?*

The wall does not fail due to lower mechanical strength at elevated temperatures, but due to the stress being higher than the allowed one. A large contribution to the stress in a combustion chamber wall is the thermal stress occurring due to the thermal gradients in the wall [16]. However, it is too extensive to determine the exact stress in the wall. Therefore, as a representation for the thermal stress, the thermal gradients are evaluated.

- (c) *What is the distribution of coolant in a transpiration cooled engine that will minimize the coolant mass flow?*

As mentioned in section 1.1, the heat flux in a rocket engine is not constant and peaks in the throat. Therefore, not all parts of the engine require the same amount of cooling. This allows for the minimization of the transpiration coolant by providing the precise amount of required coolant at every (axial) location.

- (d) *What are the differences in specific impulse between the cooling techniques?*

A higher specific impulse will increase the engine performance and thus the capability of the launcher to carry a heavier payload which will lower the price per kilo of payload.

- (e) *What are the differences in engine dry mass of the different cooling techniques?*

The dry mass of the cooling techniques is potentially different. This will offset any specific impulse gains and should be investigated. Dry mass is defined as the combination of the combustion chamber and injector mass. The required turbo pump can also be accounted to this, but now changes to the pump are considered in this thesis.

- (f) *What are the differences in delta-v achieved by the reference engine for the three cooling techniques?*

In the end, any increase in specific impulse might be offset by an increase in dry mass. Therefore, an objective way to compare the cooling methods is to evaluate their total delta-v obtained. This also requires the mass parameters of the small satellite launcher.

- (g) *How do the above results change when copper is used as wall material instead of Inconel?*

The reference engine is designed to be manufactured from Inconel which has a low thermal conductivity. The comparison between the three cooling methods might change when a higher conductive material is used as this has better cooling performance by default. As the most common (inner) wall material for engines is copper [16], this material is selected as the higher conductive material.

2. Goal: *determine if additive manufacturing of a rocket combustion chamber wall can be used to produce a transpiration cooled 68 kN bipropellant liquid rocket engine that can compete with its regenerative + film cooled variant.*

- (a) *Can the required wall properties for a transpiration cooled wall be produced using additive manufacturing?*



It was determined in section 1.4 that the hole/pore sizes producible with additive manufacturing are larger than commonly seen in transpiration cooled applications. Therefore, the required wall properties need to be determined and then be compared to what is possible to produce.

(b) *How does varying the porosity within the wall in radial direction affect cooling performance?*

The flexibility of additive manufacturing can allow for a variation of porosity within the radial direction of the wall. This possibility has not been encountered in the common fabrication methods used for transpiration cooling. It will be investigated if and how this variation can affect the transpiration cooling performance.

(c) *How does the pore size and its variation within the wall affect cooling performance?*

Same reasoning as for the porosity. Pore size is defined as the diameter of the pores or as the diameter of the used spherical particles. This is further explained in chapter 3.

## 1.6. Research plan

To determine the temperature in the wall, three models for regenerative, film and transpiration cooling are developed in Matlab. The main outputs of all models are the maximum wall temperature and the thermal gradients. The decision is made to use simplified heat transfer models to allow for a quick variation of parameters. This can then be used to perform parametric analyses, sensitivity analyses and optimization. All three models are limited to steady state. As the engine will burn for 190 s, it is safe to say that steady state will be reached and this simplifies the analysis considerably. The components of the three models and the required actions to be taken are discussed below.

- Regenerative cooling model:
  - Uses NASA's Chemical Equilibrium with Applications (CEA) [13] to determine the combustion gas properties.
  - Convective heat transfer modelled using the Bartz equation [47].
  - Radiative heat transfer is included and modelled using empirical relations [12].
  - The Dittus-Boelter equation is used to determine the convective heat transfer on the coolant side.

Once the regenerative cooling model is developed, it is verified and validated by comparing it to a more extensive CFD model obtained from literature due to lack of test data available for the reference engine. It is known that the Bartz equation deviates from the actual heat transfer in rocket engines, especially in the cylindrical section [7, 48]. Ideally, one would perform a calibration with test data of the actual reference engine. However, as the reference engine is not tested, a calibration is performed using another kerosene and oxygen fuelled rocket engine from literature.

- Transpiration cooling model:
  - The incoming heat flux is modelled the same way as for the regenerative cooling model.
  - A model with the local thermal equilibrium (LTE) and local thermal non-equilibrium (LTNE) assumption are developed.
  - The Darcy-Forchheimer equation is used to model the pressure drop in the wall.
  - The heat transfer within the porous wall is modelled using empirical relations [49, 50].
  - The reduction in heat transfer due to blowing effects is modelled using an empirical relation from Meinert et al. [51].

Two options exist for modeling a transpiration cooled wall: the local thermal equilibrium (LTE) and local thermal non-equilibrium (LTNE) assumption. The first one assumes that the heat transfer within the porous wall is so fast that the solid and coolant are locally the same temperature. The latter is more accurate, but is

computationally more expensive. Both models are implemented and after the specification of the required boundary conditions, it is investigated which model is the best for the application in this thesis. Verification and validation of the transpiration cooling model is performed. Little test data in literature is available on transpiration cooling and thus the validation was a challenge. After this, the model will be used to perform a parametric analysis to answer some of the research questions. Furthermore, a sensitivity analysis is performed to find the sensitivity of some assumptions and choices made. Secondly, it is used to investigate how well a transpiration cooled engine will work in an actual application with oscillating chamber pressure and changing heat flux. Lastly, the coolant distribution is optimized for the Inconel chamber.

- Film cooling model:
  - The incoming heat flux is modelled the same way as for the regenerative cooling model.
  - The heat transfer on the coolant side is modelled the same way as the regenerative cooling model.
  - A new transcritical film cooling model is developed by the combination of:
    - ◊ The NASA annex B film cooling model that describes the temperature once the film coolant is gaseous [11].
    - ◊ The behaviour of the transcritical liquid film is modelled based on a model developed by Höglauer [10].
    - ◊ The effect of the evaporating liquid coolant is modelled based on the film cooling model developed by Shine et al. [52] and this uses the Meinert et al. equation [51] that is also used in the transpiration cooling model.

The coolant in the reference engine has transcritical behaviour: it is injected as a compressible liquid and when heated up, it turns into a supercritical fluid. This means that there is no heat of vaporization associated with this phase transition. While most rocket engines operate in exactly this condition, no film cooling model was found to model this. They are limited to purely gas or liquid coolants. Therefore, a new transcritical film cooling model is developed by combining three existing models into a single one. This model is validated by comparing it to a combination of CFD data and tests obtained from literature. Then it is used to determine the required film coolant to cool the reference engine.

Additionally, the developed film cooling model is compared to another film cooling model that results in higher heat fluxes. This model is the film cooling model in the commercial software Rocket Propulsion Analysis (RPA). A calibration of the developed model is performed to match the RPA model. This calibrated version and the uncalibrated version (that matches the test data) are both used in the rest of the thesis.

Once all three models are finished, they are applied to the reference engine for two different wall materials: Inconel and copper as an alternative. This will result in the required injected coolant for film and transpiration cooling to achieve certain wall temperatures. Additionally, the wall temperature of a purely regenerative cooled wall is found. The coolant mass flows can be used to determine the losses in specific impulse. Secondly, an estimation of the dry mass is made and this can then finally be used in a delta-v calculation to objectively compare the cooling techniques.

A conclusion on the use of additive manufacturing is that the larger pore sizes (compared to commonly used materials for transpiration cooling) result in a too low pressure drop over the wall. A minimum pressure drop is required to make sure no back flow can occur. As the pressure drop per length is low, this will result in very thick walls to achieve the minimum pressure drop. This will then result in very heavy walls. Therefore, additionally to the theoretical work performed in this thesis, some experiments were performed on the pressure drop of additively manufactured porous walls in an attempt to create higher pressure drops by using different geometries.

## 1.7. Thesis outline

This thesis is structured in a way that follows the described research plan. The required background information on the cooling techniques, the reference engine and material properties have been introduced in this chapter. Every cooling method is described in its own chapter. The regenerative cooling model is described

first in chapter 2 as components of this model will be reused in the transpiration and film cooling model. In chapter 3 the transpiration cooling model is described. In this chapter, the model is also used to perform the parametric and other analyses on solely transpiration cooling. This answers some of the research questions. The film cooling model is then described in chapter 4. Finally, in chapter 5, the three cooling techniques are compared by applying them to the reference engine. The experiments on pressure drop are described in chapter 6. Lastly, the conclusions and recommendations are given in chapter 7.



# 2

## Regenerative cooling model

In this chapter the regeneratively cooling model is discussed. This model was implemented in Matlab and consists of the heat transfer on the hot and cold sides of regeneratively cooled wall. Components of the model are used as building blocks for the transpiration and film cooling model described in chapter 3 and chapter 4. The determination of the hot side heat transfer from convection and radiation will also be used in transpiration model and the whole film cooling model will be built around the model presented here.

Models for regeneratively cooled engines have been used by others and these range from simple 1D analytical models [53, 54] - as will be done in this thesis - to more extensive work modelling the coolant channels with 3D CFD tools and using conjugated heat transfer analysis [5]. The simple model of [53] was compared to the more extensive CFD model from [5] and it was found that the wall temperature had a difference of 150 K on a maximum temperature of around 600 K. However, the pressure drop and increase of coolant temperature in the channels were estimated within 10%. Furthermore, the hot gas side heat transfer of the simple model deviated with around 25% compared to experiments. Naraghi et al. [55] used simple heat transfer correlations for the coolant, but modelled the conduction in the wall in two dimensions using a finite difference method. Secondly, for the hot gas side heat transfer, the commercial software Two Dimensional Kinetics is used. Cho et al. [56] used a 1D model for the preliminary design of a regenerative cooled combustion chamber. The convective heat transfer is determined using empirical relations and NASA's CEA is used to determine the hot gas properties. While validation of the model is discussed, no exact values for the accuracy of the heat transfer analysis are given. The conclusion from these works is that 1D models are less accurate than more extensive methods, but they can be used for sensitivity analysis and preliminary design. The model in this thesis will be limited to a simple 1D model regardless. A more extensive modelling is out of the scope. Furthermore, the main interest is in comparing the three cooling methods and any absolute errors in the incoming heat flux are present in all models and thus cancel out.

The computational model of this thesis is described in section 2.1. The method of determining the combustion gas properties is explained which can then be used to determine the convective and radiation heat transfer to the combustion chamber wall. Once the convective heat transfer on the cold side is determined, the wall temperature can be calculated. The chapter is concluded with a summary of the model and the made assumptions. Then, verification and validation is performed on the model in section 2.2. In this section the calibration for the heat transfer coefficient on the hot side is also presented.

### 2.1. Model description

The model description is divided into three parts. Firstly, the determination of the combustion gases is discussed. Then, the hot side heat transfer is presented. Thirdly, the coolant side heat transfer is described. Afterwards, a summary of the model with the required inputs and assumptions made is given.

### 2.1.1. Combustion gas properties

The properties of the combustion gases are obtained from NASA's Chemical Equilibrium with Applications (CEA) [13]. For a certain propellant combination and chamber pressure, CEA will provide the properties of the combustion products. This program is often used in (first order) modelling of combustion chambers, see for example [5, 38].

The used outputs of CEA are pressure, temperature, Mach number, isobaric specific heat, specific heat ratio, viscosity, conductivity, Prandtl number and the molar fractions of CO<sub>2</sub> and H<sub>2</sub>O gases. It is assumed that the combustion products are in equilibrium up to the throat and from the throat to the end of the nozzle they are assumed to be frozen. This means that in the section before the throat, the reactions are infinitely fast and this is reasonable due to the high temperatures in the chamber. After the throat, the temperature drops quickly and this slows down the reactions. CEA provides the properties at several stations in the convergent and divergent part of the nozzle. A linear interpolation with respect to the area ratio ( $A/A_t$ ) is used to obtain the properties between the stations.

### 2.1.2. Heat transfer hot gas side

Once the combustion gas properties are determined with CEA, these can be used to calculate the convective and radiative heat transfer from the gases to the chamber wall. The convective heat transfer is given by Equation 2.1 [17], where  $T_{w,h}$  is the temperature on the hot side of the wall, the heat transfer coefficient  $h_g$  is convective heat transfer coefficient and  $T_{aw}$  is the adiabatic wall temperature given by Equation 2.2 [17]. In this equation  $T_g$  is the static temperature of the hot gas,  $\gamma_g$  the ratio of specific heats of the hot gas,  $M_g$  the Mach number of the hot gas and  $r$  is the recovery factor for turbulent flow and is given by Equation 2.3 [17]. This factor depends on the Prandtl number  $Pr$ .

$$q_{\text{conv}} = h_g (T_{\text{aw}} - T_{w,h}) \quad (2.1)$$

$$T_{\text{aw}} = T_g \left( 1 + r \frac{\gamma_g - 1}{2} M_g^2 \right) \quad (2.2)$$

$$r = Pr_g^{1/3} \quad (2.3)$$

In this work the Bartz equation (Equation 2.4 [17, 47]) is used to determine the convective heat transfer coefficient. This equation is a function of throat diameter  $D_t$ , the dynamic viscosity at stagnation condition  $\mu_0$ , isobaric specific heat at stagnation condition  $c_{p0}$ , Prandtl number at stagnation condition  $Pr_0$ , total chamber pressure  $P_{c0}$ , characteristic velocity  $c^*$ , radius of curvature of the throat  $r_t$ , throat area  $A_t$  and the area at the location of interest  $A$ . The value of  $\sigma$  contains corrections for property variations across the boundary layer [47] and can be calculated by Equation 2.5. In this equation  $\omega$  is the temperature exponent of the viscosity equation, which for a rocket engine can be assumed to be 0.6 [47].

The Bartz equation is an empirically determined function that describes the convective heat transfer in different sections of the nozzle. It was determined for a nozzle with a contraction and expansion half angle of 30° and 15° respectively [47]. It is estimated that the relation is sufficiently accurate if the angles do not change more than 50% [47], so the contraction and expansion half angles can be 15-45° and 7.5-22.5° respectively. Secondly, the accuracy should be good when the ratio of throat diameter to throat radius of curvature  $D_t / r_c$  is smaller than 3 [47]. The value for  $D_t / r_c$  of the reference engine is 2.99 and the half angles for the reference engine are 38.9° and 26.6°. This means that the expansion half angle is 4.1° larger than for the value of which the Bartz equation is accurate for. Due to lack of other equations, this error is accepted. Generally, the Bartz equation needs to be calibrated for the engine it is used for. This is further discussed in section 2.2. Furthermore, the Bartz equation was derived for the heat transfer in nozzles, but will in this thesis also be used to determine the heat transfer in the cylindrical section of the chamber. It is known that Bartz equation deviates largely in this section from the actual heat transfer [7, 48]. This is partly accounted for by the calibration done in section 2.2 and a constant value for the heat transfer coefficient is used in the complete

cylindrical part to speed up the calculations, but it is known that close the injector the deviations are larger [7, 48].

$$h_g = \left[ \frac{0.026}{D_t^{0.2}} \left( \frac{\mu_{g0}^{0.2} c_{p_{g0}}}{Pr_{g0}^{0.6}} \right) \left( \frac{P_{c0}}{c^*} \right)^{0.8} \left( \frac{D_t}{r_t} \right)^{0.1} \right] \left( \frac{A_t}{A} \right)^{0.9} \sigma \quad (2.4)$$

$$\sigma = \frac{1}{\left[ \frac{1}{2} \frac{T_{w,h}}{T_{g0}} \left( 1 + \frac{\gamma_g - 1}{2} M_g^2 \right) + \frac{1}{2} \right]^{0.8 - \frac{\omega}{5}} \left[ 1 + \frac{\gamma_g - 1}{2} M_g^2 \right]^{\frac{\omega}{5}}} \quad (2.5)$$

The combination of these relations describe the convective heat transfer from the hot combustion gases to the chamber wall and will also be used for the transpiration and film cooling model. Some of these equations depend on the wall temperature and thus they have to be solved in an iterative manner.

In addition to the convective heat transfer, radiative heat transfer from the hot gases to the wall is included in the model. Kirchberger did experiments with a small RP-1 and gaseous oxygen rocket engine and found that the radiation causes 3% to 8% of the total heat flux [7]. Naraghi et al. found by modelling of an RP-1 and LOX engine that including the radiative heat transfer increases the final temperature up to 30% [57]. If the radiation heat transfer is indeed small, it is an option to neglect radiation in the modelling of regeneratively cooled rocket engines. However, looking ahead at the transpiration and film cooling model it is decided to include radiation. In the transpiration cooling model, the convective heat transfer is heavily reduced by the injected coolant and thus the radiation becomes a larger factor. Secondly, the film cooling model assumes that the liquid coolant film on the inside of the chamber stops the convective heat transfer to the wall, but radiation can pass through it. So, in the part where the film is liquid, radiation is the only mechanism heating up the wall and cannot be neglected. Both these processes are further discussed in chapter 3 and chapter 4.

At the wavelengths relevant for radiative heat transfer in rocket engine, gases with asymmetric molecules ( $H_2O$ ,  $CO_2$ ,  $CO$ ) have strong emission bands [16, 58]. The main gases in a rocket chamber will be  $H_2O$ ,  $CO_2$  and  $CO$ . Only  $CO_2$  and  $H_2O$  should be taken into account for combustion chambers [58] as it is estimated that the radiation by carbon monoxide is an order of magnitude lower than that of carbon dioxide and that thus considering water vapour and carbon dioxide is sufficient [7].

It is possible to use so-called Hottel charts to determine the emissivity of the gas mixture depending on the temperature and pressure of the gases. Combining this with the emissivity of the wall, the radiation can then be determined [58, 59]. However, as this thesis focuses mainly on the comparison between regenerative, transpiration and film cooling, it is chosen to use a simple empirical relation for the radiative heat transfer. The same equation is used for all cooling methods, so this allows for a fair comparison and should cancel out any errors.

Kirchberger [7] lists several of these relations and Equation 2.6 and Equation 2.7 from [12] are used. This equation takes the water and carbon dioxide into account. The partial pressure  $P$  (in Pa) is determined using CEA and varies within the engine. The  $r$  is the radius of the chamber at the location of interest. The equations were determined by experiments with 20 mm to 37 mm diameter combustion chambers using kerosene and gaseous oxygen at 30 bar and 60 bar chamber pressure. No discussion on the accuracy of these relations is given. The equation for water is valid up to  $P \cdot L$  values of 600 bar-cm, for the  $CO_2$  no range was found.

$$\dot{q}_{rad_{H_2O}} = 5.74 \left( \frac{P_{H_2O}}{10^5} r \right)^{0.3} \left( \frac{T_g}{100} \right)^{3.5} \quad (2.6)$$

$$\dot{q}_{rad_{CO_2}} = 4 \left( \frac{P_{CO_2}}{10^5} r \right)^{0.3} \left( \frac{T_g}{100} \right)^{3.5} \quad (2.7)$$

Note, that these relations do not depend on temperature to the power four, which is how radiative heat transfer actually depends on temperature [16]. So, at lower wall temperatures, this relation will give an underestimation of the radiative heat transfer. In the end, one is interested in conditions that yield a temperature close

to the maximum allowed one, so an underprediction at lower temperatures is not necessarily a problem. Furthermore, the emissivity of the wall is not included in the relations. The emissivity depends on the material used [16] and in RP-1 engines, soot can be deposited on the walls and this will change the emissivity [17]. The relations were determined for an RP-1 and oxygen engine, so one can assume that for the regenerative case of the reference engine the effect of soot is included. However, it is unknown how transpiration and film cooling affect soot formation on the wall. Lastly, Kirchberger used a copper engine instead of an Inconel one and this will have a different emissivity.

For the complete model described in this thesis, a recommendation regarding the radiation heat transfer can be given. When time is spent on improving the model, a good first step would be to include a better radiation model that takes into account the emissivity of the gas and the wall. This is quite a 'stand alone' component of the model and can be implemented without much required changes to the complete model. A recently updated database of the emissivity of water and carbon dioxide for high temperatures and pressures can be found in [60, 61].

### 2.1.3. Heat transfer coolant side

Only convection is taken into account on the cooling channel side of the wall. CoolProp [4] is used to calculate density, viscosity, isobaric specific heat and conductivity. CoolProp is an open source software tool that can determine the properties of many different fluids and can be used in Matlab using a Python wrapper. The coolant properties are used to determine the convective heat transfer coefficient by the Dittus-Boelter equation, see Equation 2.8. The convective heat transfer from the wall to the coolant is then determined using Equation 2.9. For the Nusselt and Reynolds number required for Equation 2.8, the hydraulic diameter of the cooling channel is used. The Dittus-Boelter equation is valid for turbulent flow ( $2500 < Re < 1.24 \cdot 10^5$ ), for Prandtl numbers between 0.7 and 120 and for an L/D of larger than 60 [62] or L/D larger than 10 according to [63]. This means that, due to entrance effects, in either the first 5 cm or the first 26 cm after injection of the coolant into the end of the nozzle (depending on the L/D), that the Dittus-Boelter equation is not valid. This all occurs in the divergent part of the nozzle where the heat transfer will be lower, so it is expected that this error will be small. However, the program can be easily equipped with better and more adequate heat transfer relations when different fuels are used. As the main focus of this thesis is the comparison between the cooling methods occurring the cylindrical section, investigating different relations was seen as out of scope.

$$Nu_c = 0.023 \cdot Re_c^{0.8} \cdot Pr_c^{0.4} \quad (2.8)$$

$$q_{conv} = h_c(T_{w,c} - T_c) \quad (2.9)$$

The fluid properties required for the determination of the Nusselt, Reynolds and Prandtl number, need to be determined at the bulk temperature of the fluid for Equation 2.8 [62]. In the program, the properties are determined at the bulk temperature for each station in the axial direction. When larger temperature differences occur between the fluid and wall, it is recommended to use the Siedert-Tate correlation and not the Dittus-Boelter one [63]. This would then require iterations to solve for the heat transfer coefficient and is not used to keep the program as simple as possible. This would be easy to implement if one is interested in different heat transfer relations, but as discussed before, this is seen as out of scope.

A correction is used for the effect of surface roughness on the heat transfer. This is especially important as the additively manufactured engine has a larger surface roughness than conventionally machined parts. The effect of roughness is modelled by including a factor in the Nusselt number relation and is given by Equation 2.10 as an input of  $\xi$  which is the ratio of friction factor to the friction factor when the wall is smooth (Equation 2.11) and follows from [64]. This approach is also used by [53]. The friction factor is given by Equation 2.17. Then, the heat transfer coefficient can be determined by first multiplying the Nusselt number with  $\Psi_\xi$  and then rewriting the Nusselt number to heat transfer coefficient (Equation 2.12).

$$\Psi_\xi = \frac{1 + 1.5Pr^{-1/6}Re^{-1/8}(Pr - 1)}{1 + 1.5Pr^{-1/6}Re^{-1/8}(Pr\xi - 1)}\xi \quad (2.10)$$



$$\xi = \frac{f}{f_{R_{\text{sur}}=0}} \quad (2.11)$$

$$h_c = \frac{k \cdot \text{Nu} \cdot \Psi_\xi}{D} \quad (2.12)$$

Another correction is required for the presence of ribs in the cooling channels. The fin efficiency is given by Equation 2.13 and it is a function of the heat transfer coefficient on the cold side  $h_c$ , thermal conductivity of the wall  $k$ , rib thickness  $t_{\text{rib}}$  and height of the cooling channel  $h_{\text{channel}}$ . The new heat transfer coefficient can be calculated using Equation 2.14. In this equation  $w_{\text{channel}}$  is the width of the cooling channel [65]. The parameters are also displayed in Figure 2.1.

$$\eta_f = \frac{\tanh\left(\sqrt{\frac{2 \cdot h_c \cdot t_{\text{rib}}}{k}} \frac{h_{\text{channel}}}{t_{\text{rib}}}\right)}{\sqrt{\frac{2 \cdot h_c \cdot t_{\text{rib}}}{k}} \frac{h_{\text{channel}}}{t_{\text{rib}}}} \quad (2.13)$$

$$h_{c,f} = h_c \frac{w_{\text{channel}} + 2 \cdot \eta_f \cdot h_{\text{channel}}}{w_{\text{channel}} + t_{\text{rib}}} \quad (2.14)$$

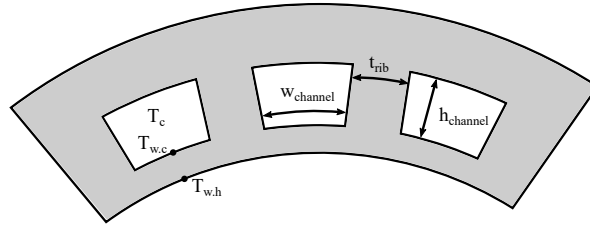


Figure 2.1: Parameters used in the calculations of the convective heat transfer and that describe the cooling channel geometry.

As the coolant flows through the channels, the velocity changes. This causes a change in static pressure and static temperature of the coolant. Furthermore, the total temperature increases due to absorption of heat. Both these phenomena are accounted for in the model. The temperature for a new station can be calculated taking into account the change due to heating and the change in velocity and is given by Equation 2.15.

$$T_{c_{i+1}} = T_{c_i} + \frac{q \cdot A_{i+1}}{c_{p_{c_{i+1}}} \cdot \dot{m}_c} - \left( \frac{v_{c_{i+1}}^2}{2 \cdot c_{p_{c_{i+1}}}} - \frac{v_{c_i}^2}{2 \cdot c_{p_{c_i}}} \right) \quad (2.15)$$

The total pressure drops due to friction losses in the channel. The pressure drop is calculated using the Darcy-Weisbach equation given by Equation 2.16 [58]. This equation is a function of friction factor  $f$ , the density of the coolant  $\rho_c$ , the length of the channel section  $L$  and the hydraulic diameter of that section  $D$ . Note that the local properties at the station evaluated are used. The friction factor for turbulent flow ( $\text{Re} > 4000$ ) is given by Equation 2.17 and is a function of the Reynolds number of the coolant  $\text{Re}_c$ , the surface roughness  $R_{\text{sur}}$  and the hydraulic diameter  $D$ . This equation for the friction factor is valid for circular and non-circular pipes and was determined for horizontal pipes [58], so any gravity forces are not included. The estimation inaccuracy is  $\pm 15\%$  [58]. Then the pressure for the station can be calculated using Equation 2.18.

$$\Delta P_c = f \cdot \rho_c \frac{L}{D} \frac{v_c^2}{2} \quad (2.16)$$

$$\frac{1}{\sqrt{f}} = -2\log_{10}\left(\frac{2.51}{\text{Re}_c\sqrt{f} + \frac{R_{\text{sur}}}{3.7D}}\right) \quad (2.17)$$

$$P_{c_{i+1}} = P_{c_i} - \Delta P_c - (0.5 \cdot \rho_{c_{i+1}} \cdot v_{c_{i+1}}^2 - 0.5 \cdot \rho_{c_i} \cdot v_{c_i}^2) \quad (2.18)$$

#### 2.1.4. Model summary

A flowchart of the steps taken in the program can be seen in Figure 2.2. The coolant is injected at the nozzle exit and then flows towards the injector. Therefore, the first station is at the end of nozzle. Once the wall temperature has converged for this location, the program moves on to the next station. The inputs for the program can be seen in Table 2.1 and the outputs are the hot and cold side wall temperature and the properties of the coolant in the cooling channels.

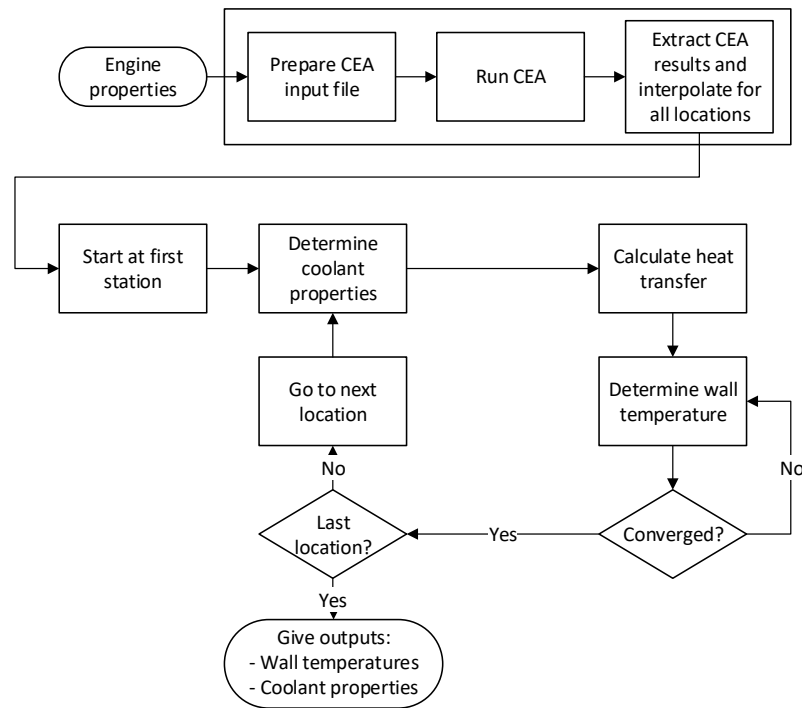


Figure 2.2: A flowchart of the program for regenerative cooling.

An overview of the assumptions made in the program and their consequences are listed below:

- The heat transfer is one dimensional only in the radial direction. This will overestimate the temperature at locations where there are strong temperature gradients in the axial direction, which mainly occurs at the throat of the nozzle.
- The thermal conductivity of the wall is constant with temperature. For Inconel the value at room temperature is taken. The thermal conductivity goes up with temperature, so this a conservative approach. For the copper alloy uses, no data is available.
- The wall and cooling geometry do not change under stresses applied by heating and the pressure.
- The hot gas properties in the cylindrical section of the chamber are set equal to the properties at the start of the convergent part of the nozzle. This means that no pressure drop occurs in the cylindrical

Parameter	Unit	Type	Comment
Engine contour (L,r)	m	CSV file	
Chamber pressure	bar		
Fuel type	-	String	
Oxidiser type	-	String	
OF ratio (mass)	-		
Total mass flow	kg/s		
Wall thickness	m		Constant
Wall thermal conductivity	W/mK		
Number of cooling channels	-		
Cooling channel geometry	m	CSV file	Width, height, rib thickness
Coolant fluid	-	String	Limited to CoolProp fluids
Coolant inlet pressure	bar		
Coolant inlet temperature	K		
Surface roughness cooling channel	m		

Table 2.1: The inputs for the regeneratively cooling model.

part of the combustion chamber. This pressure drop is small, so it is not expected that this will change the analysis.

- No radiation occurs from the cooling channel to the coolant as this radiation will be low.

The regeneratively cooled model has been described. The determination of the combustion products and the hot side heat transfer will be reused in the transpiration and film cooling model. For the film cooling model, also the complete coolant side heat transfer is reused. In the next section, the program is verified and validated.

## 2.2. Verification and validation

Verification is performed to ensure that the above described equations are implemented correctly. Once the code is verified, validation is performed to ensure that the code can actually predict the performance of a regeneratively cooled wall to a certain accuracy.

The verification consisted of checking the code for any errors and checking the implementation of the equations. Once that was done, simple sanity checks and a comparison to the commercial software Rocket Propulsion Analysis (RPA) were made as well. These results are too extensive to be discussed here and are given in Appendix A. The conclusion from the verification is that the code is implemented correctly and that RPA and the code predict the same trends. Additionally, the properties obtained with CoolProp are compared to data from NIST, see Appendix B. Both the properties of ethanol and methane are checked. The latter coolant will be used in the validation that follows.

For validation, it would have been preferred to compare the developed model to experiments of a rocket engine similar to the reference engine. In short: an engine with the same propellants, thrust level and OF ratio. A comparison to such an engine could validate the accuracy of the one dimensional model and could also be used to calibrate the Bartz equation. The latter is required as it is an empirical equation that varies for different engines. Unfortunately, no such engine was found in literature. Also, no test data exists for the reference engine used in this thesis. Therefore, the tasks described above are split in two. Firstly, the model is compared to CFD results of a liquid oxygen and liquid methane engine from the Italian Aerospace Research Center (CIRA). After this, data from experimental tests on a small scale oxygen and kerosene engine is used to calibrate the Bartz equation that predicts the hot gas side heat transfer.

While ideally one would compare the model to actual test data, comparing the model to a more elaborate method such as CFD, is a step in the right direction regarding validation. Another advantage of a comparison to a CFD analysis is that this allows for the determination of 'difficult' to measure data such as wall tempera-

ture and the state of the coolant in the channels. This comparison is the validation of the correct modelling of the coolant properties and heat transfer in the wall. However, it does not allow for validation of the determination of the hot gas side heat transfer.

### 2.2.1. Comparison with CIRA engine

The liquid oxygen and methane engine used for the validation is described in the work of Pizzarelli et al. [5] and the nozzle and channel geometry follow partly from [53]. The engine specifications are shown in Table 2.2. The methane properties of CoolProp are validated in Appendix B. Pizzarelli et al. performed a conjugated heat transfer analysis with an axisymmetric 2D CFD simulation for the combustion gases. It was assumed that the combustion products enter the chamber completely burned and are then frozen in composition. A 3D RANS simulation is used for the cooling channels. The coolant enters the chamber at the end of the nozzle and then flow towards the injector. No radiation heat transfer is modelled. Comparing the model in this work to the simulations done on the CIRA engine allows for a comparison between a simple 1D model to a 3D one.

Table 2.2: The specifications of the CIRA engine.

Parameter	Symbol	Value	Unit
Chamber Pressure	$P_c$	56	bar
OF ratio	OF	3.35	-
Coolant mass flow	$\dot{m}_c$	1.92	kg/s
Number of cooling channels		96	-
Inlet pressure cooling channel	$P_{c0}$	155.8	bar
Inlet temperature cooling channel	$T_{c0}$	112.4	K
Thermal conductivity wall	$k$	365	W/mK
Surface roughness channel	$R_{sur}$	6.3	$\mu\text{m}$

The comparison of the model to the CFD results is presented below. Firstly, it can be seen in Figure 2.3 that using the current model that uses the Bartz equation overestimates the heat flux. The Bartz equation often overestimates the heat transfer coefficient, especially when it is also used for the cylindrical part of the engine, and that is the reason why calibration is required [7, 48]. The difference approaches 100% in the cylindrical part of the chamber. It turned out that the adiabatic wall temperatures of both models are virtually equal and that the difference comes from the heat transfer coefficient which follows the same trend as the heat flux, see Figure 2.4. This shows the importance of calibrating the heat transfer coefficient obtained with the Bartz equation. Lastly, the heat flux determined by the current model is constant in the cylindrical part of the chamber. This is a consequence of using constant properties in the cylindrical section.

To obtain a comparison of the models that is not influenced by the overestimated heat flux, the adiabatic wall temperature and hot gas heat transfer coefficient from Pizzarelli et al. are used as inputs in the model. Additionally, the radiation heat transfer in the model is disabled as the CIRA engine also does not account for radiation effects. A comparison between the calculated wall temperatures for the CIRA engine and the values given by Pizzarelli et al. is visible in Figure 2.5. The temperatures calculated by the model are generally lower than the reference values with a difference between the maximum temperatures of 150 K. In the part before the throat the maximum difference is 20.1%, but after the throat the error grows to 78.4%. Secondly, the 1D model predicts a peak in temperature at the location of the throat while the CIRA values show three separate local maxima in temperature. The current model especially underestimates the heat flux in the divergent nozzle region (0.3 m to 0.43 m). It appears that the choice of coolant side heat transfer coefficient affects the temperature in this region. In the model, the simple Dittus-Boelter relation is used. A similar comparison to the one here done by [53] found better agreement in this region using a specific heat transfer relation for supercritical methane, but this relation is not included in the current model. Secondly, Dittus-Boelter equation is not valid this region as the  $L/D$  is too low, so this might also be a reason for the difference.

The total temperature and total pressure of the coolant in the channels can be seen in respectively Figure 2.6 and Figure 2.7 for the case when the hot gas properties of Pizzarelli are used. As the coolant is flowing from the back of the engine to the front, the temperature increases when getting closer to the injector. The pressure in

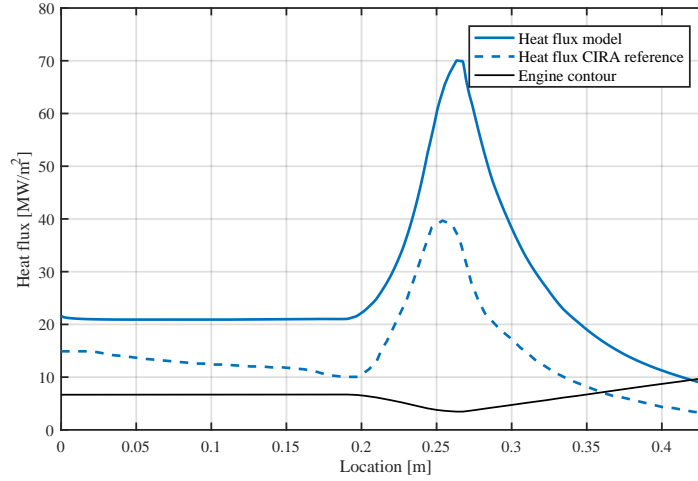


Figure 2.3: The heat flux of the CIRA engine [5] calculated with the model and the reference values; surface roughness  $1.0 \mu\text{m}$  instead of  $6.3 \mu\text{m}$  to make sure coolant pressure values remain above zero.

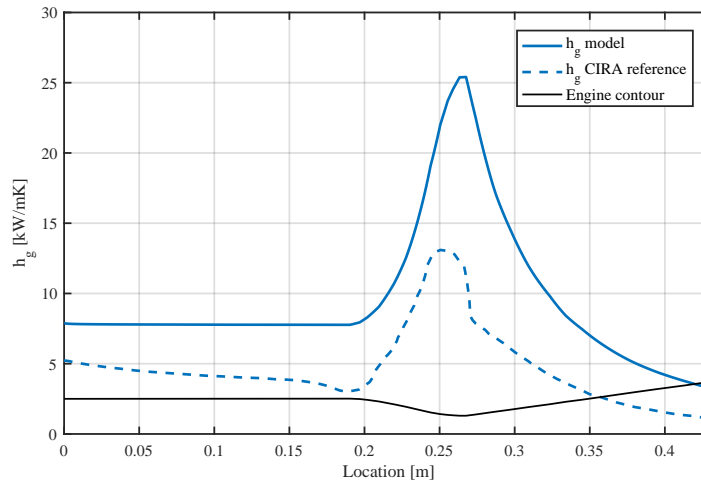


Figure 2.4: The convective heat transfer coefficient of the CIRA engine [5] calculated with the model and the reference values; surface roughness  $1.0 \mu\text{m}$  instead of  $6.3 \mu\text{m}$  to make sure coolant pressure values remain above zero.

the channels is always higher than the critical pressure of methane (46.1 bar [6]) and the critical temperature is 190.6 K [6]. So, in the throat, the coolant turns into a supercritical fluid. This shows that there is no need for the modelling of two-phase flow for the CIRA engine. The total pressure drops when getting closer to the injector. In the figures, it can be seen that the total pressure and total temperature are matching the reference values in shape, but that there is a slight difference in magnitude. For the total temperature a maximum difference is roughly 30 K on a total increase of 271 K. This translates to a difference of 11%. The pressure difference is 3.9 bar on a total pressure drop of 35.6 bar which translates to a difference of 11%. So, this shows that the program is capable of calculating the pressure and temperature in the channel to an error of around 10% when the incoming heat flux is correct.

From the above observations, it can be concluded that the 1D model overestimates the heat flux when modelling the CIRA engine. It can also be expected that this happens for other engines. Therefore, it is important to calibrate the heat transfer coefficient from the hot gases to the wall. This will happen in the next section. Furthermore, it can be concluded that the 1D model has the same trends in resulting properties as obtained using the more detailed 3D CFD work from Pizzarelli et al. This shows that the model is capable of producing results useful for first order analyses. It should be noted that in this thesis different cooling methods are com-

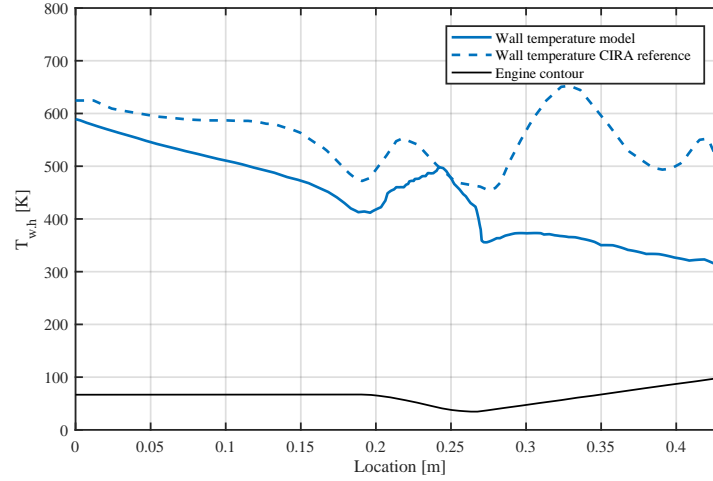


Figure 2.5: The wall temperature of the CIRA engine calculated with the model using  $T_{aw}$  and  $h_g$  values from [5] compared to the reference values of [5], radiation heat transfer is disabled.

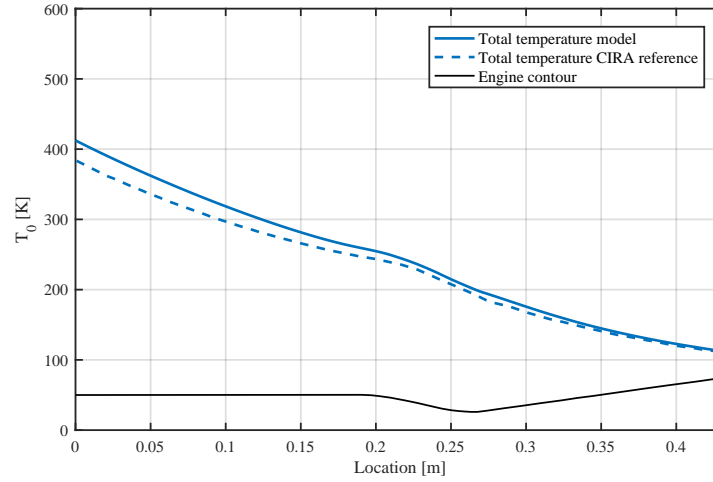


Figure 2.6: The total temperature of the coolant in the CIRA engine calculated with the model using  $T_{aw}$  and  $h_g$  values from [5] and the reference values of [5], at a coolant temperature of 190.6 K [6], the methane becomes supercritical.

pared for the same engine. So, the errors that occur in the hot gas properties affect both cooling methods and thus this error has a reduced influence on the comparison.

### 2.2.2. Calibration of the hot gas heat transfer coefficient

As already discussed in the previous section, the Bartz equation is an empirical relation and it is not uncommon that it overestimates the heat transfer [7, 48]. Therefore, it requires a calibration for the reference engine. However, no experiments with the reference engine are available and no similar LOX kerosene engine tests were found. Therefore, data from the work of Kirchberger [7] is used.

Kirchberger performed many tests on two small scale oxygen and kerosene engines, one with a diameter of 20 mm and a larger one with a diameter of 37 mm. For the 37 mm engine in total 81 data points were collected for mixture ratios between 1.4 and 3.4 and for chamber pressures between 10 bar and 80 bar. For the 20 mm engine, 45 data points are available for an OF between 2.4 and 3.2 and pressure between 40 and 80 bar. The reference engine lies between these values. Kirchberger compared the measured heat fluxes to the heat fluxes determined using the Bartz equation at different locations in the engine. This resulted in data specifying the over or under prediction of the heat flux when the Bartz equation is used. An example of the

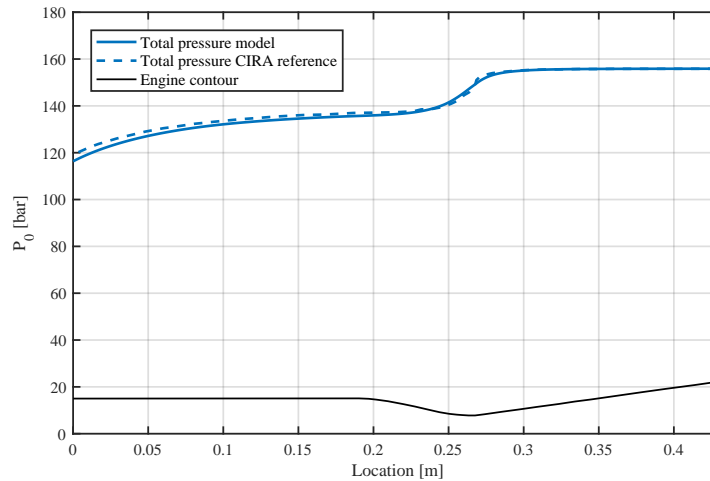


Figure 2.7: The total pressure in the coolant channel of the CIRA engine calculated with the model using  $T_{aw}$  and  $h_g$  values from [5] compared to the reference values of [5].

results can be seen in Figure 2.8. In this figure, the differences between the heat fluxes are given for a section of the cylindrical part of the engine.

It can be seen in the figure that the largest over predictions are caused by a change in OF ratio. This is attributed by Kirchberger to an increasing amount of imperfectly chemically reacting kerosene remaining in the exhaust gas and the increased production of soot [7]. For the cylindrical part of the chamber, the effect of a different chamber pressure is low. However, for the nozzle segment (not depicted in this work) a larger change with chamber pressure was seen. The main interest of this thesis lies in the cylindrical part as the transpiration cooling model and film cooling model are expected to be less accurate for the nozzle segment. Kirchberger found that for the 20 and 37 mm engine the Bartz equation over predicted the heat transfer between 75% and 100% at the beginning of the chamber and 25% to 30% at the end of the cylindrical part [7]. A constant average of these values is taken to ensure constant properties in the cylindrical section which will allow for faster modelling of the transpiration cooled engine. So, it is assumed that the Bartz equation overestimates the heat flux with roughly 55% in the reference engine. Therefore, the heat transfer coefficient obtained with the Bartz equation is multiplied with 0.65 to achieve calibration for the reference engine. This factor will be used with all the three cooling methods to guarantee it is a fair comparison and is taken as a constant such that the whole cylindrical section can be modelled with one calculation. This will speed up the transpiration cooling model, as will be discussed in chapter 3. It should be noted again: if one wants more accurate results for the reference engine, tests are required to determine the exact heat flux in the engine.

## 2.3. Conclusions

A model to determine the wall temperature in a regeneratively cooled rocket engine was presented. It accounts for convection and radiation from the hot gases to the wall and for convection from the wall to the coolant. It was determined that the hot side convective heat transfer coefficient is overestimated and is therefore scaled by a factor of 0.65. Then, when the appropriate relation for the convective heat transfer on the coolant side is used, the maximum inaccuracy of the wall temperature is 20% when compared to a 3D CFD calculation.

The validation of the model can be improved by comparing it to actual test data of a rocket engine, but this was not possible due to lack of available test data of the engine or in literature. If one wants to obtain accurate 'absolute' results on the wall temperature, the hot gas side heat transfer needs to be determined better for the reference engine. The accurate way to do this is by testing the actual engine. This will of course be a costly endeavour. However, it was seen that the heat transfer can vary up to 100% compared to analytical relations,

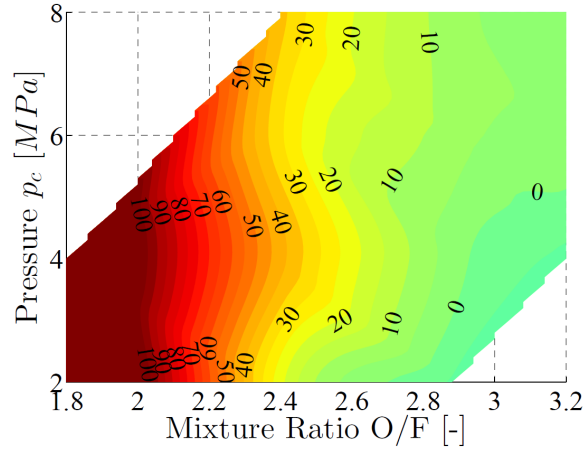


Figure 2.8: The overprediction in % of the heat flux for the 37 mm engine with the Bartz equation for the second cylindrical segment in the engine [7].

so testing is a must if one wants to get accurate results. For the goal in this thesis, which is comparing the cooling methods, the need for accurate hot gas side heat transfer estimation is less. All three cooling methods will use the same heat transfer inputs, so any errors in the estimation will cancel out when comparing the effectiveness of the cooling.

In the next chapter, the transpiration cooling model is discussed. This model uses the same method to determine the hot side heat flux and uses the same calibration factor as the regenerative cooling model.



# 3

## Transpiration cooling model

In this chapter the transpiration cooling model and the results obtained with it are discussed. Transpiration cooled rocket engines have been analysed before. Bucchi et al. [66] optimized a transpiration cooled throat section of a methane and LOX fuelled rocket engine. Landis [67] and Davis [68] focused on the wall of a hydrogen transpiration cooled rocket engine. Greuel et al. [2] described the governing equations required to model the DLR hydrogen transpiration cooled engine discussed in section 1.2. Some parts of these works are implemented in the model described in this thesis and other parts are explicitly different as these models were deemed insufficient. A complete overview of the models is too extensive, so when relevant, the similarities and/or differences will be mentioned in the discussion of the model. One important thing that all these models have in common, is that significant simplifications are required to reduce the computational time. In this work, this is also done by focusing on the cylindrical section of the chamber and assuming that it has constant hot gas properties. This allows for the modelling of a large part of the engine with a single calculation and reduces computational time. Another unfortunate thing that all these works have in common is that none of the model present any validation data. So, no estimation on the accuracy of the models can be made and this data can also not be used to validate the model in this thesis.

The hot gas properties for the transpiration cooling model are determined in the same way as for the regenerative cooling model. The reference frame used in the model is discussed in section 3.1. Then the governing equations that describe the behaviour of the coolant in the wall and the reduction in heat transfer are discussed in section 3.2. The governing equations also require boundary conditions to be able to model the engine, these are treated in section 3.3. It was found that a small difference in the boundary conditions will have a large effect on the final result. Therefore, a study into the boundary conditions is performed as well. Then, in section 3.4, the verification and validation of the model is discussed. With the finalised model, it is possible to answer some of the research questions already by performing a parametric analysis. This is done in section 3.5. Additionally, a sensitivity analysis is performed in section 3.6. In section 3.7 the coolant flow in the complete engine is optimized. Finally, the conclusions and recommendations for the modelling and the results are given section 3.8.

### 3.1. Reference frame

A cylindrical coordinate system is required as the cylindrical form of the energy equations are used. This allows for the modelling of the effect of the changing area that occurs at larger wall thicknesses - this is required as the transpiration cooled walls can be thick. It is assumed that the coolant flows in one direction which is normal to wall and that there is no heat transfer in axial direction within the wall. This means that the cylindrical reference system cannot be used in parts that are convergent or divergent as the direction in which the coolant flows is not equal to the radial direction in the reference frame. Therefore, the transpiration cooling analysis is limited to the cylindrical part of the chamber. Similar choices were made in other transpiration cooling investigations [68]. For the scope of this work, this is seen as sufficient: the differences between film and transpiration cooling that occur in the cylindrical section are also occurring in the convergent and divergent part of the nozzle. Secondly, in the convergent and divergent part there are larger axial temperature

gradients and thus the assumption that no axial heat transfer occurs is less valid in these regions anyway. Potentially, when a cartesian reference frame is used, the nozzle can be split up a lot of small sections and can be modelled this way (see [66]). However, this will increase the computational time and is therefore not pursued.

The reference frame can be seen in Figure 3.1. The x-direction is parallel to the center line of the engine and is zero at the start of the cylindrical part (so at the injector). The y-direction is the distance normal to the wall and is zero at the outer radius of the wall. The latter is used for the continuity and momentum equation and data plotting purposes. The energy equations are used in their cylindrical form. The continuity and momentum equation are calculated in cartesian coordinates (using y) as this allows for easy calculations of flat plates if this is needed. In case flat plates are modelled, the energy equations have to be changed to their cartesian form.

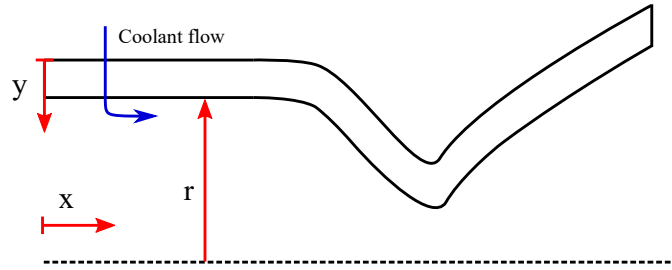


Figure 3.1: The reference frame for the transpiration cooling model.

## 3.2. Governing equations

In this section, the governing equations that are required to model a transpiration cooled wall are discussed. In total four different conservation equations are required: the continuity equation, the momentum equation, the energy equation and the equation of state. As the burn time is 190 s, the steady state versions are presented [2, 68, 69].

### 3.2.1. Continuity equation

Before the continuity equation for flow through porous media can be given, another variable needs to be introduced. This is the Darcy velocity (other names include: superficial velocity, seepage velocity, filtration velocity [69]) defined by Equation 3.1. The Darcy velocity is not the actual velocity of the fluid, but the apparent one taken over area of the porous medium, so the combination of open space and solid material. It can be obtained by multiplying the actual velocity  $v_{\text{actual}}$  with the porosity  $\epsilon$ . Other ways of determining the Darcy velocity is taking the mass flow over the medium and then dividing this by the density and total surface area of the porous medium (so the area including the open and closed spaces).

$$v = \epsilon v_{\text{actual}} \quad (3.1)$$

The continuity equation for a steady state flow through a porous medium is given by Equation 3.2 [69], where  $\epsilon$  is the porosity,  $\rho_c$  is the coolant density and  $v$  is the Darcy velocity. Only one dimensional heat transfer is considered and the mass flow is constant due to the steady state assumption. Therefore, the continuity equation reduces to Equation 3.3. Here, the area  $A$  is the total cross sectional area that depends on the radius. The area is a function of radius as the coolant flows normal to the axis.

$$\epsilon \frac{\partial \rho_c}{\partial t} + \nabla \cdot (\rho_c \mathbf{v}) = 0 \quad (3.2)$$

$$\dot{m}_c = \rho_c A(r) \cdot v \quad (3.3)$$

### 3.2.2. Momentum equation

As the coolant flows through the porous wall, the pressure will drop. This pressure drop in porous media can be determined by Darcy's law (Equation 3.4 [69]) or by the Forchheimer extended version (Equation 3.5 [1]). Both equations describe the pressure drop over length and their differences are discussed below. In these equations  $\mu_c$  and  $\rho_c$  are the viscosity and density of the fluid and  $v$  is the Darcy velocity. The permeability coefficients  $K_D$  and  $K_F$  are determined by empirical relations, which will be discussed below.

$$\frac{dP}{dy} = -\frac{\mu_c}{K_D} v \quad (3.4)$$

$$\frac{dP}{dy} = -\frac{\mu_c}{K_D} v - \frac{\rho_c}{K_F} v^2 \quad (3.5)$$

In combination with macroscopic parameters (such as porosity and permeability), these equations allow for modelling the porous medium as a homogeneous material. This is less computationally intensive than modelling the exact geometry. Which one of the two equations should be used, depends on the pore Reynolds number defined by Equation 3.6 where  $D_p$  is the particle or pore diameter. The choice for the used diameter depends on the material investigated and is discussed in further detail below.

$$\text{Re}_p = \frac{\rho v D_p}{\mu} \quad (3.6)$$

Darcy's law is valid for pore Reynolds number smaller than unity. When the pore Reynolds number increases, an extra term needs to be added that accounts for quadratic form drag [69]. This change is due to inertial forces becoming of importance at higher velocities, not due to turbulence [70]. In this case the pressure drop is given by the Darcy-Forchheimer equation. Some inconsistency exists in literature on the exact value when the Darcy-Forchheimer equation becomes required. For example, [70] states that the range where Darcy-Forchheimer's law becomes required varies from Reynolds numbers between 0.1 and 75 and that the large uncertainty depends on the differences in pore structure and surface roughness. In this work it was observed that the pore Reynolds number was always larger than 100 and thus the Darcy-Forchheimer equation is used. Furthermore, at the Reynolds numbers when Darcy's law is sufficient, low flow velocities occur and thus the added Forchheimer term becomes really small as it depends on the velocity squared. Then, the Darcy-Forchheimer equation reduces to Darcy's law,

The Darcy-Forchheimer equation requires two permeability coefficients. For a bed of packed spheres they are given by Equation 3.7 and Equation 3.8 [1], also referred to as Ergun's equation. An image of a bed of packed spheres can be seen in Figure 3.2.  $D_p$  is the diameter of the spheres and  $\epsilon$  the porosity. These equations are used by most works done on transpiration cooling when the permeability coefficients are not experimentally known [66–68]. These relations are widely used and give good results for porosities between 0.2 and 0.8 and for particle sizes between 0.03 mm and 21.33 mm [8].

$$K_D = \frac{D_p^2 \epsilon^3}{150 \cdot (1 - \epsilon)^2} \quad (3.7)$$

$$K_F = \frac{D_p \epsilon^3}{1.75 \cdot (1 - \epsilon)} \quad (3.8)$$

Not all porous walls are made from a bed of packed spheres. For example: a foam can be seen as the inverse of a bed of packed spheres. The solid spheres are now 'open' volumes and the cavities between the spheres are now solid. See Figure 3.3 for an example of a porous material made using AM. Commonly, the permeability

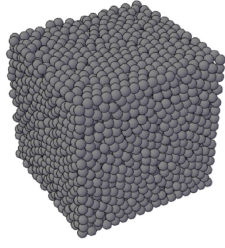


Figure 3.2: A representation of a bed of packed spheres [8].



Figure 3.3: An example of a porous structure created using additive manufacturing [9]

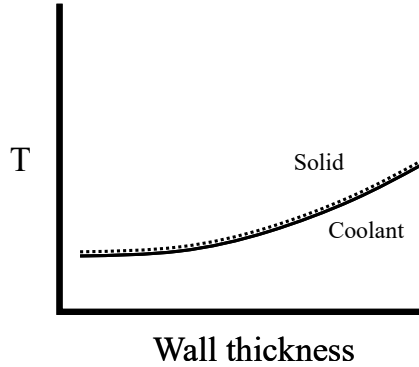


Figure 3.4: A representation of the local thermal equilibrium (LTE) temperature in a wall.

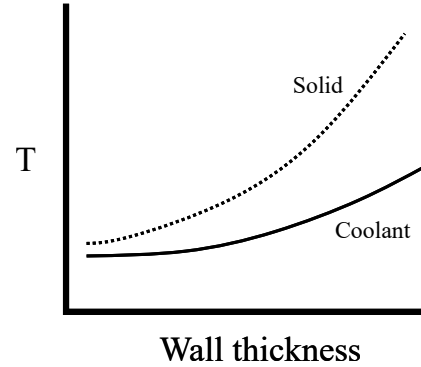


Figure 3.5: A representation of the local thermal non-equilibrium temperature (LTNE) in a wall.

coefficients of a bed of packed spheres are still used for these different shapes. Instead of using  $D_p$  for the sphere diameter, an equivalent hydraulic diameter is used [71]. In the case of additively manufactured walls in this work, the value for  $D_p$  will be the printed hole size.

In the program, a required pressure drop over the wall is specified and then the momentum equation is used to iteratively determine the velocity in the wall. A minimum pressure drop is required for two reasons. Firstly, to prevent hot combustion gases flowing into the wall when oscillations in chamber pressure occur. Secondly, to make sure the mass flow does not change much with small changes in combustion chamber pressure. The transpiration cooled engine developed by DLR used a drop of approximately 5 bar over the wall [30] on a chamber pressure between 55 to 91 bar [3]. As the pressure of the reference is 65 bar, the recommendation of 5 bar was followed. This pressure boundary condition drives the mass flow and thus the cooling performance. However, as will be seen in the discussion of the results, this required really thick walls. Therefore, the pressure drop was lowered to 1 bar. Note, that this is added to the chamber pressure of 65 bar, but that the static pressure is lower than this in the chamber. The maximum static pressure in the chamber is 63.4 bar, so the minimum pressure drop is 2.6 bar. In the nozzle this will be larger as the pressure drops there. A more elaborate discussion on the pressure drop will follow in section 3.6.

### 3.2.3. Energy equation

To obtain the temperature distribution in the wall, the energy equation for porous media is required. Two different options are available. One can assume that the heat transfer from the solid to the coolant is infinitely fast and thus the solid and coolant are locally the same temperature. This is called the local thermal equilibrium (LTE) assumption [69]. An example of this can be seen in Figure 3.4. In this case, one energy equation is required. If one assumes that the heat transfer is not infinitely fast, local thermal non-equilibrium (LTNE) is used [69]. An example can be seen in Figure 3.5. This case requires an energy equation for the solid and another one for the coolant. Therefore, the LTNE case is more computationally expensive. In the code, both cases are implemented and a comparison in their performance and applications is discussed in section 3.3.

**Energy equation: local thermal equilibrium** As mentioned, the local thermal equilibrium (LTE) assumes that the heat transfer from the solid wall to the coolant is infinitely fast and thus the solid and fluid are locally the same temperature. The energy equation for steady state for LTE in cylindrical coordinates can be seen in Equation 3.9 [68]. The thermal conductivity  $k_m$  is the combined thermal conductivity of the wall material ( $k_s$ ) and the coolant ( $k_c$ ) and is given by Equation 3.10 [69]. The density of the coolant, isobaric specific heat and the Darcy velocity are respectively given by  $\rho_c$ ,  $c_{p_c}$  and  $v_c$ .

$$\frac{1}{r} \frac{d}{dr} \left( k_m \cdot r \frac{dT}{dr} \right) - \rho_c c_{p_c} v_c \frac{dT}{dr} = 0 \quad (3.9)$$

$$k_m = (1 - \epsilon) \cdot k_s + \epsilon \cdot k_c \quad (3.10)$$

For completeness, the energy equation is also given for a cartesian reference system, see Equation 3.11 [46]. This equation can be used when flat plates are modelled and is a bit easier to understand. In this equation it is clear that the energy equation consists of a conduction part (the first term) and an advection component (the second term).

$$\frac{d}{dy} \left( k_m \frac{dT}{dy} \right) - \rho_c c_{p_c} v_c \cdot \frac{dT}{dy} = 0 \quad (3.11)$$

**Energy equation: local thermal non-equilibrium** In case of local thermal non-equilibrium (LTNE), the heat transfer is not infinitely fast and thus the coolant and solid have locally different temperatures. These are both unknown. Therefore, two energy equations are required: one for the solid and one for the coolant. The solid energy equation for steady state in cylindrical coordinates is given in Equation 3.12. The one for the coolant can be seen in Equation 3.13 [68, 72]. In addition to already mentioned variables,  $T_s$  is the solid temperature and  $h_v$  is the volumetric heat transfer coefficient in  $\text{W/m}^3\text{K}$ .

$$\frac{1}{r} \frac{d}{dr} \left( k_s (1 - \epsilon) r \frac{dT_s}{dr} \right) - h_v (T_s - T_c) = 0 \quad (3.12)$$

$$\frac{1}{r} \frac{d}{dr} \left( k_c \epsilon \cdot r \frac{dT_c}{dr} \right) - \rho_c c_{p_c} v_c \frac{dT_c}{dr} - h_v (T_c - T_s) = 0 \quad (3.13)$$

Again, the energy equations are given in cartesian form as well for completeness and to more easily grasp what the different terms mean. The first term in the solid energy equation (Equation 3.14 [67, 69]), is the heat equation that describes the conduction through the solid wall. The second term represents the heat that is transferred from the solid to coolant by convection within the wall. The terms in the liquid energy equation (Equation 3.15 [67, 69]) are as follows: heat conduction through the coolant (that will be very low), advection heat transfer and convective heat received from the coolant to the solid. Note that when the porosity drops to zero, i.e. the wall is completely solid, no heat transfer *within* the wall exists. Then Equation 3.15 reduces to zero. What remains from Equation 3.14 is the heat equation for a solid.

$$\frac{d}{dy} \cdot (k_s (1 - \epsilon) \frac{dT_s}{dy}) - h_v (T_s - T_c) = 0 \quad (3.14)$$

$$\frac{d}{dy} \cdot (k_c \epsilon \frac{dT_c}{dy}) - \rho_c c_{p_c} v_c \cdot \frac{dT_c}{dy} - h_v (T_c - T_s) = 0 \quad (3.15)$$

**Volumetric heat transfer coefficients** Now that the two energy equations are known for the LTNE, one parameter is still not specified: the volumetric heat transfer coefficient  $h_v$ . This value is determined using empirical relations. As the volumetric heat transfer has as unit  $W/Km^3$ , one needs to multiply the 'normal' heat transfer coefficient in  $W/Km^2$  with the specific surface area per unit volume  $a_{sc}$  (Equation 3.16 and Equation 3.17 [69]).

$$a_{sc} = \frac{6(1-\epsilon)}{D_p} \quad (3.16)$$

$$h_v = h \cdot a_{fs} \quad (3.17)$$

Several semi-empirical relations that describe the heat transfer coefficients in a porous wall can be found in literature. They are either obtained using experiments or numerical modelling using CFD. An overview of these relations can be seen in Table 3.1 and their ranges of validity in Table 3.2. The resulting Nusselt numbers for different pore Reynolds numbers can be seen in Figure 3.6. The plots span over the given the range of validity as listed Table 3.2.

Some notes must be made regarding the Kuwahara relation that is presented in Table 3.1. Pallares et al. [73] investigated several relations and found that the Kuwahara relations for volumetric heat transfer did not match with other known relations. He suggested to multiply the Kuwahara relation by a factor of two to get better agreement with other (experimental) works. This recommendation is followed in this work and this is indicated by 'Kuwahara x2' relation. So, the value obtained from the Kuwahara relation in Table 3.1 requires a multiplication of two to achieve this.

Source	Year	Equation
Kuwahara et al. [49]	2001	$Nu = \left(1 + \frac{4(1-\epsilon)}{\epsilon}\right) + \frac{1}{2}(1-\epsilon)^{1/2}Re^{0.6}Pr^{1/3}$
Whitaker [50]	1972	$Nu = \frac{1-\epsilon}{\epsilon}(0.5Re^{1/2} + 0.2Re^{2/3})Pr^{1/3}$
Wakao et al. [74] ‘	1978	$Nu = 2 + 1.1Re^{0.6}Pr^{1/3}$
Handley and Heggs [75] [76]	1968	$Nu = \frac{0.255}{\epsilon}Re^{2/3}Pr^{1/3}$
Gunn [77]	1978	$Nu = (7 - 10\epsilon + 5\epsilon^2)(1 + 0.7Re^{0.2}Pr^{1/3}) + (1.33 - 2.4\epsilon + 1.2\epsilon^2)Re^{0.7}Pr^{1/3}$

Table 3.1: The various Nusselt number relations found for heat transfer in porous media; the corresponding ranges of validity for the relations can be found in Table 3.2.

Table 3.2: The range in different parameters for the Nusselt relations listed in Table 3.1.

Source	Determined by	Re range	Pr range	$\epsilon$ range	Particle sizes
Kuwahara et al. [49]	CFD	$3 \cdot 10^{-3}$ to 5000	$10^{-2}$ to $10^2$	0.2-0.9	n/a
Whitaker [50]	Experiments	22 to 8000	0.7	0.4-0.74	n/a
Wakao et al. [74]	Experiments	20 to 8500	0.7 to 1	n/a (0.4)	0.1 to 25.4mm
Handly and Heggs [75]	Experiments	100 to 4000	n/a	0.36 to 0.39	3.05 to 9.5 mm
Gunn [77]	Experiments	up to $10^5$	0.7 to 7.5	0.35 to 1	n/a

The equations in Table 3.1 are plotted for their valid range of Reynolds number in Figure 3.6 for a porosity of 0.39 as this is the only porosity that is valid for all relations. The Nusselt numbers of all relations appear to

be similar, but as they are plotted on a log scale the actual differences vary with a maximum of 70%. At other porosities, the differences between relations become larger. For example, for a porosity of 0.7 the maximum difference is 260%. In general, it is known that for lower Reynolds numbers (smaller than 100) there is a large scatter in the Nusselt numbers with two order of magnitudes difference [76]. Furthermore, it is established that the shape of the particles influences the Nusselt number. For example, square particles have a lower Nusselt number. So, while great effort was put into finding proper heat transfer coefficients for flow in porous media, this will remain a source of error. In section 3.5 it will be found that for small pore sizes ( $<0.1$  mm for conditions in this work), the heat transfer becomes very large and that the differences between the solid and coolant temperature are small. So, for these conditions, better models for the volumetric heat transfer are not necessary. For the pore sizes producible with additive manufacturing (0.3 mm to 0.5 mm), differences in temperature occur. So, for these sizes it is recommended to find better correlations. However, the relations used in this work can still be used to predict the trends occurring and are sufficient to answer the research questions.

For the remainder of this work, the Kuwahara equation multiplied by two will be used as this one has the largest range for porosity and Prandtl number. The lowest porosity is 0.2 and this value will be used as the lowest porosity in this work. A second reason for this is that at lower porosities the wall still be porous, but a uniform distribution of the injected becomes less likely. The porosity of this exact 'border' is not known, but 0.2 appears to be a good engineering guess.

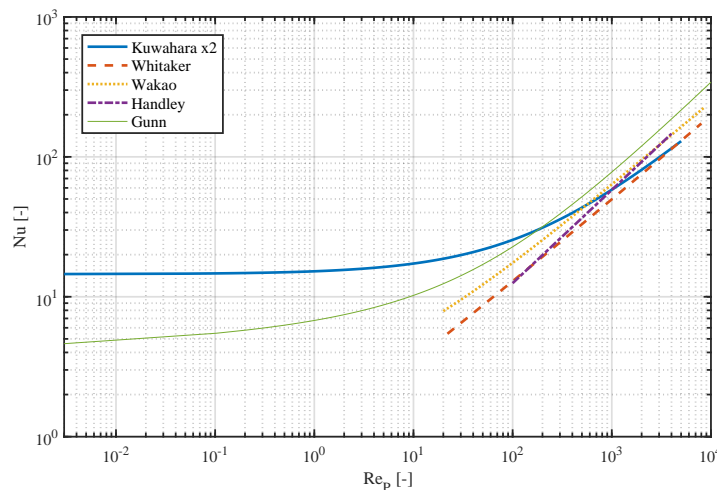


Figure 3.6: Comparison of the Nusselt numbers relations from Table 3.1 for Pr of 0.7 and porosity of 0.39.

The magnitude of the volumetric heat transfer coefficient of the Kuwahara relation versus the porosity and pore size is investigated as these two parameters are the main parameters to change in the wall. In Figure 3.7 the volumetric heat transfer coefficient can be seen for different porosities and three different Reynolds numbers. These lines are obtained by determining the heat transfer coefficient and multiplying it with the specific area from Equation 3.16. The specific area has to be included to account for the change of total surface area with changing porosity. It can be seen in the figure that when the porosity decreases - and reaches the lower value of the valid porosity range ( $\epsilon=0.2$ ) - the heat transfer coefficient increases drastically. This means that at low porosities the heat transfer becomes very large and the temperature of the coolant and solid will be similar. In other words, then the LTE assumption can potentially be used.

The fact that heat transfer coefficient increases for lower porosity is confirmed by works of [78] where the heat transfer coefficient increases with more than 900% when the porosity is changed from 0.95 to 0.5. Secondly, in the CFD work of [79] the heat transfer coefficient increases 100% when the porosity changed from 0.8 to 0.5.

In Figure 3.8 the volumetric heat transfer coefficient depending on the pore size for three different Reynolds numbers can be seen. When the pore size reduces the volumetric heat transfer approaches infinity. Thus, the

same conclusion as for the porosity can be made: when the pore size reduces, the LTNE case converges to the LTE assumption.

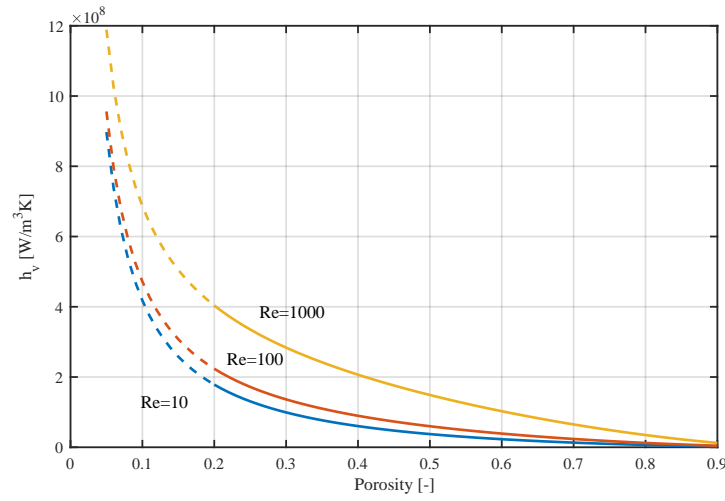


Figure 3.7: The volumetric heat transfer coefficient determined with the Kuwahara Nusselt number relation for different porosities;  $Pr=0.7$ ,  $D_p=0.1$  mm,  $k=1$  W/mK; the dashed lines are outside the porosity range of the relation.

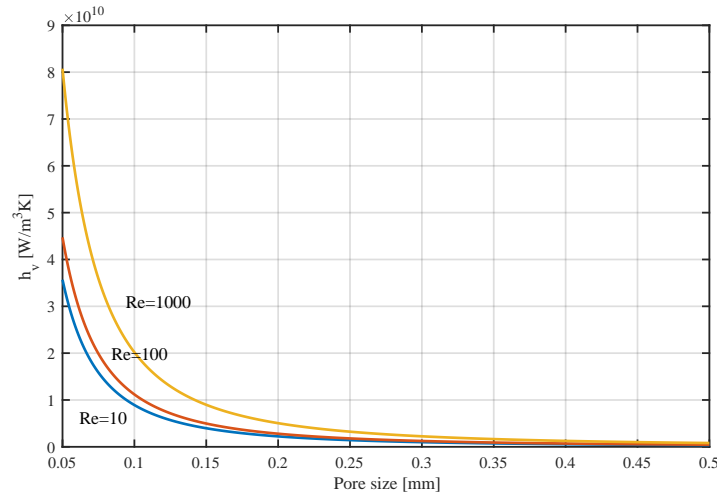


Figure 3.8: The volumetric heat transfer coefficient determined with the Kuwahara Nusselt number relation for different pore sizes;  $Pr=0.7$ ,  $\epsilon=0.2$ ,  $k=1$ .

### 3.2.4. Equation of state

The final required equation is the equation of state. In the program the coolant properties are determined using CoolProp [4] which requires temperature and pressure as input and can then provide density, isobaric specific heat, viscosity and thermal conductivity of the coolant. Validation of the coolant properties for ethanol are available in Appendix B.

### 3.2.5. Reduction in heat transfer due to presence of blowing

All required equations have been introduced, but one important phenomenon still needs to be modelled. This is the reduction in convective heat transfer caused by the blowing effect when the coolant is injected into the combustion chamber. The injected coolant changes the temperature of the boundary layer and this reduces the convective heat transfer into the wall. It is assumed that the coolant film is transparent for radiation.



Several relations exist to determine the reduction in heat flux due to blowing. The most detailed analysis was done by Meinert et al. [51] and is used in this work. Meinert et al. takes the analytical relation for reduction in heat transfer due to blowing determined by Kays and Crawford [80] and adds two correction factors to account for gas property and temperature effects. The correction factors were determined using experiments. The relation can be seen in Equation 3.18. The driving factor is the blowing ratio  $F$  defined by Equation 3.19. The blowing ratio is determined by the coolant density and coolant velocity at the end of the wall and the density and velocity of the main gas flow. Other parameters in Equation 3.18 are  $St_0$ , which is the Stanton number when no blowing is present.  $k_M^*$  is the correction factor for using different coolants and is given by Equation 3.20 and depends on the ratio of the molecular masses of the hot gas ( $M_g$ ) to the coolant ( $M_c$ ). Finally,  $k_T^*$  is the correction factor for the difference in temperature between the wall and the gas and is given by Equation 3.21.

$$\frac{St}{St_0} = \frac{\frac{F}{St_0} k_M^* k_T^*}{e^{\frac{F}{St_0} k_M^* k_T^*} - 1} \quad (3.18)$$

$$F = \frac{\rho_c \nu_c}{\rho_g \nu_g} \quad (3.19)$$

$$k_M^* = \left( \frac{M_g}{M_c} \right)^{0.6} \quad (3.20)$$

$$k_T^* = \left( \frac{T_{aw}}{T_w} \right)^{0.3} \quad (3.21)$$

A graph showing the reduction in convective heat transfer coefficient can be seen in Figure 3.9. The drop is very steep and at a blowing ratio 0.02 it has reduced to practically zero.

The correction factors of Equation 3.18 were obtained from experiments with nitrogen, argon, helium, air and freon-12. The porosity of the material was 0.3. The blowing ratio range varied from 0 to 0.8%. The range of molecular masses of the gases used to determine Meinert's equation was between 4 g/mol (helium) and 39.9 g/mol (argon) and it was determined in a wind tunnel with air as hot gas. The molecular mass of ethanol is 46.1 g/mol and is thus outside of the range of tested gases.

As mentioned above, the correction factors were determined for gaseous coolants. However, the coolant used in this work is a (compressible) liquid. So, one could wonder how this affects the use of this equation. The critical temperature of ethanol is 516 K. For any reasonable rocket chamber wall material, the maximum allowable temperature will be above this point. Therefore, the ethanol turns into a supercritical fluid within the wall and it is assumed that this state can be seen as a gas. In cases with high blowing ratios when coolant does not heat up to the critical temperature, the ethanol stays liquid. This introduces some uncertainty in the reduction in heat transfer. It is assumed that if the coolant exits the wall in liquid phase, that it instantly vaporizes and that it then acts the same as a gas.

Furthermore, the accuracy of the reduction in heat transfer could heavily benefit from a repeating of the experiment but with longer chain hydrocarbons instead of relatively 'light' gases such as nitrogen. Ethanol is slightly out of the range. However, keeping in mind that ideally one cools the wall with kerosene and that the average molecular mass of kerosene is 167 g/mol [81], this might alter the blowing effects. Furthermore, kerosene consists of different species with different molecular masses. As the reduction in blowing is not a linear relation it might be that this variation also has effects. In the model, the reduction due to blowing is the largest factor contribution to the lower heat flux to the wall. Quantifying the effect is difficult, but a more accurate estimation of this will greatly improve the accuracy of the model. It is therefore recommended to do more research on the blowing effects of kerosene when used as a transpiration coolant.

One note about the correction factor for different coolants can be made. One might expect that a ratio of the isobaric specific heat values is more logical than the ratio of molecular masses. This was also proposed in the work of Kays and Crawford, but Meinert et al. found better agreement with the ratio of molar masses.

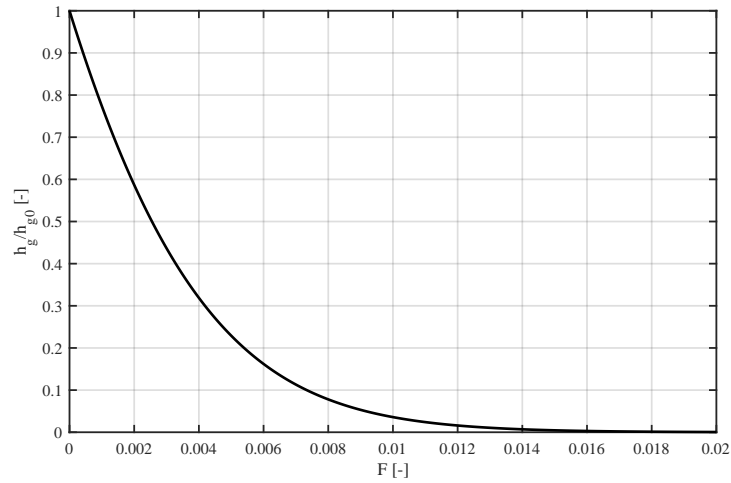


Figure 3.9: An example calculation for the reduction in convective heat transfer coefficient versus blowing ratio; for ethanol as coolant; located in the cylindrical section of the reference engine.

**Critical blowing ratio** Meinert et al. also performed tests on the so-called critical blowing ratio in transpiration cooled walls. The critical blowing ratio is the blowing ratio at which the boundary layer separates from the wall. Experiments with argon, air, nitrogen and helium give the following empirical relation for the critical blowing ratio:

$$\frac{2F_{\text{crit}}}{c_{f0}} \left( \frac{M_g}{M_c} \right)^{0.9} \approx 5.0 \quad (3.22)$$

Other relations show that the ratio  $2 \cdot F_{\text{crit}}/c_{f0}$  is between 3.5 and 6 for different gases [51]. Note that with this equation, if the molar masses are higher (for kerosene for example) the critical blowing ratio will be low.

Opinions differ on if surpassing the critical blowing ratio is beneficial or not. Meinert et al. states that once the critical blowing ratio is reached, it is likely that there is no 'classic' boundary layer anymore but a film of only coolant next to the wall. This film then increases in thickness with increasing blowing ratio. Meinert et al. states that there is no danger of thermal overheating when the film is present. However, Kirchberger [7] states that the critical blowing ratio should be avoided as otherwise local hot spots can occur at the wall when the boundary layer reattaches or vortices transport hot gases to the wall. However, in practice the reduction in heat transfer to the wall due to blowing is so effective that it is not required to reach the critical blowing ratio [51].

### 3.2.6. Model summary

In the previous sections, all required governing equations have been presented. Boundary conditions need to be imposed to complete the calculations. However, before this is discussed, a summary of the program structure and the inputs is given.

In addition to the inputs that were treated for the regenerative cooling design (engine contour, chamber pressure, etc.), the extra required inputs are listed in Table 3.3. The outputs of the program are the solid and coolant temperature distribution in the wall, coolant properties distribution and the final mass flow, mass flux and blowing ratio for the location evaluated.

A flowchart of the steps occurring for the LTNE program can be seen in Figure 3.10. For the LTE, the steps taken are similar with the exception that only the coolant temperature is calculated instead of both the solid

Parameter	Unit
Porosity	-
Sphere /pore diameter	m
Porous wall thickness	m
Required pressure drop over wall	bar
Heat transfer coefficient cold side	W/mK

Table 3.3: The additional inputs of the code modelling a transpiration cooled wall, in addition to the ones listed in Table 2.1 (minus the cooling channel parameters).

and coolant one. The temperature distribution is calculated and with this new temperature the coolant properties are updated. This is continued until the specified convergence criteria that assesses the change in solution are reached.

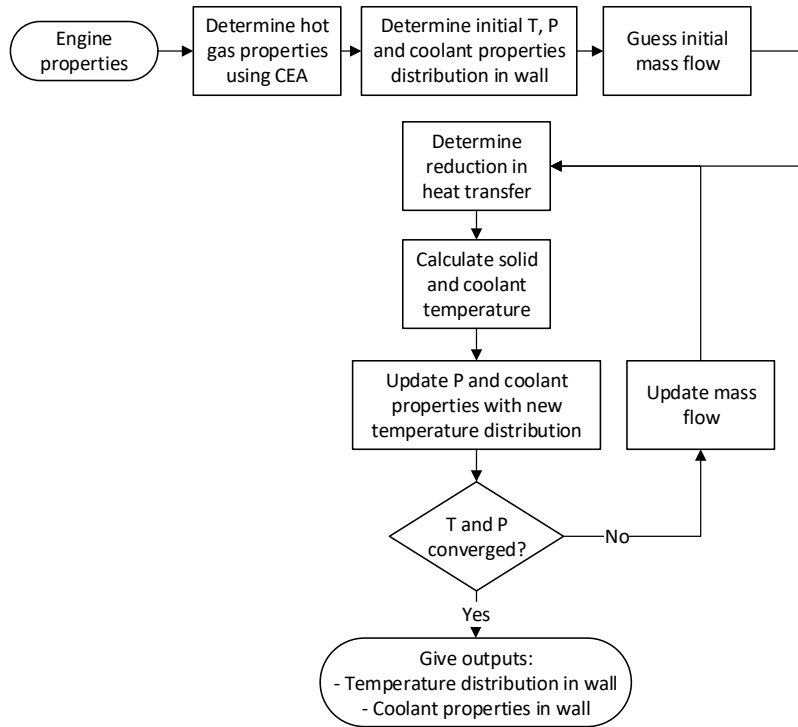


Figure 3.10: A flowchart of the program that calculates the wall temperature for a transpiration cooled wall for a single station and for the local thermal non-equilibrium (LTNE) assumption. The local thermal equilibrium (LTE) case is similar with the exception that no solid wall temperature is calculated.

Furthermore, the spike in the isobaric specific heat around the critical point (Figure 1.5) caused trouble with convergence. Therefore, it is possible to under-relax the solution. Secondly, sometimes for very thick walls, the pressure would reach negative values and the program would crash. To alleviate this, the pressure in the wall can also be under-relaxed. The under-relaxation for  $c_p$  is given by Equation 3.23 [82] and the one for pressure follows the same scheme. Here,  $\alpha$  is the under-relaxation factor and in case it is 1, no under-relaxation is used.

$$c_p^{\text{new,used}} = c_p^{\text{old}} + \alpha(c_p^{\text{new,predicted}} - c_p^{\text{old}}) \quad (3.23)$$

A list of the assumptions made and their consequences is given below:

- The heat transfer is one-dimensional and occurs normal to the wall. At locations with strong axial thermal gradients, this will overestimate the temperature. In the engine, this occurs at the region close to the throat.
- It is assumed that the super critical fluid acts as a gas.
- The injected coolant does not alter the combustion products. In reality it would change and this will change the mixture ratio in the engine. This will then alter the gas temperature and the heat flux. As the reference engine operates close to the optimal OF ratio, it would reduce the heat flux.
- The thermal conductivity of the wall material does not change with temperature, see discussion in section 2.1.
- The wall geometry does not change due to thermal stresses and pressure forces.

### 3.3. Boundary conditions

The required (differential) equations to determine the temperature in the transpiration cooled wall are now known. However, that is only one part of obtaining the solution. The second part is the correct implementation of boundary conditions. The pressure boundary condition is simple: at the upstream side of the wall the pressure equals the reservoir pressure that is constant in the axial length, and at the downstream side it equals the chamber pressure at that axial position. The mass flow and coolant properties are iterated to satisfy this boundary condition.

For the energy equations for both the LTE and LTNE the boundary conditions are more complicated. This is discussed in the following sections. The LTE case needs two boundary conditions to solve for the energy equation, while the LTNE case needs four boundary conditions: two for the solid energy equation and two for the coolant one. In subsection 3.3.1 the boundary conditions are defined and in subsection 3.3.2 a comparative study between the boundary conditions and their effect on the LTNE and LTE cases are discussed.

#### 3.3.1. Boundary conditions definition

In the following sections the different options for the boundary conditions following from literature are discussed and the final chosen ones are presented.

**Hot side boundary condition** On the hot side, a Neumann boundary condition is specified. The heat flux due to radiation and convection determines the gradient at this side. While the majority of literature follows this type of boundary condition, small variations occur. Some set the heat transferred into the liquid to zero such that all heat flows into the solid [39, 83]. Others divide the heat flux between the solid and coolant according to their respective thermal conductivity and porosity [40]. In the latter case, only a small amount of heat flows into the coolant as the thermal conductivity of the coolant is low compared to the solid. Alomar et al. [84] tried these two conditions plus two alternatives with minor variations and found that the choice does not greatly affect the final temperature. Alomar et al. recommends to use the boundary condition that sets the heat flux to the coolant to zero and thus this one is used in this work. The boundary condition for the LTNE case on the hot side is as given below. For the LTE assumption the first row is used and the condition that the gradient of the coolant is zero is not required.

$$y = L \begin{cases} q_{\text{rad}} + q_{\text{conv}} = q_s = (1 - \epsilon) k_s \frac{dT_s}{dy} \\ q_c = 0 = \epsilon k_s \frac{dT_c}{dy} \end{cases}$$

**Cold side boundary conditions** For the boundary conditions at the cold side, various options are used in literature. As this study is applied to a rocket engine, the boundary conditions for literature regarding transpiration cooling in rocket engines were consulted. Davis [68] (LTE) sets the wall temperature on the cold side equal to the coolant reservoir temperature. Bucchi et al. [66] (LTNE) does the same for both the wall and coolant temperature.

This boundary condition is examined here. It is reasoned by the author that this assumption is only valid in the case that all heat flowing into the wall is absorbed by the coolant before the heat 'reaches' the cold side. This only happens when the walls are sufficiently long or when the thermal conductivity is low enough. As a result, the temperature gradient at the cold side is zero and thus the constant temperature boundary condition is justified.

However, once the wall length decreases or wall conductivity increases, the heat 'reaches' the cold side before it is all absorbed by the coolant. In this case, it does not physically make sense that the temperature at the start of the wall stays equal to the coolant reservoir temperature. In other words: for this to happen, a convective heat transfer should occur with an infinite high heat transfer coefficient and the heat that flows into the coolant reservoir just disappears into nothing. Both these effects would be nonphysical. So, while the constant cold side wall and coolant temperature are used by some works on transpiration cooling in rocket engines, it is deemed not to *always* match reality. Some conditions exist where it is a good enough representation. However, ideally a boundary condition is used that is always valid.

Different boundary conditions were examined. Landis [67] (LTNE) uses a different approach and viewed the coolant side similar to a regenerative cooled channel. He specified a convective heat transfer boundary condition for the solid energy equation. The heat transfer coefficient was determined using Dittus-Boelter equation, but any other relation could be used. For the liquid temperature, the coolant reservoir was used. As the coolant flows axially past the wall, it would make sense that the coolant temperature increases with axial length but no specific mention of this was found in [67].

In this thesis, it is not assumed that a regenerative coolant channel on the cold side of the wall is present, but rather a large coolant reservoir that connects all transpiration cooled walls with a certain reservoir temperature and pressure. The coolant velocity is very low in the reservoir and the coolant only flows normal to the wall and then into the pores. This means that heat transfers from the wall into the coolant by convection. When the coolant then flows into the porous wall, this absorbed heat also 'flows' back into the wall. This boundary condition is used for the LTNE case and follows from [39, 40, 83]. To the author of this thesis, this boundary condition seems to make the most sense from a physical point of view. The mathematical expression of this boundary condition for the cold side for LTNE is:

$$y = 0 \left\{ \begin{array}{l} k_s(1 - \epsilon) \frac{dT_s}{dy} = h_c(T_s - T_{c0}) \\ h_c(T_s - T_{c0}) = \nu_c \rho_c c_{p_c}(T_c - T_{c0}) \\ T_{c0} = \text{constant} \end{array} \right.$$

Note that, to be fully correct, one should not look at the difference  $\nu_c \rho_c c_{p_c}(T_c - T_{c0})$  but actually at the enthalpy difference as  $c_p$  is not constant. However, the changes in temperature are generally small as the mass flux is high and therefore this is deemed negligible.

One extra unknown parameter is introduced using this boundary condition: the convective heat transfer coefficient on the cold side of the wall  $h_c$ . As it was assumed that the coolant is supplied by a large reservoir and flows with a low velocity normal to the wall, it can be expected that  $h_c$  has a low value. Langener [1] hypothesised that the heat transfer is partly caused by natural convection and partly by radiation into the reservoir. Combining estimations for both, a heat transfer coefficient of around 20 to 34 W/m<sup>2</sup>K for air was obtained [85]. Dong et al. [39] used value of 31.4 W/m<sup>2</sup>K for water coolant. In this work a standard a value of 34 W/m<sup>2</sup>K will be used that does not change with temperature.

For the LTNE case, the above described boundary condition will be used. From a design point of view, it should be kept in mind that if the temperature on the cold side gets (too) high that a regenerative cooling channel can still be implemented. This will increase the heat transfer coefficient on the cold side of the wall and lower the temperature. However, the need for this was not found with conditions used in this work. From a system level perspective this is not preferred as now more (or all) fuel is used as coolant and this will increase the pressure drop requiring more pumping power.

The above discussed boundary condition works for the LTNE case, but when LTE is used only one boundary condition is required at the cold side. It would make sense to specify the convective heat transfer boundary

condition similar as the solid part for the LTNE. However, as will be seen in the next section where different boundary conditions are investigated, this causes some problems.

### 3.3.2. Boundary condition study

When the volumetric heat transfer increases by lowering the pore size and/or porosity, the solid and liquid temperature locally become virtually equal for the LTNE case. Then, it becomes possible to use the LTE assumption and this will reduce the computational time. However, it was found that when comparing the LTE and LTNE for high values of  $h_v$  that they only match at certain boundary conditions. To analyse this, a simplified model was made using constant coolant properties and using a cartesian coordinate system. The inputs of the model can be seen in Table 3.4.

Table 3.4: The constant properties for the analysis.

Parameter	Symbol	Unit	Value
Porosity	$\epsilon$	-	0.2
Thermal conductivity solid	$k_s$	W/mK	200
Thermal conductivity coolant	$k_c$	W/mK	0.2
Density liquid	$\rho$	kg/m <sup>3</sup>	800
Isobaric specific heat liquid	$c_p$	J/kgK	1000
Velocity liquid	$v$	m/s	0.1
Volumetric heat transfer coefficient	$h_v$	W/m <sup>3</sup> K	$1 \cdot 10^{10}$
Hot gas side heat transfer coefficient	$h_g$	W/m <sup>2</sup> K	3000

In the analysis, the boundary condition on the hot side of the wall will remain the same for all cases. The convective heat transfer boundary condition is used with  $h_g$  and a constant hot gas temperature of 3000 K. The heat flux into the liquid is zero, so the gradient of the liquid temperature is zero at the hot side of the wall. The value for  $h_c$  on the cold side<sup>1</sup> is set to 20 W/m<sup>2</sup>K and the initial coolant temperature is 300 K.

When a convective heat transfer boundary condition is applied on the cold side, it is observed that for large wall lengths the LTNE and LTE case are the same. See Figure 3.11 for an example. For the LTNE case, the solid and liquid temperature are virtually equal due to the high volumetric heat transfer coefficient. The heat enters the wall on the hot side and is then conducted into it. As the heat is absorbed by the liquid, the wall temperature drops. A short distance away from the hot side, the temperature dropped to the initial coolant temperature and then stays constant. Note that as the temperature drops to the reservoir temperature, the same results can be achieved when a constant temperature boundary condition is used. Therefore, while it was reasoned earlier that a constant temperature boundary condition is not physical, some conditions exist where it is still applicable and this is one of them.

So, until now there is no problem with the boundary conditions. Both the LTE and LTNE case are the same for the convective boundary condition applied. However, when the wall length is decreased, differences start to occur. The temperature distribution for a convective boundary condition on the cold side with a wall length of 0.02 m can be seen in Figure 3.12. A difference in temperature can be seen. In this case the liquid and solid temperature of the LTNE are still equal but the LTE temperature is higher than the LTNE case. It was found that when increasing the heat transfer coefficient on the cold side, the absolute difference became smaller, but a difference remained. Note that in the figure, it appears that the LTNE case has a value of the reservoir temperature (300 K) but the results are slightly higher. The increase is small because of the low heat flow and large mass flow, but there is a slight difference.

To verify that this difference occurs because of the boundary condition, a case with a wall of 0.02 m with a constant temperature boundary condition on the cold side can be seen in Figure 3.13. Now the LTE and LTNE case are equal again. So, the difference between the LTNE and LTE temperature is caused by the boundary condition. This means that using the LTE assumption for a wall with small pores - and thus when the heat transfer in the wall is high - instead of LTNE to reduce computational time, will not yield the same results in

<sup>1</sup>Note that a  $h_c$  of 20 W/m<sup>2</sup>K is different than the earlier specified 34 W/m<sup>2</sup>K. This is a small inconsistency, but for the purpose of this analysis, it does not matter what value is chosen.

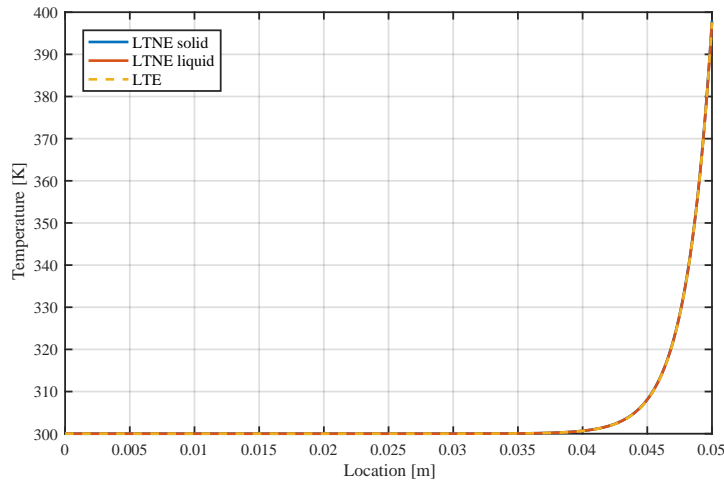


Figure 3.11: Temperature distribution for a convective boundary condition on the cold side for a wall length of 0.05 m.

certain conditions.

This means that for walls with low thermal conductivities (e.g. Inconel) and small pores, the LTE assumption with a constant temperature boundary condition can be used. The same applies for thick enough walls. But once a temperature gradient exists at the cold side and one is using a constant temperature boundary condition, this is not adequate anymore. The LTNE case is then required and unfortunately this will increase computational time.

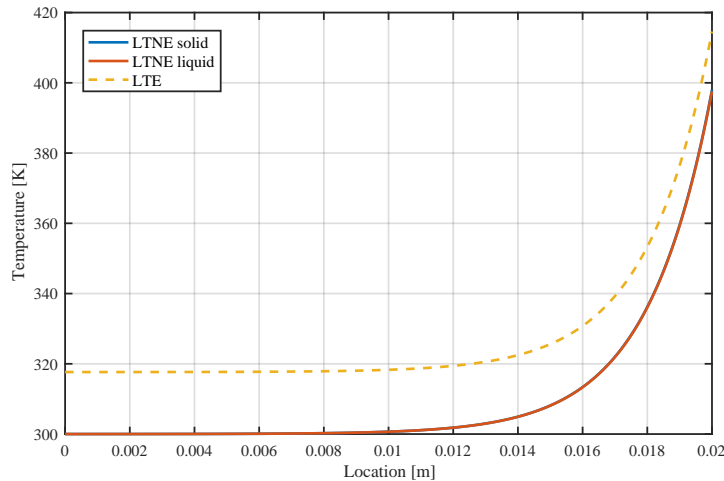


Figure 3.12: Temperature distribution for a convective boundary condition on the cold side for a wall length of 0.02 m.

### 3.3.3. Conclusions

The boundary conditions were determined and reviewed. The boundary conditions set the heat flux on the hot side equal to the heat flow into the solid. On the cold side, the most physical the boundary condition has to take into account that the heated up coolant flows back into the wall. A discrepancy occurs between the LTNE and LTE case for this boundary condition. This will result in the LTE case being different from the LTNE case when the wall is thin or has a high thermal conductivity. Therefore, it is decided to use the LTNE case in the remainder of this work even though this increases computational time.

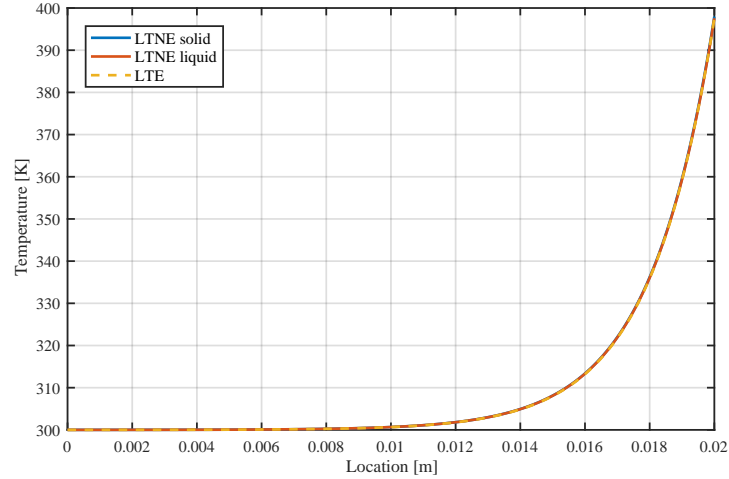


Figure 3.13: Temperature distribution for a constant temperature boundary condition on the cold side for a wall length of 0.02 m.

### 3.4. Verification and validation

Once all the equations were implemented in the program, verification and validation was performed. The verification consists mainly of comparing the solutions of the program to simplified analytical solutions and is discussed in subsection 3.4.1. For the validation, one would ideally compare the results to experiments of a real transpiration cooled rocket engine. However, no such data is available. Therefore, separate parts of the program are validated using different sets of data. This is discussed in subsection 3.4.2

#### 3.4.1. Verification

The different verification steps are discussed here.

**Comparison LTNE and LTE** The first verification result that is presented is the behaviour of the LTNE case when the pore size is reduced. When reducing the pore size, the volumetric heat transfer increases and the solid and coolant temperature should progressively match each other more closely. In the end, the LTNE case should match the LTE case with the same conditions (depending on the boundary condition of course, as discussed in the previous section). If this is the case, it is a sign that both equations are implemented correctly.

The behaviour that the solid and coolant temperature for the LTNE case match each other when the pore size is reduced, is illustrated by Figure 3.14. All parameters, except the pore size, are kept equal. A difference between the solid temperature (solid lines) and the coolant temperature (dashed lines) occurs at a pore size of 1 mm. For a pore size of 0.4 mm, this difference gets smaller. Finally, for a pore size of 0.08 mm, only a small difference between the solid and coolant temperature exists. A comparison between a LTNE and LTE case with pore size of 0.08 mm can be seen in Figure 3.15. The LTNE and LTE case match very well. This is an initial indication that the energy equations of the LTE and LTNE case are implemented correctly. Note that in Figure 3.14 the absolute temperature of the smallest pore size is between the other pore sizes. This is caused by a combination of higher heat transfer and a lower total mass flow due to the smaller pore size.

**LTE comparison to analytical solution** When constant coolant properties are used, it is possible to compare the temperature distribution obtained from the LTE energy equation with an analytical solution. As it is difficult to find an analytical solution for the energy equation in cylindrical coordinates, the cartesian variant is used for the analytical solution. To make sure it differs as little as possible from the cylindrical version, the radius is increased by 5 m so that the effect of the changing radius is kept minimal. The properties used can be seen in Table 3.5. On the cold side, a constant temperature boundary condition is used with a magnitude of 298 K. On the hot side a convective heat transfer boundary condition is used and no radiation is used:



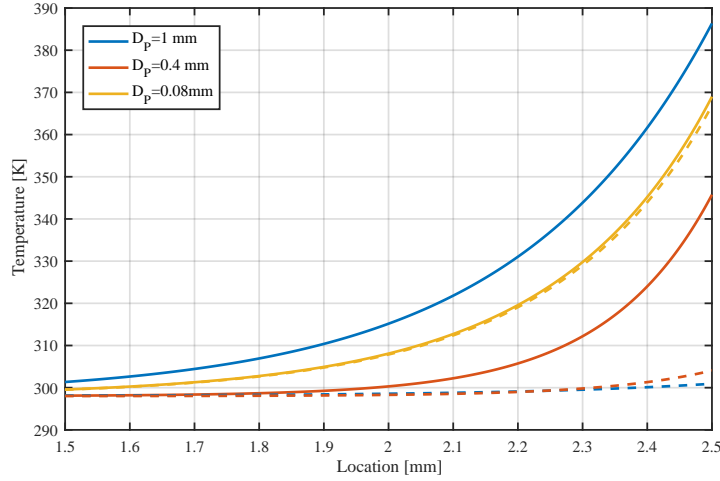


Figure 3.14: The effect of smaller pore diameters on the solid temperature (solid lines) and the coolant temperature (dashed lines); porosity 15%;  $k=11.4$  W/mK;  $\Delta P=1$  bar; ethanol as coolant.

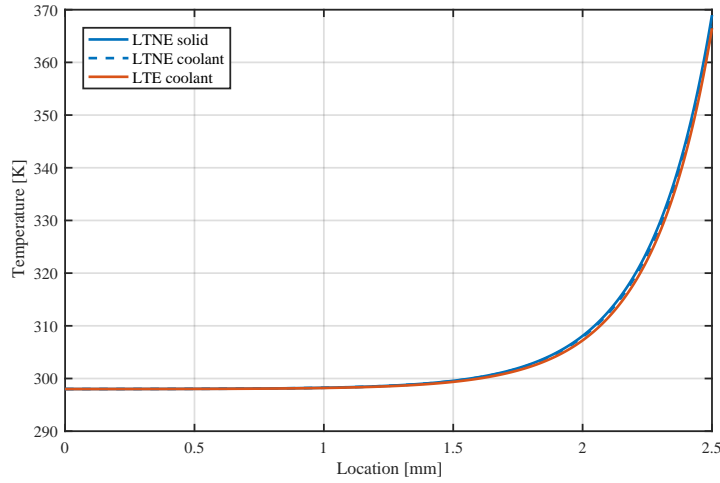


Figure 3.15: A comparison between the temperature data of Figure 3.14 with pore size of 0.08 mm to the LTE case with the same parameters.

$$k_m \left. \frac{dT}{dy} \right|_{y=0.01} = h_g \left( T_{aw} - T \right|_{y=0.01} \right)$$

The comparison between the numerical and analytical solution can be seen in Figure 3.16 and they match with each other. This is another proof that the energy equation of the LTE case is implemented correctly. As it was seen earlier that the LTNE converges to the LTE case at low pore sizes, this is another confirmation that the energy equation of the LTNE case has been implemented correctly.

**LTNE zero heat transfer** When no heat transfer occurs within the wall (so  $h_v$  becomes zero), the solid energy equation should reduce to the steady state heat equation of a solid wall. This allows for a comparison between the numerical solution and an analytical one. The temperature should in this case follow the temperature of a purely regeneratively cooled wall. In the case of a flat plate, the temperature would then vary linearly and in the case of cylindrical coordinates the curve will be slightly non-linear. To achieve this condition in the program a small change is made to the boundary condition: the cold side temperature is fixed. At the the hot side, the temperature is calculated using  $h_g(T_{aw} - T_{w,h})$  as the radiation is neglected. The inputs can be seen in Table 3.6 and the comparison between the analytical and numerical solution in Figure 3.17.

Parameter	Unit	Value
$\rho$	kg/m <sup>3</sup>	200
$k_m$	W/mK	20
$c_p$	J/kgK	1000
$v$	m/s	0.04
$t$	mm	10
$T_{aw}$	K	3607.5
$h_g$	W/Km <sup>2</sup>	425.29

Table 3.5: Inputs for the verification case of the simplified solid energy equation

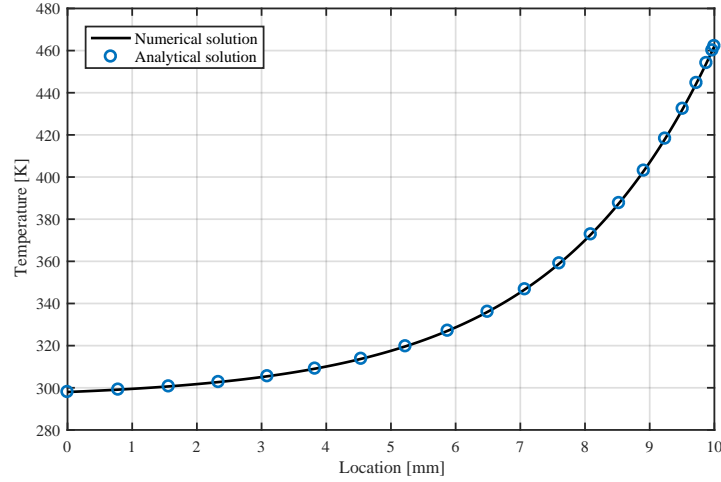


Figure 3.16: Comparison between the numerical and analytical solution for the LTE case with constant properties as given in Table 3.5.

As can be seen, an exact match between the two occurs. Furthermore, the coolant temperature should not increase in this case, as no heat transfer from the solid to the liquid exists. This is the case as well.

Parameter	Unit	Value	Comment
$T_{aw}$	K	3607.5	
$h_g$	W/m <sup>2</sup> K	4098.3	
$k_m$	W/mK	187	Effective (Equation 3.10)
$t$	m	0.05	
$r_{inner}$	m	0.0764	
$T_{cold}$	K	298	

Table 3.6: Inputs for the verification case where the heat transfer in the wall is set to zero.

**LTNE simplified solid energy equation** In the previous section it was confirmed that the conductive part of the solid heat equation is implemented correctly by comparing it to an analytical solution. However, it is not yet confirmed if the heat transfer term  $h_v(T_s - T_c)$  is implemented correctly as it was set to zero. Some simplifications are made to do this. Again, cartesian coordinates are used as the solution of the analytical solution in cylindrical coordinates is complicated. However, the radius is increased by 5 m to make sure the effect of the radius is small. Another simplification is that the  $h_v$  and  $T_c$  are set to constants. The boundary conditions are equal to the ones in the section before. The inputs can be seen in Table 3.7 and the comparison of the analytical and numerical solution in Figure 3.18. The numerical solution matches the analytical one.

**Grid independence** Another important thing to be proven is grid independence of the solution. If the number of nodes in the radial direction in the wall is increased, the solution should converge to a single solution

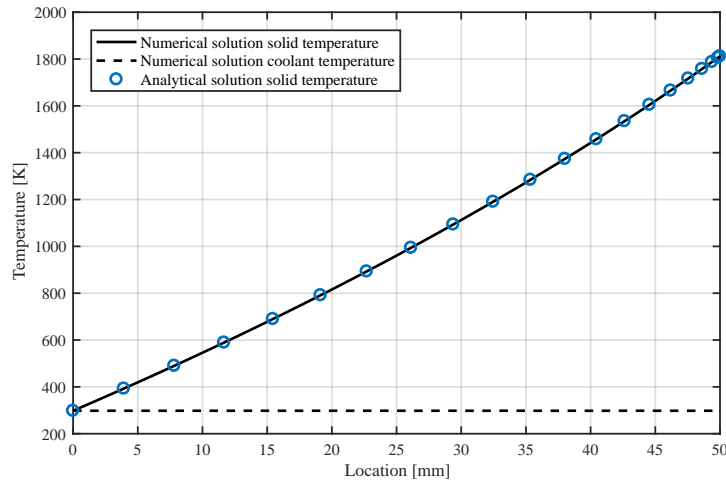


Figure 3.17: The numerical results compared to the analytical solution in case when the heat transfer in the wall is set to zero.

Parameter	Unit	Value	Comment
$T_{aw}$	K	3607.5	
$h_g$	W/m <sup>2</sup> K	4853.6	
$k_m$	W/mK	187	Effective (Equation 3.10)
$h_v$	W/m <sup>3</sup> K	15000000	
$t$	m	0.05	
$r_{inner}$	m	0.0764	
$T_{cold}$	K	298	

Table 3.7: Inputs for the verification case where the heat transfer in the wall is set to zero.

for that axial location. Figure 3.19 shows the grid convergence by showing the maximum solid temperature for different number of nodes. It can be seen that from 200 nodes onward the maximum value is almost stable. In the program, 2000 nodes were used as minimum as this did not affect the computational time significantly. Furthermore, it should be noted that for larger wall lengths, more nodes are required as generally the increase in temperature occurs in the small section close (<10 mm) to the hot side of the wall. A non-uniform node distribution could be implemented, but as the thick walls are not of interest, this is not done.

### 3.4.2. Validation

The above treated parts verify the correct implementation of the equations, but do not show if the equations actually solve a transpiration cooled wall correctly. This is done in this section by comparing the numerical results to test data available in literature. As no data for a transpiration cooled rocket engine is available, several parts are validated individually.

**Validation of pressure drop** To validate the momentum equation, test results from Langener [1] are used. He determined the permeability coefficients of several carbon carbon (C/C) samples experimentally. But before doing this, he calibrated the test setup with a bed of packed spheres and this data can be used as validation data here. The bed has a porosity of 37% and the sphere size is 2.5 mm. Langener determined the resulting coolant velocity for various different pressure with samples of three different thicknesses. The results were compared to the pressure drop obtained with Ergun's equation - the equation that determines the permeability coefficients in a bed of packed spheres, see Equation 3.7 and Equation 3.8. It was found that for the 5 mm and 10 mm long samples, the match with Ergun's equation was overestimating the pressure drop per unit length. With a length of 34 mm the match was good. It was concluded that the flow needs a few sphere layers to settle [1]. Therefore, the current model is compared to the sample of 34 mm.

In the numerical model, the mass flow is iterated until the correct pressure drop was achieved. The outlet

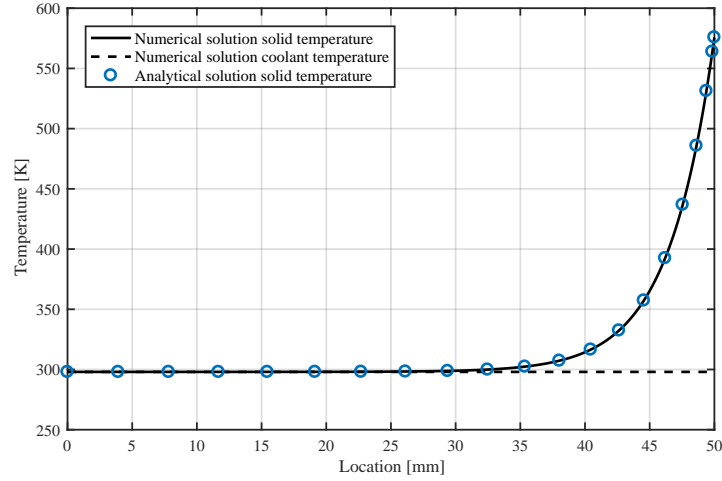


Figure 3.18: The numerical results compared to the analytical solution in case when the volumetric heat transfer is specified and the coolant temperature is kept constant.

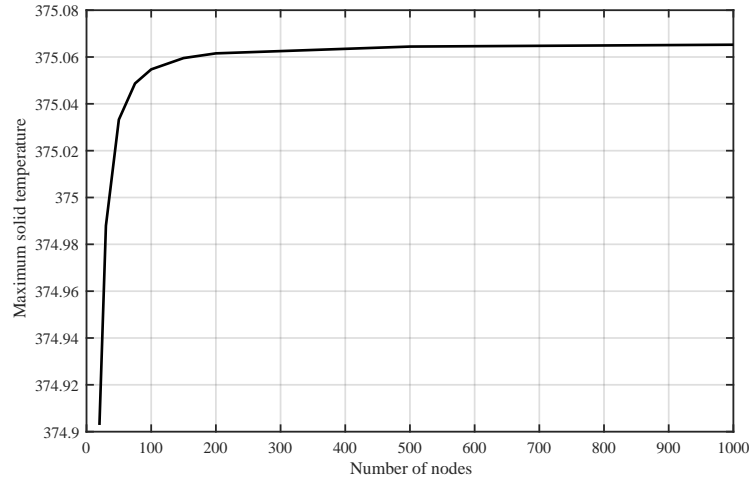


Figure 3.19: Grid convergence.

pressure is the ambient pressure of 1 atm. A constant coolant velocity is given in the validation data. This velocity is specified as the inlet velocity in the numerical model but in the numerical model the velocity will change in the sample, but the total mass flow will of course stay constant. The results are compared to the data from Langener in Figure 3.20. The maximum difference between the reference data and the model is 5.5% for a coolant velocity of 3.8 m/s, but for the lower velocities the error is near zero. This shows that the Darcy-Forchheimer equation and the determination of the permeability coefficients for a bed of packed spheres can be used to model the pressure drop.

**Validation of wall temperature distribution** While a lot of experimental data is available on the hot side temperature of a transpiration cooled wall [1, 25, 26, 44], little data is available on the temperature distribution within the wall. It is difficult to measure the temperature distribution within a wall as the thermocouples required tend to be larger than the pores and will alter the flow. However, one data set was found in literature. Langener [1] measured the temperature at different locations within C/C samples tested in a hot air flow wind tunnel for different blowing ratios. These conditions are modelled with the model developed in this thesis and the results are compared to the test data from Langener. While some of the test data is described in [1] and [85], not the complete data set was available. The missing data was made available by Mr. Langener on request.

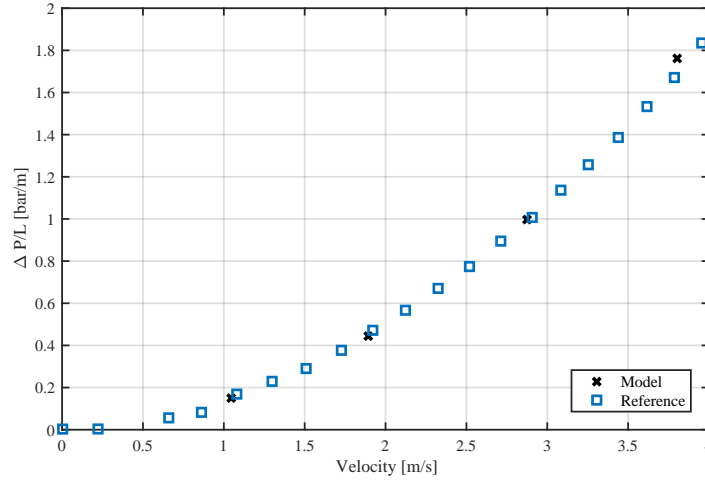


Figure 3.20: The pressure drop per unit length for the bed of packed spheres with  $\epsilon$  of 0.37 and  $D_p$  of 2.5mm, the velocity is the Darcy velocity at the inlet. The reference data is obtained from [1].

The experimental data consists of the temperatures within the wall measured using thermocouples, the hot side wall temperature determined by averaging the surface temperature measured by an IR camera and the bulk coolant temperature in the plenum. The data from C/C sample PH1606-1 is used. The properties of this sample can be seen in Table 3.8.

Langener compared the test results to a 1D transpiration cooled wall using LTE and constant properties and found a decent match. In this analysis, the properties can change but the same boundary conditions are used as in the analysis of Langener. These differ from the actual rocket engine model and this analysis thus only validates the flow within the wall. On the hot side of the wall, the temperature is set equal to the temperature obtained from the tests. On the cold side a natural convection boundary is set and the heat transfer coefficient follows from the data supplied by Langener. In mathematical form this is as follows:

$$k \left. \frac{dT_c}{dx} \right|_{x=0} = h_c \left( T_c \Big|_{x=0} - T_{c0} \right)$$

$$T_c \Big|_{x=L} = T_{w,h}$$

The value for  $h_c$  is 20 W/m<sup>2</sup>K. The bulk coolant temperature, coolant density and derived pressure for each blowing ratio can be seen in Table 3.9. The pressure on the hot side is set to 0.9553 bar and the coolant used is air.

Table 3.8: The properties of the PH1606-1 CMC sample [1].

Parameter	Symbol	Value	Unit
Length	L	0.015	m
Area	A	61x61	mm <sup>2</sup>
Porosity	$\epsilon$	11.3	%
Thermal conductivity	k	1.4	W/mK
Darcy permeability	$K_D$	$1.25 \cdot 10^{-13}$	m <sup>2</sup>
Forchheimer permeability	$K_F$	$0.88 \cdot 10^{-8}$	m

The results from the numerical model are compared to the test data in Figure 3.21. For the blowing ratio of 0.001, the test results match the model between 0.006 m and 0.015 m. Below that it deviates slightly. For the blowing ratios of 0.002 and 0.01, the model predicts a lower temperature than measured. However, in both

Table 3.9: The input data for the CMC sample PH1606-1 for different blowing ratios [1].

F	$T_{c0}$	$\rho$	$P_0$
[-]	[K]	[kg/m <sup>3</sup> ]	[bar]
0.001	336.35	3.38	3.26
0.002	319.06	4.90	4.48
0.01	296.62	12.8	10.9

cases the shape of the temperature distribution follows the test data. For the blowing ratio of 0.01, the temperature stays constant for almost the complete wall length and then starts to increase around 0.011 m. For the blowing ratio of 0.002, a constant increase in temperature occurs in both the test and numerical data. It is likely that the boundary condition on the cold side changes the absolute values. The  $h_c$  of 20 W/m<sup>2</sup>K was a theoretical value and also taken constant for all blowing ratios, so it is likely that a more accurate value of  $h_c$  would result in a more accurate match with the test data.

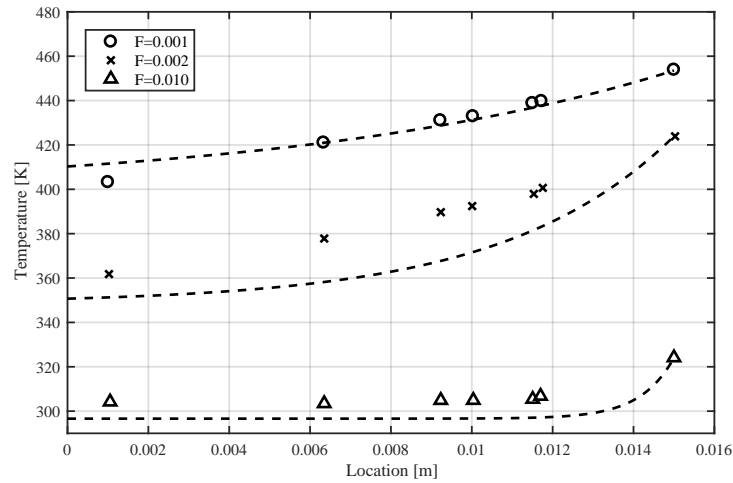


Figure 3.21: The measured wall temperatures from Langener [1] (markers) and the wall temperature from the model (lines) for three different blowing ratios for the PH1606-1 sample.

The comparison to the data from Langener shows that the energy equations can model the temperature distribution in a transpiration cooled wall.

**Conclusions** This concludes the validation of the model. Great effort was put into finding useful experimental or CFD data that could provide validation of the model. All data that was found and useful was presented in this section. However, it will be admitted that the validation presented here is far from perfect. The major part missing is the validation of the reduction of the heat transfer due to blowing. The equation used was determined experimentally, but the confidence in the model would greatly benefit from a validation from different experiments and/or for the exact conditions used in the model. The validation on other components of the model can also be improved, such as the volumetric heat transfer coefficient, but this will have a smaller effect on the final result.

### 3.5. Parametric analysis

The verified and validated model can now be used to perform a parametric analysis of the influence of different parameters on the wall temperature distribution. This analysis will answer some of the research questions on the effect of changing the properties within the wall.

The results in the following sections were all determined with the LTNE case. The wall material in all cases is Inconel with a thermal conductivity of 11.4 W/mK, except for the case when the effect of the thermal conductivity is investigated. As discussed earlier, once the coolant passes the critical temperature within the wall, it takes longer for the solution to converge. Many simulations had to be run for this parametric analysis. Therefore, the results presented here only go up until the critical temperature to speed up the process. The main point of interest lies around the maximum tolerable wall temperature, which for Inconel would be around 923 K, but it is expected that the trends occurring at the lower ranges also occur at higher temperatures. For the final comparison between film and transpiration cooling, discussed in chapter 5, the data above the critical point will be used.

Other parameters that require mentioning are the calibration of the Bartz equation which is 0.65 for all cases. Secondly, the location where the temperature is determined is the cylindrical part of the combustion chamber. Finally, a pressure difference over the wall of 1 bar is used as it was determined that 5 bar will yield thick walls. The effect of this choice is further investigated in section 3.6. Lastly, the results are presented as a function of mass flux and not as a function of blowing ratio which is commonly used in literature. Using the mass flux allows for an easier comparison later to film cooling. The mass flux is taken as the (constant) mass flow divided by the area on the inner surface.

### 3.5.1. Effect of pore size

The effect of different pore sizes on the maximum temperature and the maximum temperature gradient can be seen in Figure 3.22 and Figure 3.23 respectively. The x-axis on both plots represents the mass flux and different curves for different pore sizes are given. The porosity for all points is 0.2. Furthermore, for the pore size of 1 mm, only results for high mass fluxes are given. To obtain data for smaller mass fluxes, very large wall thicknesses are required (>10 m). This is not only impractical in reality, but also caused difficulties with convergence and thus lead to long computational time.

In Figure 3.22, it can be seen that the maximum wall temperature is roughly constant at high mass fluxes but quickly increases at lower mass fluxes. This can be explained by the fact that at higher mass fluxes, the blowing ratio is so high that the convective heat transfer reduces to zero. Then, only radiation heats up the wall and in the current model the radiation is a constant value for a single location. In reality, the radiative heat transfer would increase if the wall temperature is lower, so the temperatures for the high mass fluxes will be higher in reality.

Also, it can be observed that the larger pore sizes have a higher temperature at the same mass flux. This difference becomes smaller when the pore size becomes smaller and the temperature will converge to a single value. This can be explained by the fact that for pore sizes larger than 0.4 mm, a difference between coolant and solid wall temperature still occurs due to the smaller volumetric heat transfer coefficient. At lower pore sizes, the heat transfer coefficient increases and the difference between solid and coolant temperature becomes smaller. Furthermore, this effect is less pronounced at lower mass fluxes - probably because there is less liquid to heat up and thus it will reach the same temperature as the wall quicker.

Figure 3.23 which shows the maximum thermal gradients, no difference between different pore sizes can be seen. Furthermore, the gradients reduce to a constant value at a mass flux of roughly 15 kg/(s<sup>2</sup>m). The fact that the gradients are constant at the higher mass fluxes can be explained by the fact that the convective heat transfer reduces to zero here and only the (constant) radiation heats up the wall. The gradient depends directly on the heat flux into the wall. The fact that they are also (almost) equal at lower mass fluxes is likely caused by the fact that, as the wall temperatures are close here, the convective heat flux into the wall is almost equal for all cases.

The data from Figure 3.22 can also be plotted as a function of wall length. It was already briefly mentioned that the larger pore sizes require very thick walls to achieve a low mass flux that gives a temperature close to the allowable temperature. It is of course the objective to get as close to this temperature as this will result in a lower mass flow of injected coolant which will result in a better specific impulse of the engine. The wall temperature for the pore size of 0.05 mm, 0.1 mm and 0.4 mm can be seen in Figure 3.24. The results for the 1 mm pore size are excluded to make the figure more clear. Note that the wall length is given on a logarithmic axis.

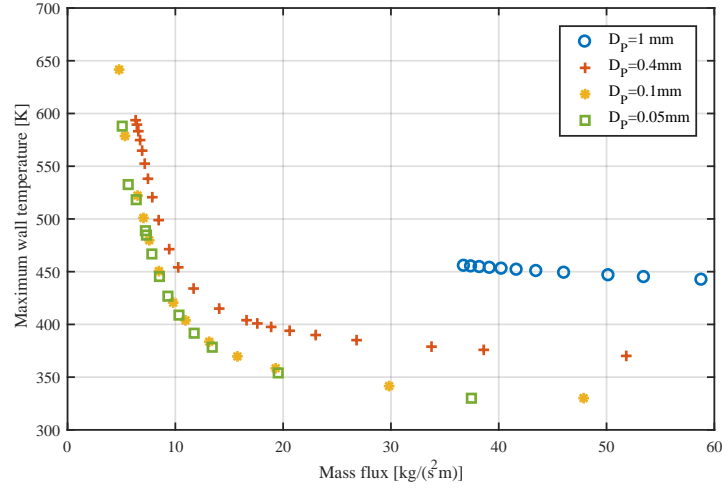


Figure 3.22: The maximum wall temperature occurring for different mass fluxes and pore sizes; porosity 0.2; thermal conductivity 11.4 W/mK.

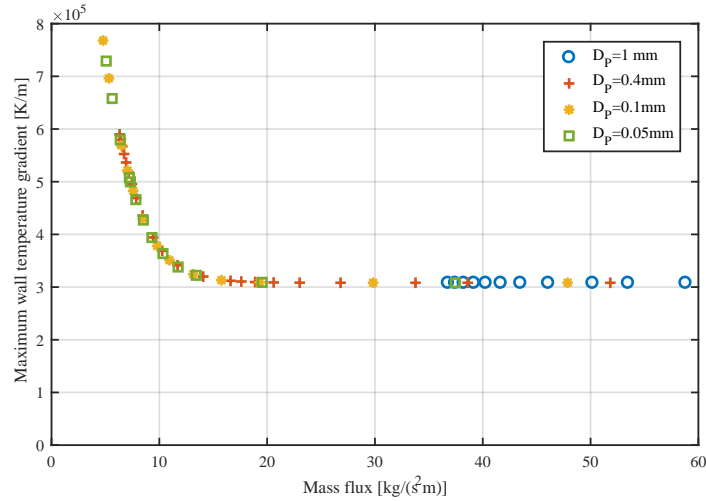


Figure 3.23: The maximum wall temperature gradient occurring for different mass fluxes and pore sizes; porosity 0.2; thermal conductivity 11.4 W/mK.

In the figure, it can be seen that for the pore size of 0.4 mm wall thicknesses of more than 10 m are required to achieve wall temperatures close to maximum allowable temperature of 923 K. When the pore size drops to 0.1 mm this thickness quickly decreases and only around 5 cm is required. It was determined in section 1.4 that the current smallest pore size printable with Selective Laser Melting printers is in the range of 0.3 mm to 0.5 mm. The figure shows that these pore sizes are too large to achieve feasible rocket engine designs as the walls will be too thick. Therefore, in the rest of this work pore size of 0.1 m and 0.05 mm will be used for the analysis, but it is clear that these results cannot be achieved using additive manufacturing at this stage. In the end, these wall thicknesses depend directly on the pressure drop in the wall which is determined by the pore size and porosity, but also the geometry of the coolant passages. Therefore, different geometries that may cause a higher pressure drop are investigated in chapter 6.

### 3.5.2. Effect of porosity

Figure 3.25 shows the effect of different porosities on the maximum temperature. Again, the x-axis represents the mass flux. The porosity was changed between 0.4 and 0.15. As can be seen in the figure, the effect of changing the porosity on the maximum wall temperature is small compared to the effect if changing the



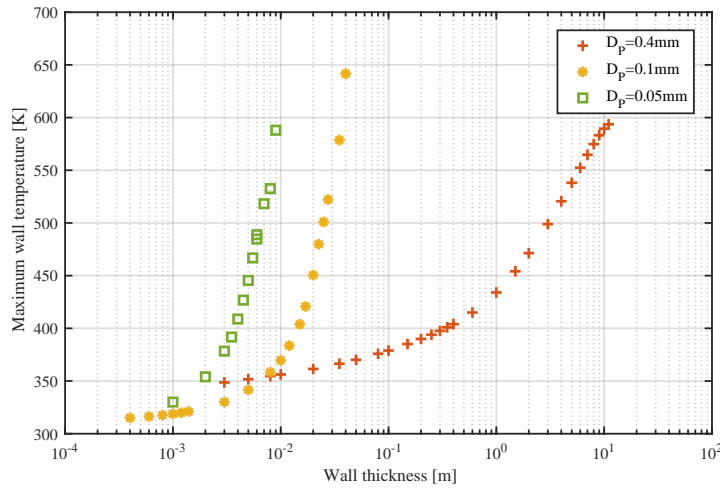


Figure 3.24: The maximum wall temperature as a function of wall thickness; porosity 0.2; thermal conductivity 11.4 W/mK.

mass flux. It must be noted that for the same mass flux, a different porosity will of course yield a different wall length. So, from this perspective, a lower porosity is better.

The effect of changing porosity on the maximum temperature gradient is larger, see Figure 3.26. Changing from 0.4 to 0.15 gives a reduction in gradient of around 30%. The fact that an effect on the gradient occurs, while the actual temperature does not change can be easily explained. While the heat flux into the wall will be the same for all porosities, the thermal gradient depends on the effective thermal conductivity of the wall. This depends on the thermal conductivity of the material but also on the porosity, see subsection 3.3.1. So, a lower porosity will lower the thermal gradients in the wall.

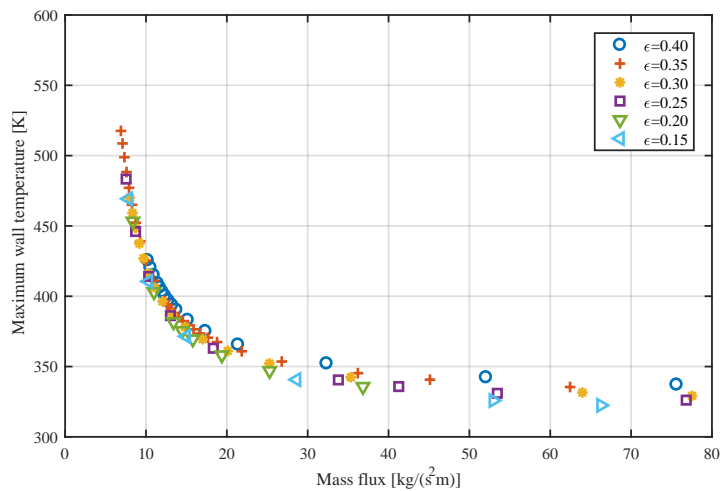


Figure 3.25: The maximum wall temperature occurring for different mass fluxes and porosities; pore size 0.1 mm; thermal conductivity 11.4 W/mK.

### 3.5.3. Effect of porosity distribution

One of the research questions of this work is if altering the porosity distribution within the wall could change the temperature profile and the thermal gradients in the wall. To investigate this, first the temperature in walls with constant porosity of 0.2 is calculated. Then, a case where the porosity starts at 0.15 on the cold side and increases to 0.25 on the hot side is calculated. The third case is exactly opposite: it starts with a porosity of 0.25 and this goes down to 0.15 at the cold side. The pore size is 0.1 mm.

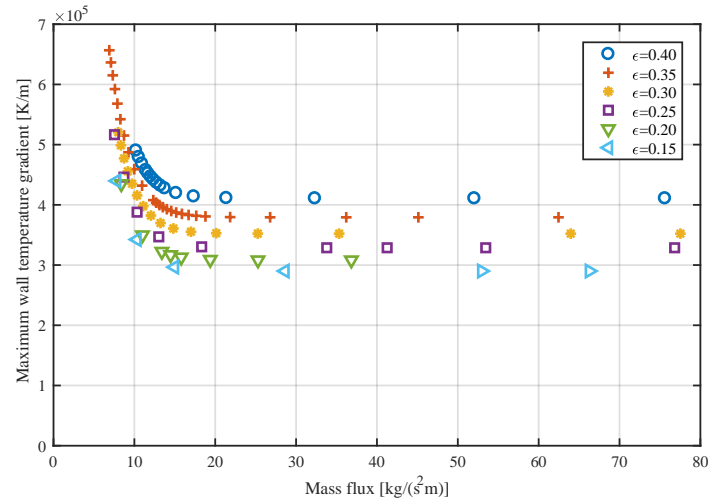


Figure 3.26: The maximum wall temperature gradient occurring for different mass fluxes and porosities; pore size 0.1 mm; thermal conductivity 11.4 W/mK.

In Figure 3.27 the results can be seen. The mass flow changes slightly for walls of the same length. However, the effect on temperature with the same mass flux is small. Therefore, it is to be expected that the different distribution has an effect on the maximum thermal gradient. And indeed, as can be seen in Figure 3.28, it shows the same behaviour as changing the complete porosity. In this case, having a lower porosity closer to the hot side of the wall will result in lower thermal gradients.

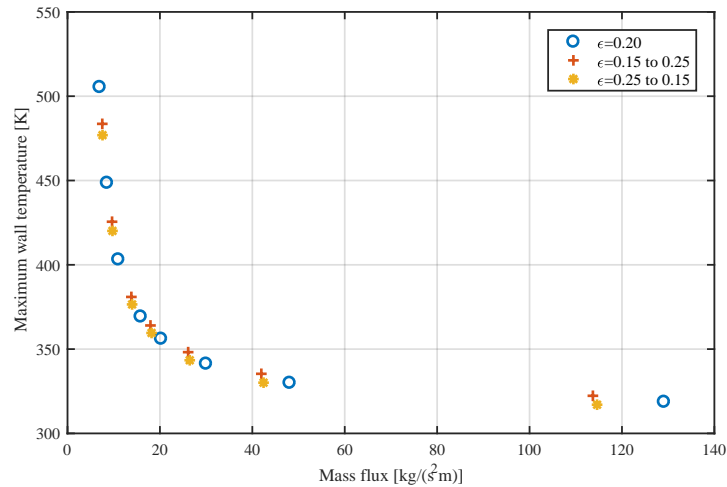


Figure 3.27: The maximum wall temperature occurring for different mass fluxes and porosity distributions; pore size 0.1 mm; thermal conductivity 11.4 W/mK.

### 3.5.4. Effect of pore size distribution

Another property that can be varied within the wall is the pore size distribution. The nominal pore size for this investigation has a value of 0.05 mm and the porosity is 0.2. Then, two linear distributions are used: one that starts at 0.03 mm on the cold side and increases to 0.07 mm and one that does exactly the opposite. In Figure 3.29 and Figure 3.29 the results can be seen. The first figure shows the effect on the different distributions on the maximum wall temperature and the second one on the maximum temperature gradients. It is clear from both figures that the pore size distribution does not have any effect on both of the parameters. This is in line what was observed for changes in pore sizes in Figure 3.22 and Figure 3.23 where no effect at all

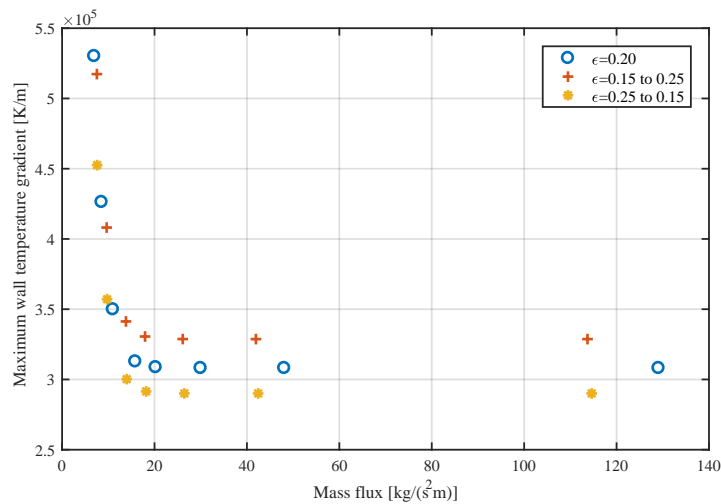


Figure 3.28: The maximum wall temperature gradient occurring for different mass fluxes and porosity distributions; pore size 0.1 mm; thermal conductivity 11.4 W/mK.

occurred for the gradient and no effect on temperature occurred at pore sizes smaller than 0.1 mm. In theory at larger pore sizes, a difference might occur, but these sizes are not realistic as they will result in thick walls.

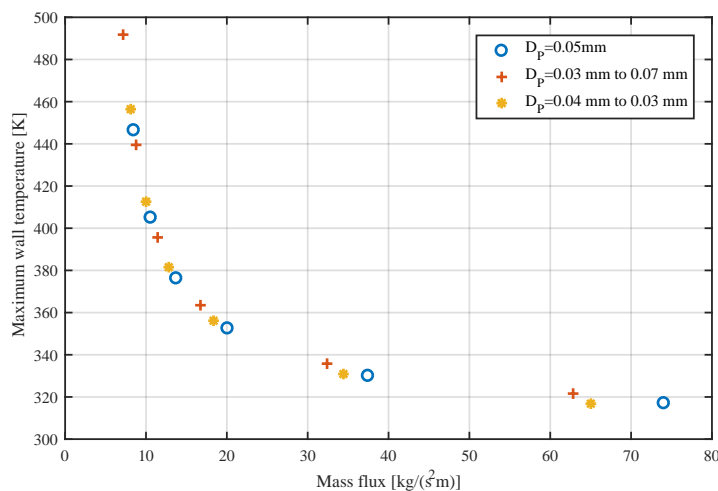


Figure 3.29: The maximum wall temperature occurring for different mass fluxes and pore size distributions; porosity 0.2; thermal conductivity 11.4 W/mK.

### 3.5.5. Effect of wall thermal conductivity

Another parameter that can be investigated is the thermal conductivity of the wall material. This will determine how much heat is conducted into the wall before it is absorbed by the coolant and has the potential to greatly alter the temperature distribution. This was investigated using two walls with different pore sizes to verify that the trends occurring are independent of the pore size. The first wall has a pore size of 0.1 mm and a thickness of 25 mm. The second wall has a pore size of 0.05 mm and a thickness of 5 mm. Both walls have a porosity of 0.2.

The effect of the thermal conductivity of the solid material can be seen in Figure 3.31 which shows both the maximum temperature and the maximum gradient. It can be seen that at lower thermal conductivities both the temperature and gradient are higher. Both reduce at higher thermal conductivities. However, the gradient reduces very quickly and is reduced to very low values (compared to the peak) from a conductivity from

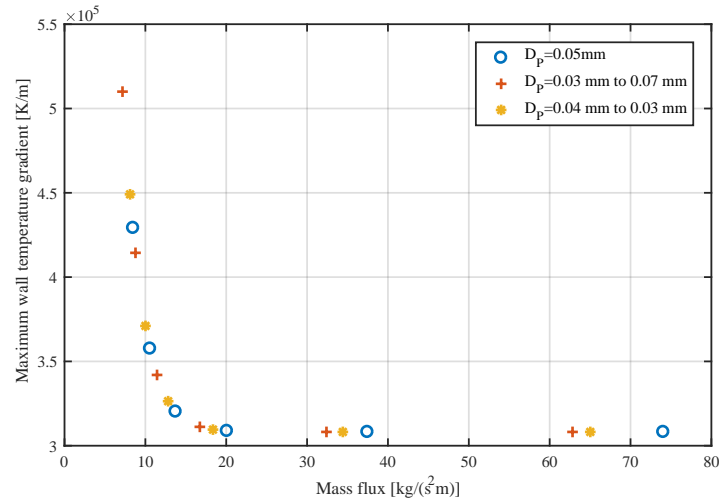


Figure 3.30: The maximum wall temperature gradient occurring for different mass fluxes and pore size distributions; porosity 0.2; thermal conductivity 11.4 W/mK.

roughly 100 W/mK onward.

Another effect of the higher thermal conductivity is that for the same wall length and pore size, the mass flow increases, see Figure 3.32. For the pore size of 0.1 mm the mass flux increases from 6.9 kg/(m<sup>2</sup>s) for a conductivity of 11.4 W/mK to 10.1 kg/(m<sup>2</sup>s) for a conductivity of 220 W/mK. This is an increase of 46 %. This increased mass flow will cool the wall better as more coolant reduces the temperature. So, this is a secondary effect to the increased thermal conductivity. From a system point of view it is not ideal as either more coolant is used which will reduce the efficiency of the engine or thicker walls are required to lower the mass flux.

When the temperature behaviour versus the mass flux of two different conductivities is plotted against the mass flux, an interesting results appear. The results for an Inconel and copper wall is plotted in Figure 3.33. It can be seen that for the same mass flux, no large difference occurs in maximum temperature for an Inconel or copper wall. Keep in mind that for this same mass flux, both walls have a different length, and the copper one is longer. When looking at the maximum gradient in Figure 3.34, a large difference occurs between the Inconel and copper wall. The Inconel gradients are around 19 to 20 times larger than the copper gradients. The thermal conductivity of copper is 19.3 times larger than the one of Inconel. So, this explains the results.

To further help visualize the effect of a larger thermal conductivity on the temperature profile, see Figure 3.35. Here the temperature distribution for the Inconel case and the copper alloy case are plotted. It can be seen that in the case of the Inconel, the temperature is constant until a sharp increase occurs at the hot side of the wall. The copper wall conducts heat faster into the wall and causes the temperature profile to be more smoothed out.

### 3.5.6. Other coolants

Until now, the coolant in all analyses has been (compressible) liquid ethanol, as this was determined to be a decent substitute for RP-1. However, different coolants might result in different temperature distributions due to the different properties. Density and specific heat are a 'big' part of the energy equations and these values change when switching to different coolants. Furthermore, it was found that the mass flow is a big driver for the cooling performance, but that often thick walls are required to keep the mass flows low enough to be useful. Gaseous coolants have a significantly lower density and might alter the mass flow through a wall. Of course, they also have a different (and lower) flow resistance to the porous wall.

In this section several extra gaseous coolants are investigated. They are limited to gases that can potentially be found on a launch vehicle because of already present pressurization or reaction control systems. The coolants are listed in Table 3.10 together with their relevant properties. Note that methane is likely only available on

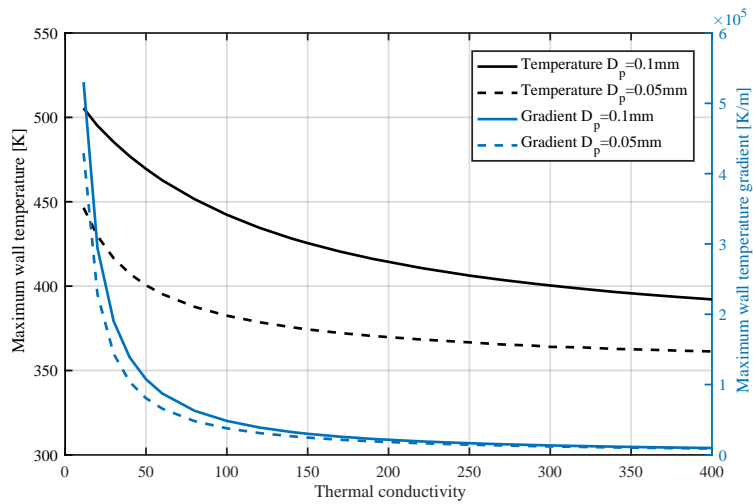


Figure 3.31: The effect of the solid material thermal conductivity on the maximum temperature and maximum temperature gradient for two different pore sizes.

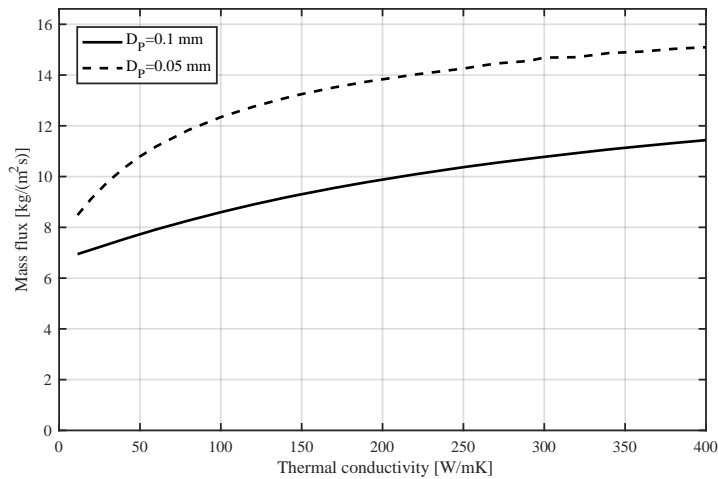


Figure 3.32: The effect of the solid material thermal conductivity on the mass flux for two different pore sizes.

a rocket when it uses a methane fuelled engine. Other potential coolant options are cryogenic liquids, such as liquid hydrogen, liquid oxygen and liquid methane. These are excluded as these have a different reservoir temperature and therefore it will be difficult to compare them to the other coolants. The results presented here are for an Inconel wall with porosity of 0.2 and pore size of 0.05 mm.

The effect of different coolants on the maximum wall temperature can be seen in Figure 3.36. The x-axis represents the mass flux. As reference, ethanol is given in the purple squares. It can be seen that methane is close in performance with ethanol. Oxygen and nitrogen are close to each other and will result in a significantly higher maximum temperature than ethanol. The performance of methane is close to that of ethanol. Lastly, helium gives the best results. The maximum temperature gradients can be seen in Figure 3.37. Similar as to the temperature, helium yields the lowest temperature gradient for the same mass flux compared to other coolants. Of all coolants, ethanol performs the worst with respect to the thermal gradient. Also, unlike the temperature case, methane now no longer performs similar to ethanol.

From simple analyses of a transpiration cooled wall with constant properties, it is known that for a convective heat transfer condition the wall temperature drops when the factor  $\rho_c c_{p_c} v_c$  increases. However, this causes an increase in thermal gradients. As the data in the figures is plotted as a function of mass flux, the factor  $\rho_c c_{p_c} v_c$

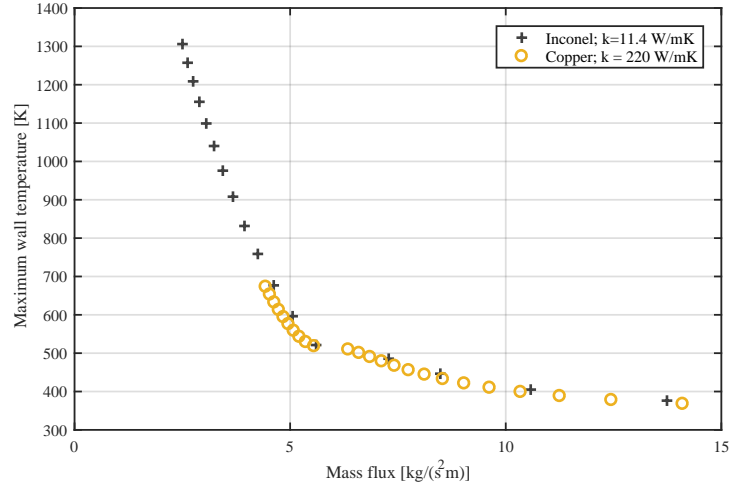


Figure 3.33: The maximum wall temperature for Inconel walls ( $k=11.4$  W/mK) and copper walls ( $k=220$  W/mK) as function of mass flux; porosity is 0.2 and pore size 0.05 mm.

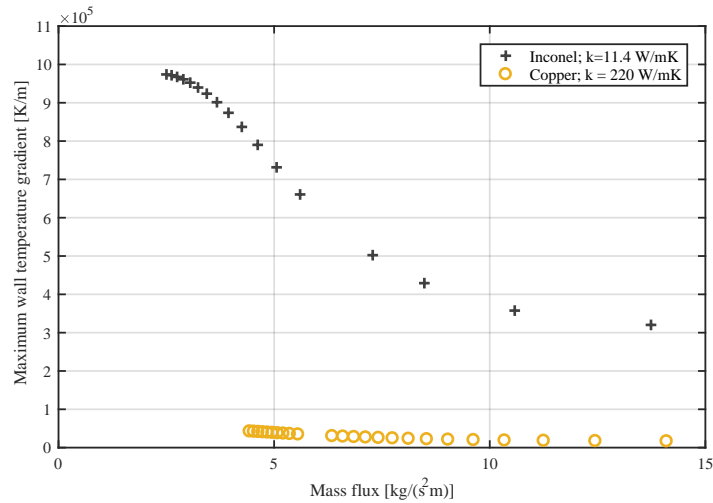


Figure 3.34: The maximum wall temperature gradient for Inconel walls ( $k=11.4$  W/mK) and copper walls ( $k=220$  W/mK) as function of mass flux; porosity is 0.2 and pore size 0.05 mm.

cancels out and this behaviour should only depend on  $c_{pc}$ . This explains why helium yields the lowest temperatures as the  $c_p$  of helium is highest of all coolants, see Table 3.10. However, the thermal gradient is also lowest for helium, this is not expected when only looking at the heat transfer within the wall. As thermal conductivity, porosity and adiabatic wall temperature are all the same, the lower gradient for helium means that less heat is coming into the wall. This can be explained by the reduction due to blowing given by Meinert's equation (Equation 3.18) which yields better reduction for lower molecular masses. Helium has the lowest molecular mass of coolants analysed and thus yields the largest reduction due to blowing. Ethanol has the highest molecular mass and also performs the worst regarding thermal gradient.

Note that this unveils a potential shortcoming of representing RP-1 with ethanol. The molecular mass of ethanol is 46.1 g/mol while that the average of all components of RP-1 is around 167 g/mol [81].

The second question that is answered is: does using gaseous coolant result in thinner walls for the same mass fluxes? This would be beneficial from a systems point of view as the dry mass of the engine can then decrease. The data presented in the previous two figures is now plotted with mass flow versus the wall length in Figure 3.38. It can be seen that oxygen, nitrogen and methane all require longer wall lengths than ethanol to

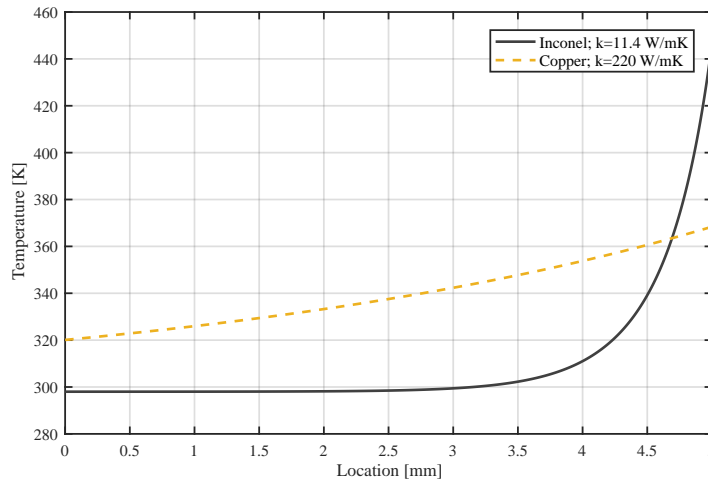


Figure 3.35: The temperature distribution in a transpiration cooled wall for two Inconel and copper.

Coolant	$M_w$ [g/mol]	$\rho$ [kg/m <sup>3</sup> ]	$c_p$ [J/kgK]
Ethanol	46.1	790.9	2425.0
Oxygen	32.0	87.1	1027.6
Nitrogen	28.0	73.7	1145.6
Methane	16.0	47.0	2701.0
Helium	4.0	10.2	5195.3

Table 3.10: The molecular mass, density and isobaric specific heat of the different coolants analyzed; determined using CoolProp [4]; density and isobaric specific heat determined at 65 bar and 298 K.

reach the same mass flux. For the same wall thickness, the mass flux of the gases is roughly twice as high. On the other hand, helium results in a lower mass flux which is roughly 60% of the ethanol mass flux for the same wall thickness.

The results in this section can be summarized as follows: the ideal coolant from a cooling perspective has a low molecular mass to shield the wall better from the convective heat transfer caused by the blowing effects. Secondly, a high isobaric heat capacity is preferred to keep the wall to lower temperatures. A coolant that meets both these requirements is helium. It was clear from the results, that of the investigated coolants, helium performs the best. Of course, from a systems point of view helium might not be preferable due to its high cost and required storage volume. Furthermore, helium is inert and will not contribute to any combustion.

### 3.5.7. Conclusions

A summary of the parametric analysis performed is given here. It is best to reduce the pore size as much as possible as this will lower the maximum temperature occurring in the wall. For the conditions in this work, the effect stabilizes at a pore size of around 0.1 mm. Disregarding any structural considerations, a smaller pore size is also better as it will reduce the thickness of the wall required to achieve low flow rates and this will result in a lower dry mass. While the smallest pore sizes producible with additive manufacturing are between 0.3 mm and 0.5 mm (section 1.4), in the remainder of this report pore sizes of 0.1 mm and 0.05 mm will be used as it is clear that otherwise unfeasible thick walls (> 10 mm) are obtained.

For the porosity, it can also be concluded that a smaller porosity is better. It has no effect on the maximum temperature, but will reduce the maximum gradients. Going from a porosity of 0.4 to 0.15 reduces the gradients by roughly 30% for the conditions in this report. Furthermore, a smaller porosity will also reduce the required wall thickness to achieve the same mass flow. However, it should be noted that when the porosity reduces a lot, the wall cannot be seen as a homogeneous porous medium. The blowing effects that reduce

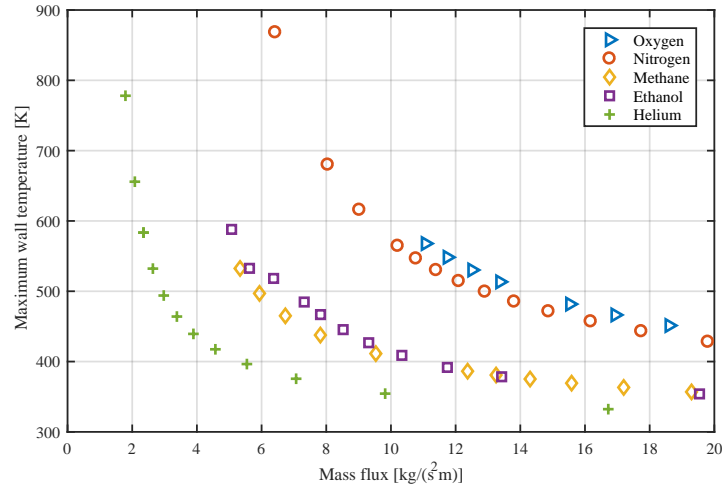


Figure 3.36: The maximum wall temperature for different coolants versus the mass flux;  $k=11.4$  W/m; porosity 0.2; pore size 0.05mm.

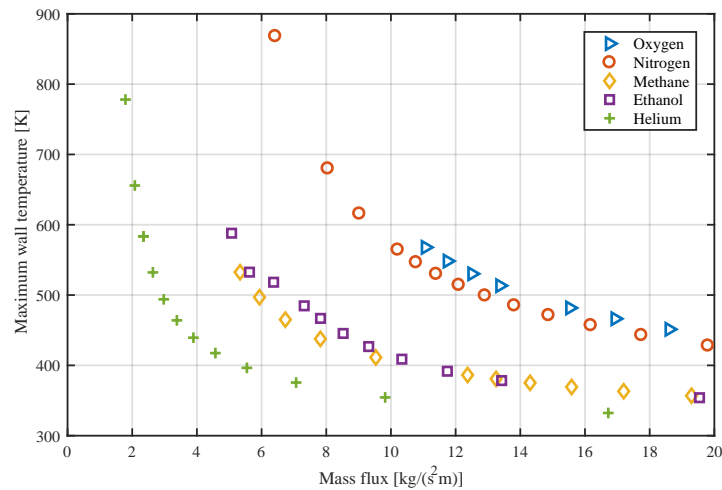


Figure 3.37: The maximum wall temperature gradient for different coolants versus the mass flux;  $k=11.4$  W/m; porosity 0.2; pore size 0.05mm.

the convective heat transfer into the wall might vanish. It would then be closer to a few coolant jets injected into the chamber at some locations while at the rest of the wall there is no cooling, similar to film cooling. At what porosity this boundary lies is not known, but a porosity of 0.2 appears to be a good engineering estimate and coincides with the lower values found in literature

Furthermore, the effect of altering the porosity within the wall was investigated. A lower porosity at the hot side of the wall gives lower thermal gradients. However, it is better to just use a constant low porosity in the complete wall. This will create thinner walls and reduce dry mass. The same applies for a pore size distribution: a constant small pore size is better.

Also, a higher thermal conductivity of the wall material will both lower the maximum temperature and gradients. However, for the same wall thickness and pore size it will also increase the mass flow (which also helps in better cooling). When comparing the maximum temperature for Inconel and copper as a function of coolant mass flux, they yield the same temperatures. The thermal gradients are 19 to 20 times lower for copper for the same mass flux though.

Lastly, the most ideal transpiration coolant has a low molecular mass to shield the wall better from the con-



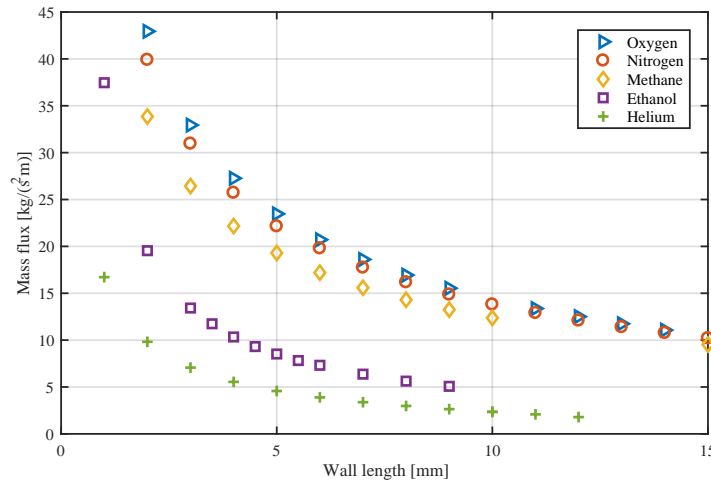


Figure 3.38: The maximum wall temperature gradient for different coolants versus the mass flux;  $k=11.4$  W/m; porosity 0.2; pore size 0.05 mm.

vective heat transfer and has a high isobaric heat capacity to achieve better cooling in the wall. Of the investigated coolants, helium shows the best cooling results. If this choice is the best from a total systems point of view is doubted.

### 3.6. Sensitivity analysis

The developed model can also be used to find the sensitivity of several parameters. This is treated in this section. First two 'inputs' of the model are analysed: the choice of the volumetric heat transfer model and the effect of the choice for the pressure drop over the wall. It is determined how sensitive the results are with respect to these aspects and if more accurate models and values are required. Afterwards, more operational aspects are investigated: the sensitivity to oscillations in chamber pressure and what happens if the heat flux increases.

#### 3.6.1. Choice of volumetric heat transfer model

Various empirical models for the volumetric heat transfer within the porous wall were discussed in section 3.2. Two of them were implemented in the model: the Kuwahara x2 relation and the Whitaker relation. The Kuwahara relation is used for the results in this report. However, in this section, it is compared to the Whitaker relation to see how sensitive the results are to the choice of  $h_v$  model.

The increases in solid wall temperature from the starting temperature of 298 K for walls with different pore sizes for the Kuwahara and Whitaker relation can be seen in Table 3.11. At pore sizes of 1 mm and larger, the Kuwahara relation obtains a higher temperature than the Whitaker one with a maximum difference of 26.7%. For pore sizes of 0.2 mm and 0.3 mm, the difference is still 19.5% but reversed: now the Kuwahara relation predicts a lower temperature. At pores sizes of 0.1 mm and 0.05 mm, the difference between the models becomes small with a maximum difference of 1.84%.

The fact that a small difference occurs at lower pore sizes makes sense: at these pore sizes, the heat transfer becomes really high and the solution converges to the local thermal equilibrium case for both  $h_v$  models. As discussed in section 3.5, pore sizes of 0.05 mm and 0.1 mm will be used in the remainder of this work as otherwise the walls will be too thick. So, for these pore sizes, the choice of  $h_v$  model does not matter. If one wants to do more research on the pore sizes applicable for additive manufacturing (0.3 mm tot 0.5 mm), better models for the volumetric heat transfer are required as the differences in temperature are up to 20%.

$D_p$ [mm]	$\Delta T_s$ Whitaker [K]	$\Delta T_s$ Kuwahara x2 [K]	Difference [%]
2.0	135.9	185.3	-26.7
1.5	117.7	154.4	-23.8
1.0	97.7	119.1	-18.0
0.3	75.8	64.7	17.2
0.2	89.7	75.0	19.5
0.1	366.5	359.9	1.84
0.05	1645.7	1643.1	0.16

Table 3.11: The increases in solid wall temperature for Whitaker and Kuwahara x2 volumetric heat transfer model and their differences for various pore sizes; wall thickness 40 mm,  $k=11.4$  W/mK.

### 3.6.2. Sensitivity to pressure drop over the wall

As already discussed, using the recommend pressure drop of 5 bar over the wall resulted in too thick walls. Therefore, the pressure drop was reduced to 1 bar. However, this choice is rather arbitrary and thus the effect of the chosen pressure drop is investigated to see how sensitive the results are on this choice.

The mass flux for different pressure drops over a transpiration cooled wall can be seen in Figure 3.39. Note that this pressure difference is added to the total pressure in the chamber of 65 bar, while at this location the actual pressure is 63.5 bar. So, the actual pressure drop is 1.5 bar higher. This is also the reason that, when extrapolated, at a pressure drop of 0 bar, still a nonzero mass flux is occurring.

A pressure drop of 1 bar is taken as the nominal case. This means that increasing the pressure drop to 2 bar, increases the mass flux with 36%. Increasing it to 5 bar, raises the mass flux with 145%. In an actual engine, the goal is to tailor the mass flux such that the wall temperature is close to the allowed material limit. If the pressure drop changes, the wall thickness has to be adapted to obtain the required mass flow for this temperature. While no sensitivity study of the wall length versus mass flow is done, looking at Equation 3.5, it will be close to linear for relative small changes in thickness. This means that changing the pressure drop over the wall from 1 to 2 bar, will increase the wall thickness with 36%. Lowering it to 0.5 will decrease the length with 42%. This thickness change will also directly affect the dry mass of the wall. It can be concluded that the choice of required pressure drop over the wall has a big impact on the dry mass of the engine.

It is recommended to do further research into the required pressure drop as no required value is known and the results are sensitive to the choice of pressure drop. A more elaborate discussion on this topic follows in the next section.

### 3.6.3. Sensitivity to chamber pressure change

In a rocket engine the combustion chamber is not constant, but oscillates with time. Assuming that the upstream pressure stays constant (i.e the pump outlet pressure), a change in combustion chamber pressure will changes the pressure drop over the wall. This directly alters the mass flow through the wall and will thus have an effect on the maximum temperature. It must be ensured that the temperature will not vary to a large extend with small variations of pressure. In this section the sensitivity regarding a change in combustion chamber pressure is investigated. It is assumed that the engine pressure oscillates between -5% and +5% of the nominal chamber pressure, which is classified as smooth combustion by[16].

While a pressure difference over the wall of 5 bar was recommend by DLR, it was already discussed earlier that a pressure drop of 1 bar is used. Otherwise, the required wall thicknesses become very large. With this pressure drop, if the chamber pressure increases with more than 1 bar it would flow into the reservoir. However, this 1 bar pressure drop is only a simplification of reality. In a pump fed engine, the coolant will leave the pump at a significantly higher pressure. Part of the fuel required for the coolant is than tapped of from the main supply to the injector and guided to the transpiration cooled wall. The coolant mass flow will be regulated by a valve in this line and a large pressure drop in the valve will occur. See Figure 3.40 for a representation of this. Now a change in combustion chamber pressure will have a smaller effect on the mass flow and no back flow can occur as the upstream pressure is much higher.

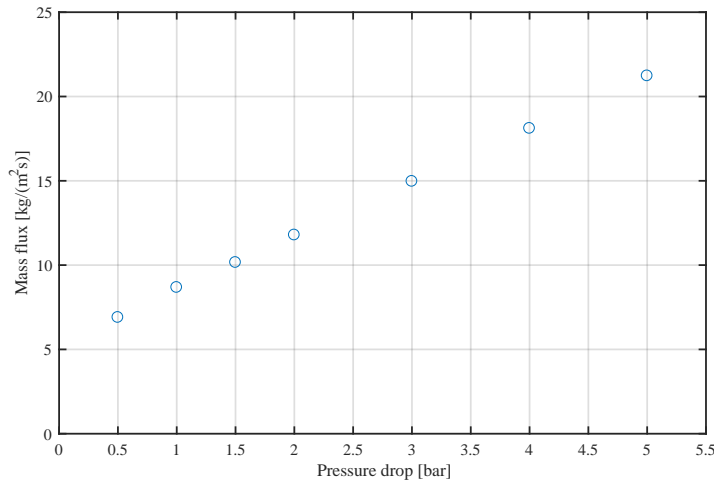


Figure 3.39: The change in mass flux for different specified pressure drops over the wall,  $k=11.4 \text{ W/mK}$ , porosity 0.2, pore size 0.1 mm and wall thickness 20 mm.

Taking into account the above explanation, one could lower the pressure drop even further to very low values. However, the porous wall should provide enough 'resistance' to ensure a uniform distribution of the coolant in the reservoir. This exact pressure drop is unknown and should be found by testing. Additionally, it might be that locally in axial direction the combustion chamber pressures are different and local back flow into the wall then occurs. This also requires additional research. It is clear that an as low as possible pressure drop is beneficial, as this will result in thinner and thus lighter walls. However, the exact required pressure drop needs to be found by additional modelling or testing.

For the reference engine, the upstream pressure is 100 bar. Note that this is the upstream pressure for the regenerative cooled case, and if only transpiration cooling is used, it could reduce as less pressure drop occurs due to the absence of cooling channels. The preferred pressure drop over the wall is 1 bar and that means that the valve has to drop the pressure from 100 bar to 66 bar. To achieve this pressure drop, a valve is set to a certain setting and this setting can be represented by the flow factor  $K_v$ . The pressure drops due to friction in the lines is not taken into account. While it could be possible to have the valve regulate the coolant flow over time, it is assumed here that the valve is set to one value to achieve the mass flow required for the nominal case. Then the effect of pressure drop can be modelled using this valve setting in the system.

The equation for the flow coefficient can be seen in Equation 3.24.  $K_v$  is the flow coefficient, SG the specific gravity (0.823 for ethanol) and  $\Delta P$  the pressure drop in bar. With this equation the required  $K_v$  for a nominal chamber pressure can be calculated and then with this set  $K_v$  the new case can be simulated while the  $K_v$  stays constant. The analysis is performed for an Inconel wall with a length of 5 mm. The porosity is 0.2 and the pore size 0.05 mm. To achieve the nominal mass flow a  $K_v$  value of 0.876 is used. This is a value easily in the reach of a simple needle valve.

$$K_v = Q \sqrt{\frac{SG}{\Delta P}} \quad (3.24)$$

The change in mass flow and change in temperature for a change in chamber pressure can be seen in Figure 3.41. It can be observed that when the chamber pressure drops, the mass flux increases with the same percentage. So, an increase of chamber pressure of 5% lowers the mass flow with 4.5%. On the final maximum temperature the effect is opposite and less pronounced. For an increase in chamber pressure of 5%, the temperature increases 2.5%.

It is difficult to quantify if these results are good enough for a practical rocket engine, but they are at least promising. A change in chamber pressure will affect the maximum temperature in the wall, but the effect

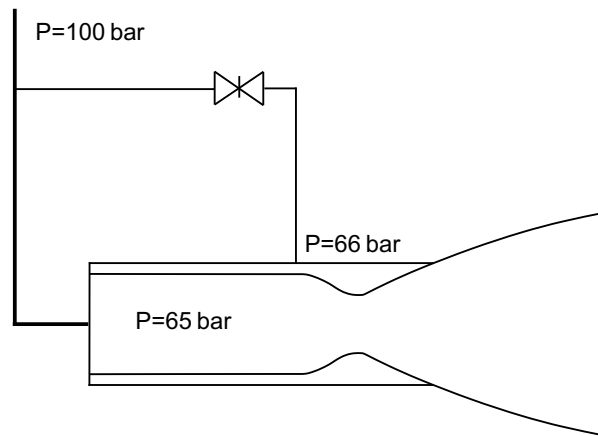


Figure 3.40: A diagram of the engine, the tap-off line from the main fuel supply to the injector and the valve that regulates the flow.

is relatively small. Therefore, it is easy to account for these fluctuations by adding a small margin. For the reference engine this would be a margin of 2.5%.

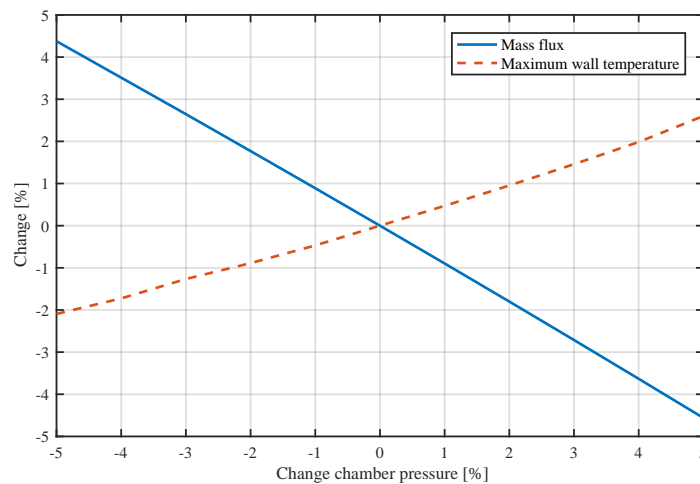


Figure 3.41: The effect of a chamber pressure change on the mass flux and maximum wall temperature; thermal conductivity 11.4 W/m; porosity 0.2; pore size 0.05 mm.

#### 3.6.4. Sensitivity to increase in heat flux

Another effect that can occur in the engine is that the heat flux to the wall is not constant and actually oscillates over time. The sensitivity of changing the heat flux on the wall temperature is investigated here. An Inconel wall is used with a porosity of 0.2 and a pore size of 0.05 mm. The heat flux is varied with -40 % and 40 %.

The results can be seen in Figure 3.42. When the heat flux increases, the mass flux also increases albeit at a lower rate. For an increase of heat flux of 40% the mass flux increases with 1.5%. This is a beneficial effect as the increase in mass flux provides more coolant and thus can counteract the increase in heat flux, but the effect is small. The maximum temperature still increases when the heat flux increases, but at a lower rate. For an increase in heat flux of 40%, the maximum wall temperature increases with only 9.4%. These seem like reasonable margins to take into account.

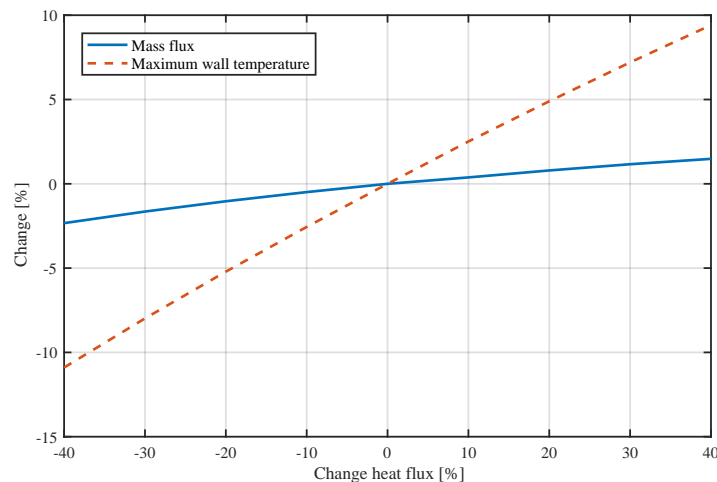


Figure 3.42: The effect of a heat flux change on the mass flux and maximum wall temperature; thermal conductivity 11.4 W/m; porosity 0.2; pore size 0.05 mm.

### 3.6.5. Conclusions

From the sensitivity analysis it can be concluded that the choice of volumetric heat transfer model will not affect the results in this thesis. However, at larger pore sizes, temperature difference of up to 17% will occur. Furthermore, it was found that the results depend largely on the specified pressure drop over the wall. Currently, 1 bar is used, but the wall thicknesses and thus dry mass are greatly affected by this choice. Further research is required to find the needed pressure drop. Thirdly, a varying chamber pressure of 5% will result in an increase of maximum wall temperature of 2.5%. Lastly, an increase in heat flux of 40% increases the maximum wall temperature with 9.4%. This sensitivity analysis shows that these increases are moderate and can be taken into account with some safety factors on the maximum allowed wall temperature.

## 3.7. Optimized coolant distribution

Finding the most optimal coolant distribution for a transpiration cooled engine is one of the research questions of this thesis. Most optimal is defined as the case when everywhere in the engine, the temperature of the wall is the maximum allowable one. In this section, the determination of the optimal coolant distribution for an Inconel transpiration cooled engine is discussed. Some simplifications to the model are required to make this possible.

Ideally, the coolant distribution can be found using the developed model and simulating the whole engine. However, several problems occur that make this impractical. These problems and the required adaptations are discussed below:

- The computational time to obtain the required mass flux for a single location is substantial due to the required under-relaxation for the specific heat. To model the whole engine, the engine needs to be split up in several stations and this will result in a long computational time. Therefore, a constant density and a constant isobaric specific heat are used. The constant density does not alter the final wall temperature, as this depends on the mass flux and the coolant velocity is adjusted to the density. The constant isobaric specific heat will be determined with the temperature of hot side of wall and the chamber pressure at the evaluated location. Comparing this adapted model to the 'fully detailed' model resulted in a 30% difference in mass flux to attain the same wall temperature for the cylindrical section. So, the magnitude of the coolant required will deviate, but this will still provide an assessment of the optimal coolant distribution in the engine.
- The chamber pressure of 65 bar is very close to the critical point of ethanol at 62.7 bar [4]. In the nozzle the chamber pressure drops below the critical pressure. Once this happens, the coolant is not supercritical anymore but will have a liquid to vapor transition including the related heat of vaporization.

This requires two-phase flow modelling and the model is not capable of doing this. Two-phase flow in porous media can be modelled, but this is far more extensive [39, 40].

- For the energy equation, cylindrical coordinates are used to model the effect of the thick wall on the temperature distribution. This works fine in the cylindrical part of the engine, but in the nozzle this causes a mismatch between the 1D heat flow (that is normal to the wall) and the coordinates. The maximum temperature can still be modelled as seeing the nozzle as a lot of small cylindrical parts, but the temperature distribution in the wall is not valid anymore. Therefore, only the maximum temperature will be given as output.

This adapted model is used to determine the required mass flux to cool the Inconel wall to a temperature of  $923 \pm 2$  K which was determined to be the maximum allowed temperature, see section 1.4. The heat flux in axial direction of the engine will vary and is given by the Bartz equation. As the full engine is modelled now, not a single calibration factor is used but one that changes with axial location. Again, the data from [7] is used and the calibration points for different axial locations can be seen in Table 3.12. In the table it can be seen that close to the injector the Bartz equation severely overestimates the heat flux. These local effects close to the injector are caused by effects of the flame length [48]. A linear interpolation is used to determine the points in between.

Location [m]	Calibration factor [-]
0.000	0.571
0.101	0.758
0.208	0.800
0.315	0.769
0.788	0.820

Table 3.12: The calibration factors used for different axial locations in the engine, obtained from [7].

The resulting mass flux is presented in Figure 3.43. In the cylindrical section the effect of the linear interpolation is visible by the sudden change in gradient. The required mass flux increases in the throat region as the heat flux is higher. The resulting mass flux follows the shape of the heat flux in the engine almost one to one. When integrating the mass flux, a total coolant mass flow of 1.34 kg/s is obtained, which translates to 6.1% of the total mass flow of the engine. But as determined, this mass flow can have an error of 30%.

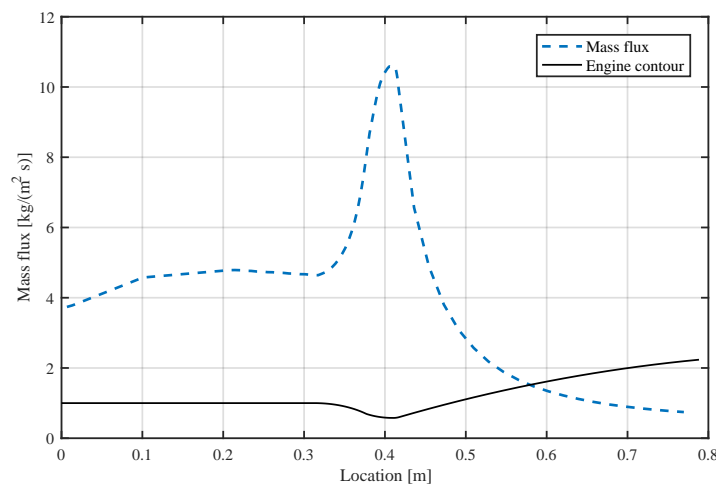


Figure 3.43: The mass flux distribution required to maintain a wall temperature of 923 K for the Inconel transpiration cooled engine.

### 3.8. Conclusions and recommendations

A model has been developed that predicts the wall temperature distribution in a transpiration cooled rocket engine using supercritical or gaseous coolants. The model was verified and validated. The model showed that the local thermal equilibrium (LTE) assumption and the local thermal non-equilibrium (LTNE) case show the same results for a majority of the conditions present in a transpiration cooled wall. However, errors are introduced by the application of the boundary conditions when LTE is used. Therefore, the LTNE case has to be used even though it has a longer computational time.

The model was used to perform a parametric analysis, a sensitivity analysis and to find the optimal coolant distribution in the engine. The main conclusions from the parametric analysis are that the pore size and porosity should be kept as small as possible. This will yield the lowest temperature and temperature gradients and will result in thinner walls to achieve the same coolant mass flux. The latter is important for the engine dry mass. It was also found that varying the pore size and porosity within the wall does not result in any large variations in the temperature. When compared at the same mass flux, no effect of thermal conductivity on the temperature occurs. A higher thermal conductivity yields lower gradients but also will require a thicker wall to achieve the same mass flux compared to the lower conductive walls. A brief look into different coolants showed that helium is the best transpiration coolant due to its low molecular mass and high isobaric specific heat.

A sensitivity analysis performed showed that the results depend heavily on the choice for the pressure drop over the wall. Currently, the required value is not known and thus this introduces a large uncertainty in the model. It is recommended to find this required pressure by additional modeling or testing. The pressure drop should be high enough to account for oscillations in chamber pressure and to distribute the coolant in the manifold uniformly. Secondly, it was found that the choice of the volumetric heat transfer model does not affect the results in thesis. The sensitivity analysis also showed that a variation of chamber pressure of 5% will increase the temperature with 2.5% and a variation of heat flux of 40 % changes the maximum temperature with 9.4 %. A simple safety factor of around 1.12 on the allowed temperature can account for these variations. The optimized coolant distribution showed that the coolant mass flux follows the curve of the heat flux in the engine.

Several other recommendations can be made to improve the accuracy of the model. These are limited to the recommendations that will have the largest impact. The determination of the pressure drop and the volumetric heat transfer are based on empirical relations that are not necessarily applicable for the geometry used in an actual transpiration cooled wall. To improve these relations, it is recommended to perform CFD or experiments to find these estimations for the geometry used. It has been found that the pressure drop has a large influence on how thick the porous wall will be and thus better estimation of this pressure drop will yield more accurate results.

This concludes the discussion on the transpiration cooling model and the parameters that influence the cooling. In the next chapter the film cooling model is discussed and then in chapter 5, the regenerative, film and transpiration cooling model are used to make a comparison between them.





# 4

## Film cooling model

The film cooling model is an addition to the regenerative cooling model described in chapter 2 and is described here. The film coolant behaves as a transcritical fluid. While most rocket engines operate in this regime, the film cooling models available in literature limit themselves to the application of either purely gaseous coolants or liquid ones. Therefore, a new film cooling model is developed that combines parts of three already existing film cooling models. These models are the NASA Annex B model [11], the Höglauer film cooling model [10] and Shine's liquid film cooling model [52]. The models will be extensively discussed in this chapter.

Firstly, the general aspects of film cooling modelling are given in section 4.1. Then the governing equations and the combination of the three film cooling models is discussed in section 4.2. Verification, validation and calibration of the model is performed in section 4.3. Two different calibrations of the model are presented. Finally, the models can be used to predict how much film coolant the Inconel and copper chamber require. This is treated in section 4.4.

### 4.1. General aspects film cooling modelling

Before the governing equations of the film cooling model are presented, some general aspects of film cooling modelling are discussed. A common parameter to express film cooling performance is the adiabatic film cooling effectiveness  $\eta$ , see Equation 4.1 [7]. This ratio can be determined by experiments, semi-empirical relations or numerical modelling. Different empirical relations for this effectiveness exist [22, 86, 87]. The adiabatic wall temperature  $T_{aw}$  in this expression has a lower value than the adiabatic wall temperature of Equation 2.2. When no film cooling is present, they would be the same.  $T_{c_0}$  is the temperature of the coolant at the injection point and  $T_g$  is the temperature of the hot gas. The heat transfer to the wall is then determined using the new and lower adiabatic wall temperature by Equation 4.2. Generally, the difference between the heat transfer coefficient  $h_g$  with and without film cooling is small, so the heat transfer coefficient without film cooling can also be used for the calculation when film cooling is present [7]. This means that the adiabatic wall temperature is the only driving factor in lowering heat transfer.

$$\eta = \frac{T_{aw} - T_g}{T_{c_0} - T_g} \quad (4.1)$$

$$\dot{q}_{conv} = h_g(T_{aw} - T_{w,h}) \quad (4.2)$$

A non-dimensional parameter to express the amount of film coolant injected is the film mass fraction  $\mu$ . As the film coolant is usually the fuel, this fraction is expressed as the film coolant mass flow to the total fuel mass flow, see Equation 4.3 [7, 10].

$$\mu = \frac{\dot{m}_{\text{film}}}{\dot{m}_{\text{film}} + \dot{m}_{\text{fuel}}} \quad (4.3)$$

For the reference engine, the coolant is injected in a (compressible) liquid phase. After the injection the coolant heats up and turns into gas. Both these phases require a different modelling approach.

The general trend for liquid film cooling models is to assume that only convective heat transfer heats up the film and that the film is transparent to radiation [86, 88]. While several works make this assumption, no evidence for the correctness of this assumption is presented in literature. An attempt was made to find the transmittance for liquid ethanol at the wavelengths relevant for radiative heat transfer, but no such data was found. The convective heat transfer heats up the film to the vaporisation temperature. Once it reaches this condition, in a pure liquid film the temperature stays constant and the heat is used to vaporize the liquid. For a supercritical coolant, no heat of vaporisation is present, so the liquid will not reach a constant temperature. When the complete film is evaporated, gaseous cooling models can then be used to model the part downstream of this point. Another phenomenon that some models take into account is the entrainment of the liquid with the main gas and this reduces the liquid film coolant mass quicker. The entrainment factor is commonly an empirically determined value.

Empirical film cooling models are generally determined for flows on flat plates [86, 89]. This requires the assumption that the cylindrical part of the rocket engine can be seen as a flat plate. Once the film reaches the nozzle, the contraction and diverging contour alter the entrainment and a correction is needed [11, 86]. Not all models allow for this and some tend to break down in the nozzle showing nonphysical behaviour.

Many different empirically determined film cooling models are available in literature. A complete discussion of all these models is deemed out of the scope of this work, and the interested reader is referred to the works of [7] and [90] where these models are extensively discussed. The main point that can be taken away from these models is that they are either developed for liquid or gaseous cooling, while in this work - and in most rocket engines - transcritical film coolants are utilized. This means that the pressure of the coolant is above the critical pressure, but the temperature is below the critical temperature. After injection, the coolant heats up and passes the critical temperature.

No empirical models were found that are dedicated to transcritical film cooling and also the number of experiments and detailed numerical modelling is very limited. The only tests done on a transcritical kerosene film cooled engine can be found in the - earlier discussed - work of Kirchberger [7] and Höglauer et al. [10]. They both use the same test engine, but with small variations in expansion ratio. Kirchberger compared several film cooling models to the transcritical test results and found that most of them significantly underestimated the cooling performance. One model was close to the test results and this was the NASA Annex B model: it predicts the location of the increase in heat flux when the model turns gaseous with an inaccuracy of less than 20%, and then the heat flux in the gaseous part is estimated within 20% [7]. Therefore, this model will be used as a baseline in this work. It still requires some adaptations and extensions, which will be discussed in the next section.

## 4.2. Governing equations

In this section the developed film cooling model is described. The basis is the NASA annex B model that prescribes the gaseous part of the film cooling. As discussed in chapter 1, the film coolant in the reference engine is transcritical. It is injected as a compressible liquid and when heating up, it turns into a supercritical fluid. No heat of vaporization is associated with this phase change. While most liquid rocket engines operate in this regime, no empirical transcritical film cooling model was found in literature. They are either limited to gaseous or subcritical liquids. Therefore, a new transcritical film cooling model is developed here that combines three existing film cooling models. The NASA annex B model is used for the gaseous part [11]. The part of the NASA annex B model that models the liquid turned out to be insufficient when compared to validation data. Therefore, it is adapted based on the model of Höglauer [10]. Added to this, Shine's model is used to

determine the reduction in heat transfer to the liquid film due to evaporation [52].

A problem that occurs, is that no clear boundary exists between liquid and gaseous phase in supercritical fluids. Therefore, it is assumed that the coolant behaves as a liquid for temperatures below the critical point. Above the critical point, the coolant is seen as a gas. The NASA Annex B model was adapted for transcritical film cooling in several other works [7, 87, 90]. However, it is not described in detail in these works how the NASA Annex B model was adapted for supercritical coolants. In the adaptation in this work, the 'liquid' part of the NASA Annex B model is replaced by a calculation on how long it takes to heat up the coolant film from its injection temperature to the critical temperature, as also done in [86, 91]. In the NASA Annex B model, entrainment relations of the liquid coolant with the main flow are used. Also, a heat transfer augmentation factor is used for liquid surface roughness that increases the heat transfer. Both these parameters depend on surface tension and as supercritical fluids do not have surface tension, these parameters are neglected. So, for the liquid part there is no entrainment and thus it can simply be seen as an energy balance. While no real substantiation for these choices can be given, it will later be seen that this model matches with test data.

The adaptation of the liquid film behaviour based on the model of Höglauer [10] and Shine et al. [52] is discussed in subsection 4.2.1. Then, in subsection 4.2.2 the governing equations of the NASA Annex B model are given that model the gaseous part. Lastly, a summary of the model is given in subsection 4.2.3.

#### 4.2.1. Adaptation liquid film behaviour

As discussed earlier, for the liquid part, an energy balance is used. The heat flux is determined using the heat transfer coefficient obtained using the (calibrated) Bartz equation and then the increase in temperature of the coolant is calculated using Equation 4.4.

$$\dot{Q}_{\text{conv}} = A \cdot h_g(T_{\text{aw}} - T_{\text{crit}}) = \dot{m}_c c_{p_c} \Delta T \quad (4.4)$$

In this case, it is assumed that the (compressible) liquid homogeneously heats up until the critical temperature and at that point transfers into gas all at once. However, this assumption has several problems. Firstly, when comparing this model to tests from [10] (discussed further in section 4.3), this model severely under predicted the liquid film length. Secondly, from a physical perspective, a temperature gradient in the coolant film will exist - the part close to the hot gases will be warmer than the part close to the wall. This means that coolant close to the hot gas will already turn into gas while the part closer to the wall is still a (compressible) liquid. Thirdly, the 'evaporated' mass will shield the liquid from the heat - similar to transpiration cooling - and thus reduces the heat flowing into the liquid [10, 52]. Several modifications are made to the liquid film behaviour to solve these problems, which are discussed below.

Höglauer [10] created a CFD model that can handle transcritical film cooling in rocket engines for Astrium's<sup>1</sup> in-house tool, Rocflam-II. The CFD analysis was compared to test data of the same engine that Kirchberger used and good agreement was found, which will be presented later in this work. This test data will also be used later in this work. Höglauer described how the transcritical film is modelled in the CFD tool and this will be used for the model of this thesis. The two reasons why Höglauer used this model were that it allowed for a temperature gradient occurring in the film and the numerical solver could not handle the instantaneous 'evaporation' of the liquid [10].

Höglauer assumed that while the film heats up, it partially 'evaporates' before the bulk temperature reaches the critical temperature. This evaporation starts when a certain ratio of bulk film temperature to critical temperature is reached (Equation 4.5). Höglauer uses a  $\Lambda$  of 0.6. Once this ratio is reached, a certain percentage of the heat flux into the film (Equation 4.6) is used to increase the temperature from the bulk temperature to critical temperature and it turns gaseous instantly. Höglauer used a  $\Pi$  of 0.2. The other part of the heat is used to keep on heating the film. See Figure 4.1 for a representation of this process. Note again that no substantiation can be given for the correctness of these assumption, but the results obtained with it match with test data. Höglauer also mentioned that different  $\Lambda$  and  $\Pi$  ratios can be used for different coolants [10] and this likely also applies for different conditions in the engine. Another assumption is that the top of the

<sup>1</sup>Now Airbus Defence and Space

film always equals the critical temperature and thus this temperature is used for the convective heat transfer calculation in Equation 4.4.

$$\Lambda = \frac{T_{\text{film}}}{T_{\text{crit}}} \quad (4.5)$$

$$\Pi = \frac{\dot{q}_{\text{vap}}}{\dot{q}_{\text{conv}}} \quad (4.6)$$

$$\dot{m}_{\text{vap}} = \frac{\dot{q}_{\text{vap}}}{c_p (T_{\text{crit}} - T_{\text{film}})} \quad (4.7)$$

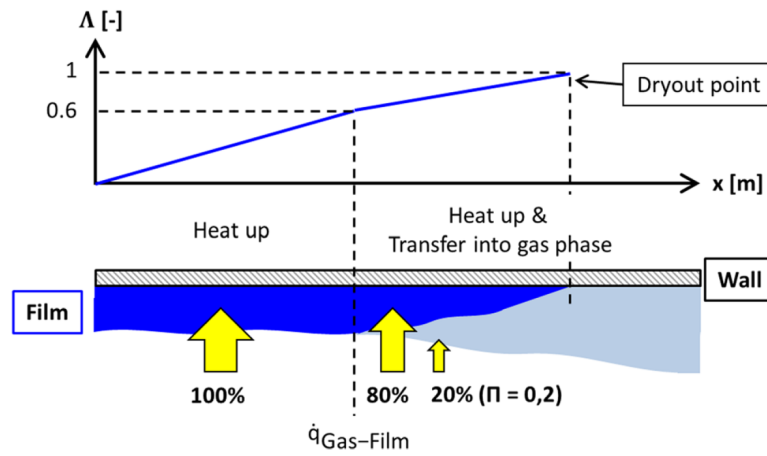


Figure 4.1: Modelling of the transcritical film [10].

In Höglauer, the evaporated mass flow is then used as a source term for the CFD solver that models the main flow and this causes less heat to transfer into the liquid film. In the model of this thesis, the influence of the evaporation on the heat transfer is modelled differently. The 'evaporated' mass flow is determined by Equation 4.7. To determine the reduction of heat to the film, there is turned to the work of Shine et al. [52]. This work created a new (subcritical) liquid film cooling model and assumed that the evaporated mass flow shields the film against heat similar as seen in transpiration cooling. Shine uses Meinert's empirical equation [51] that predicts the reduction in Stanton number due to blowing in a transpiration cooled wall (as described in subsection 3.2.5). The same will be done for this thesis by converting the evaporated mass flow into a blowing ratio and then determining the reduction in convective heat reaching the film.

The above described modifications were implemented. It was found that numerical problems occur when the coolant temperature is getting close to the critical temperature. At this condition, it takes only a low amount of heat to evaporate a large amount of coolant and as a consequence the blowing ratio attains high values. Subsequently, due to the high blowing ratio, the reduction in heat transfer becomes very large. Then the heat transfer coefficient effectively goes to zero. Then, for the next station, no evaporation occurs as no heat went into the film in the previous station. This causes a low blowing ratio and thus high heat transfer to the film. The blowing ratio and reduction in heat transfer oscillates between very high and very low values until the film is completely heated up or evaporated. To solve this oscillatory behaviour, the values of the blowing ratio from the last four stations are averaged. This solution achieves a smooth curve for the blowing ratio and the reduction in heat transfer coefficient, as can be seen in Figure 4.2. For the first few points an oscillation exists, but it quickly dampens out. It can also be seen that this increases the liquid film length drastically. The model without averaging is completely evaporated at index 5800 and the one with averaging at around index 10000.

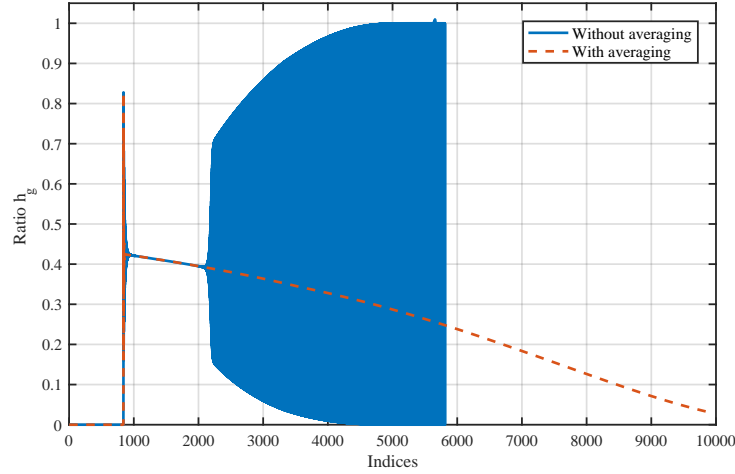


Figure 4.2: The ratio of heat transfer coefficient  $h_g$  with reduction due to blowing effects to the one without for the Höglauer engine with  $\mu$  is 15%, the blue area is oscillatory behaviour of the ratio.

To avoid other numerical problems when the coolant temperature is close to the critical temperature, the transition from liquid to gas occurs when the coolant temperature reaches 99.5% of the coolant temperature or when the coolant mass flow is less than 1% of the initial coolant mass flow.

#### 4.2.2. Gaseous behaviour from NASA Annex B

The modelling of the liquid film coolant was discussed in the previous section. Once the coolant is gaseous, the NASA Annex B model is used to model it. The governing equations are discussed in this section. The model is described in imperial units, but most equations use ratios and are thus unitless.

The downstream effectiveness  $\eta$  equals Equation 4.8.  $W_E$  is the entrainment mass flow and  $W_C$  the film coolant mass flow and the ratio is the entrainment flow ratio given by Equation 4.9. The shape factor of the mixing layer profile  $\theta$  is defined by Equation 4.18 or Equation 4.19.

In Equation 4.9,  $W$  is the total mass flow in the chamber, so including the film coolant,  $\psi_L$  is the reference entrainment ratio defined by Equation 4.10. Note that the term  $\frac{\rho_c \nu_c s_i}{\mu_c}$  is the Reynolds number, where  $s_i$  is the mixing layer height at the point where the coolant turns gaseous. It is unclear from the documentation if  $\psi_L$  is constant or changes with downstream distance. However, only sensible results were obtained when it was taken constant at the phase transition point. Therefore, this is used. [11] states that  $\psi_L$  lies between 0.025 and 0.06 for rocket engines. Equation 4.13 defines the effective contour distance  $\bar{x}$ ,  $r_i$  is the chamber radius at the injection point and  $(W_E)_L$  is the entrainment ratio at the start of the gaseous phase and is defined by Equation 4.15.

$$\eta = \frac{1}{\theta \left(1 + \frac{W_E}{W_C}\right)} \quad (4.8)$$

$$\frac{W_E}{W_C} = \frac{W - W_C}{W_C} \left[ 2\psi_L \frac{\bar{x}}{r_i} \sqrt{1 - \frac{(W_E)_L}{W - W_C}} - \left(\psi_L \frac{\bar{x}}{r_i}\right)^2 \right] + \frac{(W_E)_L}{W_C} \quad (4.9)$$

$$\psi_L = \frac{0.1 \left(\frac{\nu_{c0}}{\nu_g}\right)}{\left(\frac{\rho_c}{\rho_g}\right)^{0.15} \left(\frac{\rho_c \nu_{c0} s_i}{\mu_c}\right)^{0.25} f} \quad (4.10)$$

In Equation 4.10 that gives  $\psi_L$ ,  $\nu_{c0}$  is the injection velocity of the coolant. In none of the works that use this model, it is mentioned how the coolant velocity is determined [7, 11, 90]. As the mass flow is specified and

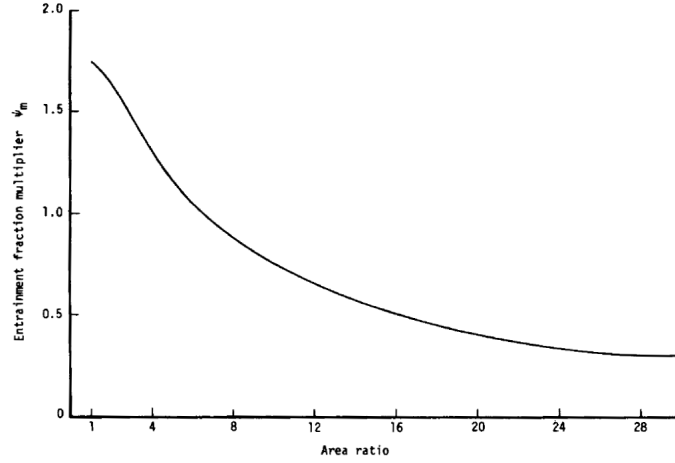


Figure 4.3: The entrainment fraction multiplier  $\psi_m$  as a function of expansion ratio in the divergent section, taken from [11].

the total pressure drop  $\Delta P$  is known (the difference between the chamber pressure at the location of injection and the pressure of the coolant in the cooling channel at the injection point), the velocity is determined using Bernoulli's equation with a constant discharge coefficient of 0.7, see Equation 4.11. For a schematic of the injection of the film coolant, see Figure 1.1. The thickness of the coolant film  $s_i$  is determined with this velocity. It is assumed that the coolant immediately 'spreads' across the whole chamber circumference with even thickness. The velocity-ratio correlation factor  $f$  is defined by a figure in [11], but as the velocity ratio in this work is always smaller than unity,  $f$  is given by Equation 4.12.

$$v_c = 0.7 \sqrt{\frac{2\Delta P}{\rho_c}} \quad (4.11)$$

$$f = \left( \frac{v_c}{v_g} \right)^{1.5} \quad (4.12)$$

The non-dimensional contour distance  $\bar{x}$  is defined by Equation 4.13 and it is integrated from the point  $L$  where the coolant turns into gas. An entrainment fraction multiplier  $\psi_m(x)$  is used. Its value depends on the location in the chamber. It starts at 3 or 4 at the injection point and then reduces linearly to 1.75 at the throat [11]. From there onward it follows the curve as can be seen in Figure 4.3. This curve is digitized in the program and interpolation is used to find the values. The term  $\psi_m$  accounts for rocket turbulence levels, coolant injection configuration, flow turning and acceleration and is an empirical factor. As it is not clear what the ratio of the 1D and 2D components mean in neither [11], [7] and [90] it is assumed to equal unity. For each location, the step in  $dx$  is calculated using Equation 4.14.

$$\bar{x} = \int_L^x \frac{r_i}{r} \frac{(\rho_e u_e)_{2D}}{(\rho_e u_e)_{1D}} \psi_m(x) dx \quad (4.13)$$

$$dx = \sqrt{(\Delta l)^2 + (\Delta r)^2} \quad (4.14)$$

The determine  $(W_E)_L/W_C$  in Equation 4.15, Equation 4.16 and Equation 4.17 are required. In these equations,  $H_{t,g}$  is the total enthalpy of the hot gases,  $H_g$  is the enthalpy of the hot gases,  $H_{c,sv}$  is the enthalpy of the coolant at saturation condition and  $H_c$  is the enthalpy of the coolant. In this case, the coolant is supercritical and the saturation temperature enthalpy  $H_{c,sv}$  could be replaced by the enthalpy at critical temperature. However, this ratio becomes negative when the coolant enthalpy is larger than the critical enthalpy, which gives unrealistic results. Therefore,  $\eta_L$  is assumed to be one which gives initial entrainment ratio of 0.66. The entrainment ratio goes up to roughly 5, so this difference does not introduce large errors.

$$\frac{(W_E)_L}{W_C} = \frac{1}{0.6\eta_L} - 1 \quad (4.15)$$

$$\eta_L = \frac{B}{1+B} \quad (4.16)$$

$$B = \frac{H_{t,g} - H_g}{H_{c,sv} - H_c} \quad (4.17)$$

The shape factor  $\theta$  is defined by Equation 4.18 or Equation 4.19, depending on the entrainment mass flow.

$$\theta = 0.6 + 0.263 \frac{W_E - (W_E)_L}{W_C} \text{ for } W_E < (W_E)_L + 0.6W_C \quad (4.18)$$

$$\theta = 0.758 \text{ for } W_E \geq (W_E)_L + 0.6W_C \quad (4.19)$$

Finally, after all these calculations, the adiabatic wall temperature can be determined by Equation 4.20 for a non-reactive case and no decomposition of the film occurring, where  $H_{aw}$  is given by Equation 4.21.

$$T_{aw} = \frac{H_{aw} - \eta H_{c,sv} + \eta c_{p,v} T_{if} + (1 - \eta)(c_{p,g} T_{t,g} - H_{t,g})}{\eta c_{p,v} + (1 - \eta)c_{p,g}} \quad (4.20)$$

$$H_{aw} = H_{t,g} - \eta(H_{t,g} - H_c) - (1 - Pr_w^{1/3})(H_{t,g} - H_g) \quad (4.21)$$

However, as CoolProp and CEA have different reference values for enthalpy that are not equal, a different relation is used. Similar to [87] a different ratio is used. This can be seen in Equation 4.22.

$$T_{aw} = \eta(T_{c_0} - T_g) + T_g \quad (4.22)$$

### 4.2.3. Model summary

The governing equations for the film cooling model were given in the previous sections. The steps taken in the film cooling model can be seen in Figure 4.4. The film cooling model is an addition to the regenerative cooling model. This way it reuses the determination of the hot gas properties and the determination of the properties in the cooling channels. Basically, the film cooling model is used to determine the new adiabatic wall temperature that is then used in the regenerative model. A few iterations are required until the film injection temperature (which is the temperature at the end of the cooling channels) is converged. The only additional input required in the program is the amount of film coolant mass flow. The outputs are the same as regenerative model.

An overview of the assumptions made in the film cooling model is given below:

- The injected film coolant does not alter the combustion process.
- The liquid and gaseous film are transparent to radiation and this means that in the section where the film is liquid, the wall is only heated by radiation.
- The supercritical coolant behaves as a liquid until the critical temperature and afterwards as a gas.
- No mass transfer occurs from the 'liquid' part of the film coolant, so no evaporation and entrainment.
- In case that the wall temperature is higher than the coolant film, it is assumed that there is no heat transfer back into the film.

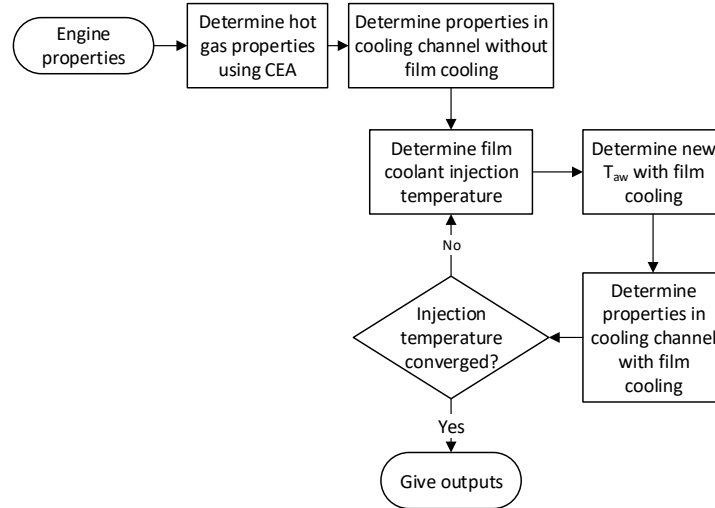


Figure 4.4: A flowchart of the steps taken in the film cooling model.

### 4.3. Verification, validation and calibration

The film cooling model has been discussed in the previous sections. The verification of the model is performed by ensuring that all equations were implemented correctly. For validation, experimental results of a kerosene film cooled rocket engine are used. This will be discussed in subsection 4.3.1. A good agreement was found. However, there are indications that the liquid film length is overestimated in this model. Therefore, an extra step was taken by comparing it to the film cooling model of the software Rocket Propulsion Analysis (RPA). In the end, this results in two different calibrations for the model.

#### 4.3.1. Comparison to experimental data

Höglauer compared his CFD model to tests performed with a kerosene and gaseous oxygen engine from the Technical University of Munich (TUM). This is the same engine that Kirchberger [7] used, albeit with a different nozzle contraction ratio. A 3D-model of the engine can be seen in Figure 4.5. It consists of three cylindrical sections and a nozzle section that are all individually cooled with water. This allows for heat flux measurements. The film coolant is radially injected after the second small cylindrical section. The engine properties can be seen in Table 4.1. As not all required data is given in [10], some parameters are determined from different papers on the same engine or estimated to match the results without film cooling. This is indicated in the table.

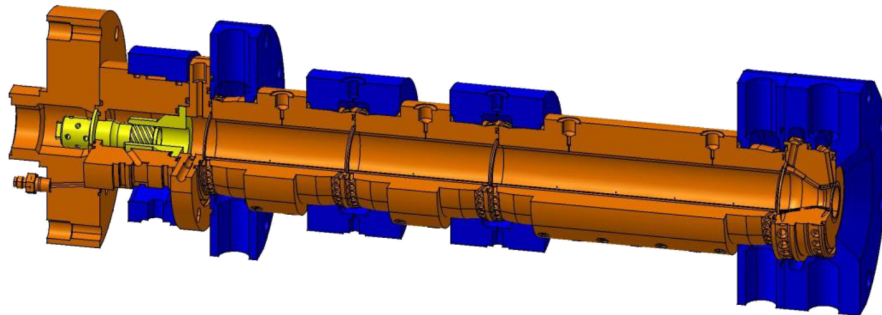


Figure 4.5: The engine used in the Höglauer tests [12], the film coolant is injected after the second (small) segment.

Höglauer used the heat flux data from the test to validate his developed CFD tool [10]. In the test, the film



Table 4.1: The engine properties of the Höglauer tests.

Parameter	Symbol	Value	Unit	Source
Chamber pressure	$P_c$	60	bar	[10]
Oxidiser to fuel ratio	OF	2.9	-	[10]
Total mass flow	$\dot{m}$	1.283	kg/s	[10]
Film mass fraction	$\mu$	10 and 15	%	[10]
Contraction ratio	$\epsilon$	2.8	-	[10]
Regenerative coolant		Water		[7]
Regenerative coolant mass flow	$\dot{m}_{\text{coolant}}$	0.8	kg/s	Estimated to match [10] w/o film cooling
Wall thickness		0.009	mm	Estimated from [10]
Wall thermal conductivity	$k$	391	W/mK	Obtained from [92]
Upstream pressure	$P_0$	100	bar	Estimated
Film coolant inlet temperature	$T_0$	298	K	Estimated

mass fraction  $\mu$  was 15%. The measured heat flux data has low spatial resolution as there are only four cooled sections. Therefore, the obtained heat flux of the CFD tool is integrated to the same resolution and is then compared to the test data. This was done for the case when no film cooling is present and for the case when  $\mu$  is 15%. Höglauer's results can be seen in Figure 4.6 and the agreement between the experimental and numerical heat flux is good. In order to compare the model described in this thesis, the numerical (CFD) data from Höglauer is used as it has a better spatial resolution. As the integrated values match the test data, this indirectly compares the results to test data.

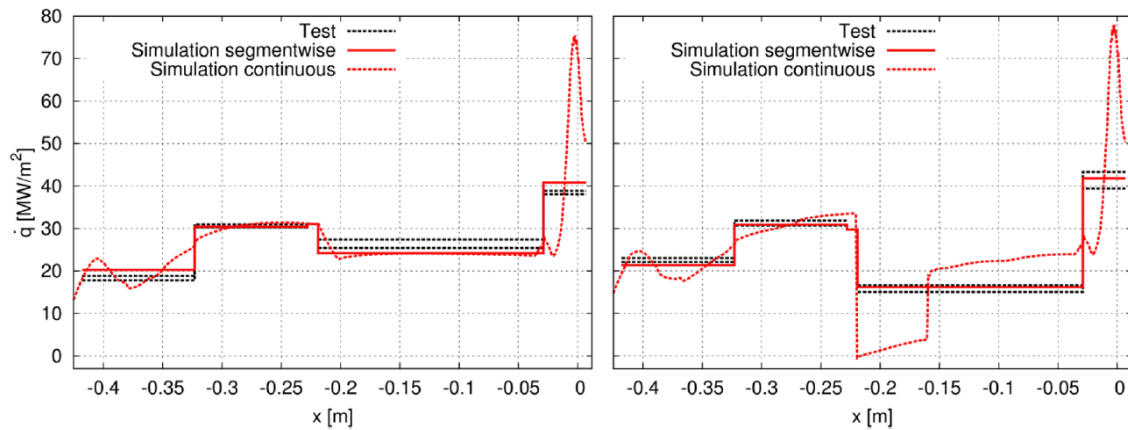


Figure 4.6: The measured and calculated wall heat flux without (left) and with film cooling (right) from [10],  $\mu = 15\%$  and  $P_c = 60$  bar; note that two tests were performed.

Höglauer used kerosene as film coolant, so the model for validation of this thesis should use that as well. To achieve this, the relevant properties of kerosene are required. CoolProp, which is used in the model, does not have kerosene properties. Therefore, a mix of different literature for the conditions of the engine is used by lack of a proper data set. The critical temperature and pressure are set to respectively 684.26 K and 23.44 bar [38]. The isobaric specific heat versus temperature and pressure follows from [35] and the density from [34]. This provides a limited data set for the conditions of the tests, but it is not sufficient to model all conditions in this thesis. Therefore, ethanol is still used as coolant substitute.

In the model in this work, the reference entrainment factor  $\Psi_L$  is calculated using Equation 4.10. Furthermore, the heat transfer coefficient obtained from the Bartz equation is scaled with 0.65. The thickness of the wall is estimated to be 0.9 mm and the height cooling channel to be 2.5 mm (both estimated from [10]). The results for the case when  $\mu$  is 15% can be seen in Figure 4.7. It is zoomed in to the section right after the film injection, which happens in the middle of cylindrical section, until the start of the nozzle.

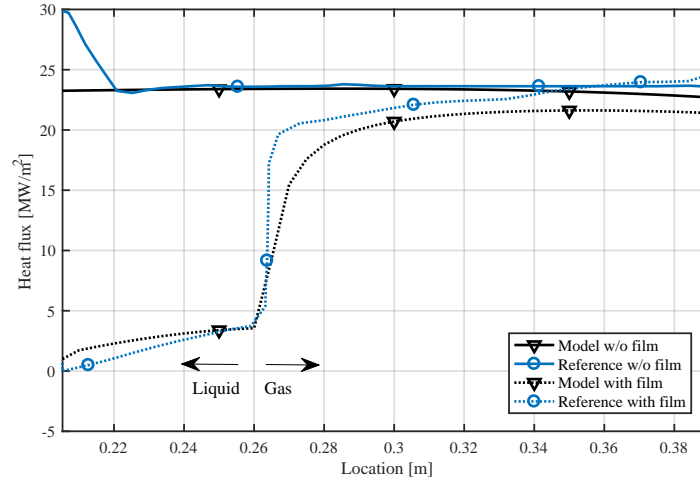


Figure 4.7: The heat flux of the model compared to the heat flux of the reference for  $\mu=15\%$ , OF 2.9 and  $P_c=60$  bar.

As can be seen, the general trend of the heat flux when film cooling is present is similar as the reference data and the transition point from liquid to gas is predicted spot on. When the liquid layer is present, the heat flux stays low. Then, once the film coolant turns into gas, the heat flux increases rapidly and converges to the heat flux without film cooling present. The gaseous part does not match the reference data exactly. The difference of the gaseous part is minimum 6% and maximum 12%, except for the part where the heat flux increases rapidly. This gives locally higher errors, but this effect on the temperature of the engine will be small.

It was found that the heat flux of the gaseous part changes by altering the reference entrainment ratio  $\Psi_L$ . In Figure 4.7 this value was calculated using Equation 4.10, but the velocity of the coolant is not exactly known from the Höglauer test data as the upstream pressure and hole sizes are not specified and the coolant is injected radially. For rocket engines  $\Psi_L$  lies between 0.025 and 0.06 [11]. The calculated value in Figure 4.7 was 0.0261. A calibration was performed to get a better match with the test data.  $\Psi_L$  was iterated and with a value of 0.06 better agreement of the gaseous part was achieved, see Figure 4.8. Now the errors in the gaseous part are 1.5% up to 0.34 m and afterwards it rises to 11%.

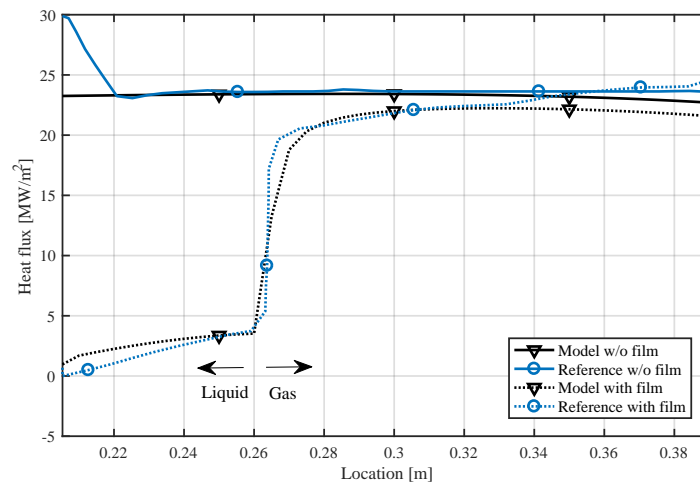


Figure 4.8: The calibrated heat flux of the model compared to the heat flux of the reference for  $\mu=15\%$ , OF 2.9 and  $P_c=60$  bar with a calibrated value for  $\Psi_L$  of 0.06.

To test if this calibrated model also works for other film mass fractions, it is compared to CFD data from Höglauer with a film mass fraction  $\mu$  of 10%. Note that Höglauer did not compare these results to experiments. The heat flux obtained with the model compared to the reference can be seen in Figure 4.9 and it can be seen that the match is good here as well. The heat flux with film cooling appears to be slightly larger than the heat flux without cooling for location of 0.32 m and beyond, but this is mainly attributed to inaccuracy of obtaining the data from [10] by use of a curve digitizer.

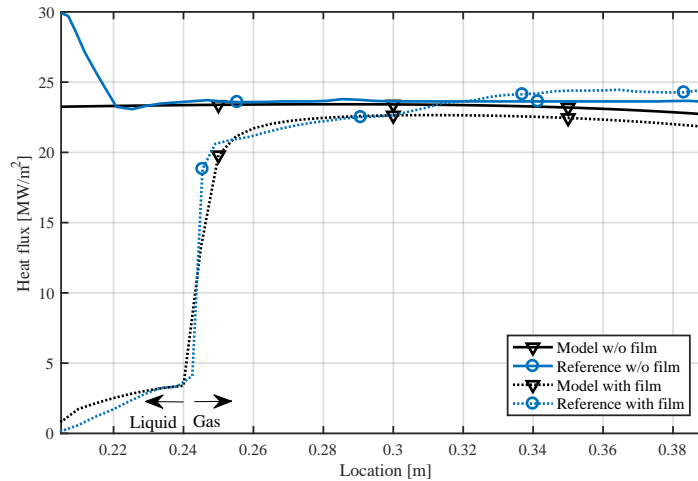


Figure 4.9: The heat flux of the model compared to the heat flux of the reference for  $\mu=10\%$ , OF 2.9 and  $P_c=60$  bar with a specified value for  $\Psi_L$  of 0.06.

**Conclusions** It can be concluded that the newly developed film cooling model that consists of a combination of the NASA Annex B model [11], the transpiration cooling effects of Shine's model [52] and the transcritical liquid film behaviour as described in Höglauer [10] predicts the general trend of the film coolant well when comparing it to rocket engine tests with transcritical kerosene film coolant [10]. Without any calibration, the liquid film length and the heat flux in the liquid section are estimated correctly. Afterwards, in the gaseous part the heat flux is underestimated with a maximum difference of 12%. When calibration is applied, this difference can be reduced to 1.5% in the section of interest.

However, only one real test data set was found and this uses a different coolant than the one in this thesis (kerosene versus ethanol). This is a very limited data set to perform validation and calibration. It is recommended to acquire more data, either by a more extensive search in literature or, preferred, by doing own experiments on the actual reference engine.

#### 4.3.2. Comparison to film cooling model of Rocket Propulsion Analysis

Some notes should be made regarding the model developed in this work compared to other (empirical) film cooling models available in literature. Other models commonly include a factor that accounts for the entrainment of the liquid with the main flow. So, while a good match for the liquid film length between the test data from Höglauer exists, this is a point of concern. Models that include an entrainment factor will give lower liquid film lengths. This will change the wall temperature drastically. Therefore, the model is compared to the film cooling model of the commercial software Rocket Propulsion Analysis (RPA) in the next section.

Rocket Propulsion Analysis has the option to do a thermal analysis on the chamber and include film cooling. In the documentation [91], a gaseous and liquid film cooling model are described and while no mention is made on how supercritical coolants are handled, the film cooling model gives outputs for supercritical conditions as well. These cases have similarities to the liquid film cooling model. The underlying models follow from Russian literature and are therefore not accessible to the author.

The liquid film cooling model works as follows: first a liquid is heated up to vaporization temperature, then

the liquid keeps a constant temperature until evaporated and then a gaseous film cooling model is used. The liquid section is similar to the one used in the model of this work. The convective heat flux heats up the film and the radiation passes through and is the only source that heats up the wall. However, the temperature increase per station is increased due to 'the stability of the film'. This increase depends on the Reynolds number of the film and goes from no increase at a Reynolds number of 0 to an increase of 2 at a Reynolds number of 5000. Once the film reaches vaporization temperature, this factor is not included anymore to determine the evaporated mass flow. The evaporated mass flow mixes with the surface layer and creates a layer with a new mixture ratio and this shields the film from heat. Once all coolant is gaseous, a gaseous coolant model is used. This model depends on the 'Ievlev's correlation for similar conditions' and again this follows from Russian literature, so it is difficult to understand the underlying principles. As only the RPA manual is available and the underlying literature cannot be used, the RPA model is used as a black box to compare the model described in this work.

The engine used in RPA to which the model is compared is very similar to the reference engine. It is regeneratively cooled with additional film cooling supplied at the injector. The engine contour is determined by RPA and imported into the model of this thesis. The propellants are RP-1 and liquid oxygen, but the regenerative and film coolant used is ethanol as RP-1 coolant properties are not well defined in RPA. The other properties of the engine can be seen in Table 4.2. In the model, radiation is turned on and the heat transfer coefficient is determined in both the model and RPA with the Bartz equation. A calibration factor of 0.886 is used on the value of RPA as it was found that it gives a 11.4% higher value (as is shown in Appendix A). Two cases with film coolant mass flow of 5% of the total mass flow ( $\mu = 17\%$ ) and 10% of total mass flow ( $\mu = 34\%$ ) are compared and as a reference the heat fluxes without film cooling are given as well.

Parameter	Symbol	Value	Unit	Comment
Chamber pressure	$P_c$	65	bar	
Oxidiser to fuel ratio	OF	2.4	-	
Total mass flow	$\dot{m}$	21.8	kg/s	
Film mass fraction	$\mu$	17 and 34	%	
Contraction ratio	$\epsilon$	3	-	
Regenerative coolant		Ethanol		
Regenerative coolant mass flow	$\dot{m}_{\text{coolant}}$	6.41	kg/s	Total fuel flow
Wall thickness		0.7	mm	
Wall thermal conductivity	$k$	220	W/mK	
Upstream pressure	$P_0$	100	bar	
Film coolant inlet temperature	$T_0$	298	K	

Table 4.2: The engine properties for the RPA comparison.

The total heat flux for the case when  $\mu$  is 17% and  $\mu$  is 34% can be seen in respectively Figure 4.10 and Figure 4.11. As expected, the liquid length following from RPA is shorter than the film cooling model used in this thesis. For the case when  $\mu$  is 17%, it can be seen that while the liquid film length is overestimated, once the film coolant is gaseous it matches the RPA results better. In the region of the liquid section the maximum error is 350% while in the gaseous part the smallest difference is between 17%, but this increases again up to 86% at the end of the nozzle. For the case when  $\mu$  is 34%, the errors are larger and the differences are between 80% and 340% at the throat.

It is possible to calibrate the model of this thesis by changing the convective heat flux that goes into the liquid film with a calibration factor and by changing the reference entrainment factor  $\Psi_L$  that alters the gaseous behaviour. It was found that for the  $\mu = 17\%$  case the liquid length matched the RPA model by multiplying the heat transfer coefficient by a factor 6. By using a specified  $\Psi_L$  value of 0.003 the gaseous part can be matched. Note that the latter is 10 times lower than the lower value seen in rocket engines as given by [11]. However, also note that the calculated value of  $\Psi_L$  is already under this value anyway with a magnitude of 0.0082. The heat flux of the calibrated model compared to the RPA film cooling model can be seen in Figure 4.12. The differences in heat flux between the models in the majority of the cylindrical section and the throat is below 10%. In the first 0.1 m, the differences are 35% and after the throat the error gradually increases to 107%. The

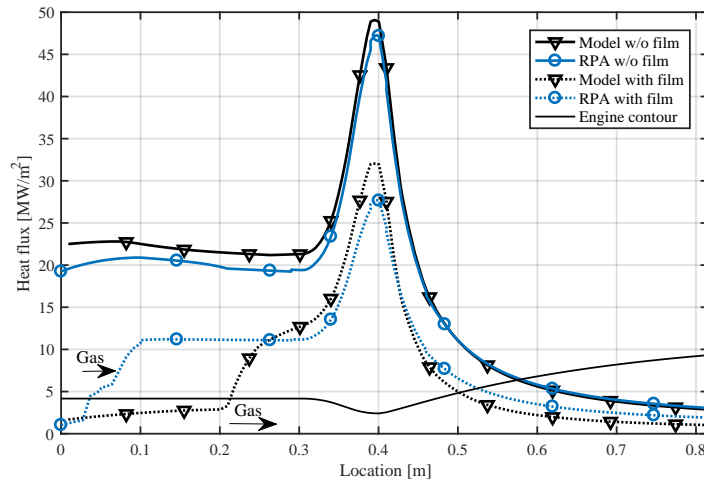


Figure 4.10: The total heat flux of the uncalibrated model compared to the RPA film cooling model for  $\mu=17\%$ , the coolant transitions to gas/supercritical state at the start of the arrows.

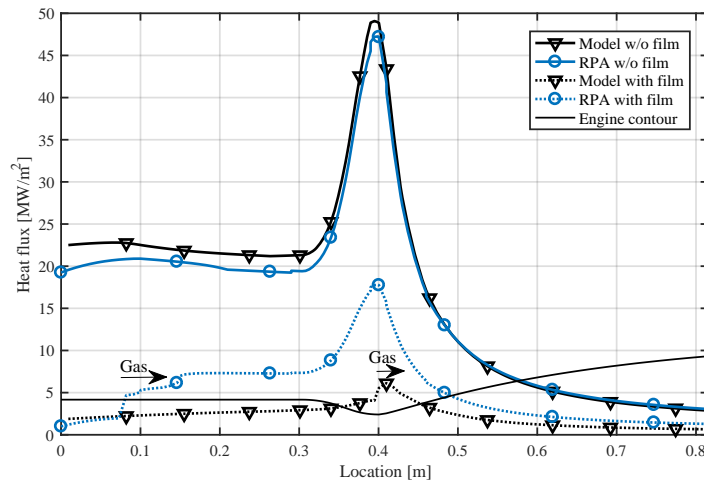


Figure 4.11: The total heat flux of the uncalibrated model compared to the RPA film cooling model for  $\mu=34\%$ , the coolant transitions to gas/supercritical state at the start of the arrows.

latter is caused by the fact that the heat fluxes reduce to small numbers, so any error has a larger influence. The absolute difference stays almost the same. In the regions of the most importance (the cylindrical part and throat), the difference is below 10%.

To test if the same calibration factors also work on a different mass flow, they are used for the case when  $\mu=34\%$ . These results can be seen in Figure 4.13. The match between the models is less good at the end of cylindrical section and the throat. The error peaks at 33% in the first 0.1 m and then reduces to 24 %. Afterwards, the difference increases again gradually to 68%, but this is mainly caused by the fact that total heat flux drops.

**Conclusions** While the developed film cooling model was validated using test data and a good match was achieved (subsection 4.3.1), an additional comparison was made to another film cooling model. The film cooling model of Rocket Propulsion Analysis (RPA) shows greatly different results, especially for the liquid length that is much shorter in RPA. The heat transfer to the liquid in the developed model had to be multiplied with a factor of 6 to achieve similar lengths as RPA. It should be noted that the RPA model is not validated with test data and in the documentation no validation is provided either. Comparing it to Höglauer data will be worthless as it is clear the results will be vastly different. So, while the RPA model is not validated, it will

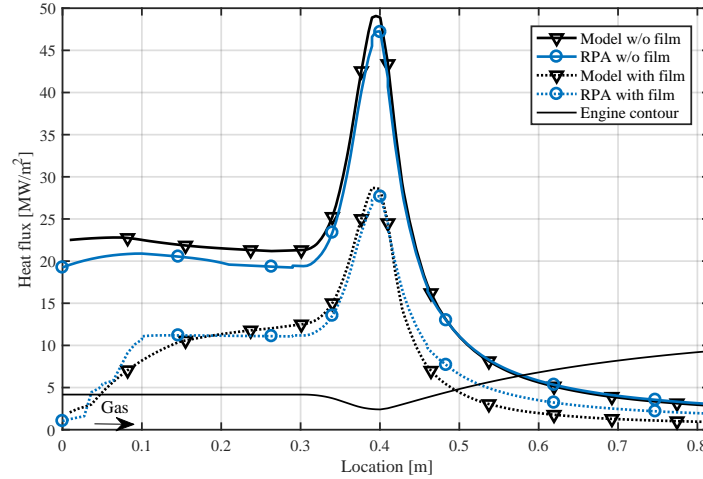


Figure 4.12: The total heat flux of the calibrated model compared to the RPA film cooling model for  $\mu=17\%$  with a calibration factor for heat transfer coefficient of 6 and specified  $\Psi_L$  of 0.003, the coolant transitions to gas/supercritical state at the start of the arrows.

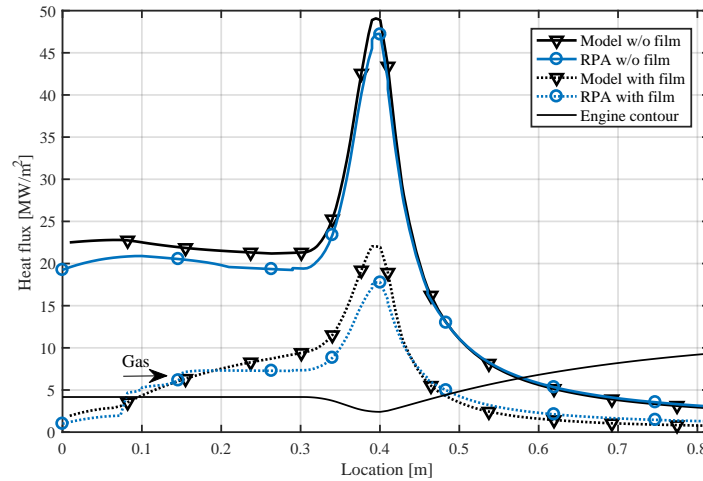


Figure 4.13: The total heat flux of the calibrated model compared to the RPA film cooling model for  $\mu=34\%$  with a calibration factor for heat transfer coefficient of 6 and specified  $\Psi_L$  of 0.003, the coolant transitions to gas/supercritical state at the start of the arrows.

be used alongside the developed model to provide a 'sensitivity' to the film cooling performance. This is required as indications exist that the developed model - even though it matches with the scarcely available test data - overestimates the liquid length [7].

The way the RPA results will be used, is by using the found calibration. So, the heat transfer to the liquid is increased with a factor of 6 and the reference entrainment ratio of 0.003 will be used. This model will be referred to the 'RPA calibrated' model. The uncalibrated model that matches the Höglauer data will be referred to as the 'uncalibrated' model.

#### 4.4. Film cooling results

Now that the film cooling model has been developed and validated, the required film coolant mass flow to keep the temperature below the wall limit in the engine can be determined. Two different version of the film cooling model were presented. The 'uncalibrated' model does not use any calibration and matches the Höglauer test data in liquid film length. The heat flux in the gaseous part is underestimated between 6% and 12%. The other version of the model is the 'RPA calibrated' model and was calibrated using the Rocket

Propulsion Analysis (RPA) film cooling model. This model has a difference between 10% and 35% with RPA depending on the location on the engine. The uncalibrated model predicts the lowest heat fluxes and the RPA calibrated one higher ones. Therefore, the latter will predict more conservative film coolant mass flows.

For Inconel, the maximum temperature was determined to be 923 K. For copper, the limit is 723 K, see Table 1.3. For both materials, the film coolant mass flow was iterated until a value was reached that caused the temperature in the engine to be lower than the respective allowable maximum. The required coolant is expressed as percentage of the total mass flow to later easily compare it to the transpiration cooling performance. The results can be seen in Table 4.3. Note that these values are obtained with a 1D heat transfer analysis and that in the throat this over predicts the temperature. This is the location of the highest temperatures as can be seen in Figure 4.14 and Figure 4.15. Some small peaks are above the temperature limit as it was difficult to get these below the limit, In reality, heat transfer in the axial direction occurs and thus the required film coolant will be lower and these peaks will smooth out. Furthermore, the coolant channel geometry was designed for an Inconel wall, but the same geometry is used to determine the behaviour of the copper chamber. However, when using a copper chamber, the most optimum channel geometry will likely be different. This is likely also the reason why the copper temperature shows some local minima at the throat.

In the table it can be seen that for the Inconel engine, the coolant total mass flow varies between 7.1% for the uncalibrated model and 14.5% for the RPA calibrated model. In the latter case, this would mean that 49% of the fuel is injected as film coolant. For the copper engine the percentage of total coolant varies between 5.0% and 6.0%.

It follows from these results that an Inconel engine requires more film coolant compared to a copper one, even though the allowed wall temperature is 200 degrees higher. This was expected as Inconel has a lower thermal conductivity. Secondly, the spread of the results between the two calibrations is different for both materials. The copper mass flow only varies 1% between the two calibrations, while for Inconel the difference is 7.4%.

Material	Calibration	Film coolant percentage [%]
Inconel	Uncalibrated	7.1
Inconel	RPA calibrated	14.5
Copper	Uncalibrated	5.0
Copper	RPA calibrated	6.0

Table 4.3: The percentage of film coolant compared to the total mass flow required to keep the maximum wall temperature in the whole engine below the set limits for Inconel and copper.

## 4.5. Conclusions

As no film cooling model was found in literature that can model transcritical coolants, a new film cooling model was developed. This model combines the NASA Annex B model [11], the transcritical liquid film behaviour as described in Höglauer [10] and the transpiration cooling effects of Shine's model [52]. Comparing the model to tests with a supercritical kerosene film cooled rocket engine shows that the behaviour is predicted well, especially the liquid film length. However, differences in magnitude of predicted heat fluxes occurred. In the end two different calibrated version of the model are presented. The 'uncalibrated' model predicts the heat flux within 6% to 12% compared to the tests. The 'RPA calibrated' model gives a higher heat flux and differs to the film cooling model of Rocket Propulsion Analysis by 10% to 35%. Furthermore, this calibration showed that if the right reference entrainment ratio is known, that the match for the gaseous behaviour can be quite precise.

The model was used to predict the film coolant required to cool the reference engine. For Inconel this varied between 7.1% and 14.5% of the total mass flow depending on the calibration used. For copper this was 5.0% or 6.0%. Assuming the worst case mass flows, this shows that Inconel needs 2.4 times more film coolant than

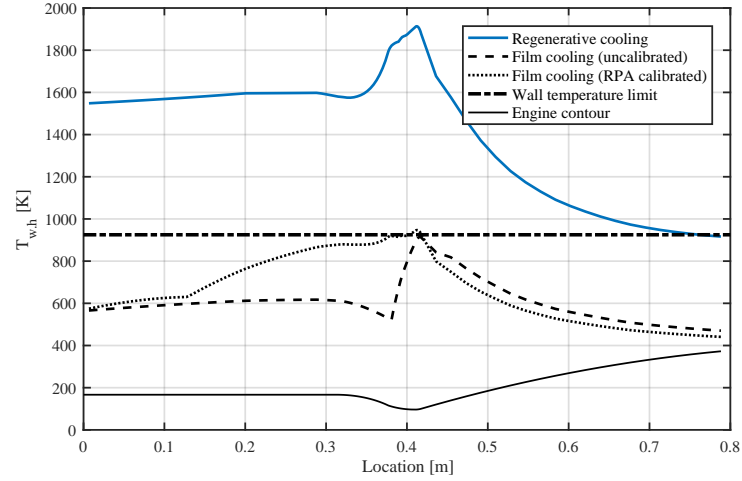


Figure 4.14: The wall temperature on the hot side of the inner wall for the Inconel chamber for regenerative cooling and film cooling.

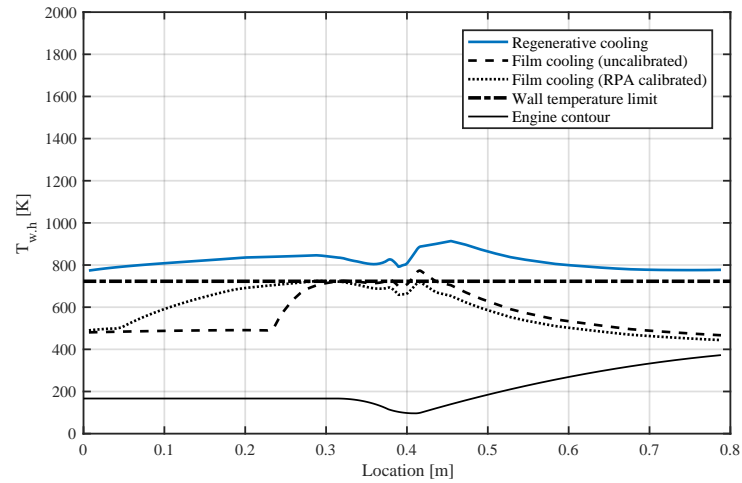


Figure 4.15: The wall temperature on the hot side of the inner wall for the copper chamber for regenerative cooling and film cooling.

the copper chamber. This will lower the specific impulse of the engine. A full comparison between specific impulse of the different cooling methods and different chamber materials will be given in the next chapter.

The two versions of the film cooling model show large differences in heat flux and thus in required film coolant to keep the wall temperature below the limit. This difference is especially large for the Inconel engine, where twice the coolant is required for the RPA calibrated version. This means that the uncertainty in the film cooling model will introduce a large uncertainty in the final cooling analysis. It is difficult to determine which model is more correct, due to the limited available test data. While the uncalibrated version matches with some test data, a single match with data does not create a lot of confidence in the model. Therefore, it is recommended to find additional validation data or, ideally, perform tests with the film cooled reference engine and measure the heat flux.



# 5

## Comparison cooling techniques

In chapter 2 to chapter 4 the regenerative, transpiration and film cooling model have been described and been validated. Now, these models can be used to perform a comparison between all cooling methods which is applied to the reference engine, which was introduced in section 1.3. This comparison is treated in this chapter. In section 5.1 the required coolant mass flow and the effect on the temperature and temperature gradients are investigated. Then with these coolant mass flows, an estimation of the losses in specific impulse of the engine is determined in section 5.2. The transpiration cooled engines require a thicker wall and are thus heavier than the film cooled option. The dry mass differences caused by this are determined in section 5.3. It was found that transpiration cooled engines have a better specific impulse but higher dry mass than a film cooled option. Therefore, in section 5.4 a final comparison on the achieved  $\Delta v$  is performed.

### 5.1. Wall temperature comparison

The comparison of the three cooling techniques is performed only for the cylindrical section of the engine. The reason for this is threefold. Firstly, as the coolant is close to the critical point, it takes very long for the solution to converge due to the spike in isobaric specific heat. Assuming that the cylindrical section has constant properties allows for faster modelling of a large part of the engine. Secondly, the critical point of the ethanol used is 62.7 bar. This is very close to the chamber pressure, but in the cylindrical section the coolant is still supercritical. When the chamber pressure drops in the throat and beyond, the coolant will have a liquid to gas transition and would require two-phase flow modelling. While transpiration cooling models exist that can do this, this requires much more computational effort [39, 40]. Lastly, the cylindrical form of the energy equations is used. This allows for the effect of modelling the temperature distribution in cylindrical walls. However, at the convergent and divergent sections the coolant flow is normal to the wall, while the equations model the temperature in 'pure' radial direction. This means that the 1D heat transfer and the coolant flow do not line up anymore.

The engine properties, engine contours and specifications for the regenerative cooled engine were given in section 1.3. The shape and combustion gas properties do not change for the transpiration and film cooled engine. The configuration of the transpiration cooled engine can be seen in Figure 5.1a. The coolant flows through the inlet into a manifold that distributes the coolant uniformly over the porous wall. As a result, it is assumed that the coolant in the manifold flows very slowly and the boundary conditions that were described in chapter 3 are valid. In this analysis, the results are plotted as a function of coolant mass flow. For the transpiration cooled engine, this mass flow is regulated by changing the wall thickness. The temperature was evaluated for a pore size of 0.05 mm and 0.1 mm, but when plotted as function of mass flow, the results are the same. The wall thickness is not important for the analysis discussed here, but will be used in section 5.3. The nozzle is not cooled as the primary consideration of this analysis is the cylindrical section. It is clear that if one wants to design an actual transpiration cooled engine, that the nozzle also needs to be cooled. Various options exist for this: it can either be transpiration cooled too or this part can be regeneratively cooled and then the injected transpiration coolant at the cylindrical part acts as film coolant in the nozzle.

The film cooling configuration can be seen in Figure 5.1b. The film cooled configuration is exactly the same as the regenerative cooled engine (described in section 1.3), except that additional coolant is injected at the injector. The coolant is injected at the end of the nozzle and then flows towards the injector. There, part of the coolant is then injected as film coolant. So, while the wall temperature is only evaluated at the cylindrical part (indicated by the box), the nozzle is also modelled. The reason for this is that the coolant heats up in the channels and this alters the injection conditions (temperature and pressure) of the film coolant. Lastly, the regeneratively cooled engine is also completely modelled, but only the results of the cylindrical section are used.

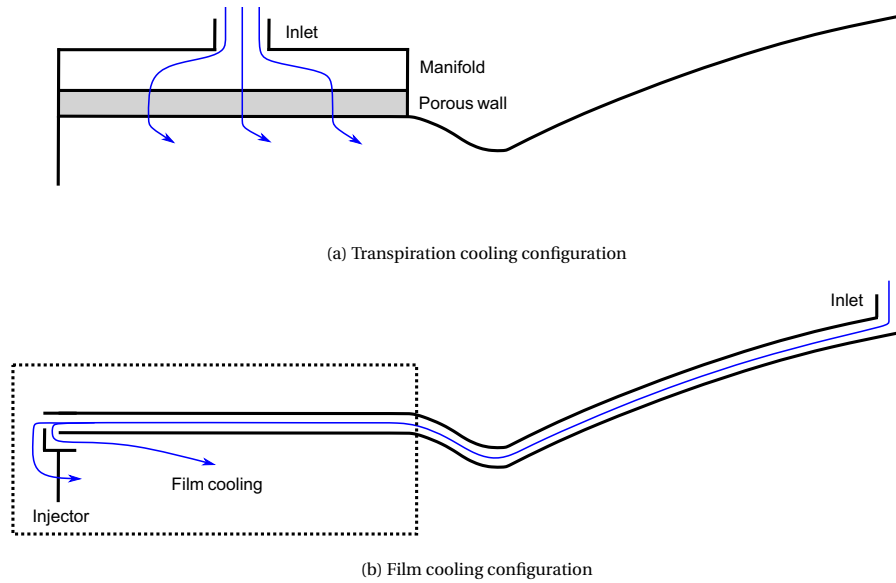


Figure 5.1: The configuration for the transpiration cooled section and the coolant flow (a) and for the film cooled engine (b).

Commonly, transpiration cooling performance is expressed as a function of blowing ratio  $F$  and film cooling as a function of film cooling fraction  $\mu$ . To allow for a comparison between the cooling methods, a common parameter is required. Therefore, the cooling performance will be expressed as the percentage of injected coolant required compared to the total mass flow in the chamber (so fuel and oxidizer combined).

The results for the maximum wall temperature for the Inconel chamber can be seen in Figure 5.2. The used transpiration cooling data is for a porosity of 0.2 and pore size of 0.05 mm. However, as seen in chapter 3, the porosity and pore size will not affect the results much when plotted as a function of mass flux.

The result for the regeneratively cooled chamber shows a maximum temperature of 1600 K. Clearly, the reference engine requires more than only regenerative cooling to be operational. In the figure, two lines for film cooling are plotted: one for the uncalibrated model and one for the RPA calibrated one. The uncalibrated film cooling model shows a constant temperature of around 600 K from a cooling percentage of 6% and higher. From this point onward, the coolant stays liquid in the complete cylindrical part and thus the maximum wall temperature attains an almost constant value of 600 K due to the radiation. The transpiration cooling results are given by the blue line.

When comparing film and transpiration cooling, it can be seen that the transpiration cooling will yield lower wall temperature for the same coolant mass flow. Taking the goal of the wall temperature to be 923 K, transpiration cooling only requires around 2.5% cooling while the film cooling requires 5.4% or even 12.9% depending on which calibration for the film cooling model is used. All results can be seen in Table 5.1, also for the copper chamber discussed below.

In Figure 5.3 the maximum temperature gradients are plotted for the three cooling methods for the Inconel

engine. It shows that the regenerative cooling has the highest temperature gradient. Furthermore, the gradients from the film cooling and transpiration cooling are in the same order for the mass flux. However, the film cooling requires a larger mass flux to keep the wall temperature below the limit. Thus, in this situation the gradients will be lower. Taking this into account, the gradients for the transpiration cooled wall will be two times higher.

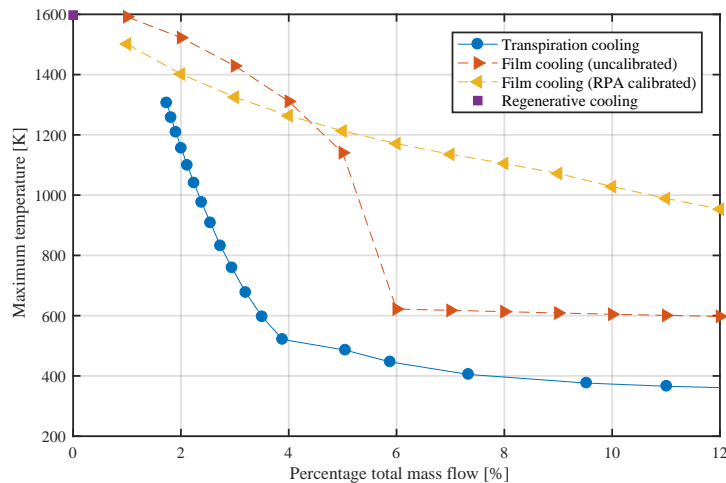


Figure 5.2: The maximum wall temperature versus the percentage injected coolant of the total mass flow for transpiration, film and regenerative cooling for Inconel; pore size 0.05 mm and porosity of 0.2.

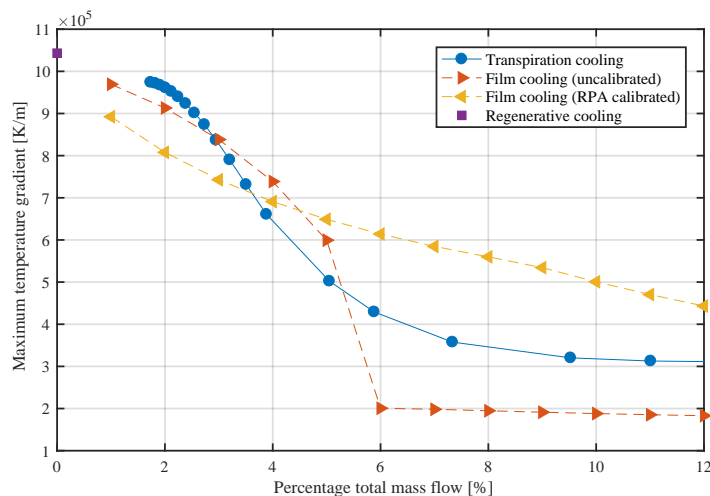


Figure 5.3: The maximum wall temperature gradient versus the percentage injected coolant of the total mass flow for transpiration, film and regenerative cooling for Inconel; transpiration cooling pore size 0.05 mm and porosity of 0.2.

The above results were for the Inconel engine. The maximum temperature and maximum temperature gradient for the copper chamber can be seen in respectively Figure 5.4 and Figure 5.5. Again, the regeneratively cooled case has a high temperature. However, the effect of the higher thermal conductivity is clear: the maximum temperature is only 846 K instead of the 1600 K for Inconel.

For transpiration and film cooling, the same behaviour as for the Inconel chamber can be seen. The transpiration cooled engines generally require a lot less coolant than the film cooling ones. In the copper case, for the maximum copper temperature of 723 K, the transpiration cooling needs 2.9% coolant mass flow and the film cooling requires 5.0% to 6.1% depending on the film cooling model used. With regards to the maximum

gradient, some differences appear with respect to the Inconel case. For copper, the transpiration cooling gradients are generally lower than for the film cooling ones, while for the Inconel case they were equal. Again considering that at the maximum temperature the coolant mass flows will be different: in the copper case the gradients will then be equal.

Another observation can be made in the temperature results of both the Inconel and copper chamber. The temperature steadily increases when the coolant mass flow is reduced, but at a temperature of around 520 K the increase levels out for a short temperature range. This effect is present in both plots, but much more clear in the one for copper. This point coincides with the critical point of the ethanol coolant. At this point, a large peak in specific heat occurs. So, it is possible that this increases the cooling effectiveness around this temperature and that this causes a plateau in temperature. However, it must be noted that around the critical point, convergence of the solution is difficult and the convergence criteria had to be relaxed slightly, so it could also be an artifact of this.

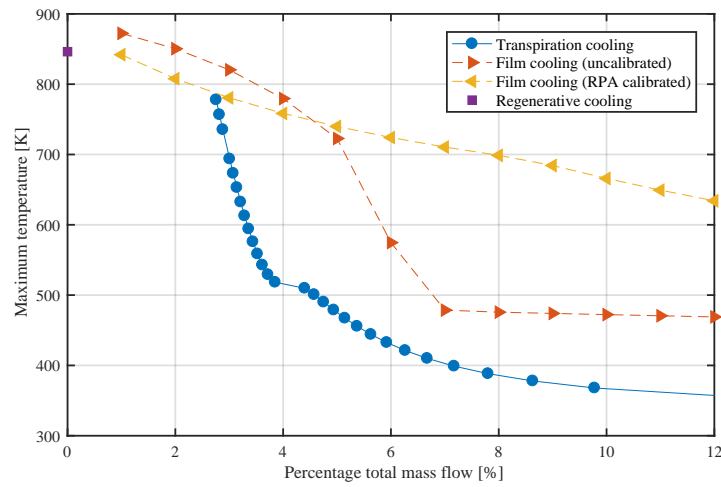


Figure 5.4: The maximum wall temperature versus the percentage injected coolant of the total mass flow for transpiration, film and regenerative cooling for copper; pore size 0.05 mm and porosity of 0.2.

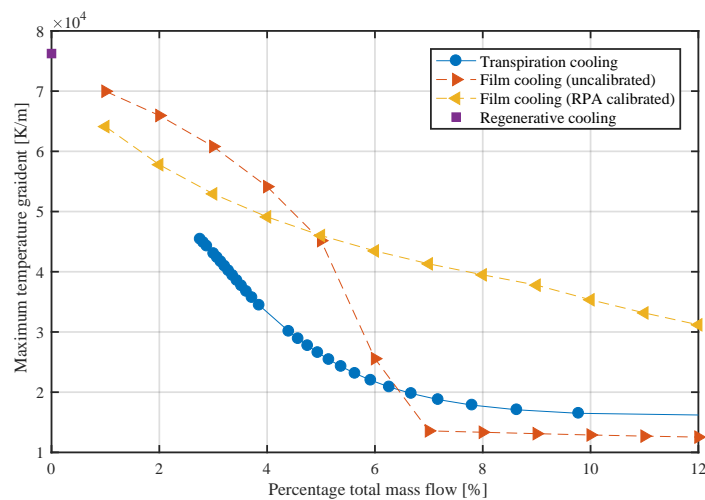


Figure 5.5: The maximum wall temperature gradient versus the percentage injected coolant of the total mass flow for transpiration, film and regenerative cooling for copper; transpiration cooling pore size 0.05 mm and porosity of 0.2.

Cooling method	Comment	Material	Coolant required [%]
Transpiration		Inconel	2.5
Film	Uncalibrated	Inconel	5.4
Film	RPA calibrated	Inconel	12.9
Transpiration		Copper	3.0
Film	Uncalibrated	Copper	5.0
Film	RPA calibrated	Copper	6.1

Table 5.1: The coolant required as percentage of the total mass flow in the engine to keep the wall temperatures to the maximum allowable temperature.

## 5.2. Specific impulse losses

The fuel is used as film or transpiration coolant and this creates a fuel rich zone next to the wall. This changes the OF ratio in this region. This will result in a different, and in most cases, a lower flame temperature. In the end, this will result in a lower specific impulse of the complete engine [23]. So, this means that for the reference engine, the regeneratively cooled engine has the optimum specific impulse as no coolant is injected. Of course, this engine option is not feasible as the maximum temperatures of the materials are exceeded. It was determined that the transpiration cooled engine requires less coolant than the film cooled option. The next question that arises is: what will be the difference in specific impulse for these options?

The reduction in specific impulse can be modelled by assuming that two different gas layers in the rocket exist that do not mix. The OF ratios of these layers would result in a different specific impulse in case the whole engine is modelled with the OF ratio of the individual layer. The resulting total specific impulse can then be found by taking the mass flow average of these two flows, see Equation 5.1 [22, 23]. The overall OF ratio of the engine will remain 2.4. So, the amount of coolant (the fuel) injected changes not only the OF of the layer next to the wall, but also the OF ratio of the core stream.

$$I_{sp_{tot}} = \frac{\dot{m}_{wall}}{\dot{m}_{tot}} I_{sp_{wall}} + \frac{\dot{m}_{core}}{\dot{m}_{tot}} I_{sp_{core}} \quad (5.1)$$

A problem with this method is that the exact OF ratio in the wall layer is not known. This can be determined using experimental methods or CFD modelling [23], but that is out of the scope of this thesis. Therefore, the differences in specific impulse are given for a range of wall zone OF ratios from 0.01 to 2.4. The specific impulses for different OF ratios are taken from NASA's CEA [13]. The values used are for the vacuum specific impulse.

Another problem that occurs is that ethanol has a lower optimal OF ratio (1.75 vs 2.60 of RP-1 with LOX), see Figure 5.6. So, when ethanol is used to calculate the specific impulse in the wall zone, the OF ratio will actually be closer to optimal. Thus, injecting more coolant actually increases the performance. This phenomenon is definitely not realistic. Taking this into account, it is decided to determine the specific impulse for an RP-1 and LOX reaction, but the coolant mass flows used are those obtained with ethanol as coolant. So, while the actual values in specific impulse might not be realistic, this analysis will still give a comparison between film and transpiration cooling. Still, in the results plots presented below, both the results for RP-1 and ethanol are given.

The specific impulses are determined for the coolant flows from Table 5.1. The vacuum specific impulses as function of wall zone OF ratio for the Inconel and copper chamber can be seen respectively in Figure 5.7 and Figure 5.8. It can be seen that if the specific impulse of ethanol is used that the  $I_{sp}$  actually increases when the OF ratio reduces from the overall ratio of 2.4.

For the most extreme case, which is the lowest OF ratio, the differences between the cooling methods can be seen in Table 5.2. The differences are given with respect to the regenerative cooling case when no coolant is injected. This case thus has the most optimal specific impulse which is 335.1 s.

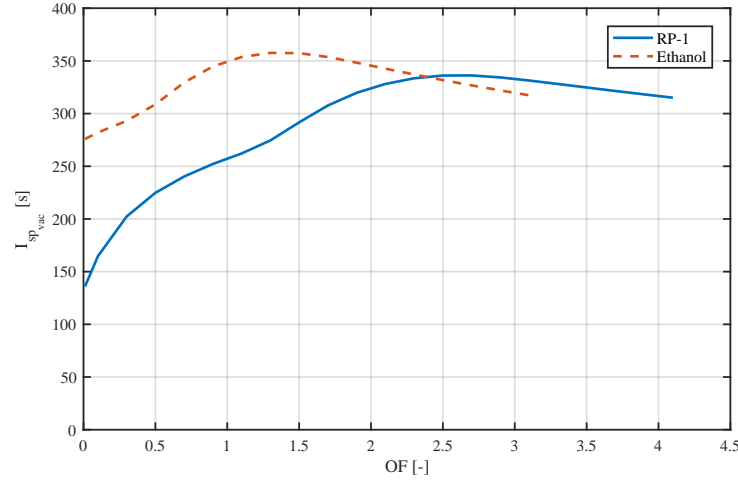


Figure 5.6: The vacuum specific impulse for RP-1 and ethanol combustion with liquid oxygen for a chamber pressure of 65 bar, obtained using NASA's CEA [13]; this shows the combustion without reductions due to the introduction of coolant in the chamber.

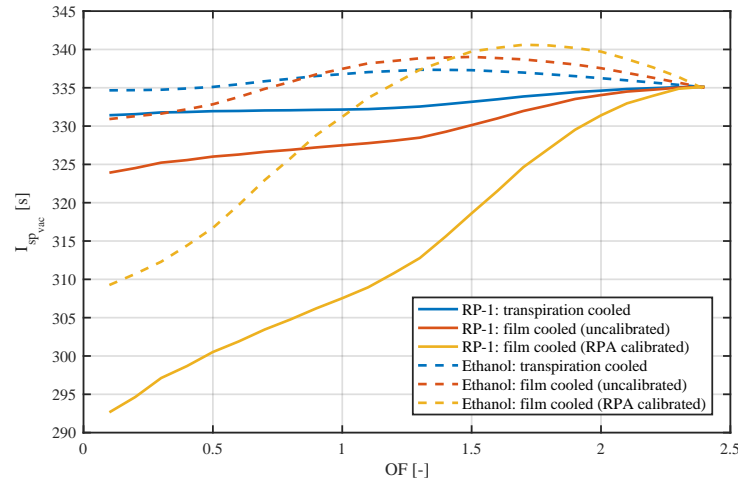


Figure 5.7: The vacuum specific impulse given for different wall region OF ratios; for the different cooling methods and for the different OF ratios for the Inconel engine.

It was determined that the RPA calibrated film cooling model for the Inconel engine requires 5.2 times more coolant than the transpiration cooled engine. This will result in a reduction in  $I_{sp}$  to 292.6 s. At the same OF ratio, the transpiration cooled engine has an  $I_{sp}$  of 331.4 s. So, this is a difference of 38.8 s which is a difference of 13.3%. For the uncalibrated film cooled engine, the differences are less pronounced. This case has an  $I_{sp}$  of 323.9 s which is a difference of 7.5 s (2.32 %).

For the copper engine, the effects are less pronounced as the differences in coolant mass flows are smaller. The RPA calibrated film cooling model gives an  $I_{sp}$  of 321.6 s and the transpiration cooled case one of 330.7 s. This is a difference of 9.1 s (2.83%). The uncalibrated film cooled  $I_{sp}$  is 325.2 s which results in a difference to the transpiration case of 5.5 s (1.69%).

The above results compared transpiration and film cooling to the regeneratively cooled engine. While this gives the most optimal specific impulse, an engine with solely regenerative cooling will not be feasible as the wall temperature is too high. By lowering the chamber pressure and/or the OF ratio, the heat transfer in the engine can be reduced. It is analysed how much the chamber pressure and OF ratio have to change to make a regeneratively cooled engine feasible. Lowering the chamber pressure and changing the OF ratio will also

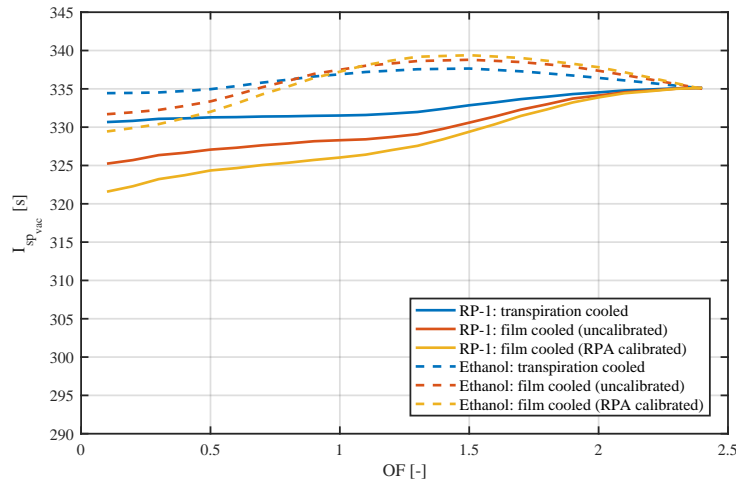


Figure 5.8: The vacuum specific impulse given for different wall region OF ratios; for the different cooling methods and for the different OF ratios for the copper engine.

change the specific impulse. To keep it a fair comparison, only the temperature in the cylindrical section is looked at. In the nominal case, the pressure at the end of the channel is 10 bar higher than the chamber pressure. So, a minimum difference of 10 bar between the pressure at the end of the cooling channel and the chamber pressure is set as a requirement.

For the Inconel chamber, it was impossible to find a chamber pressure and OF ratio combination that allowed for only regenerative cooling. The wall temperature becomes lower, but not low enough.

For the nominal pressure of 65 bar, the copper chamber needs an OF ratio of 1.55 and this results in a total mass flow to keep the chamber pressure of 23.9 kg/s. No changes were made to the coolant channel geometry. The specific impulse of this option is 295.8 s which is 11.7% lower than the regenerative case with 65 bar. For the copper engine, this is a larger decrease than the film and transpiration cooling. So, changing the OF ratio to make use of a regenerative cooled engine is not worth it. The other option is to keep the OF ratio the same, but to lower the chamber pressure. As less fuel is required, the velocity in the coolant channels becomes lower and this reduces the heat transfer. Therefore, the height of the coolant channels is also changed by a constant ratio along the complete length. The width of the channels and the number of channels remains constant. A suitable case has a chamber pressure of 35 bar and a total mass flow of 12.0 kg/s and the height of the channels is divided by 1.7. This option has an  $I_{sp}$  of 334.1 s which is only 0.3% lower than the nominal regenerative case. However, as the mass flow of the engine is 45% lower, the final thrust will also be 45% lower assuming that the thrust coefficient remains constant. This means that almost twice the number of engines is required to obtain the same thrust level.

Cooling method	Comment	Inconel $I_{sp_{vac}}$ [s]	Difference [%]	Copper $I_{sp_{vac}}$ [s]	Difference [%]
Regenerative		335.1	-	335.1	-
Transpiration		331.4	-1.10	330.7	-1.31
Film	Uncalibrated	323.9	-3.34	325.2	-2.95
Film	RPA calibrated	292.6	-12.7	321.6	-4.03
Regenerative	Lower OF	n/a	n/a	295.8	-11.7
Regenerative	Lower $P_c$	n/a	n/a	334.1	-0.3

Table 5.2: The vacuum specific impulses for the case when RP-1 is used as coolant for the lowest wall OF ratio as given in Figure 5.7 and Figure 5.8.

From these results, it is concluded that transpiration cooling will give a better specific impulse. Furthermore, similar to the temperature results, the differences between  $I_{sp}$  for the different cooling methods are more

pronounced for an Inconel engine than for a copper one. However, this depends on which calibration is used for the film cooling model. If the uncalibrated model is used, the differences are very small between copper and Inconel.

### 5.3. Engine dry mass

It was determined in the previous section that the transpiration cooled engines will have a higher specific impulse than the film cooled ones. However, this comes at the cost of a higher engine dry mass. A thicker wall is required to achieve the lower coolant mass flow for the pressure drop over the wall. An estimation of this dry mass increase is given in this section, both for an Inconel and copper chamber. Again, this only focuses on the cylindrical section of the engine.

The determination of the mass of the regeneratively and film cooled engine are discussed first. The film cooled engine differs from the regeneratively cooled one only by the introduction of holes required for injection of the film coolant. So, the mass of both is seen as the same. The cylindrical section of regeneratively and film cooled engine consist of three separate sections that all have a different mass, see Figure 5.9. The geometry is given by the design of the reference engine and is listed below:

1. The inner wall with a thickness of 0.7 mm.
2. The cooling channels with a height of 3 mm and rib thickness of 2.54 mm. The number of cooling channels is 70.
3. A close-out or shell on the outside that seals the channels. This thickness needs to be determined still and the method is given below.

The thickness of the close-out still needs to be determined. As the engine is designed to be produced using additive manufacturing, it is assumed that the close-out is made from the same material as the rest of the wall. The thickness of the close-out can be calculated using the hoop stress of a cylinder, see Equation 5.2. The yield stresses of the materials are used, which can be seen in Table 5.3. A safety factor on the pressure of 1.25 is used. The pressure used for the regenerative cooled engine is 100 bar which equals the pump outlet pressure.

$$\sigma = \frac{Pr}{t} \quad (5.2)$$

The transpiration cooled wall consists of three sections, see Figure 5.10, and they are described below:

1. The porous wall: the thickness and porosity follow from the calculations performed.
2. A manifold between the porous wall and the close-out to ensure uniform coolant distribution. The assumed height of this space is taken as 3 mm. In practice, some ribs will be required for strength or a porous layer with a lower porosity can be printed here.
3. A close-out on the outside that seals the porous layers. Again a safety factor of 1.25 is used. However, now the pressure used is only 66 bar as this is the manifold pressure. This means that a valve causes a pressure drop between the pump outlet and manifold, see Figure 3.40.

Material	Yield stress [MPa]	Density [kg/m <sup>3</sup> ]	Source
Inconel	1200	8200	[41]
Copper alloy	500	8840	RFA

Table 5.3: The yield stresses and densities for the materials used in the mass calculations, all properties are for additive manufacturing variants.

The results for the transpiration cooled engines can be seen in Table 5.4 for the two cases: one with a pore size of 0.05 mm and one with 0.1 mm. In Table 5.5 the masses for the film and regeneratively cooled engine



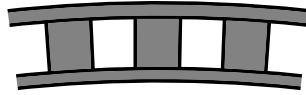


Figure 5.9: A representation of the regeneratively cooled wall.

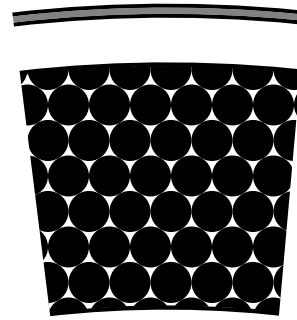


Figure 5.10: A representation of the transpiration cooled wall

can be seen. It shows that the cylindrical part of the chamber for the regeneratively and film cooled engine have a mass of 3.34 kg and 5.27 kg for Inconel and copper respectively. The most optimal masses for the transpiration cooled engine occur for the pore size of 0.05 mm. In this case, the masses are 15.2 kg and 45.6 kg for Inconel and copper respectively. These masses are respectively 4.6 and 8.7 times higher than for the film cooled engine. For the pore size of 0.1 mm the masses for the transpiration cooling become 78.8 kg and 167.8 kg, which is 23.6 and 31.8 times higher respectively.

In Table 5.5 it can also be observed that the wall thicknesses of the copper walls are higher than for the Inconel ones when the same pore size is used. This has two reasons: firstly, the required coolant mass flow for copper is lower, so a thicker wall is required to achieve this. Secondly, it was seen in subsection 3.5.5, that for the same mass flow, the copper wall is thicker than the Inconel one.

Cooling method	Material	Film coolant [%]	Inner wall thickness [mm]	Inner wall mass [kg]	Close-out mass [kg]	Total mass [kg]
Regen & film	Inconel	5.4 to 12.9	0.7	2.25	1.09	3.34
Regen & film	Copper	5.0 to 6.1	0.7	2.42	2.84	5.27

Table 5.4: The masses of the cylindrical part of the regenerative and film cooled engine for different materials.

Cooling method	Material	Pore size [mm]	Trans. coolant [%]	Porous wall thickness [mm]	Porous wall mass [kg]	Close-out mass [kg]	Total mass [kg]
Transpiration	Inconel	0.05	2.5	13.2	14.2	1.0	15.2
Transpiration	Inconel	0.1	2.5	56.5	76.7	2.1	78.8
Transpiration	Copper	0.05	2.9	32.4	42.0	3.6	45.6
Transpiration	Copper	0.1	3.0	92.7	159.2	8.6	167.8

Table 5.5: The masses of the cylindrical part of the transpiration cooled engine to achieve the maximum allowable wall temperature.

The above relative mass increases are large, especially for the pore size of 0.1 mm. However, it is only describing the mass of the cylindrical section of the chamber and not the total engine mass. The latter will also include other parts such as the injector and the turbo pumps. So, it would be interesting to have an estimation of how much the total engine mass increases. The exact masses of all these parts are not available for the reference engine. Therefore, work from Zandbergen [15] will be used to make an estimation on how much the total mass of the engine will increase. Zandbergen developed mass estimation relationships for pump-fed liquid rocket engines with thrust levels between 15 kN to 8 MN.

For kerosene and LOX engines, two different mass estimation relationships are given in [15]. The most extensive one is used here which depends on thrust level, number of thrust chambers (one in this case) and the expansion ratio. This equation had a fit of  $R^2$  of 0.987 and can be seen in Equation 5.3. The  $R_2$  is given by Equation 5.4 where  $y_i$  are the measured variables,  $\hat{y}_i$  is value estimated from the regression and  $\bar{y}_i$  is the mean value of data points. Using the thrust of the reference engine of 68 kN and an expansion ratio of 15, an engine mass of 126.8 kg is obtained.

$$m = (1.079 \cdot 10^{-3} \cdot F + 53.0165) \cdot 1^{0.0369} \cdot \epsilon^{-0.00184} \quad (5.3)$$

$$R^2 = 1 - \frac{\sum_{i=1}^n (\hat{y}_i - \bar{y}_i)^2}{\sum_{i=1}^n (y_i - \bar{y}_i)^2} \quad (5.4)$$

To make an estimation of the total dry mass increase, it is assumed that the increase in cylindrical section mass is the only increase. This is the most optimistic scenario for the transpiration cooled engine. Then the mass increase for the Inconel engine with a pore size of 0.05 mm (the most optimum case) is 9.4%. The worst increase is for the copper chamber with a pore size of 0.1 mm and equals of 128%. All increases can be seen in Table 5.6. Note that the dry mass of the Inconel and copper regenerative and film cooled engine are the same. This is caused by the fact that the dry mass correlation from Zandbergen does not account for differences in material. For the delta-v calculation that follows, only the mass differences are used. The results show once again the importance of the small pore size to achieve a thin wall. Furthermore, it also shows again that transpiration cooling yields better result for the Inconel chamber compared to the copper one.

Material	Cooling method	Pore size [mm]	Mass [kg]	Increase [kg]	Increase [%]
Inconel	Film & regen		126.8	-	-
Inconel	Transpiration	0.05	138.66	11.86	9.4
Inconel	Transpiration	0.1	202.26	75.46	59.5
Copper	Film & regen		126.8	-	-
Copper	Transpiration	0.05	167.13	40.33	31.8
Copper	Transpiration	0.1	289.33	162.53	128

Table 5.6: The mass increases compared to a dry mass for the regeneratively and film cooled engine, the regenerative and film cooled mass are determined by the relation from Zandbergen [15] and the mass from Table 5.5 is added to find the transpiration cooled engine mass.

## 5.4. Delta-v budget

It is clear now that transpiration cooled engines have a higher specific impulse than film cooled engines, but they have a higher dry mass. To find out how the engines compare to each other, a delta-v calculation is performed. This combines the changes in specific impulse and mass to make a comparison. The purely regenerative cooled engines are not considered, as these are not feasible.

The velocity increase of the engine is given by the Tsiolkovsky rocket equation which can be seen in Equation 5.5. The inputs required for the delta-v calculation are the specific impulse, which was determined in section 5.2, and the mass fraction. For the latter, the masses of a representative first stage that would utilize the reference engine is used, see Table 5.7. This gives a mass fraction of 3.89 for the nominal case that uses a film cooled engine. As the OF ratio of the wall layer is still unknown, the calculations will be performed for the complete range of OF ratios.

$$\Delta v = 9.81 I_{sp} \ln\left(\frac{m_0}{m_f}\right) \quad (5.5)$$

Parameter	Value	Unit
First stage propellant	41000	kg
Total launcher wet mass	55200	kg
Number of engines	9	-

Table 5.7: The masses and other parameters used for the delta-v calculation.

With the mass fraction of the nominal case known, the delta-v can be determined using the specific impulse of the film cooled engine. Then, for the transpiration cooled engine, the allowed extra dry mass can be calculated to achieve the same delta-v. Finally, the determined mass increases can then be compared to the obtained mass values from section 5.3.

An example calculation is given here for the worst case film cooling that occurs for the RPA calibrated model and the lowest OF ratio. The specific impulse is 292.6 s. This yields a delta-v of 3897.2 m/s for the film cooled engines. The specific impulse of the transpiration cooled engine at the same OF ratio is 331.4 s. This allows for lowering the mass fraction to 3.32 to achieve the same delta-v. This corresponds to an extra allowed dry mass of 3503 kg for the first stage. Divided by the required nine engines, this gives an allowed extra mass per engine of 389.3 kg.

The results for the complete OF ratio range for both calibrations of the film cooling model and the Inconel and copper chamber are presented in Figure 5.11. The markers indicate the OF ratio in the wall zone where the transpiration cooled engine outperforms the film cooled engine. These values are also listed in Table 5.8. When taking the masses from section 5.3 into account, it shows that the most optimal Inconel transpiration cooled chamber (pore size 0.05 mm) starts becoming better than the film cooled engine at an OF ratio 1.77 for the calibrated model and at 2.14 for the RPA calibrated model. While the exact OF ratio in the wall layer remains uncertain, these values appear to be achievable. No OF ratio exists where the Inconel chamber with a pore size of 0.1 mm is better than the uncalibrated film cooled model. For the RPA calibration, it becomes better at OF of 1.73.

The most optimal copper transpiration cooled chamber (pore size 0.05 mm) becomes viable at an OF ratio of 1.21 or 0.30 depending on the calibration of the film cooling model. The OF ratios are low and it is questionable if these are reached in the engine. For the pore size of 0.1 mm, the transpiration cooled engine always performs worse than the film cooled one.

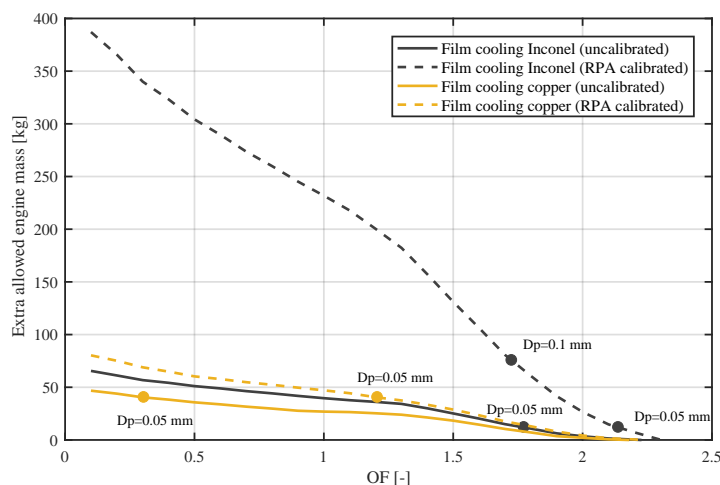


Figure 5.11: The allowed extra engine mass for the Inconel and copper transpiration cooled chamber compared to the different film cooled engines for different film layer OF ratios; the markers indicate the OF ratio where below it the transpiration cooled engines perform better. If no marker is given, the film cooled engine always performs better.

Material	Pore size [mm]	Trans. Coolant [%]	Extra mass [kg]	OF ratio in wall zone [-]	
				Uncalibrated	RPA calibrated
Inconel	0.05	2.5	11.86	< 1.77	< 2.14
Inconel	0.1	2.5	75.46	-	< 1.73
Copper	0.05	2.9	40.33	< 0.30	< 1.21
Copper	0.1	3.00	162.53	-	-

Table 5.8: The OF ratio in the wall zone for which the transpiration cooled engines outperform the film cooled engines with respect to total delta-v achieved.

## 5.5. Conclusions

In this chapter, regenerative, film and transpiration cooling were compared when applied to the reference engine. The results of the wall temperature of a purely regenerative cooled engine show that for both an Inconel and copper engine, the wall temperature is above the allowable maximum temperature. The Inconel wall reached a temperature of 1600 K where 923 K was allowed. The copper wall reached a temperature of 846 K where a maximum of 723 K was allowed.

When comparing transpiration and film cooling, the transpiration cooling resulted in lower temperatures for the same coolant mass flow. The transpiration cooled Inconel engine needs a coolant mass flow compared to the total mass flow of 2.5%, where film cooling requires 5.4% to 12.9% depending on which calibration of the film cooling model is used. For the copper engine the results are closer and especially the spread for the film coolant is smaller. The copper transpiration cooled engine needs 3.0% coolant flow while the film cooling requires 5.0% to 6.1%.

The thermal gradients of the transpiration cooled engines are either equal with mass flow to the film cooled ones for Inconel or smaller for copper. However, as film cooling requires more coolant, the Inconel transpiration cooled engine will have two times higher thermal gradients than the film cooled engine. The gradients for the copper engine will be equal for transpiration and film cooling.

As the transpiration cooled engines required less coolant, the specific impulse is higher. However, the dry mass of these engines will be higher as they require a thicker wall to achieve the required pressure drop. The exact differences are hard to quantify as the OF ratio in the fuel rich wall zone is not known. What is clear is that it is unlikely that the copper transpiration cooled engine will perform better with pore sizes as small as 0.05 mm. For the Inconel engine with pore size of 0.05 mm, the transpiration cooled engine is most likely better. These results can change when smaller pore sizes are used and when the specified pressure drop over the wall is lowered. Then, the transpiration cooled engines will start to perform better.

These results show that transpiration cooling for Inconel engines has more benefits than for copper ones. For the copper film cooled engine, the temperatures are already lower and thus transpiration cooling does not add a lot.

It is clear that the above results in delta-v depend largely on the pressure drop in the wall. A larger pressure drop will cause a thinner wall and thus lower dry mass. The bed of packed spheres used to model the pressure drop is not a shape that would be produced with additive manufacturing. Therefore, in the next chapter the pressure drop of an additive manufactured porous wall is experimentally determined to compare it. Secondly, other geometries are investigated to see if these can cause higher pressure drops.

# 6

## Pressure drop experiments

The preliminary conclusion on the use of additive manufacturing for a transpiration cooled rocket engine is that the pressure drop over the wall is too low due to the fact that the minimal printable pore size is still too large. This requires very thick walls to achieve reasonable mass flows that can compete with film cooling. The above conclusion was based on calculations performed for a bed of packed spheres. For this shape, empirical relations exist that describe the pressure drop. When using additive manufacturing, other shapes can and will likely be used that are better suited for 3D printing. This is investigated by experiments on additively manufactured porous walls with different geometries. Furthermore, a different geometry designed to cause a larger pressure drop is tested.

In section 6.1 the two test goals and their reasoning are discussed. Then, in section 6.2 the test setup, the used sensors and the data acquisition system are presented. Section 6.3 gives a short overview of the followed test procedures. A bed of packed spheres is used to calibrate the test setup and this method is treated in section 6.4. Then, the two test samples are described in section 6.5. The test results of the calibration sample and the test samples are given in section 6.6. Finally, in section 6.8, the conclusions and recommendations are given.

### 6.1. Test goals

A different geometry will alter the pressure drop in the wall. This is illustrated by tests from Moreira et al. who looked into the permeability of cellular structures and found that the permeability deviated between 30% and 480% from known empirical relations [93]. Furthermore, it might also be possible that by using additive manufacturing, different shapes can be used that cause a larger pressure drop – which would be preferable.

Lastly, increased accuracy on the occurring pressure drop leads to a better accuracy of the resulting mass flow. Mass flow in turn is the most important driving mechanism on the cooling performance: mass flow multiplied with isobaric specific heat governs the cooling in the wall and the mass flow dictates the reduction in (convective) heat transfer that reaches the wall. Therefore, the modelling of an additively manufactured wall can benefit from better accuracy of the occurring pressure drop.

The goals of the experiment are as follows:

1. Find out how the pressure drop of additively manufactured porous geometries compares to the commonly used bed of packed spheres.
2. Find geometries that can be manufactured using additive manufacturing that provide higher pressure drops over length.

A small recap of the relevant equations is presented here. In section 3.2, it was discussed that the pressure drop over length in a porous wall follows the Darcy-Forchheimer equation, which is restated in Equation 6.1. The pressure drop is a function of the superficial velocity  $v$ , the viscosity, the density and the permeability

coefficients  $K_D$  and  $K_F$ . In the experiments the mass flow is measured which can be converted into the superficial velocity. Then using the occurring pressure drop, the permeability coefficients for that test sample can be determined.

$$\frac{dP}{dL} = -\frac{\mu}{K_D} v - \frac{\rho}{K_F} v^2 \quad (6.1)$$

## 6.2. Test setup

An overview of the feed system used for the test can be seen in Figure 6.1. The main components are the water tank and the test section. The latter is discussed in detail below. The water tank is pressurized using pressurized air that comes from the pressurized air system in the workshop. It has a maximum pressure of 9 bar and is regulated by a manual pressure regulator. Two pneumatically operated ball valves are used: one to pressurize the tank and one to open and close the water flow into the test section. A coriolis mass flow meter is situated between the tank and the main valve. The pressure sensor is directly connected to the plenum in the test section. Furthermore, the coriolis mass flow meter measures density and temperature of the water.

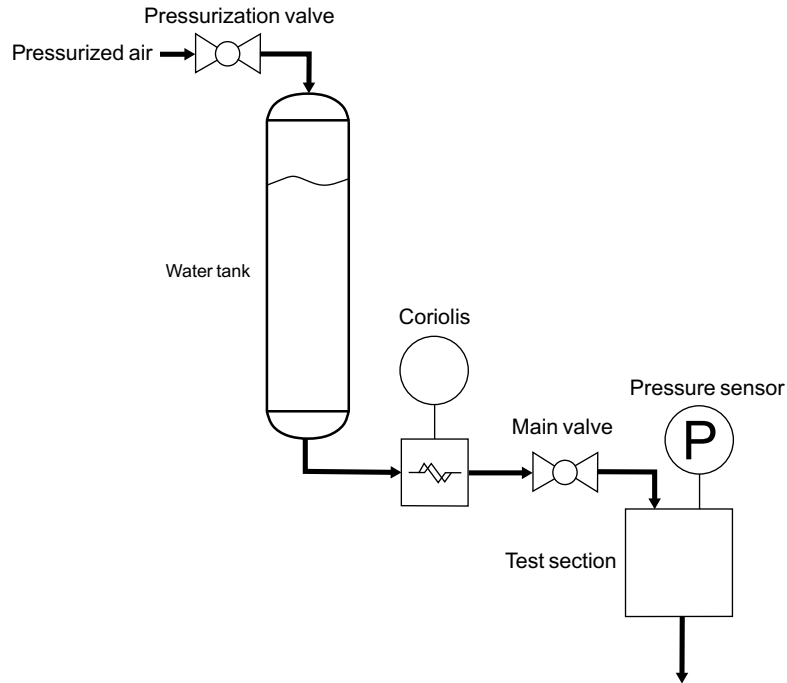


Figure 6.1: The feed system for the test setup.

The test section can be seen in Figure 6.2. It consists of two stainless steel bulkheads welded onto a stainless steel pipe. The plenum fills with pressurized water from the tank and then this flows through the sample. A watertight seal between the sample and the test section is created using an NBR gasket. A mounting location for the pressure sensor is present in the top bulkhead. The sample visible in the figure requires a spacer ring to be able to clamp it in place, but the need for this depends on the exact sample. All test samples 'stick' out into the plenum. This is partly a result of the test section design, but also ensures that the inlet is provided by undisturbed water.

### 6.2.1. Sensor

An *OMEGA PD23-C-10* differential pressure sensor is employed to measure the pressure in the plenum with respect to the ambient pressure. It has a measurement range of 0.2 to 10 bar. The mass flow is measured using a *TRICOR TCM 5500* coriolis mass flow meter. It has a maximum mass flow of 1528 g/s and is rated up

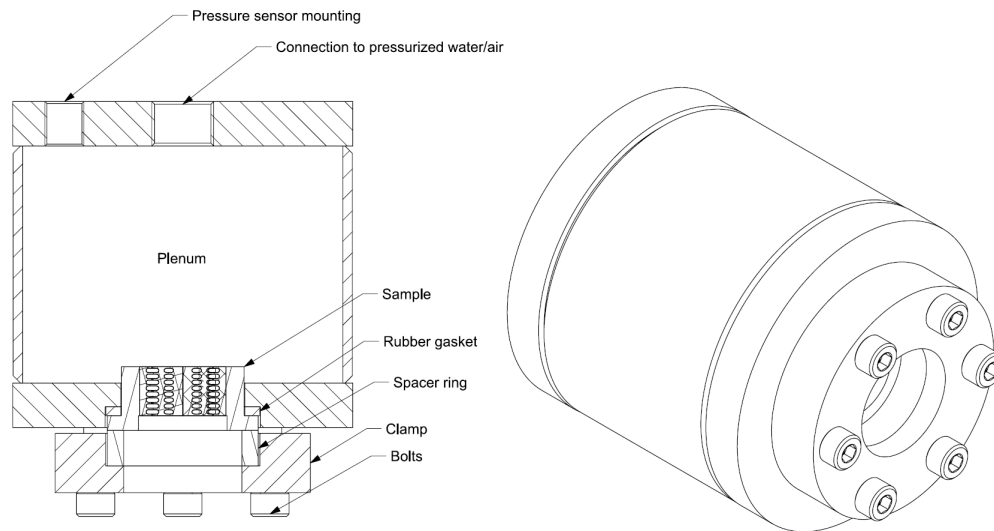


Figure 6.2: The test section

to pressures of 345 bar. The accuracy of the sensors is discussed in subsection 6.6.4.

### 6.2.2. Data acquisition system

The data acquisition is a *National Instruments CompactDAQ System* and it can be operating using *LabVIEW*. This system is able to control the valves and data logging. A sampling frequency of 1 kHz is used. An automated sequence is used to open the valves and to start the data logging, see next section for more details.

## 6.3. Test procedures

A summarized version of the test procedures is given below for the case when the test sample is installed in the test section.

1. Fill the tank with water.
2. Set the pressure of the air to the required pressure by adjusting the pressure regulator manually.
3. Start the automatic sequence:
  - (a) Open pressurization valve to pressurize the water tank
  - (b) Open the main valve to start that water flow through the test section
  - (c) Let water flow until oscillations in pressure and mass flow stabilize
  - (d) Log data for 3 seconds
  - (e) Close main valve
4. Repeat test at (roughly) the same pressure.

As the test section is always open to the atmosphere on the downstream side, before starting the data acquisition the water needs to flow for a few seconds to assure a stable water flow. Furthermore, some oscillations in the pressure and mass flow measurements occur in the first instance after opening the valve. This is likely aggravated due to the distance between the mass flow meter and the test section of roughly 2 meters. Therefore, a delay between opening the valve and data acquisition is used. The following delay times resulted in stable measurements: 3 seconds for the calibration sample, 5 seconds for the gyroid sample and 6 seconds for the visco jet sample (the samples will be introduced in section 6.5).

Tests were repeated either two or three times at the same pressure setting. However, as the pressure is regulated by a manual pressure regulator, the pressure in the repeated tests is not exactly the same. In some tests

the water ran out and only air was flowing through the samples in part of the time when data was acquired. These tests results were discarded.

## 6.4. Validation of test setup

To determine if the test setup is capable of measuring the pressure drop versus flow velocity, a validation of the setup is performed. This validation is similar in approach as done in [1]. In that work a bed of packed spheres with a porosity of 0.37 and particle diameter of 2.5 mm was used to determine the pressure drop over length versus the superficial flow velocity. These results were then compared to the well established empirical relations that predict the pressure drop in a bed of packed spheres (see section 3.2). Good agreement was found.

While in the work of [1] a custom made bed of packed spheres was used, in this work a commercial-off-the-shelf solution is used. A bed of packed spheres can be found in filters and silencers. They are commonly made from sintered bronze spherical particles. When knowing the particle size and porosity of the commercial available parts, they can be used as a validation sample.

A standard 1" BSP silencer was used that can be seen in Figure 6.3. The sample can be mounted in a disk which is then mounted into the test section. The threaded connection is sealed using Teflon tape. However, a few problems occur with this sample. Firstly, a groove is present in the material to tighten the silencer. This groove will affect the measurements as the thickness is not uniform. Secondly, the sides of the filter are open and thus the flow is not one dimensional. This was solved by applying Teflon tape to the sides (see Figure 6.3). The way the sample is mounted into the test section ensures that the pressure on the outside is higher than on the inside. So, this will keep the tape 'sticking' to the sample and will prevent radial inflow. Lastly, the particle size is not uniform. It ranges between 0.2 mm and 0.315 mm as supplied by the supplier. Knowing that the pressure drop depends on the particle size squared, this will result in a large variation of expected pressure drop.

One missing parameter is the porosity. With the means that were available, it was impossible to measure the exact porosity. Bed of packed spheres have a theoretical maximum porosity of 0.37 [1, 94] and this value is used. The other properties of the sample can be seen in Table 6.1.

In section 6.6, the pressure drop from the additively manufactured samples (which are discussed shortly) are compared to the relations for a bed of packed spheres. To make this a fair comparison, one would like to remeasure the pressure drop of a bed of packed spheres produced using the same 3D printer. This would account for variations in material such as surface roughness and inaccuracies introduced by the printing. An attempt was made to 3D print a bed of packed spheres, but this was not successful as the pores were all blocked.

Parameter	Value	Unit
Porosity	0.37	-
Particle diameter	0.2 to 0.315	mm
Thickness	4.3	mm
Inner diameter	26.1	mm
Outer diameter	33	mm

Table 6.1: The properties of the used calibration sample.

## 6.5. Test samples

Two different additively manufactured test samples will be used and they are discussed in this section. Both samples were printed on a *SLM 280* printer which is a selective laser melting (SLM) metal printer. The samples are made from a copper alloy. The sole reason this material was used is that it was available. The pressure



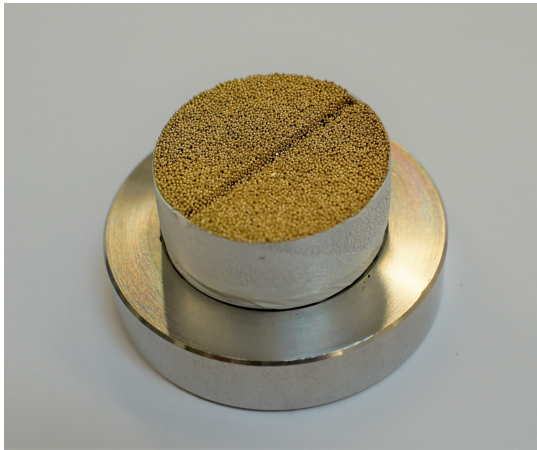


Figure 6.3: The used sample for validation of the test setup threaded into its mounting plate.



Figure 6.4: A different view of the validation sample where the difference in inner and outer diameter is visible, note that no Teflon is applied yet.

drop should in theory not be influenced by the material properties, only by the geometry. However, when comparing the 3D printed samples to additively manufactured objects made from steel alloys, it was observed that the surface of the copper parts was rougher. However, no quantitative measure for the surface roughness can be given.

As the main interests lies in the shape of the porous walls, a larger than absolute minimal possible pore size was used. The smallest pore size is 1.5 mm instead of the possible 0.3 mm to 0.5 mm. It was difficult to ensure powder removal of the parts at smaller sizes. However, with some effort the pore size could be reduced as done in other works, see section 1.4. Once the samples were produced, they were installed in the test section and then pressurized air was blown through them to make sure all powder was removed.

In the sections below, the two samples are treated in further detail.

### 6.5.1. Sheet gyroid sample

The first test goal is to see how the pressure drop in additively manufactured porous walls compares to common sintered walls. Using additive manufacturing to create porous walls firstly requires different geometries due to limitations with printing. For example, shapes that need support material cannot be used as the support material within the wall cannot be removed. Secondly, 3D printing allows for the creation of different shapes due to the flexibility in manufacturing that are not possible with traditional methods.

As the number of possible shapes is infinite, a single good representative shape is chosen. Quite extensive studies are available in literature on additively manufactured porous structures, mainly in the research for bone implants [95–97]. One class of shapes that is promising in these works are the triply periodic minimal surfaces (TPMS). These shapes are given by mathematical equation that describe an infinite amount of repetitions of its shape. The elements have the minimum possible area [96].

Al-Ketan et al. [97] performed mechanical strength tests of additively manufactured metal geometries on several TPMS shapes. He found that the sheet gyroid was performing well with respect to peak stress and Young's modulus. Therefore, this shape was chosen as representative shape for additively manufactured porous walls. The shape is given by Equation 6.2 [98] and the porosity can be changed by varying  $t$ . A value of  $t$  was iterated until a porosity of (roughly) 0.2 was achieved. The gyroid shape was made in MathMod<sup>1</sup> and then imported into a CAD program to transform it into a physical part that could be printed.

$$U = (\cos(2\pi x)\sin(2\pi y) + \cos(2\pi y)\sin(2\pi z) + \cos(2\pi z)\sin(2\pi x))^2 - t^2 \quad (6.2)$$

A unit cell of the geometry used in this work can be seen in Figure 6.5 and this shape is patterned several times in all three directions to obtain the sample. The fluid flows on the inside of the 'tubes'. Note that the

<sup>1</sup><https://sourceforge.net/projects/mathmod/>

nature of the sheet gyroid provides two open volumes that are not connected to each other. This unit cell was patterned until a sample of six layers and a length of 51.65 mm was created. The final measure thickness was slightly larger and this is used in the calculations. See Table 6.2 for the full list of properties and the sample is displayed in Figure 6.6.

Parameter	Value	Unit
Porosity	0.223	-
Pore size	1.5	mm
CAD thickness	51.65	mm
Measured thickness	52.3	mm
Diameter	33.8	mm

Table 6.2: The properties of the additively manufactured sheet gyroid sample.

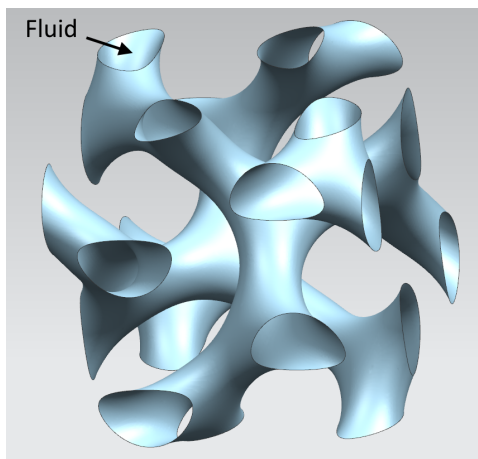


Figure 6.5: The shape of one unit cell of the sheet gyroid.

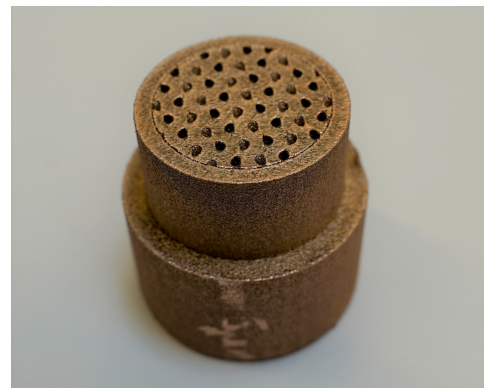


Figure 6.6: The additively manufactured sheet gyroid sample.

### 6.5.2. Visco jet sample

The second test goal is to find a shape that creates a larger pressure drop. In the search to find a geometry that creates a as large as possible pressure drop over length, the 'visco jet' from The Lee Company<sup>2</sup> was found. The working principle is depicted in Figure 6.7. The fluid is injected into a chamber and starts spinning around in it. Then it flows through a small hole in the middle of the chamber to the next one and the process is repeated. This will result in a high pressure drop.

The Lee Company produces these shapes in disks that can be stacked on top of each other. For this work the geometry has to be adapted for additive manufacturing. A single channel can be seen in Figure 6.8 and the dimensions of a single cell can be seen in Figure 6.9. The corners are rounded to ensure it can be printed without the use of support material, as this cannot be removed in the chambers. In one channel, a total of eight repetitions occur and the complete sample has six of these channels. The total length of the sample is less than the gyroid as it was feared that it would be difficult to remove the powder otherwise.

To define the visco jet as porous material is stretching the (poor) definition of a porous medium. The sample varies especially compared to the two other ones in the fact that the channels are not connected to each other. Furthermore, it consists of six exit holes that are spaced far apart, see Figure 6.10. So, when injecting the coolant into the chamber it is not uniformly distributed.

To ensure a comparison can be made to the other samples, an equivalent diameter of the sample is calculated that gives it the same volumetric porosity as the other samples. This diameter can then be used to calculate

<sup>2</sup><https://www.theleeco.com/products/precision-microhydraulics/restrictors/lee-visco-jets/>

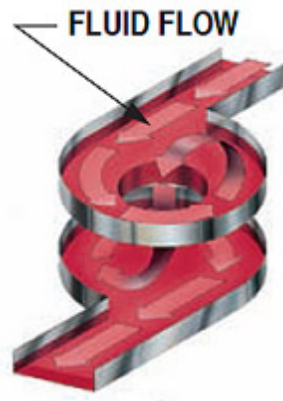


Figure 6.7: The working principle of the Lee visco jet [14].

the superficial velocity. See Table 6.3 for the diameter and the other properties.

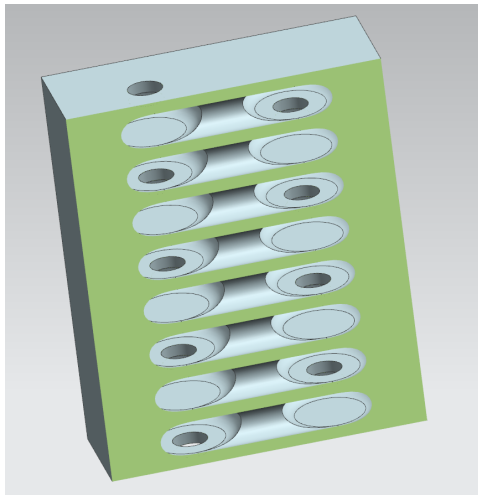


Figure 6.8: A 3D representation on one 'channel' of the visco jet sample.

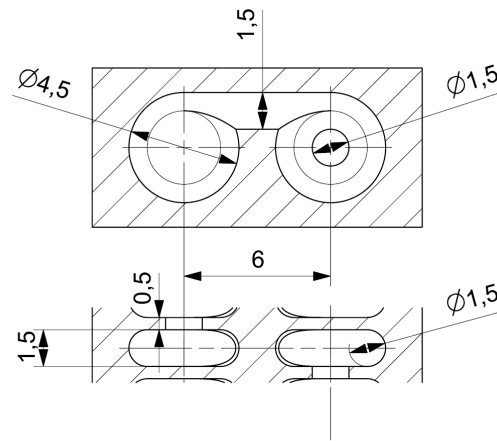


Figure 6.9: A drawing of one cell of the visco jet sample, dimensions in mm.

## 6.6. Test results

In this section the test results are discussed. Due to the numerous experiments performed, not all raw data can be presented. However, an example of the unfiltered data obtained for the validation sample can be seen in Figure 6.11 for the measurement time of 3 seconds. This raw data is processed and presented for the different samples in this section. The pressure drop is taken directly from the measurements and the superficial velocity is calculated using Equation 6.3. It can be seen in the figure that the setup was not able to keep a constant upstream pressure and thus the pressure drop and mass flow drop over the 3 seconds of test time. Therefore, the superficial velocity is determined for every single measurement point and afterwards the mean and standard deviation are determined.

$$v = \frac{\dot{m}}{A\rho} \quad (6.3)$$

### 6.6.1. Validation results

The results of the validation can be seen in Figure 6.12 and Table 6.4. The black lines represent the theoretical upper and lower limit calculated using the Darcy-Forchheimer equation and the empirical relations for

Parameter	Value	Unit
Porosity	0.223	-
Pore size	1.5	mm
CAD thickness	16.5	mm
Measured thickness	17.3	mm
Diameter	28.25	mm

Table 6.3: The properties of the additively manufactured visco jet sample.



Figure 6.10: The additively manufactured visco jet sample.

the permeability coefficients (see section 3.2). An upper and lower limit are given as the exact particle size is unknown. So, the upper line represents the minimum particle size (0.2 mm) and the lower one the maximum size (0.315 mm), as supplied by the manufacturer.

While only one experiment was performed, two data sets are plotted in Figure 6.12. During the experiment, mass flow and pressure drop are measured. To obtain the superficial velocity, the mass flow has to be divided by the area of the sample. However, due to the construction of the validation sample, the inlet area is larger than the outlet area, see Figure 6.4. It turns out that the pressure drop depends heavily on the chosen area. Therefore, two data sets are presented in the figure: one using the inner diameter and the other using the outer diameter. This mean that the actual result will most likely be between these data sets. Depending on the choice of particle diameter and then used diameter, the pore Reynolds numbers varies from 35 or 89 to 154 or 387.

Looking at the results, it can be observed that the data set using the outer diameter lies outside of the theoretical range. The other data set is within the range and lies close the lower limit. These results do not provide a precise calibration, which was to be expected due to the uncertainties with the sample. However, the results are within the order of magnitude of the empirical relations. This provides confidence that the test setup is designed and used correctly and that the subsequent data analysis is adequate.

### 6.6.2. Sheet gyroid

The results for the sheet gyroid sample can be seen in Figure 6.13 and Table 6.5. The error bars indicate the standard deviation. The pore Reynolds number varied between 359 and 964 for these tests.

Using the data points, a quadratic trend line that intersect the origin can be obtained that has an  $R^2$  value of 0.9999 which is given by Equation 6.4. The good fit with the quadratic function shows that the Darcy-Forchheimer is the right equation to model pressure drop for this range of velocities.

$$\frac{\Delta P}{\Delta L} = 26.712 \cdot 10^5 \cdot v + 329.99 \cdot 10^5 \cdot v^2 \quad (6.4)$$

Using the coefficients from the trend line and taking a constant viscosity and density, the permeability coefficient  $K_D$  and  $K_F$  can be determined. The water temperature for this test was 22.9 °C which gives a viscosity

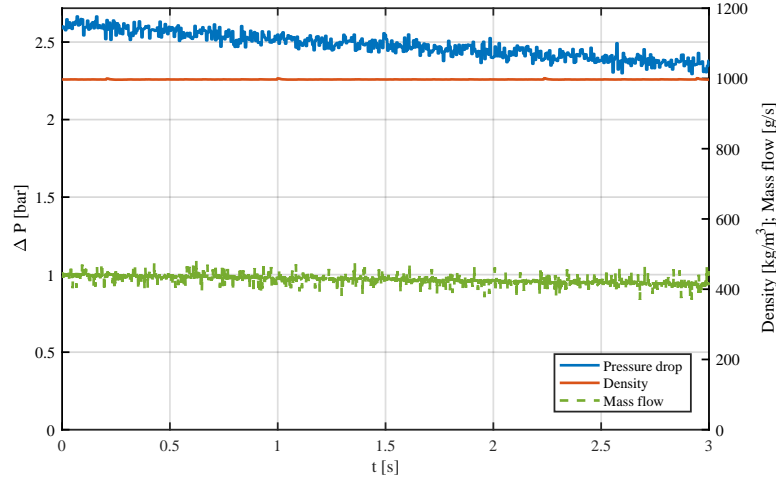


Figure 6.11: An example of the unfiltered data for pressure drop and mass flow for the validation sample.

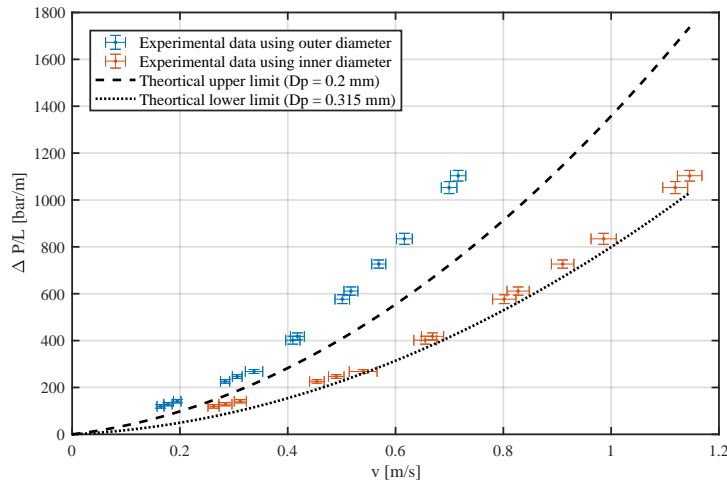


Figure 6.12: The pressure drop over length versus the superficial velocity of the experiment and the theoretical lower and upper ranges.

of  $934 \mu\text{Pa} \cdot \text{s}$  and a density of  $997 \text{ kg/m}^3$ . The value for  $K_D$  is then  $3.50 \cdot 10^{-10} \text{ m}^2$  and  $K_F$  equals  $3.02 \cdot 10^{-5} \text{ m}$ .

### 6.6.3. Visco jet

The pressure drop versus superficial velocity of the visco jet can be seen in Figure 6.14 and Table 6.6. The range of superficial velocities is about ten times lower than for the gyroid which results in the standard deviation being relatively larger. The pore Reynolds numbers vary between 43 and 121 in these tests. Again, a quadratic trend line is obtained which is given by Equation 6.5. It has a  $R^2$  of 0.9998.

$$\frac{\Delta P}{L} = 706.76 \cdot 10^5 \cdot v + 72566 \cdot 10^5 \cdot v^2 \quad (6.5)$$

Subsequently, the permeability coefficients were determined. The water temperature was  $22.1^\circ \text{C}$  which gives a viscosity of  $952 \mu\text{Pa} \cdot \text{s}$  and a density of  $997 \text{ kg/m}^3$ . Then permeability coefficients are:  $K_D$  equals  $1.35 \cdot 10^{-11} \text{ m}^2$  and  $K_F$  equals  $1.37 \cdot 10^{-7} \text{ m}$ .

Now that the permeability coefficients of the test samples have been determined, they can be compared to each other and to the empirical relations that describe the pressure drop in a bed of packed spheres.

$\nu$ [m/s]	$\sigma_\nu$ [m/s]	$\Delta P$ [bar/m]	$\sigma_{\Delta P}$ [bar/m]
0.262	0.0104	119.2	7.5
0.284	0.0122	128.7	7.0
0.312	0.0113	141.4	7.4
0.454	0.0135	225.9	7.6
0.490	0.0144	246.5	8.0
0.540	0.0258	268.3	8.4
0.655	0.0212	401.7	16.8
0.669	0.0206	418.1	14.8
0.802	0.0217	576.7	18.9
0.827	0.0206	611.2	17.6
0.910	0.0208	726.6	17.5
0.986	0.0234	834.2	23.5
1.119	0.0231	1052.8	25.6
1.146	0.0227	1103.5	22.8

Table 6.4: The processed data from the experiments with the validation sample and the standard deviation  $\sigma$ , for the minimum area of 534.6 mm<sup>2</sup>.

$\nu$ [m/s]	$\sigma_\nu$ [m/s]	$\Delta P$ [bar/m]	$\sigma_{\Delta P}$ [bar/m]
0.2242	0.0071	23.0	0.62
0.2366	0.0073	25.0	0.66
0.2534	0.0080	28.0	0.67
0.3279	0.0085	44.6	0.77
0.3465	0.0086	49.0	0.74
0.4018	0.0091	63.9	0.84
0.4072	0.0089	65.3	0.99
0.4255	0.0102	70.7	1.32
0.5002	0.0115	95.5	2.25
0.5084	0.0115	98.4	2.03
0.5092	0.0108	98.8	1.87
0.5505	0.0111	115.4	1.77
0.6016	0.0118	135.9	2.02

Table 6.5: The processed data from the experiments with the sheet gyroid sample and the standard deviation  $\sigma$ .

#### 6.6.4. Uncertainty analysis

A differential pressure sensor is employed to measure the pressure in the plenum with respect to the ambient pressure. An *OMEGA PD23-C-10* differential pressure sensor is used that has a measurement range of 0.2 to 10 bar and an accuracy of 0.2% of the maximum value, which results in an error of 0.02 bar.

The mass flow is measured using a *TRICOR TCM 5500* coriolis mass flow meter. It has a maximum mass flow of 1528 g/s and is rated up to pressures of 345 bar. The mass flow meter also provides the density and the temperature of the fluid flowing through it. It has an inaccuracy of  $\pm 0.3\%$  of the measured value for mass flow when liquids are used. However, at mass flows smaller than 3.5% of the maximum mass flow, the inaccuracy increases. This happens at a mass flow of around 54 g/s. The accuracy then increases to  $\pm 0.8\%$  for a mass flow of 23 g/s. No accuracy is given for mass flows lower than these values. The accuracy on the density is 1.0 kg/m<sup>3</sup> and the temperature has an accuracy of 1 degree.

Knowing the accuracy of the sensors, an uncertainty analysis can be done. The uncertainty of the pressure drop over length can be calculated by [99]:

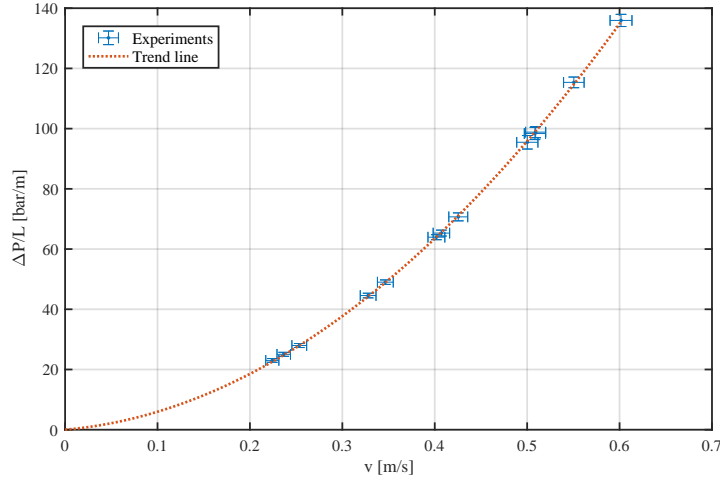


Figure 6.13: The pressure drop over length versus the superficial velocity of the gyroid sample and the obtained trend line; error bars indicate  $1\sigma$  in both directions.

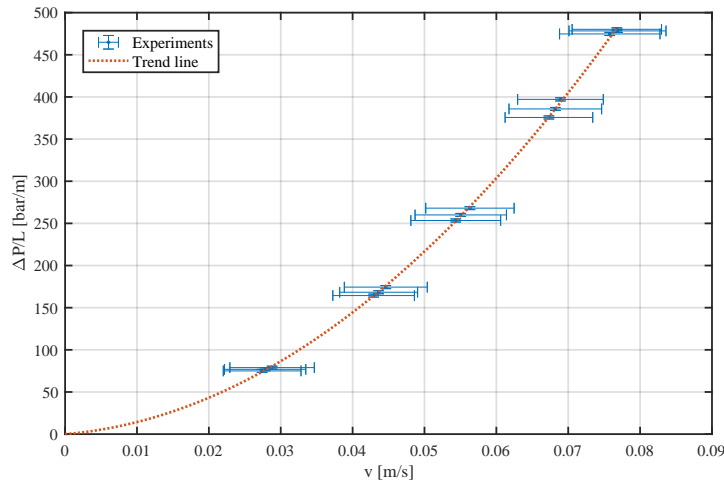


Figure 6.14: The pressure drop over length versus the superficial velocity of the visco jet sample and the obtained trend line; error bars indicate  $1\sigma$  in both directions.

$$\frac{\delta P/L}{P/L} = \sqrt{\left(\frac{\delta P}{P}\right)^2 + \left(\frac{\delta L}{L}\right)^2} \quad (6.6)$$

The superficial velocity is determined by:

$$v = \frac{\dot{m}}{A\rho} = \frac{\dot{m}}{\pi r^2 \rho} \quad (6.7)$$

The uncertainty then follows:

$$\frac{\delta v}{v} = \sqrt{\left(\frac{\delta \dot{m}}{\dot{m}}\right)^2 + \left(\frac{2\delta r}{r}\right)^2 + \left(\frac{\delta \rho}{\rho}\right)^2} \quad (6.8)$$

When the geometrical uncertainties are neglected, this will result in the uncertainty of the instruments. The pressure in the experiments varies between 0.513 bar and 8.3 bar. Then the uncertainties for pressure become 3.90% at the lowest measured pressure to 0.24% at the highest measured pressure. For the uncertainty in superficial velocity the minimum error (at higher mass flows) is 0.32% and the maximum at lower mass flows is 0.81%.

$\nu$ [m/s]	$\sigma_\nu$ [m/s]	$\Delta P$ [bar/m]	$\sigma_{\Delta P}$ [bar/m]
0.0274	0.0054	75.0	1.81
0.0278	0.0057	76.9	1.74
0.0288	0.0059	78.9	1.72
0.0429	0.0057	164.4	1.77
0.0436	0.0054	168.3	1.83
0.0446	0.0058	174.4	1.83
0.0544	0.0062	253.4	1.81
0.055	0.0064	260.0	1.78
0.0563	0.0061	268.1	1.77
0.0673	0.0061	375.7	1.82
0.0682	0.0064	385.8	1.76
0.0689	0.0060	397.1	1.86
0.0758	0.0070	474.7	1.88
0.0768	0.0062	480.2	1.77
0.0769	0.0067	478.3	1.89

Table 6.6: The processed data from the experiments with the visco jet sample and the standard deviation  $\sigma$ .

## 6.7. Analysis of test results

The obtained data can be used to compare the permeability coefficients of the different geometries and to see how this will affect a transpiration cooled rocket engine.

### 6.7.1. Comparison permeability coefficients

The permeability coefficients of the geometries were determined from the trend lines in the previous section. Comparing the permeability coefficients corrects the results for any differences in viscosity and density. The  $K_D$  and  $K_F$  values are given in Table 6.7 along with the theoretical values for a bed of packed spheres with the same porosity and particle diameter. Furthermore, the ratio of values of the samples compared to the bed of packed spheres is given. Remember that lower values of  $K_D$  and  $K_F$  will yield a higher pressure drop. Below, the differences in permeability coefficients are presented and discussed. How this will affect the actual pressure drop and performance of a transpiration cooled wall is discussed later.

It can be seen that  $K_D$  of the gyroid is 1.27 times higher than that of a bed of packed spheres. The  $K_F$  value is 2.47 times higher. This means that the gyroid will yield a lower pressure drop than the bed of packed spheres. The visco jet has a lot lower values for the permeability coefficients than the bed of packed spheres: 0.049 times for  $K_D$  and 0.011 times for  $K_F$ . So, the visco jet will create the highest pressure drop of all three geometries.

Geometry	$\epsilon$ [-]	$D_p$ [mm]	$K_D$ [m <sup>2</sup> ]	Ratio [-]	$K_F$ [m]	Ratio [-]	Re range	Comment
Bed of packed spheres	0.223	1.5	$2.76 \cdot 10^{-10}$	1	$1.22 \cdot 10^{-5}$	1		Empirical
Sheet gyroid	0.223	1.5	$3.50 \cdot 10^{-10}$	1.27	$3.02 \cdot 10^{-5}$	2.47	359 to 964	Experimental
Visco jet	0.223	1.5	$1.35 \cdot 10^{-11}$	0.049	$1.37 \cdot 10^{-7}$	0.011	43 to 121	Experimental

Table 6.7: The determined permeability coefficients for the tested shapes compared to the empirical ones for a bed of packed spheres, all for the same volumetric porosity and a minimum pore size of 1.5 mm.

An attempt is made to link the outcomes of the experiments to the known theory about the pressure drop in porous media. The first term in the Darcy-Forchheimer equation depends on viscosity, velocity and  $K_D$ . This term represents the friction losses in the medium and is the dominant term at lower velocities (i.e. lower Reynolds numbers). The second term depends on the density, velocity squared and  $K_F$ . This term represents



the form drag due to solid obstacles in the flow [69] and this one will be more dominant at larger velocities.

Looking at the results from the experiments, the  $K_D$  for the gyroid and the bed of packed spheres are almost similar with a factor of 1.27, but the  $K_F$  difference is larger with a value of 2.47. When looking at the geometry of the gyroid, it can be seen that the channels are quite streamlined while the bed of packed spheres has many 'spheres' blocking the flow path. So, it makes sense that the form drag in the gyroid is lower than the bed of packed spheres. Exactly the result seen in the tests as well.

For the visco jet both permeability coefficients are a lot lower. This lower  $K_D$  can be explained by the fact that the visco jet is essentially a very long channel and thus the friction losses will be larger. Furthermore, every time the fluid flows into the next chamber it discharges through a small orifice and this will increase the form drag.

### 6.7.2. Effect on pressure drop

Now that the permeability coefficients are known, the effect on the actual pressure drop can be investigated. The pressure drop depends on the permeability coefficient, but also on the flow velocity and the fluid properties. Therefore, at different fluid states and velocities, different pressure drops will occur. To narrow this analysis down to the application in rocket engines, it is therefore important to use the relevant parameters. As cooling fluid liquid ethanol is used as in most of the wall the fluid is liquid and only in the part close to the wall it turns gaseous. The properties are evaluated at a pressure of 65 bar and a temperature of 298 K and they can be seen in Table 6.8. From chapter 3, it is known that to get a wall temperature close to the maximum temperature a mass flux of around  $3.5 \text{ kg}/(\text{m}^2\text{s})$  is required. Using the density from the table, this results in a superficial flow velocity of  $0.0044 \text{ m/s}$ .

P [bar]	T [K]	$\rho \text{ kg}/\text{m}^3$	$\mu \text{ [Pas]}$
65	298	790.9	$1.129 \cdot 10^{-3}$

Table 6.8: The used properties for liquid ethanol, obtained using CoolProp [4].

Using this data, the pressure drop over length can be plotted for the three different geometries. As we are interested in the relative pressure drop between the three geometries, the pressure drop over length is normalised with respect to the bed of packed spheres. Furthermore, as the differences are large, they are plotted on a logarithmic scale, see Figure 6.15.

In the figure it can be seen that the sheet gyroid and the bed of packed spheres are relatively close. The sheet gyroid at the velocity of  $0.0044 \text{ m/s}$  has a pressure drop that is 0.76 times higher. The pressure drop of the visco jet has a pressure drop that is 24.9 times higher at this velocity.

When applying these results to a cylindrical transpiration cooled wall, the analysis changes slightly. In this case no constant velocity occurs. Due to the increasing flow area at larger diameters, the superficial velocity reduces at these locations and this on its turn reduces the pressure drop largely. For the visco jet this would not be the case as the channels are not interconnected and they will not change in flow area, they will just be more spaced apart. This means if the switch from a bed of packed spheres to a visco jet is made, both with a pore size of  $0.4 \text{ mm}$  and a porosity of 0.2, the wall thickness can go from  $\gg 50 \text{ m}$  to around  $0.035 \text{ m}$ . With this thickness a maximum wall temperature is reached that equals the maximum allowed temperature for Inconel. It should be noted that the visco jet does not distribute the coolant uniformly. So, in practice some extra geometry should be added that ensures uniform distribution of the injected coolant. For the gyroid shape, an even thicker wall is required compared to the bed of packed spheres as the pressure drop was lower.

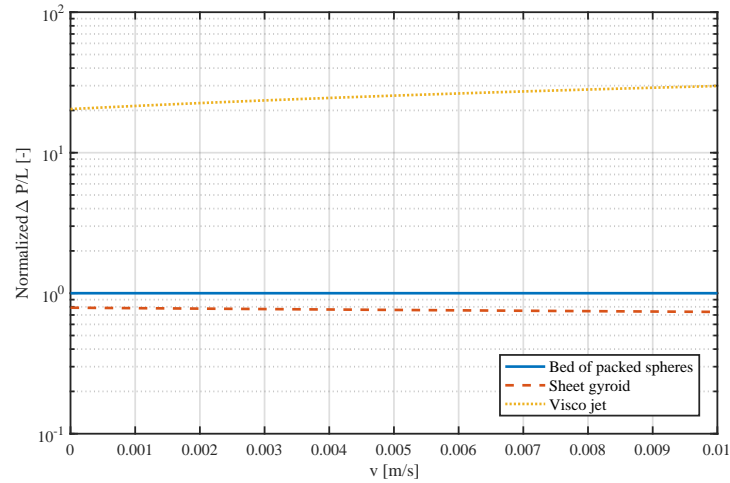


Figure 6.15: The normalized pressure drop for the additively manufactured geometries, normalized to a bed of packed spheres, for liquid ethanol

## 6.8. Conclusions and recommendations

The experiments performed on two additively manufactured porous walls had two goals. The first goal was to see how additively manufactured geometries compare in pressure drop to a bed of packed spheres. The reason for this is that a bed of packed spheres is used to model the pressure drop in this work and this allows for a comparison. The sheet gyroid shape was selected as a representative shape for an additively manufactured porous material as it had the best mechanical strength of various options. For a constant coolant velocity, the pressure drop for the gyroid was only 0.76 that of the bed of packed spheres. So, while it is lower, it is still in the same order of magnitude. This demonstrates that it is reasonable to use Ergun's relation that prescribe the pressure drop in a bed of packed spheres for other geometries. However, for more precise relations, the experiments performed here need to be repeated for a range of porosities and pore sizes for the exact shape used. Then, one gets an equation that determines the permeability coefficients depending on porosity and pore size, similar to Ergun's relations.

The second goal was to find a geometry that caused higher pressure drops. A single geometry with the highest potential was selected: the visco jet shape. This geometry caused a pressure drop that was 24.9 times higher for a constant coolant velocity when compared to the bed of packed spheres. As the coolant velocity in a porous wall is not constant, it is estimated that the wall thickness for a pore size of 0.4 mm could reduce from » 50 m to around 0.035 m. This is a huge reduction and might make it possible to use the current selective laser melting (SLM) printing methods to make a transpiration cooled wall. However, the visco jet shape does not ensure a uniform coolant injection, so additional solutions need to be found. Furthermore, powder removal for this shape at a pore size of 0.4 mm will become very difficult.

So, changing the geometry of the porous wall is a potential solution to create a higher pressure drop. Some other potential solutions were also indicated and presented below. It was already clear that the current smallest pore size producible with the conventional SLM printers is around 0.3 mm to 0.5 mm. This is an order of magnitude too large. Furthermore, SLM printers leave powder in the pores and this needs to be removed. Depending on the geometry this is a tedious process or even completely impossible. A solution needs to be found for these two problems when one wants to make use of additive manufacturing to create a transpiration cooled rocket engine.

An option to create smaller pores is still using SLM printing but modifying the creation of the pores. Sometimes, when a SLM printer malfunctions, the resulted print is porous, see Figure 6.16. Normally, this is not preferred as it compromises the integrity of the material. However, for transpiration cooling this might be an option to create porous walls with smaller pore sizes. More research is required to find the required settings

to exactly specify the required porosity and to achieve repeatable results.

While the above option might be a way to reduce the pore size, the problem with powder removal is not solved. A potential solution for this would be to use a different metal 3D printing technique. An option is directed energy deposition (DED) printing. In this case metal powder or a wire is only applied at the location where material is needed and then melted by a laser [100]. This is similar to the many commercially available FDM printers that can print plastic, but now with metal. DED is less developed than SLM printers and currently the width of layers is on the order of millimeters. So, this is too large to be used at this moment. However, if DED is developed further it might be good candidate.

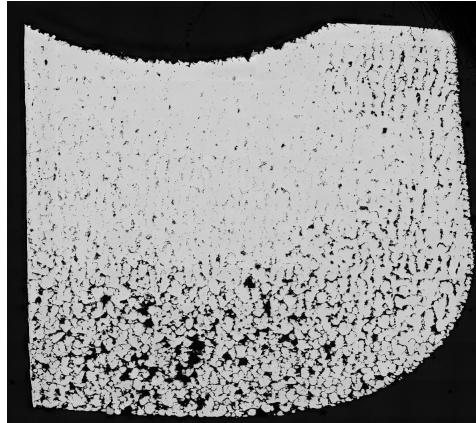


Figure 6.16: A CT scan of a by SLM additively manufactured (too) porous wall.



## Conclusions and recommendations

The primary research goal of this thesis was to compare regenerative, regenerative + film cooling and transpiration cooling in liquid rocket engines and to see which cooling methods yields a higher total engine performance for a 68 kN reference engine. The focus was on the wall temperature, the differences in specific impulse and dry mass. The latter two can be combined in the total delta-v achieved. Inconel and copper were used as wall materials to see the effect of using different materials. A secondary goal was to see if additive manufacturing could be used to produce the porous walls required for transpiration cooling.

A more elaborate discussion on the methodology will be given in section 7.3, but in short: three numerical models were developed that can model the three different cooling methods and these were applied to the reference engine. A new film cooling model was developed to model transcritical coolant behaviour by combining three existing film cooling models. Two different calibrations of the film cooling model were presented: a conservative and unconservative one. All cooling models were verified and validated using data from literature. The transpiration cooling model was used for a parametric analysis to answer some of the research questions. All three models were applied to the reference engine to allow for the comparison in performance. Additionally, experiments were performed on additively manufactured porous walls to see how the pressure drop compares to conventional porous materials and to find a geometry that causes a larger pressure drop.

In this chapter, first the individual research questions are answered in section 7.1. Then, the answers are summarized to answer if the main goals have been achieved in section 7.2. In this section, also recommendations for the obtained results are given. Lastly, in section 7.3, the main conclusions and recommendations on the methodology are given.

### 7.1. Answering research questions

The research questions are answered below. The main conclusions on the goals set will be summarized in the section after.

**1. Determine how regenerative, regenerative + film cooling and transpiration cooling compare with respect to total engine performance for a 68 kN bipropellant liquid rocket engine.**

**(a) What are the differences in maximum wall temperature between the three cooling techniques in steady state?**

For both an Inconel and copper, the solely regeneratively cooled engines reach wall temperatures above the material temperature limits. For Inconel and copper, temperatures of 1600 K and 846 K are reached respectively. Both film cooling and transpiration cooling achieve lower temperatures, depending on how much coolant is injected. Transpiration cooling requires less coolant than film cooling to achieve the same temperature.

The transpiration cooled Inconel engine needs a coolant mass flow of 2.5% of the total engine mass flow to achieve the maximum allowable temperature of 923 K. Film cooling requires 5.4% to

12.9%, depending on which calibration of the film cooling model is used. The copper transpiration cooled engine needs 3.0% coolant flow to achieve the maximum temperature of 723 K and film cooling requires 5.0% to 6.1% depending on the calibration.

**(b) What are the differences in thermal gradients in the wall between the three cooling techniques in steady state?**

The thermal gradients in the wall are highest for the regeneratively cooled engines. For Inconel, the gradients of the transpiration cooled wall are equal to the film cooled one when plotted against the coolant mass flow. However, film cooling requires more coolant to achieve the desired operating wall temperature. So, at this condition the thermal gradients in the film cooled engine will be two times lower than for transpiration cooled engine. For the copper chamber, the thermal gradients in the transpiration cooled wall are lower at the same coolant mass flow compared to the film cooled engine. As a result, the gradients are equal between the two cooling methods at the maximum wall temperature, as again the film cooled engine requires more coolant.

**(c) What is the distribution of coolant in a transpiration cooled engine that will minimize the coolant mass flow?**

A simplified model was used to determine the coolant distribution along the axial length in the Inconel transpiration cooled engine. While the absolute values for the coolant mass flow can deviate 30% with this model, it was found that the optimum coolant mass flux follows the same curve as the heat flux in the engine. This means that it peaks around the throat and then drops steeply in the nozzle.

**(d) What are the differences in specific impulse between the cooling techniques?**

The specific impulse of the regeneratively cooled engine is the highest with a vacuum specific impulse of 335.1 s. Of course, this engine is not practical as the maximum wall temperatures are exceeded. When coolant is injected into the chamber to cool it, either by transpiration or film cooling, the specific impulse will be lower. A higher coolant mass injection will result in a larger drop in specific impulse. However, no exact answer can be given on the change in specific impulse. This depends on the mixture ratio of the zone close to the wall and this is value unknown. However, for the worst case mixture ratio evaluated, the transpiration cooled engine has a specific impulse of only 1.1% and 1.3% lower than the regeneratively cooled engine for Inconel and copper respectively. For the Inconel film cooled engine, the differences are 3.3% to 12.7% depending on the calibration used. For copper, they are 3.0% to 4.0% lower. So, while no exact number can be given, it is clear that a transpiration cooled engine performs better regarding specific impulse because less coolant is injected.

**(e) What are the differences in engine dry mass of the different cooling techniques?**

The regeneratively and the regeneratively + film cooled engine have the same dry mass and are the lightest options. The mass of the transpiration cooled engine is larger as a thicker wall is required to achieve the specified pressure drop over the wall. The results depend on the specified pressure drop and the two other factors that determine the magnitude in pressure drop: the porosity and pore size. The most optimal case for the transpiration cooled engine in this report has a pressure drop of 1 bar, porosity of 0.2 and pore size of 0.05 mm. In this case the transpiration cooled engine dry mass is 9.4% higher for the Inconel engine and 31.8% higher for the copper engine. When the pore size increases to 0.1 mm, these differences increase to 59.5% and 128% respectively. This shows the importance of creating thin walls by using small pore sizes.

**(f) What are the differences in delta-v achieved by the reference engine for the three cooling techniques?**

The increased specific impulse of the transpiration cooled engines compensates for the increase in dry mass. Again, exact numbers for the achieved delta-v differences are difficult to compare as the specific impulse depends on the unknown mixture ratio in the wall zone. So, only an analysis can be done that looks at which OF ratio the extra specific impulse outweighs the mass increase.

The most optimal case occurs for an Inconel wall with a pore size of 0.05 mm. This wall has the largest range of OF ratios where it will perform better than the film cooled option. For the Inconel wall with a pore size of 0.1 mm, the results depend on the film cooling version used. Using the conservative film cooling model shows that film cooling will always be better. Using the less conservative model, the transpiration cooled engine will perform better for a large range of OF ratios. For the copper chamber with a pore size of 0.05 mm, a small range of OF ratios performs better than the film cooled engines. For the copper chamber with a pore size of 0.1 mm, the film cooled engine always has a higher delta-v than the transpiration cooled option.

**(g) How do the above results change when copper is used as wall material instead of Inconel?**

While the differences for the Inconel and copper chamber were also treated in the above research questions, a general summary can be given here. It is concluded that transpiration cooling has greater benefits compared to film cooling for Inconel chambers. The reduction in coolant required when switching from film cooling to transpiration cooling is the largest for Inconel. The copper engines require less film coolant in general, so it is less effective to use transpiration cooling. Furthermore, copper transpiration cooled engines require thicker walls to achieve the maximum wall temperature and this adds to the dry mass.

**2. Determine if additive manufacturing of a rocket combustion chamber wall can be used to produce a transpiration cooled 68 kN bipropellant liquid rocket engine that can compete with its regenerative + film cooled variant.**

**(a) Can the required wall properties for a transpiration cooled wall be produced using additive manufacturing?**

The focus on this question is not on the production of additively manufactured walls, but comparing the required properties to what is currently possible to 3D print. It was found that the minimum pore size currently producible (between 0.3 mm and 0.5 mm), results in too thick walls. These go up to more than 50 meters for the reference engine. For the Inconel engine, decent results were achieved using a pore size of 0.05 mm. So, the minimum pore size has to go down by an order of magnitude to make transpiration cooling possible when using conventional porous wall shapes.

Some pressure drop experiments were performed with additively manufactured porous walls. The pressure drop of a 3D printed geometry was compared to the geometry used in the calculations. This geometry is the 'bed of packed spheres' and was used in the model as the pressure drop is given by well established empirical relations. It was found that the pressure drop of the additively manufactured shape was in the same order of magnitude, being 0.76 of the pressure drop of a bed of packed spheres. Secondly, another porous shape was printed that produces a 24.9 times higher pressure drop than the bed of packed spheres. While this shape cannot be immediately used as a transpiration cooled wall due to a non-uniform coolant injection, this is a promising result.

**(b) How does varying the porosity within the wall in radial direction affect cooling performance?**

Varying the porosity in the wall has minimal effects on the temperature and temperature gradient. It is best to keep the porosity as low as possible as this will lower the gradients and cause a higher pressure drop that yields thinner walls. This will result in a lighter engine.

**(c) How does the pore size and its variation within the wall affect cooling performance?**

Varying the pore size in the wall has minimal effects on the temperature and the temperature gradients. Similar to the porosity, it is best to keep them as low as possible such that a higher pressure drop in the wall occurs and a thinner wall can be used. This will save on the dry mass of the engine.

## 7.2. Conclusions and recommendations of results

The main goal of this thesis was to see how a transpiration cooled liquid rocket engine compares with its regenerative and film cooled variants. From this a more interesting question follows: does a transpiration cooled engine perform better than its regenerative and film cooled variants? The answer to this question is: it depends. From the developed models applied to the 68 kN reference engine, it is clear that the engine needs additional cooling on top of regenerative cooling. When only regenerative cooling is used, the wall temperature limits are exceeded. Transpiration and film cooling can both lower the wall temperature below the material limit. Transpiration cooling results in lower temperatures than film cooling for the same coolant mass flows and this is favorable for the achieved specific impulse. However, the conditions to achieve these low mass flows require thick walls that add a lot of extra dry mass to the transpiration cooled engine. For the engine with an Inconel wall with the smallest pore size analysed of 0.05 mm, transpiration cooling achieves a higher delta-v than for the film cooled engine. However, for larger pore sizes and for the copper chamber, film cooling starts to perform better.

The above shows that it depends mainly on two factors if a transpiration cooled engine performs better than a film cooled engine. These factors are the wall thickness and the used film cooling model, and both have a high uncertainty bound to them. Focusing first on the latter: two different calibration of the film cooling model were presented. The version that was calibrated with the film cooling model of the software Rocket Propulsion Analysis (RPA) predicts higher heat fluxes and thus more coolant is required. This naturally makes the transpiration cooled engines perform better. However, the 'uncalibrated' model, which was validated with the limited available test data in literature, requires less coolant and thus these film cooled engines perform better with respect to delta-v achieved. So, to get a more precise answer on which cooling method actually performs better, a more accurate (transcritical) film cooling model is required or more validation data needs to be found to achieve higher confidence in either one of the models. A potential solution to this could be CFD modelling, but the most ideal action would be to perform experiments with the film cooled reference engine to obtain the actual heat flux in the engine.

The other aspect that introduces a large uncertainty in the analysis is the required the wall of the transpiration cooled engine. This depends on the porosity, pore size and the specified pressure drop over the wall. A pressure drop of 1 bar was used, while literature recommended one of 5 bar. The choice of these parameters and the used porosity affects the wall thickness greatly, so ideally the minimum allowed value for each is chosen. However, these minimum values are not known and it is recommended to find these via extra analysis and/or testing. The porosity should be high enough to achieve uniform injection of the transpiration coolant into the chamber. The pore size should be large enough to be producible and an analysis of other practical effects, such as clogging, should be done. The pressure drop should be high enough to be able to handle chamber pressure oscillations and provide enough resistance to achieve uniform distribution of the coolant in the manifold.

The secondary goal was to see if additive manufacturing can be used to produce a transpiration cooled wall. It was clear that the pore sizes currently producible with additive manufacturing are too large and cause a too low pressure drop resulting in too thick walls. So, it is currently not possible to produce a competitive transpiration cooled engine with additive manufacturing. To use additive manufacturing, either smaller pore sizes should be printable or shapes with a higher pressure drop should be used. Pressure drop experiments performed, showed that a different shape can cause pressure drops 24.9 times higher than the bed of packed spheres shape used in the calculations. This is a promising result, but more research is required as this shape does not provide a uniform coolant injection. Potentially, other shapes exist that provide a large pressure drop and uniform injection or a hybrid shape can be made. This will then consist of a section causing a higher pressure drop and a part achieving uniform distribution.

General recommendations for the use of transpiration cooling can be given. While this thesis showed that the use in rocket engines might be difficult, potentially it can be used in applications where an increased mass flow due to a lower wall thickness is a desirable effect. Two examples of these applications are injector faces or pre-burners of the turbo pumps where extra propellant is injected as an enthalpy reducing agent. In the latter case, no regenerative cooling is required and thus a lower pressure drop occurs in the system that can increase the total efficiency.



## 7.3. Conclusions and recommendations of methodology

An overview of the most important conclusions and recommendations of the methodology used are given in this section.

**Regenerative cooling model** A simple 1D regenerative cooling model was developed that uses the Bartz equation and NASA's Chemical Equilibrium with Applications (CEA) to determine the convective heat transfer. While it is likely that more extensive modelling such as 3D CFD will result in more accurate result, it is not needed for the goal of this thesis. Errors introduced are used in all three cooling techniques and thus cancel out. An easy step to improve the accuracy of the model would be to replace the radiative heat transfer model. Currently, radiation is determined using empirical relations that only depend on gas pressure and gas temperature. A more extensive model could be added that also lets the radiation depend on the wall temperature and wall emissivity. Additionally, the complete regenerative cooling model can be improved by comparing it to actual experimental data instead of more extensive CFD results. Ideally, one compares it to test data of the reference engine as this also allows for calibration of the heat flux.

**Transpiration cooling model** It is possible to model a transpiration cooled wall using the local thermal equilibrium (LTE) assumption and the local thermal non-equilibrium assumption (LTNE). The latter is more complete, but requires more computational time. For the wall properties in this report, the heat transfer within the wall is high and often the LTNE gives the same results as the LTE case. However, depending on the boundary conditions, these solutions start to deviate. It was determined that for the correct boundary conditions in a transpiration cooled rocket chamber wall, the LTNE case should be used.

The pressure drop in the wall was determined using empirical relations. Relations for a bed of packed spheres were used. While the pressure drop experiments showed that an additively manufactured geometry has a pressure drop in the same order of magnitude, the model can benefit largely from a better estimate of the pressure drop. The pressure drop directly influences the required wall thickness and this has a direct impact on the dry mass of the wall. This drives the delta-v comparison between a transpiration and a film cooled engine. These relations can either be found by using similar experiments as performed in this work, but then for a larger set of parameters such as different pore sizes and porosities. Alternatively, these relations can be found using CFD analysis.

The heat transfer within the wall was also determined using empirical relations. Two different volumetric heat transfer models were analysed. The results show that at the small pore sizes used for the main conclusion of this report ( $< 0.1$  mm), both models predict the same maximum temperature with a difference of only 1.8%. This is caused by the fact that at these small pore sizes, the heat transfer is very high and the solution converges to the LTE case. Then, the solid and coolant are locally the same temperature and no volumetric heat transfer coefficient is required. However, if one wants to do more research on the pore sizes producible with additive manufactured walls (0.3 mm to 0.5 mm), differences up to 17% in temperature occur between the two models. So, for these walls, the choice of volumetric heat transfer model will affect the results and thus it is recommended to use an appropriate model for the porous shape used. For new shapes, these models can either be determined using CFD analyses or experiments.

An empirical relation (Meinert's equation) was used to determine the reduction in convective heat transfer from the hot gas to the wall caused by the blowing effects of the transpiration cooled engine. The coolant used in this work had a molecular mass that was higher than the ones used in the experiments used to determine the relation. It was found in the experiments that molecular mass has a decent influence on the reduction in heat transfer. This reduction on its turn has a large effect on the final wall temperature, and therefore it is recommended to repeat these experiments with the actual (liquid) coolant used.

While validation was performed on separate components of the transpiration cooling model, data in open literature on the temperature distribution in an actual transpiration cooled rocket engine was not found. Therefore, it is recommended to find this data, potentially by contacting institutions that have worked on transpiration cooled engines, or perform own tests with a transpiration cooled engine. It must be noted that measuring the temperature in a transpiration cooled engine will not be an easy task: using common calorimetric

chambers to measure the heat flux will not be possible as the coolant is injected into the chamber and inserted thermocouples will affect the flow in porous wall and might not be precise enough due to the high gradients in wall temperature.

**Film cooling model** A new transcritical film cooling model was developed by combining three existing film cooling models. The results matched with experimental analysis of a kerosene film cooled engine (differences in heat flux below 12%). However, there are indications that this model gives very long liquid film lengths and thus gives lower wall temperatures than other film cooling models. Therefore, two different calibrations for the film cooling model were presented. One is the 'uncalibrated' version and matches the test results. The other one is the 'RPA calibrated' version and this one is calibrated to the film cooling model used in the commercial software Rocket Propulsion Analysis (RPA). The latter model gives higher wall temperatures for the same coolant mass flow. As already mentioned in section 7.1, this uncertainty in the film cooling models directly affects the comparison between transpiration and film cooling. Therefore, it is recommended to find better models or additional validation data to see which one is more accurate.

**General** This work used simple numerical models to be able to quickly vary the parameters used. However, two different models for transpiration and film cooling were used. In reality, film cooling should converge to transpiration cooling when more and more injection points are added. A possible way to solve these problems is to do a CFD analysis for a limited amount of coolant flows and compare transpiration and film cooling this way. A downside of this approach is that evaluating a large variation of parameters will be more time consuming, but this might not be needed anymore with the results from this thesis.

Lastly, the actual factor that determines if a wall can handle the heat loads are not the wall temperature and the temperature gradients as used in this work, but the actual stress in the wall. To simplify the analysis in this thesis, the material temperature that still gives a high yield strength was used as maximum wall temperature. Secondly, the thermal gradients were analysed which are a measure for the thermal stress. However, to give a real measure of the stresses, a more detailed structural analysis is required. Finite elements analysis could be used to do this.

# Bibliography

- [1] T. Langener, *A Contribution to Transpiration Cooling for Aerospace Applications Using CMC Walls*. PhD thesis, Jan. 2011.
- [2] D. Greuel, A. Herbertz, O. Haidn, M. Ortelt, and H. Hald, "Transpiration cooling applied to c/c liners of cryogenic liquid rocket engines," in *40th AIAA/ASME/SAE/ASEE Joint Propulsion Conference and Exhibit*, American Institute of Aeronautics and Astronautics, jul 2004.
- [3] A. Herbertz, M. Ortelt, I. Müller, and H. Hald, "Transpiration cooled ceramic thrust chamber applicability for high-thrust rocket engines," in *48th AIAA/ASME/SAE/ASEE Joint Propulsion Conference & Exhibit*, (Atlanta), American Institute of Aeronautics and Astronautics, jul 2012.
- [4] I. H. Bell, J. Wronski, S. Quoilin, and V. Lemort, "Pure and pseudo-pure fluid thermophysical property evaluation and the open-source thermophysical property library CoolProp," *Industrial & Engineering Chemistry Research*, vol. 53, pp. 2498–2508, jan 2014.
- [5] M. Pizzarelli, B. Betti, F. Nasuti, D. Ricci, P. Roncioni, F. Battista, and V. Salvatore, "Cooling channel analysis of a LOX/LCH<sub>4</sub> rocket engine demonstrator," in *50th AIAA/ASME/SAE/ASEE Joint Propulsion Conference*, American Institute of Aeronautics and Astronautics, jul 2014.
- [6] National Institute of Standards and Technology, "Nist chemistry webbook." available online at: <https://webbook.nist.gov/chemistry/>. Accessed June, 2019.
- [7] C. U. Kirchberger, *Investigation on Heat Transfer in Small Hydrocarbon Rocket Combustion Chambers*. PhD thesis, 2014.
- [8] L. Amiri, S. A. Ghoreishi-Madiseh, F. P. Hassani, and A. P. Sasmito, "Estimating pressure drop and ergun/orchheimer parameters of flow through packed bed of spheres with large particle diameters," *Powder Technology*, vol. 356, pp. 310–324, nov 2019.
- [9] S. M. Ahmadi, R. Hedayati, Y. Li, K. Lietaert, N. Tümer, A. Fatemi, C. D. Rans, B. Pouran, H. Weinans, and A. A. Zadpoor, "Fatigue performance of additively manufactured meta-biomaterials: The effects of topology and material type," *Acta Biomaterialia*, vol. 65, pp. 292–304, jan 2018.
- [10] C. Höglauer, B. Kniesner, O. Knab, G. Schlieben, C. Kirchberger, S. Silvestri, and O. J. Haidn, "Modeling and simulation of a GOX/kerosene subscale rocket combustion chamber with film cooling," *CEAS Space Journal*, vol. 7, pp. 419–432, may 2015.
- [11] "Liquid rocket engine self-cooled combustion chambers," Tech. Rep. NASA SP-8124, NASA Space Vehicle Design Criteria (Chemical Propulsion), 1977.
- [12] C. Kirchberger, R. Wagner, H.-P. Kau, S. Soller, P. Martin, M. Bouchez, and C. Bonzom, "Prediction and analysis of heat transfer in small rocket chambers," in *46th AIAA Aerospace Sciences Meeting and Exhibit*, American Institute of Aeronautics and Astronautics, jan 2008.
- [13] S. Gordon and B. J. McBride, *Computer Program for Calculation of Complex Chemical Equilibrium Compositions and Applications I. Analysis*. National Aeronautics and Space Administration, 1994. NASA RP-1311-P1.
- [14] The Lee Company, "Lee visco jets." available online at: <https://www.theleeco.com/products/precision-microhydraulics/restrictors/lee-visco-jets/>. Accessed May 27, 2020.
- [15] B. T. C. Zandbergen, "Simple mass and size estimation relationships of pump fed rocket engines for launch vehicle conceptual design," in *6th European Conference For Aeronautics And Space Sciences (EU-CASS)*, 2015.

- [16] G. P. Sutton and O. Biblarz, *Rocket Propulsion Elements*. John Wiley & Sons, eighth ed., 2010.
- [17] D. K. Huzel and D. H. Huang, "Modern engineering for design of liquid-propellant rocket-engines," *Progress in Astronautics and Aeronautics*, vol. 147, 1992.
- [18] S. R. Shine and S. Shri Nidhi, "Review on film cooling of liquid rocket engines," *Propulsion and Power Research*, vol. 7, pp. 1–18, mar 2018.
- [19] D. Haeseler, C. Maeding, V. Rubinskiy, V. Gorokhov, and S. Khisanfov, "Experimental investigation of transpiration cooled hydrogen-oxygen subscale chambers," in *34th AIAA/ASME/SAE/ASEE Joint Propulsion Conference and Exhibit*, American Institute of Aeronautics and Astronautics, jul 1998.
- [20] J. E. Terry and G. J. Caras, "Transpiration and film cooling of liquid rocket nozzles," tech. rep., Redstone Scientific Information Center, Mar. 1966.
- [21] E. R. G. Eckert and N. B. Livingood, "Comparison of effectiveness of convection-, transpiration-, and film-cooling methods with air as coolant," Technical Report 1182, National Advisory Committee for Aeronautics, 1954.
- [22] R. C. Stechman, J. Oberstone, and J. C. Howell, "Design criteria for film cooling for small liquid-propellant rocket engines," *Journal of Spacecraft and Rockets*, vol. 6, pp. 97–102, feb 1969.
- [23] V. Yang, *Liquid Rocket Thrust Chambers: Aspects of Modeling, Analysis, and Design*. American Institute of Aeronautics and Astronautics, jan 2004.
- [24] W. D. Rannie, "A simplified theory of porous wall cooling," Progress report 4-50, Jet Propulsion Laboratory, Nov. 1947.
- [25] G. Huang, Z. Min, L. Yang, P.-X. Jiang, and M. Chyu, "Transpiration cooling for additive manufactured porous plates with partition walls," *International Journal of Heat and Mass Transfer*, vol. 124, pp. 1076–1087, sep 2018.
- [26] Z. Min, G. Huang, S. Parbat, L. Yang, and M. Chyu, "Experimental investigation on additively manufactured transpiration and film cooling structures," *Journal of Turbomachinery*, vol. 141, jan 2019.
- [27] A. J. P. van Kleef, B. A. Oving, C. J. Verberne, B. Haemmerli, M. Kuhn, I. Müller, and I. Petkov, "Innovative small launcher," tech. rep., Netherlands Aerospace Centre, Nov. 2015.
- [28] L. Timmermans, N. Bernving, A. van Kleef, B. Haemmerli, M. Kuhn, I. Müller, M. Petrozzi, and G. Psoni, "Small innovative launcher for Europe results of the H2020 project SMILE," in *69th International Astronautical Congress*, (Bremen), 2018.
- [29] M. Ortelt, H. Hald, S. Michaelides, H. Seiler, and G. Herdrich, "Advancement of rocket engine performance through novel approaches for thrust chamber design," in *68th International Astronautical Congress*, (Adelaide), 2017.
- [30] H. Hald, A. Herbertz, M. Kuhn, and M. Ortelt, "Technological aspects of transpiration cooled composite structures for thrust chamber applications," in *16th AIAA/DLR/DGLR International Space Planes and Hypersonic Systems and Technologies Conference*, American Institute of Aeronautics and Astronautics, oct 2009.
- [31] M. Ortelt, H. Hald, I. Fischer, D. Greuel, O. Haidn, and D. Suslov, "Empirical verification of effusion cooled CMC rocket thrust chambers," in *41st AIAA/ASME/SAE/ASEE Joint Propulsion Conference and Exhibit*, American Institute of Aeronautics and Astronautics, jul 2005.
- [32] Ultramet, "Transpiration cooled systems." available online at: <https://ultramet.com/propulsion-system-components/liquid-rocket-engines/#transpiration>. Accessed April, 2019.
- [33] W. Zinner, D. Haeseler, C. Maeding, V. Rubinskij, V. Gorochoy, S. Hrisanfov, and G. Nikulin, "Development of advanced technologies for future cryogenic thrust chamber applications," in *33rd Joint Propulsion Conference and Exhibit*, American Institute of Aeronautics and Astronautics, jul 1997.

- [34] I. M. Abdulagatov and N. D. Azizov, "Density of rocket propellant (RP-1 fuel) at high temperatures and high pressures," *Fuel*, vol. 89, pp. 1731–1735, jul 2010.
- [35] I. M. Abdulagatov and N. D. Azizov, "Heat capacity of rocket propellant (RP-1 fuel) at high temperatures and high pressures," *Fuel*, vol. 90, pp. 563–567, feb 2011.
- [36] H. W. Deng, K. Zhu, G. Q. Xu, Z. Tao, C. B. Zhang, and G. Z. Liu, "Isobaric specific heat capacity measurement for kerosene RP-3 in the near-critical and supercritical regions," *Journal of Chemical & Engineering Data*, vol. 57, pp. 263–268, dec 2011.
- [37] I. M. Abdulagatov and L. A. Akhmedova-Azizova, "Viscosity of rocket propellant (RP-1) at high temperatures and high pressures," *Fuel*, vol. 235, pp. 703–714, jan 2019.
- [38] C. Kirchberger, G. Schlieben, and O. Haidn, "Assessment of film cooling characteristics in a GOX/kerosene rocket combustion chamber," in *49th AIAA/ASME/SAE/ASEE Joint Propulsion Conference*, American Institute of Aeronautics and Astronautics, jul 2013.
- [39] W. Dong, J. Wang, S. Chen, B. Ai, and X. Luo, "Modelling and investigation on heat transfer deterioration during transpiration cooling with liquid coolant phase-change," *Applied Thermal Engineering*, vol. 128, pp. 381–392, jan 2018.
- [40] C. Xin, Z. Rao, X. You, Z. Song, and D. Han, "Numerical investigation of vapor–liquid heat and mass transfer in porous media," *Energy Conversion and Management*, vol. 78, pp. 1–7, feb 2014.
- [41] 3D Systems, "LaserForm® Ni718 (A)," 2017. available online at: <https://www.3dsystems.com/sites/default/files/2017-12/3d-systems-laserform-ni718%28a%29-datasheet-usen-2017-12-07-web.pdf>. Accessed April 28, 2020.
- [42] Q. Ran, W. Yang, Y. Hu, X. Shen, Y. Yu, Y. Xiang, and K. Cai, "Osteogenesis of 3d printed porous ti6al4v implants with different pore sizes," *Journal of the Mechanical Behavior of Biomedical Materials*, vol. 84, pp. 1–11, apr 2018.
- [43] Toolcraft, "Metal Laser Melting." available online at: [https://www.toolcraft.de/fileadmin/user\\_upload/download/broschueren/Metall-Laserschmelzen-Broschuere.pdf](https://www.toolcraft.de/fileadmin/user_upload/download/broschueren/Metall-Laserschmelzen-Broschuere.pdf). Accessed April 23, 2019.
- [44] G. Xu, Y. Liu, X. Luo, J. Ma, and H. Li, "Experimental investigation of transpiration cooling for sintered woven wire mesh structures," *International Journal of Heat and Mass Transfer*, vol. 91, pp. 898–907, dec 2015.
- [45] G. Huang, Y. Zhu, Z. Liao, X. Ouyang, and P. Jiang, "Experimental investigation of transpiration cooling with phase change for sintered porous plates," *International Journal of Heat and Mass Transfer*, vol. 114, pp. 1201–1213, nov 2017.
- [46] M. F. Ashby, T. Evans, N. A. Fleck, J. W. Hutchinson, H. N. G. Wadley, and L. J. Gibson, *Metal Foams: A Design Guide*. Elsevier Science, 2000.
- [47] D. R. Bartz, "A simple equation for rapid estimation of rocket nozzle convective heat transfer coefficients," *Journal of Jet Propulsion*, vol. 27, pp. 49–51, jan 1957.
- [48] T. Govaert, "Analysis and prediction of the influence of high frequency combustion instabilities on heat transfer in a sub-scale LOX/H<sub>2</sub> rocket thrust chamber," Master's thesis, Delft University of Technology, June 2019.
- [49] F. Kuwahara, M. Shirota, and A. Nakayama, "A numerical study of interfacial convective heat transfer coefficient in two-energy equation model for convection in porous media," *International Journal of Heat and Mass Transfer*, vol. 44, pp. 1153–1159, mar 2001.
- [50] S. Whitaker, "Forced convection heat transfer correlations for flow in pipes, past flat plates, single cylinders, single spheres, and for flow in packed beds and tube bundles," *AIChE Journal*, vol. 18, pp. 361–371, mar 1972.

- [51] J. Meinert, J. Huhn, E. Serbest, and O. Haidn, "Investigations on the effect of foreign gas transpiration on a turbulent boundary layer," in *36th AIAA/ASME/SAE/ASEE Joint Propulsion Conference and Exhibit*, American Institute of Aeronautics and Astronautics, jul 2000.
- [52] S. R. Shine, S. S. Kumar, and B. N. Suresh, "A new generalised model for liquid film cooling in rocket combustion chambers," *International Journal of Heat and Mass Transfer*, vol. 55, pp. 5065–5075, sep 2012.
- [53] L. Denies, "Regenerative cooling analysis of oxygen/methane rocket engines," Master's thesis, Delft University of Technology, Dec. 2015.
- [54] C. H. Marchi, F. Laroca, A. F. C. da Silva, and J. N. Hinckel, "Numerical solutions of flows in rocket engines with regenerative cooling," *Numerical Heat Transfer, Part A: Applications*, vol. 45, pp. 699–717, apr 2004.
- [55] M. Naraghi, S. Dunn, and D. Coats, "A model for design and analysis of regeneratively cooled rocket engines," in *40th AIAA/ASME/SAE/ASEE Joint Propulsion Conference and Exhibit*, American Institute of Aeronautics and Astronautics, jul 2004.
- [56] W. K. Cho, W. S. Seol, M. Son, M. K. Seo, and J. Koo, "Development of preliminary design program for combustor of regenerative cooled liquid rocket engine," *Journal of Thermal Science*, vol. 20, pp. 467–473, sep 2011.
- [57] M. Naraghi, S. Dunn, and D. Coats, "Modeling of radiation heat transfer in liquid rocket engines," in *41st AIAA/ASME/SAE/ASEE Joint Propulsion Conference and Exhibit*, American Institute of Aeronautics and Astronautics, jul 2005.
- [58] Y. A. Çengel, *Heat Transfer: A Practical Approach*. McGraw-Hill series in mechanical engineering, McGraw-Hill, second ed., 2003.
- [59] H. Ziebland and R. C. Parkinson, *Heat transfer in rocket engines*. North Atlantic Treaty Organization, Advisory Group for Aerospace Research and Development, Sept. 1971.
- [60] M. Alberti, R. Weber, and M. Mancini, "Re-creating hottel's emissivity charts for water vapor and extending them to 40 bar pressure using HITEMP-2010 data base," *Combustion and Flame*, vol. 169, pp. 141–153, jul 2016.
- [61] M. Alberti, R. Weber, and M. Mancini, "Re-creating hottel's emissivity charts for carbon dioxide and extending them to 40 bar pressure using HITEMP-2010 data base," *Combustion and Flame*, vol. 162, pp. 597–612, mar 2015.
- [62] A. Bejan, *Convection Heat Transfer*. John Wiley & Sons, Inc., fourth ed., apr 2013.
- [63] F. P. Incropera, D. P. DeWitt, T. L. Bergman, and A. S. Lavigne, *Fundamentals of heat and mass transfer*. Hoboken, NJ: John Wiley & Sons, Inc., sixth ed., 2007.
- [64] M. Niino, A. Kumakawa, N. Yatsuyanagi, and A. Suzuki, "Heat transfer characteristics of liquid hydrogen as a coolant for the LO<sub>2</sub>/LH<sub>2</sub> rocket thrust chamber with the channel wall construction," in *18th Joint Propulsion Conference*, American Institute of Aeronautics and Astronautics, jun 1982.
- [65] M. Popp and G. Schmidt, "Rocket engine combustion chamber design concepts for enhanced life," in *32nd Joint Propulsion Conference and Exhibit*, American Institute of Aeronautics and Astronautics, jul 1996.
- [66] A. Bucchi, C. Bruno, and A. Congiunti, "Transpiration cooling performance in LOX/methane liquid-fuel rocket engines," *Journal of Spacecraft and Rockets*, vol. 42, pp. 476–486, may 2005.
- [67] J. A. Landis, "Numerical study of a transpiration cooled rocket nozzle," Master's thesis, Air Force Institute of Technology, Dec. 1995.
- [68] P. A. Davis, "Theoretical analysis of transpiration cooling of a liquid rocket thrust chamber wall," Master's thesis, Embry-Riddle Aeronautical University, 2006.

- [69] D. Nield and A. Bejan, *Convection in Porous Media*. Springer, third ed., 2006.
- [70] F. A. L. Dullien, *Porous media : fluid transport and pore structure*. San Diego: Academic Press, 1992.
- [71] W. Regulski, J. Szumbariski, L. Laniewski-Wollk, K. Gumowski, J. Skibiński, M. Wichrowski, and T. Wejrzanowski, "Pressure drop in flow across ceramic foams—a numerical and experimental study," *Chemical Engineering Science*, vol. 137, pp. 320–337, dec 2015.
- [72] W. S. Wong, D. S. S. Rees, and I. Pop, "Forced convection past a heated cylinder in a porous medium using a thermal nonequilibrium model: Finite peclet number effects," *International Journal of Thermal Sciences*, vol. 43, pp. 213–220, mar 2004.
- [73] J. Pallares and F. X. Grau, "A modification of a nusselt number correlation for forced convection in porous media," *International Communications in Heat and Mass Transfer*, vol. 37, pp. 1187–1190, nov 2010.
- [74] N. Wakao, S. Kaguei, and T. Funazkri, "Effect of fluid dispersion coefficients on particle-to-fluid heat transfer coefficients in packed beds," *Chemical Engineering Science*, vol. 34, no. 3, pp. 325–336, 1979.
- [75] D. Handley and P. J. Heggs, "Momentum and heat transfer mechanisms in regular shaped packings," *Chemical Engineering Research and Design*, vol. 46, 1968.
- [76] A. G. Dixon and D. L. Cresswell, "Theoretical prediction of effective heat transfer parameters in packed beds," *AIChE Journal*, vol. 25, pp. 663–676, jul 1979.
- [77] D. J. Gunn, "Transfer of heat or mass to particles in fixed and fluidised beds," *International Journal of Heat and Mass Transfer*, vol. 21, pp. 467–476, apr 1978.
- [78] A. R. Raffray and J. E. Pulsifer, "MERLOT: a model for flow and heat transfer through porous media for high heat flux applications," *Fusion Engineering and Design*, vol. 65, pp. 57–76, jan 2003.
- [79] E. A. Gauna and Y. Zhao, "Numerical simulation of heat transfer in porous metals for cooling applications," *Metallurgical and Materials Transactions B*, vol. 48, pp. 1925–1932, may 2017.
- [80] W. M. Kays and M. E. Crawford, *Convective heat and mass transfer*. McGraw-Hill, third ed., 1993.
- [81] M. Rachner, "Die stoffeigenschaften von kerosin jet A-1," tech. rep., German Aerospace Center, Mar. 1998.
- [82] F. Moukalled, L. Mangani, and M. Darwish, *The Finite Volume Method in Computational Fluid Dynamics*. Springer, 2016.
- [83] Y.-Q. Liu, Y.-B. Xiong, P.-X. Jiang, Y.-P. Wang, and J.-G. Sun, "Effects of local geometry and boundary condition variations on transpiration cooling," *International Journal of Heat and Mass Transfer*, vol. 62, pp. 362–372, jul 2013.
- [84] O. R. Alomar, M. A. A. Mendes, D. Trimis, and S. Ray, "Numerical simulation of complete liquid–vapour phase change process inside porous media: A comparison between local thermal equilibrium and non-equilibrium models," *International Journal of Thermal Sciences*, vol. 112, pp. 222–241, feb 2017.
- [85] T. Langener, J. von Wolfersdorf, M. Selzer, and H. Hald, "Experimental investigations of transpiration cooling applied to c/c material," *International Journal of Thermal Sciences*, vol. 54, pp. 70–81, apr 2012.
- [86] W. M. Grisson, "Liquid film cooling in rocket engines," tech. rep., Arnold Engineering Development Center, Mar. 1991.
- [87] C. Kirchberger, G. Schlieben, and O. Haidn, "Assessment of analytical models for film cooling in a hydrocarbon/GOX rocket combustion chamber," in *48th AIAA/ASME/SAE/ASEE Joint Propulsion Conference & Exhibit*, American Institute of Aeronautics and Astronautics, jul 2012.
- [88] E. Knuth, "The mechanics of film cooling - part 2," *Journal of Jet Propulsion*, vol. 25, pp. 16–25, jan 1955.
- [89] J. L. Stollery and A. A. M. El-ehwany, "A note on the use of a boundary-layer model for correlating film-cooling data," *International Journal of Heat and Mass Transfer*, vol. 8, pp. 55–65, jan 1965.

- [90] M. Trotti, "Modelling of liquid film cooling in a GOX/kerosene rocket combustion chamber," Master's thesis, Politecnico di Milano, 2012.
- [91] A. Ponomarenko, "RPA: Tool for rocket propulsion analysis: Thermal analysis of thrust chambers," documentation, July 2012.
- [92] S. Soller, R. Wagner, C. Kirchberger, H.-P. Kau, P. Martin, and C. Maeding, "Characterisation of combustion and heat transfer using GOX/kerosene in a single-element rocket combustor," in *41st AIAA/ASME/SAE/ASEE Joint Propulsion Conference & Exhibit*, American Institute of Aeronautics and Astronautics, jul 2005.
- [93] E. A. Moreira, M. Innocentini, and J. R. Coury, "Permeability of ceramic foams to compressible and incompressible flow," *Journal of the European Ceramic Society*, vol. 24, pp. 3209–3218, sep 2004.
- [94] C. Song, P. Wang, and H. A. Makse, "A phase diagram for jammed matter," *Nature*, vol. 453, pp. 629–632, may 2008.
- [95] S. M. Ahmadi, S. Amin Yavari, R. Wauthle, B. Pouran, J. Schrooten, H. Weinans, and A. Zadpoor, "Additively manufactured open-cell porous biomaterials made from six different space-filling unit cells: The mechanical and morphological properties," *Materials*, vol. 8, pp. 1871–1896, 04 2015.
- [96] L. Yuan, S. Ding, and C. Wen, "Additive manufacturing technology for porous metal implant applications and triple minimal surface structures: A review," *Bioactive Materials*, vol. 4, pp. 56–70, dec 2019.
- [97] O. Al-Ketan, R. Rowshan, and R. K. A. Al-Rub, "Topology-mechanical property relationship of 3d printed strut, skeletal, and sheet based periodic metallic cellular materials," *Additive Manufacturing*, vol. 19, pp. 167–183, jan 2018.
- [98] D. Li, W. Liao, N. Dai, and Y. M. Xie, "Comparison of mechanical properties and energy absorption of sheet-based and strut-based gyroid cellular structures with graded densities," *Materials*, vol. 12, p. 2183, jul 2019.
- [99] R. J. Moffat, "Describing the uncertainties in experimental results," *Experimental Thermal and Fluid Science*, vol. 1, pp. 3–17, jan 1988.
- [100] J. C. Heigel, P. Michaleris, and E. W. Reutzel, "Thermo-mechanical model development and validation of directed energy deposition additive manufacturing of ti-6al-4v," *Additive Manufacturing*, vol. 5, pp. 9–19, jan 2015.
- [101] A. Ponomarenko, "RPA: Tool for liquid propellant rocket engine analysis C++ implementation," documentation, May 2010.



# A

## Additional regenerative cooling model verification

The regenerative cooling model is validated in chapter 2. As an additional verification step, a comparison to the commercial software Rocket Propulsion Analysis (RPA) was made. RPA is an analysis tool used for conceptual and preliminary designs of rocket engines. The comparison discussed in this chapter focuses on the hot side heat transfer calculation. The same calculations are used in the transpiration and film cooling model discussed in respectively chapter 3 and chapter 4.

As a verification case, a rocket engine is modelled with the regenerative cooling model of this thesis and with RPA. Due to limitations, a constant hot side wall temperature of 700 K is taken. This still allows for a comparison between the heat fluxes of both models.

A comparison between the convective heat transfer coefficient - determined in both models by the Bartz equation (Equation 2.4) - can be seen in Figure A.1. The difference between the two can be seen in Figure A.2. The two heat transfer coefficients differ with a maximum of 11.4%. An analysis was performed to explain this difference. As the equations used are exactly the same and all inputs as well, the difference is attributed to a different use of the Mach number. In RPA the Mach number is calculated using isentropic flow relations [101], while in the current model, the values obtained from NASA's CEA [13] at different area ratios are interpolated. It is the opinion of the author that the latter is more logical.

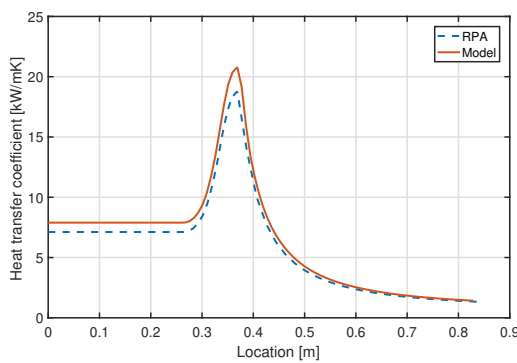


Figure A.1: The heat transfer coefficient of the model compared to one obtained from RPA for the verification case.

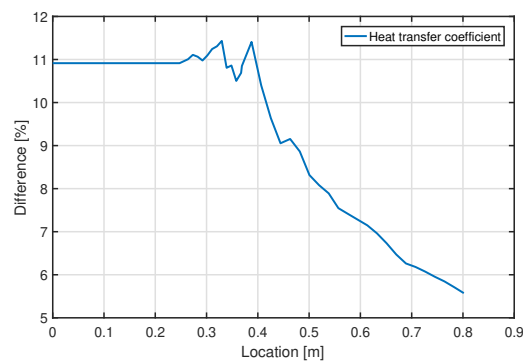


Figure A.2: The difference between the convective heat transfer coefficient of the model and RPA.

The convective and radiation heat flux of both the model and RPA can be seen in Figure A.3 and the differences in Figure A.4. A difference of 11% in the convective heat transfer coefficient is present. The difference between the radiative heat transfer is larger with a maximum of 170%, but this quickly drops to 35% in the cylindrical part of the engine. As the radiative heat transfer in the current model is based on a simple empirical relation, it is to be expected that it differs from the more sophisticated RPA model.

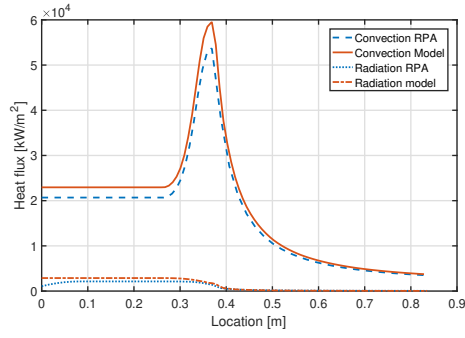


Figure A.3: The difference between the convective heat transfer coefficient of the model and RPA.

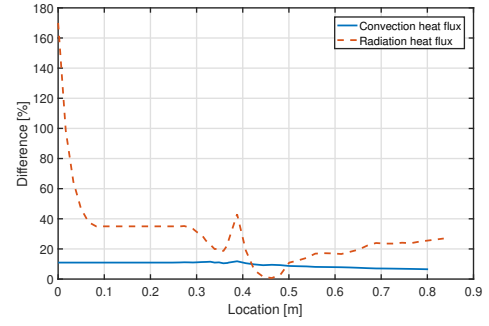


Figure A.4: The difference between the convective heat transfer coefficient of the model and RPA.

The RPA model and the model described in this thesis show the same trends in heat transfer. However, an error of 11.4% in magnitude for the convective heat transfer occurs. The radiative heat transfer also follows the same trend as the one from RPA. The error of 35% is large. However, radiation heat transfer is difficult to model and therefore this error is accepted.

Another aspect regarding the convective heat transfer is that both RPA and the model developed give a constant convective heat flux in the cylindrical part of the engine. However, it is known from literature that the heat flux predicted by the Bartz equation varies from actual one, especially in the cylindrical section [7, 48].

# B

## CoolProp validation for ethanol and methane properties

The code developed in this thesis uses the freely available tool called 'CoolProp' [4] to determine the transport and thermodynamic properties of the coolants. To validate the accuracy of the obtained properties, the CoolProp values are compared to the Chemistry WebBook of the National Institute of Standards and Technology (NIST) [6] and REFPROP in this appendix. The main coolant used in this thesis is ethanol, and its properties are compared in section B.1. A methane and LOX engine is used to validate the regenerative cooling model in chapter 2 and thus the methane properties are also compared in section B.2.

### B.1. Ethanol

The fluid properties of ethanol are not available in the NIST Chemistry WebBook, but are available in REFPROP version 8.0 which is a software tool also developed by NIST. A comparison between the density, isobaric specific heat, viscosity and thermal conductivity of ethanol obtained using CoolProp and REFPROP can be seen in Figure B.1 to Figure B.4.

The REFPROP database gives a validity range for the temperature between 120 K and 800 K and for pressures up to 2800 bar. Furthermore, the uncertainties are given. The uncertainties are 0.2% for density and 3% in heat capacity. For the viscosity the uncertainty is estimated to be 3% and this increases to 10% at pressures of 1000 bar. For the thermal conductivity, the estimated uncertainty in the liquid phase is approximately 5% and 10% in the vapor phase.

In the figures, it can be seen that the density has perfect agreement and that the isobaric specific heat has perfect agreement except at the peaks close to the critical temperature. For 80 bar, the difference is 20% and for 120 bar it is 7%. The viscosity also has perfect agreement. Lastly, the thermal conductivity differs slightly from the REFPROP values where the maximum difference stays below 5%. The results are summarized in Table B.1.

Property	REFPROP uncertainties	Differences with CoolProp	Comment
$\rho$	0.20%	0%	
$c_p$	3%	0%-20%	Large differences only at peak of $c_p$
$\mu$	3%	0%	
$k$	5%	5%	

Table B.1: Summary of the uncertainties for ethanol in REFPROP and the differences with CoolProp.

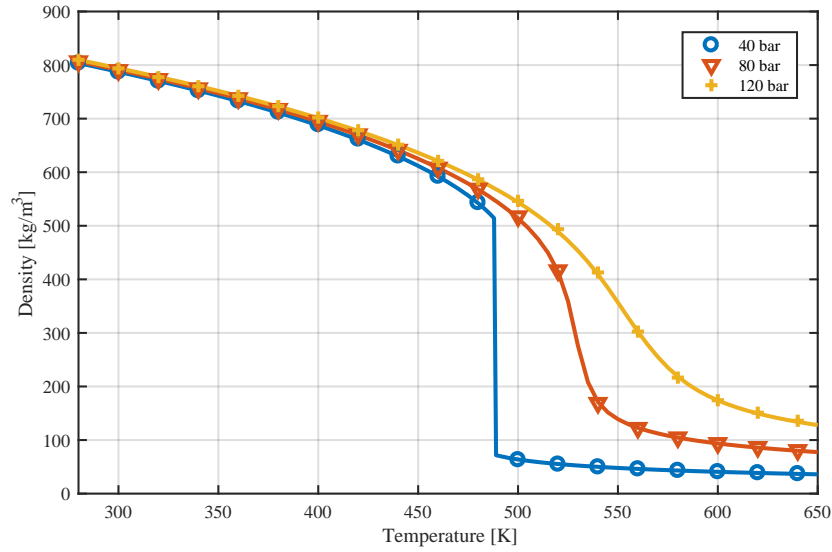


Figure B.1: Comparison of the density of ethanol of CoolProp (markers) to the one of REFPROP (lines) at different pressures and temperatures.

## B.2. Methane

A comparison of the properties for methane between CoolProp and the NIST Chemistry WebBook can be seen in Figure B.5 to Figure B.8. The properties for methane are valid for a temperature range between 90.7 K and 625 K. The uncertainties in density are 0.03% for pressures below 120 bar and temperatures below 350 K and up to 0.07% for pressures less than 500 bar. The heat capacities have an uncertainty of 1%. The uncertainty in thermal conductivity of the dilute gas between 130 and 625 K is 2.5%. Excluding the dilute gas, the uncertainty is 2% between 110 K and 725 K at pressures up to 700 bar. Near the critical point, the uncertainty is 5% or greater. Lastly, the uncertainty in viscosity is 2%, except in the critical region where it is 5% [6].

In the four figures, it can be seen that the values obtained from NIST match the ones from CoolProp perfectly for all properties. Taking into account the described accuracies of the NIST data and the match between the NIST data and the CoolProp, it can be concluded that CoolProp is validated for the use of methane.

Property	NIST uncertainties	Differences with CoolProp
$\rho$	0.03%-0.07%	0%
$c_p$	1%	0%
$\mu$	2%-5%	0%
$k$	2%-2.5%	0%

Table B.2: Summary of the uncertainties for methane in NIST [6] and the differences with CoolProp.

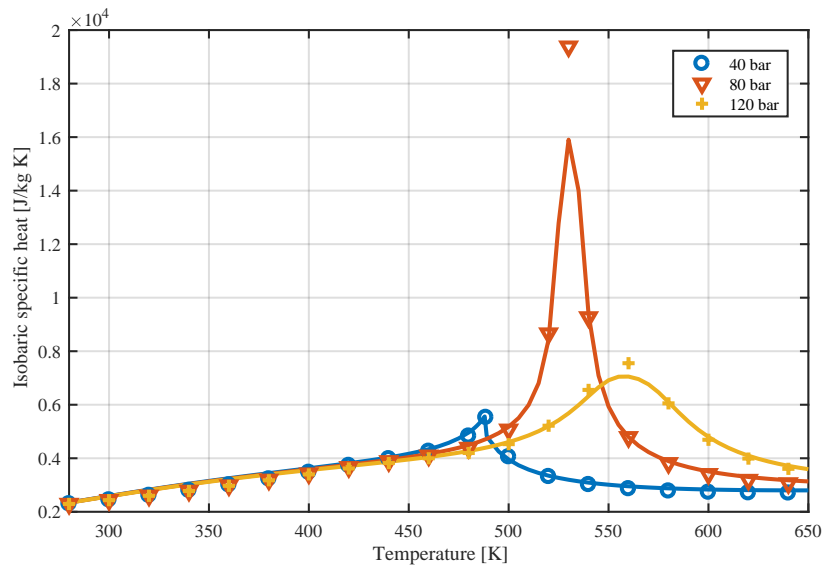


Figure B.2: Comparison of the isobaric specific heat of ethanol of CoolProp (markers) to the one of REFPROP (lines) at different pressures and temperatures.

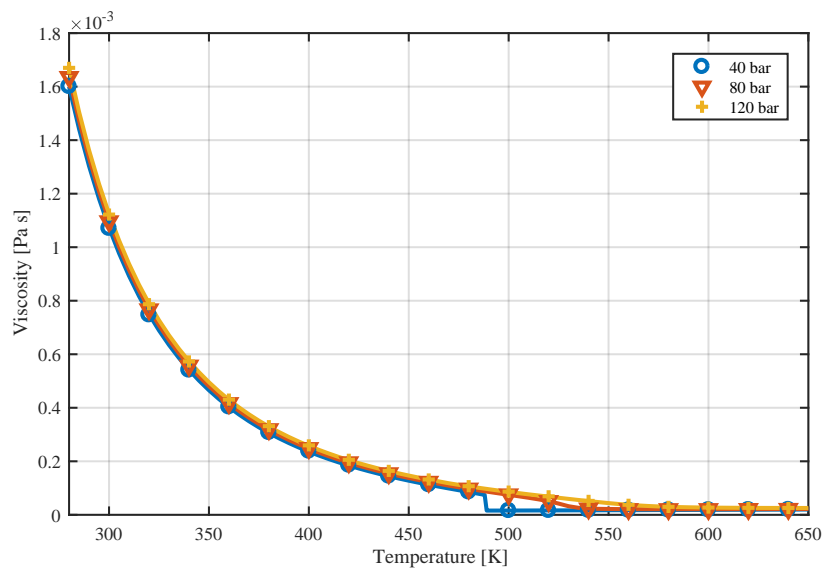


Figure B.3: Comparison of the viscosity of ethanol of CoolProp (markers) to the one of REFPROP (lines) at different pressures and temperatures.

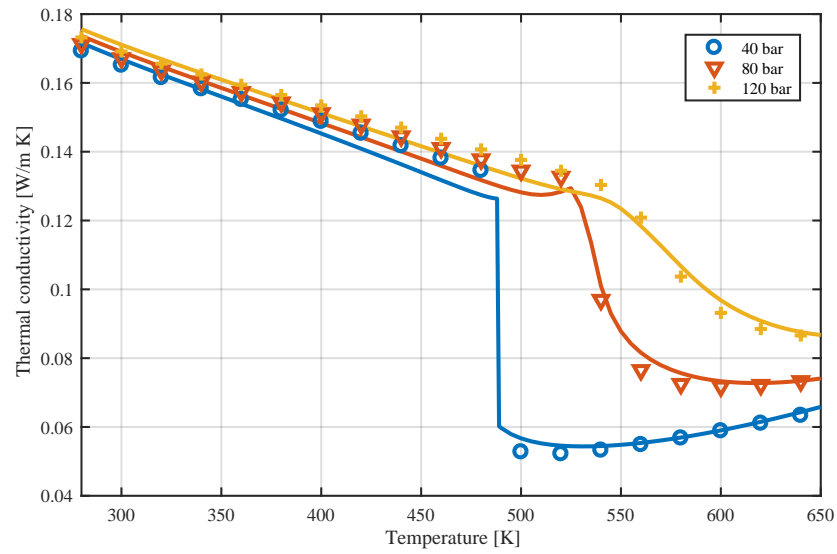


Figure B.4: Comparison of the thermal conductivity of ethanol of CoolProp (markers) to the one of REFPROP (lines) at different pressures and temperatures.

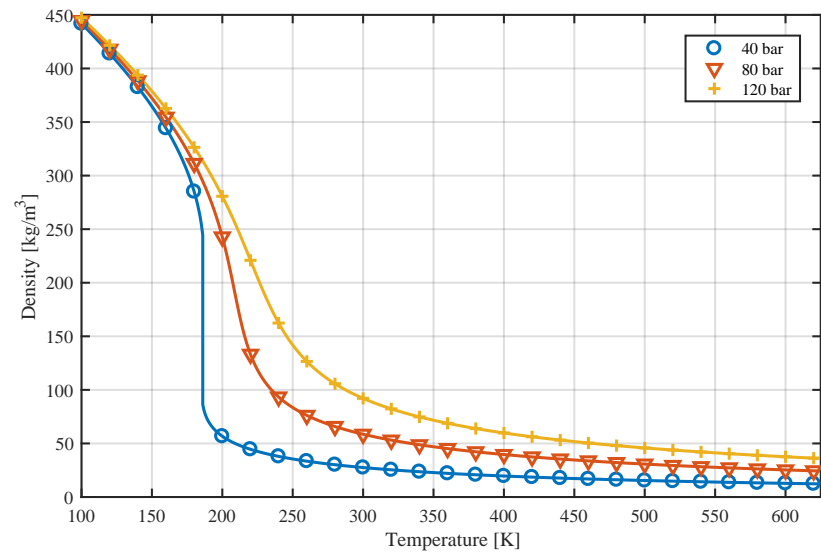


Figure B.5: Comparison of the density of methane of CoolProp (markers) to the one of NIST [6] (lines) at different pressures and temperatures.

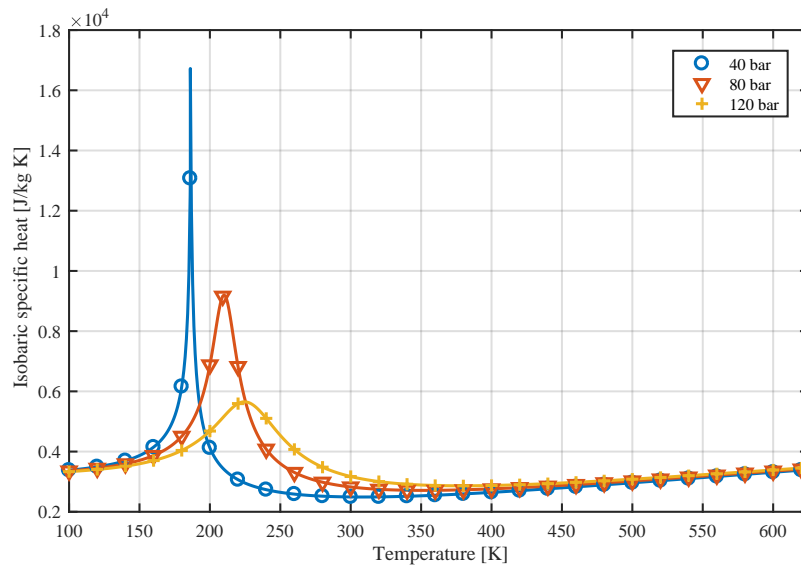


Figure B.6: Comparison of the isobaric specific heat of methane of CoolProp (markers) to the one of NIST [6] (lines) at different pressures and temperatures.

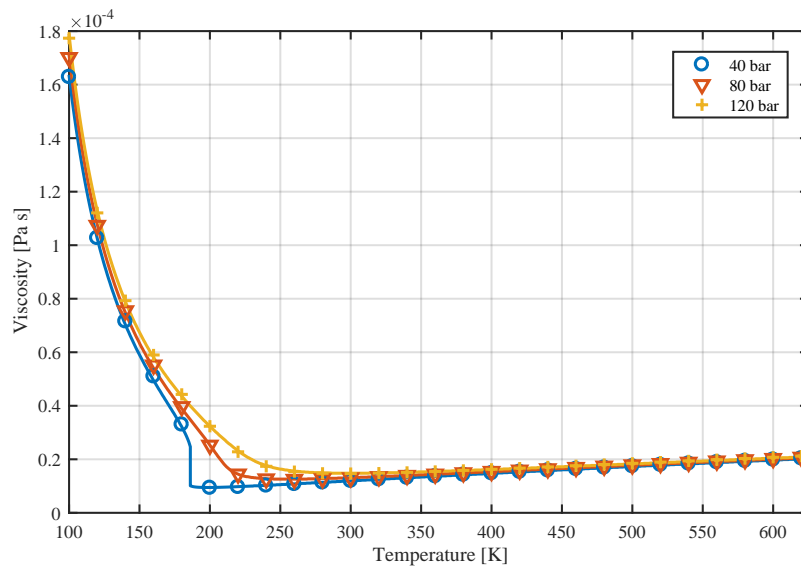


Figure B.7: Comparison of the viscosity of methane of CoolProp (markers) to the one of NIST [6] (lines) at different pressures and temperatures.

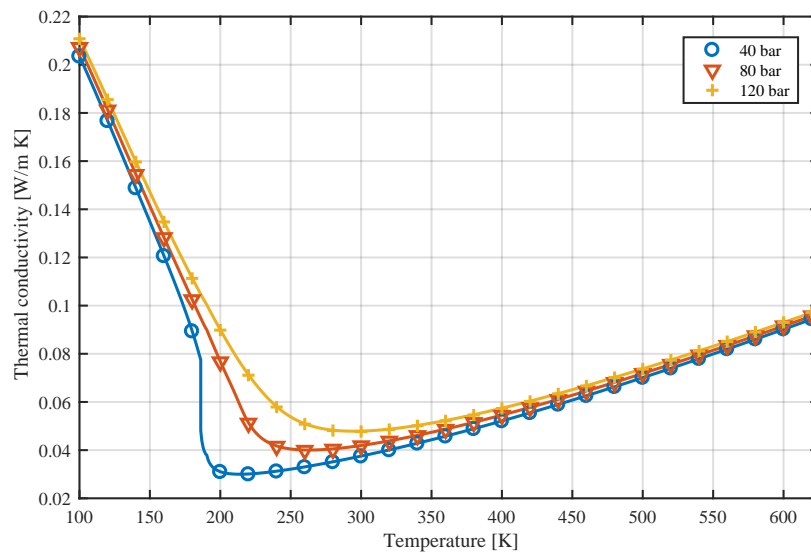


Figure B.8: Comparison of the thermal conductivity of methane of CoolProp (markers) to the one of NIST [6] (lines) at different pressures and temperatures.



# C

## Implementation of the transpiration cooling model

Some parts of the implementation of the transpiration cooling model treated in chapter 3 are too extensive for the main body. Therefore, they are discussed in this appendix.

From the required governing equations, the implementation of the continuity and momentum equation (given by the Darcy-Forchheimer equation) are straightforward. The coolant properties vary in the wall due to the change in pressure and temperature. This is taken into account by solving the equation for every single location. The implementation of the energy equations is more extensive and is discussed in section C.1. Then in section C.2, the used grid is described.

### C.1. Code implementation energy equations

Two different options exist for the energy equations. One can assume that the heat transfer within the porous wall is infinitely fast and that the solid and coolant are locally the same temperature. This is called the local thermal equilibrium (LTE) assumption. If one assumes that the heat transfer is not infinitely fast and that the solid and coolant can locally be different temperatures, the local thermal non-equilibrium (LTNE) assumption is used.

The energy equations for both the local thermal equilibrium and the local thermal non-equilibrium require further derivation to be implemented. Then they need to be rewritten as a system of first-order equations to be used in the code. The energy equations are second order differential equations and a standard Matlab function is used to solve these equations. For one iteration, the properties (density, velocity, etc.) are seen as constant and then the 'bvp4c' function can be used. Using a standard Matlab function was preferred due to its robustness, but the speed of solving is reduced as the function requires many interpolations to find the coolant properties. The further derivation and the system of first-order equations for the LTE and LTNE case are discussed in the next sections.

#### C.1.1. Energy equation local thermal equilibrium

The energy equation for LTE for steady state in cylindrical coordinates was introduced by Equation 3.9 and is restated in Equation C.1. To use the equation in the bvp4c Matlab function, it is required to write it as a system of first-order equations. To obtain these, it first needs to be rearranged and this is done below. Note that the thermal conductivity of the medium  $k_m$  is a function of radius and is thus not constant.

$$\frac{1}{r} \frac{d}{dr} \left( k_m \cdot r \frac{dT}{dr} \right) - \rho_c c_{p_c} v_c \frac{dT}{dr} = 0 \quad (C.1)$$

$$\frac{1}{r} \left( \frac{d}{dr} (k_m r) \frac{dT}{dr} + k_m r \frac{d^2 T}{dr^2} \right) - \rho_c c_{p_c} v_c \frac{dT}{dr} = 0 \quad (C.2)$$

$$\frac{1}{r} \left( \left( \frac{d}{dr} (k_m) r + k_m \frac{dr}{dr} \right) \frac{dT}{dr} + k_m r \frac{d^2 T}{dr^2} \right) - \rho_c c_{p_c} v \frac{dT}{dr} = 0 \quad (C.3)$$

$$k_m \frac{d^2 T}{dr^2} + \frac{d}{dr} (k_m) \frac{dT}{dr} + \frac{1}{r} k_m \frac{dT}{dr} - \rho_c c_{p_c} v \frac{dT}{dr} = 0 \quad (C.4)$$

This can be written in a system of first-order equations:

$$T'_1 = T_2 = \frac{dT}{dr} \quad (C.5)$$

$$T'_2 = \frac{\rho_c c_{p_c} v T_2 - \frac{k_m}{r} T_2 - \frac{d}{dr} (k_m) T_2}{k_m} \quad (C.6)$$

Equation C.5 and Equation C.6 can be implemented in Matlab using the `bv4pc` function and after the boundary conditions and an initial guess are specified, Matlab solves the differential equation.

### C.1.2. Energy equation local thermal non-equilibrium

For the LTNE case, two energy equations are needed. First, the solid energy equation is worked out more. The thermal conductivity of the wall is assumed to be constant. However, the porosity can vary within the wall. To simplify the further derivation, an effective thermal conductivity is used defined by Equation C.7.

$$k_{s\text{eff}}(r) = (1 - \epsilon(r)) \cdot k_s \quad (C.7)$$

The steady state solution in cylindrical coordinates was already given by Equation 3.12 and with the effective thermal conductivity this becomes Equation C.8. The further derivation is as follows:

$$\frac{1}{r} \frac{d}{dr} \left( k_{s\text{eff}} r \frac{dT_s}{dr} \right) - h_v (T_s - T_c) = 0 \quad (C.8)$$

$$\frac{1}{r} \left( \frac{d}{dr} (k_{s\text{eff}} r) \frac{dT_s}{dr} + k_{s\text{eff}} r \frac{d^2 T_s}{dr^2} \right) - h_v (T_s - T_c) = 0$$

$$\frac{1}{r} \left( \left( \frac{d}{dr} (k_{s\text{eff}}) r + k_{s\text{eff}} \frac{dr}{dr} \right) \frac{dT_s}{dr} + k_{s\text{eff}} r \frac{d^2 T_s}{dr^2} \right) - h_v (T_s - T_c) = 0$$

$$k_{s\text{eff}} \frac{d^2 T_s}{dr^2} + \frac{d}{dr} (k_{s\text{eff}}) \frac{dT_s}{dr} + \frac{1}{r} k_{s\text{eff}} \frac{dT_s}{dr} - h_v (T_s - T_c) = 0 \quad (C.9)$$

The steady state liquid energy equation in cylindrical coordinates for LTNE is given by Equation 3.13 and restated in Equation C.11. Again to simplify it, an effective thermal conductivity is used, see Equation C.10.

$$k_{c\text{eff}}(r) = \epsilon(r) \cdot k_c(r) \quad (C.10)$$

$$\frac{1}{r} \frac{d}{dr} \left( k_{c\text{eff}} r \frac{dT_c}{dr} \right) - \rho_c c_{p_c} v_c \frac{dT_c}{dr} - h_v (T_c - T_s) = 0 \quad (C.11)$$

The further derivation is discussed below. As the effective thermal conductivity changes radially as either the thermal conductivity, the porosity or both change, the product rule is required:

$$\frac{1}{r} \left( \frac{d}{dr} (k_{\text{eff}} \cdot r) \frac{dT_c}{dr} + k_{\text{eff}} r \frac{dT_c^2}{dr^2} \right) - \rho_c c_{p_c} v_c \frac{dT_c}{dr} - h_v (T_c - T_s) = 0$$

$$\frac{1}{r} \left( \left( \frac{d}{dr} (k_{\text{eff}}) \cdot r + k_{\text{eff}} \frac{dr}{dr} \right) \frac{dT_c}{dr} + k_{\text{eff}} r \frac{dT_c^2}{dr^2} \right) - \rho_c c_{p_c} v_c \frac{dT_c}{dr} - h_v (T_c - T_s) = 0$$

$$k_{\text{eff}} \frac{dT_c^2}{dr^2} + \frac{d}{dr} (k_{\text{eff}}) \cdot \frac{dT_c}{dr} + \frac{1}{r} k_{\text{eff}} \frac{dT_c}{dr} - \rho_c c_{p_c} v_c \frac{dT_c}{dr} - h_v (T_c - T_s) = 0 \quad (\text{C.12})$$

It is possible to place two differential equations in one system of differential equations in the Matlab `bvp4c` function. This increases the solution speed compared to handling the solid and coolant energy equation separately. To combine the energy equations in one system, the solid temperature is seen as  $T_1$  and the coolant temperature as  $T_3$ . The system of first-order equations is given by the four equations below and consists of the rearranged solid and liquid energy equations derived above.

$$T'_1 = T_2 = \frac{dT_s}{dr} \quad (\text{C.13})$$

$$T'_2 = \frac{h_v (T_1 - T_3) - \frac{k_{\text{eff}}}{r} T_2 - \frac{d}{dr} (k_{\text{eff}}) T_2}{k_{\text{eff}}} \quad (\text{C.14})$$

$$T'_3 = T_4 = \frac{dT_c}{dr} \quad (\text{C.15})$$

$$T'_4 = \frac{h_v (T_3 - T_1) + \rho_c c_{p_c} v_c T_4 - \frac{k_{\text{eff}}}{r} T_4 - \frac{d}{dr} (k_{\text{eff}}) T_4}{k_{\text{eff}}} \quad (\text{C.16})$$

This concludes the implementation of the energy equations in the Matlab code used in the model.

## C.2. Grid

The grid used in the wall is a Chebyshev grid which has more nodes closer towards the end of the wall (the combustion chamber side) compared to a regular spaced grid. Close to the combustion chamber, the gradients of the properties are higher, so a closer grid spacing is beneficial. The Chebyshev nodes can be found using Equation C.17 and then the values from 0 to 1 are used and multiplied with the actual wall thickness. An example of how the grid look like can be seen in Figure C.1 and it is clear that on the hot side of the wall the nodes are spaced closer together.

$$x_n = \cos \left( \frac{2k-1}{2n} \pi \right), k = 1, \dots, n \quad (\text{C.17})$$

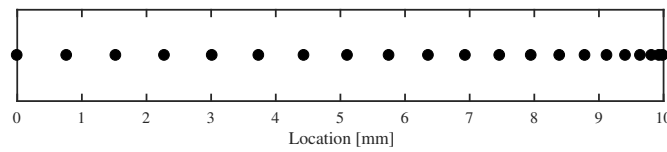


Figure C.1: An example of the Chebyshev nodes used as grid.





# Abstract Space Propulsion Conference 2020

The research conducted in this thesis will be used to write a paper for the Space Propulsion Conference 2020. The abstract given below was originally submitted and accepted.

## **A comparison between film and transpiration cooling performance in a rocket combustion chamber**

2. Propulsion for space transportation

2.11. Modelling (CFD & validation of cryogenic, liquid, solid, hybrid; application to rocket engines, fluid management in micro gravity, combustion instabilities etc)

S.T. Koehler, B.T.C. Zandbergen

*Delft University Of Technology - Delft (Netherlands)*

### **Introduction**

Transpiration cooling is an effective cooling method to shield surfaces from high heat fluxes such as rocket engine combustion chambers. Recently, there has been revived interest in transpiration cooling with a focus on using additive manufacturing techniques to produce the porous walls [1] [2]. This allows for easier production and optimizing of the transpiration cooled wall compared to the commonly used sintered metals. Furthermore, the material strength is higher than the sintered metals [1]. In the application of rocket engines, transpiration cooling is mainly competing with the combination of regenerative and film cooling. The potential benefits of transpiration cooling over film cooling are that a lower coolant mass flow is required to achieve the same wall temperatures and thus reducing the losses in specific impulse. Secondly, the pressure losses associated with the regenerative cooling channels can be reduced.

### **Discussion**

Film cooling reduces the heat flow to the wall due to the presence of a film that 'shields' the wall from the heat. Transpiration cooling also uses this principle and adds extra cooling by the coolant flowing through the porous wall. So, transpiration cooling and film cooling are similar in nature and if subsequently more film cooling holes are added, the cooling converges to transpiration cooling. While comparisons between regenerative and transpiration cooling have been made, a detailed comparison between film and transpiration cooling is currently lacking in literature. Therefore, a numerical model is developed that allows for this comparison and for rapid optimization of the parameters used.

The model is applied to a film cooled reference engine and allows for gaseous and supercritical coolants. One dimensional heat transfer radial to the wall is considered. The transpiration cooling model can handle the local thermal non-equilibrium (LTNE) and local thermal equilibrium (TLE) condition, but the LTNE is found to be sufficient for the analysis. Furthermore, Darcy-Forchheimer's law is used to model the coolant velocity within the wall.

### **Conclusion**

The temperatures and temperature gradients in the wall are compared and an estimation of the losses in specific impulse is made. This paper presents the model and the outcomes of the comparison.

**Bibliography**

- [1] Huang, G., Min, Z., Yang, L., Jiang, P.X., Chyu, M. (2018). Transpiration cooling for additive manufactured porous plates with partition walls. *International Journal of Heat and Mass Transfer* (124), 1076-1087
- [2] Min, Z., Huang, G., Parbat, S.N., Yang, L., Chyu, M.K., (2019) Experimental Investigation on Additively Manufactured Transpiration and Film Cooling Structures. *Journal of Turbomachinery* (141)